

Dissertation
submitted to the
Combined Faculties for the Natural Sciences and for
Mathematics
of the Ruperto-Carola University of Heidelberg, Germany
for the degree of
Doctor of the Natural Sciences

Put forward by

M. Sc. Patrick Udo Wilhelm

born in Rotenburg a.d. Fulda

Oral examination: 11th July 2019

**First Studies of
Low-Energy Electron Cooling
of keV Energy Ion Beams at the
Electrostatic Cryogenic Storage Ring
CSR**

Patrick Wilhelm

Referees:

Prof. Dr. Andreas Wolf
Prof. Dr. André Schöning

Zusammenfassung

In dieser Arbeit wurde ein Elektronenkühler, der auch als Target für Elektron-Ion Rekombinationsexperimente dient, am elektrostatischen kryogenen Speicherring CSR implementiert und in Betrieb genommen. Das Photokathodensystem für kalte Elektronenstrahlen des Ionenspeicherrings TSR wurde in den CSR Elektronenkühler integriert. Nach ersten Betriebstests des Elektronenstrahltransports, realisiert mit supraleitenden Magnetspulen im kryogenen Teil des Speicherrings, wurden systematische Studien zur Elektronenkühlung von gespeicherten Ionenstrahlen mit Energien im keV Bereich durchgeführt. Effiziente Elektronenkühlung der atomaren Ionen F^{6+} und O^+ sowie der molekularen Ionen HeH^+ und HD^+ wurde bei extrem niedrigen Elektronenenergien bis zu etwa 10 eV und bei niedrigen Elektronendichten im Bereich von nur wenigen 10^5 cm^{-3} realisiert und untersucht. Kühlzeiten im Bereich weniger Sekunden und transversale Strahlbreiten gekühlter Ionenstrahlen im Millimeterbereich konnten gezeigt werden. Des Weiteren wurde das Aufblähen der transversalen Strahlbreiten sowie der Bunchlängen von gekühlten Ionenstrahlen aufgrund diffusiver Aufheizprozesse wie strahlinterner Streuung durch Veränderung des Ionenstroms vermessen. Ebenso wurden Raumladungseffekte von gebunchten Ionenstrahlen im elektronengekühlten Gleichgewicht untersucht.

Abstract

In the present work a novel electron-ion merged-beam setup for electron cooling and electron-ion recombination studies has been implemented in the electrostatic cryogenic storage ring CSR and commissioned. The photocathode setup for cold electron beams previously operating at the heavy ion storage ring TSR has been integrated in the CSR electron cooler. After first tests of the electron beam transport, realized by superconducting magnets in the cryogenic part of the storage ring, systematic studies of electron cooling of stored keV ion beams were performed. Efficient electron cooling of atomic ions F^{6+} and O^+ as well as molecular ions HeH^+ and HD^+ has been realized and investigated at low electron energies down to about 10 eV and at low electron densities of only a few times 10^5 cm^{-3} . Electron cooling times in the range of only a few seconds and transverse beam widths of cooled ion beams in the millimeter range have been shown. The blow-up of the transverse beam widths and bunch lengths of electron cooled ion beams due to diffusive heating processes like intrabeam-scattering has been measured by varying the ion current. Furthermore, space charge effects of bunched ion beams have been investigated in an electron cooled equilibrium.

Contents

1	Introduction	1
1.1	Merged-beam physics in ion storage rings	1
1.2	The CSR: A novel machine for cold molecules	2
1.3	Low-energy electron cooling at the CSR	3
1.4	Outline of this work	4
2	Electron cooling in ion storage rings	5
2.1	Ion optics and phase space	5
2.1.1	Definition of phase space coordinates	5
2.1.2	Transverse beam dynamics	7
2.1.3	Definition of ion beam temperatures	11
2.1.4	Phase slip factor and dispersion function	12
2.1.5	Longitudinal beam dynamics and Rf-bunching	13
2.2	Electron cooling and diffusion heating	20
2.2.1	Motivation for phase space cooling	20
2.2.2	Basic idea of electron cooling	21
2.2.3	Electron cooling rates	22
2.2.4	Fokker-Planck equation	24
2.2.5	Binary collision model	26
2.2.6	Calculation of electron cooling rates from approximation formulae	32
2.3	Ion beam space charge effects	35
2.3.1	Space charge tune shift	36
2.3.2	Space charge limit of ion bunch lengths	37
2.4	Intrabeam-scattering	39
2.4.1	Simplified intrabeam-scattering model	40
2.5	Electron cooling and diffusion in equilibrium	41
3	The CSR electron-ion merged-beam setup	43
3.1	Overview of the CSR facility	43
3.2	GaAs photocathode cold electron source	45
3.2.1	NEA GaAs photocathodes	45
3.2.2	The electron gun design	46

Contents

3.3	Magnetized electron beam temperatures	48
3.3.1	Adiabatic magnetic expansion	49
3.3.2	Longitudinal temperature	50
3.3.3	Electron velocity distribution	50
3.4	Magnetic guiding field for electron beam transport	51
3.5	Realization of the setup in the CSR	54
3.5.1	High voltage platform and electronic circuit	59
3.5.2	Electron cooler as a cold-electron target	62
3.5.3	Performance of the HTS coil-cooling system	63
3.6	CSR ion beam diagnostics for electron cooling studies	67
3.6.1	Wire scanner beam position measurements	67
3.6.2	Capacitive current pick-ups	68
3.6.3	Bunched-beam detection of electron cooling and cooling energy	72
3.6.4	Transverse ion beam profile measurements by neutral fragment imaging	76
3.7	Electron beam profile measurements	79
3.7.1	Setup	79
3.7.2	Measurements	83
4	Low-energy electron cooling studies of keV ion beams in the CSR	90
4.1	First demonstration and tuning of electron cooling	91
4.2	Longitudinal cooling of bunched beams	93
4.2.1	Measurement procedure	93
4.2.2	F ⁶⁺ bunched-beam cooling	96
4.2.3	HeH ⁺ bunched-beam cooling	98
4.2.4	Dependencies of the longitudinal cooling rate	101
4.2.5	Ion beam intensity evolution during electron cooling	105
4.3	Longitudinal cooling of Schottky spectra	109
4.3.1	Space charge cooling point	109
4.3.2	Electron cooled Schottky spectra for HD ⁺	111
4.4	Transverse electron cooling measurements of coasting ion beams	116
4.4.1	Measurement procedure	116
4.4.2	Transverse electron cooling times	118
4.4.3	Dependency of the transverse cooling rate on the electron beam density	128
4.5	Investigation of Intrabeam-scattering at the CSR	132
4.5.1	IBS of bunched beams	132
4.5.2	IBS of coasting beams	135
4.6	Equilibrium cooled beam	139
4.6.1	Space charge limit of electron cooled ion bunches	139
4.6.2	Equilibrium of electron cooling and IBS	143

4.7 Summary of electron cooling performance	145
5 Conclusion and outlook	149
Appendices	152
A Schottky noise spectra measurements	153
A.1 HD ⁺	153
B Estimate of initial ion beam temperatures	156
B.1 Longitudinal ion beam temperature from rf-bunching simulation . .	156
B.2 Longitudinal ion beam temperature from Schottky noise spectra measurement	158
B.3 Transverse ion beam temperatures	159
C Analytical IBS model	161
References	163
Danksagung	170

1 Introduction

1.1 Merged-beam physics in ion storage rings

Fast ion beam setups, like ion storage rings, offer the opportunity to study a broad range of particle reactions, having a broad range of applications in elementary particle, nuclear, atomic and even molecular physics. On the one hand, collision beam experiments, as they are carried out for example at the CERN Large Hadron Collider (LHC), explore reactions at highest collision energies in order to investigate or even find new elementary particles. On the other hand, for atomic and molecular systems, lower energies down to the eV and meV range are of interest.

Lowest collision energies down to the order of only 1 meV can be achieved by using merged-beam techniques [1]. With this approach, a fast ion beam is merged in a collinear fashion over an extended interaction length in the storage ring with a target beam of similar velocity. An example for such a target beam is given by an electron beam which is guided and merged with the ions in a dedicated electron-ion interaction region. By a detuning of the velocity of the electrons, high energy-resolution experiments with ultra low center-of-mass energies can be performed.

Moreover, the merged-beams technique can be advantageous for studying highly reactive or short-lived systems while guaranteeing a high detection efficiency of collisional reaction products due to their high laboratory-frame velocity [1].

A strong motivation for the investigation of especially low-energy electron-ion reactions in the laboratory comes from the field of astrochemistry. Over the years, astrophysical observatories have improved their spectroscopical capabilities, leading to a steadily increasing number of molecular ions that have been observed in space [2], for example in cold molecular clouds in the interstellar medium (ISM) or planetary nebulae.

In order to understand the atomic and molecular abundances in such astrophysical plasmas, and to understand the dynamics of their complex chemical reaction networks, models are calculated relying on measured reaction cross sections. A reaction type of great importance in cold molecular clouds is dissociative recombination (DR) [3]. In this process, a molecular ion captures a free electron and subsequently undergoes a dissociative break-up. Merged-beam electron-ion colli-

1 Introduction

sion studies in storage rings in the last years have made essential advances to a deeper understanding of the DR process. DR measurements have been carried out, for example, at the CRYRING in Stockholm, Sweden [4], the TARN II storage ring in Tanashi, Japan [5], the heavy ion storage ring ASTRID in Århus, Denmark [6] and at the TSR heavy ion storage ring in Heidelberg, Germany [7].

1.2 The CSR: A novel machine for cold molecules

The above mentioned magnetic storage rings rely on magnetic bending and focusing elements for the beam guiding. This creates a mass limit at a given energy for the desired ion beam species to be stored due to the technical limit of the magnetic fields that can be created by these elements. However, the astrochemical community has a strong desire for experimental collisional reaction cross sections of heavier molecules.

In the new Cryogenic Storage Ring (CSR) at the Max Planck Institute for Nuclear Physics, all deflecting and focusing elements are electrostatic. In this case, at a given energy, a mass-independent storage can be realized. A variety of this kind of electrostatic storage devices have gone into operation in recent years, the first one being ELISA in Århus, Denmark, with a closed ion beam orbit of only 6.3 meters [8]. The TMU E-ring in Toyko, Japan, has been constructed with a similar design, with the difference that this device can be partly operated at liquid nitrogen temperature [9]. The first electron merged-beam device in an electrostatic storage ring has been taken into operation at the KEK High Energy Accelerator Research Organization in Tsukuba, Japan [10]. Even more recently, advances have been made towards operating the complete beam line of an electrostatic storage ring machine at cryogenic temperatures of about ~ 10 Kelvin. This allows for a storage of slow keV ion beams with very low beam loss due to residual gas scattering and therefore enabling long ion beam storage lifetimes. Among the CSR itself, these are DESIREE in Stockholm, Sweden [11], where merged ion-beam experiments are performed, and the cryogenic electrostatic storage ring RICE at the RIKEN Advanced Science Institute in Saitama, Japan [12].

The CSR, commissioned in 2015 [13], takes a unique spot in this rather broad landscape of ion storage ring devices. With a closed orbit of about 35 meters and ion beam injection and storing at energies up to 300 keV per charge state, it exceeds the dimension and maximum ion energies of the smaller, table-top style electrostatic storage rings listed above. In the CSR, ions are stored for up to thousands of seconds in a low-temperature radiation field given by the black-body radiation of the beamline wall at even less than 10 Kelvin. In this environment, stored molecular ions can undergo radiative relaxation toward their ro-vibrational

ground-states, making the CSR the ideal platform for experimental studies under conditions as they can be found in molecular clouds in the ISM.

A versatile range of experiments with these ions in well-defined quantum states can be performed. Besides merged-beam atom-ion, electron-ion and ion-laser interaction studies, a reaction microscope will complete the CSR facility in the near future. The CSR is up to now the only electrostatic cryogenic storage ring with a functioning electron-ion merged beam setup which is not only used for (among others) state-of-the-art DR electron-target experiments, but at the same time can be operated as a *low-energy electron cooler*.

1.3 Low-energy electron cooling at the CSR

This work is dedicated to the first electron phase space cooling operation of the CSR electron-ion merged beam setup. A process where the temperature of a stored ion beam is reduced and its density in phase space is increased is termed as phase space cooling. The idea of phase space cooling by superimposing a co-moving electron beam to the stored ion beam was first proposed by G. I. Budker in 1966 [14]. Experimentally, this idea was first realized in 1974 in the NAP-M storage ring at the BINP in Novosibirsk [15].

The electrons are continuously renewed and ideally have a much smaller energy spread than the passing ion beam. Energy exchange between the “cold” electrons and “hot” ions takes place through Coulomb collisions, effectively extracting heat from the system and thereby reducing the ion beam temperature.

At the ultra low meV electron-ion collision energies targeted with the CSR electron-ion merged-beam setup, the electron beam temperature plays a crucial role for the achievable energy resolution.

The production of cold, intense electron beams with a semiconductor photocathode electron source at the CSR [16, 17] therefore remains a relevant research topic going hand in hand with electron cooling and electron-ion collision studies.

At the CSR, phase space cooling by velocity-matching of heavy ions stored at low keV kinetic energies with a cold electron beam in the merged-beam electron-ion interaction region requires to overcome certain challenges. Ultra-low kinetic electron energies are needed, while maintaining high electron densities. The setup is designed to achieve energies as low as ~ 1 eV at an energy spread of about 1 meV.

In the course of this work, the CSR electron-ion merged beam setup has been completed and commissioned. The laboratory work performed in the framework of this thesis was dedicated to complete (large parts of) the setup and the surrounding equipment, to the development of operational techniques and the control system,

1 Introduction

and to the commissioning of the system. The very new regime of low-energy electron cooling is investigated for a number of atomic and molecular keV ion beams down to only ~ 10 eV electron cooling energy, making first steps of systematic cooling performance studies and testing the limits of the experimental setup.

1.4 Outline of this work

This introduction is first followed by a review of important concepts that are related to electron cooling in ion storage rings in chapter 2, starting with the basic notations and definitions that are needed to describe the dynamics of stored ion beams. An overview of electron cooling theory as well as diffusion processes like intrabeam-scattering is given.

Chapter 3 describes the structure and realization of the electron-ion merged beam setup. The key features for low-energy, cold electron beam operation are highlighted. Furthermore, the ion beam diagnostic techniques at the CSR that are used for the demonstration of electron cooling in this work are introduced. The experimental setup chapter concludes with a presentation of spatial profiles of the electron beams transported through the complete cryogenic beam guiding system.

The very first experimental electron cooling studies of keV ion beams at the CSR are presented in chapter 4. These cover the first demonstration of electron cooling realized for a bunched F^{6+} beam in 2017, followed by results of the first systematic studies in 2018 for longitudinal cooling of coasting and bunched beams as well as transverse cooling of coasting beams. These studies are extended by an investigation of ion beam space charge effects and the blow-up of ion beams by diffusion heating processes like intrabeam-scattering.

The concluding chapter 5 summarizes the key achievements of the low-energy electron cooling operation together with important results observed in the presented experiments. Finally, an outlook for future beam times is given.

2 Electron cooling in ion storage rings

In order to motivate electron cooling in a storage ring, the basic principles of the dynamics of a stored ion beam are summarized in this chapter. The phase space of an ion beam in a storage ring will be defined. A large part of this work's experimental studies presented in chapt. 4 are performed with ion beams that are manipulated by rf-bunching. A strong focus is therefore placed on the explanation of this particular technique and its effect on the longitudinal ion beam dynamics. The role of Liouville's theorem for phase space cooling will be pointed out before introducing electron cooling itself. Finally, a simple approach for the theoretical description of the electron cooling force is presented.

2.1 Ion optics and phase space

The term *ion optics* is used to describe the techniques for ion beam manipulation in a storage ring. It is often equally used to describe the physical processes that are involved. Depending on the type of accelerator, various elements that make use of electromagnetic fields are employed for ion beam guiding and focusing. The Lorentz force exerted on a charged particle passing, for example, a bending magnet or an electrostatic deflector is given by

$$\vec{F} = q \cdot (\vec{E} + (\vec{v} \times \vec{B})) \quad (2.1)$$

where q is the charge of the particle with velocity v . In high-energy storage rings with ion velocities close to the speed of light, magnetic fields on the order of 1 Tesla are common in the bending magnets. The much larger electric field equivalent of about $3 \cdot 10^8 \frac{\text{V}}{\text{m}}$ for 1 Tesla explains the preference for magnetic ion optics in storage ring experiments with relativistic particles.

2.1.1 Definition of phase space coordinates

The following description of the phase space coordinates and introduction to ion beam dynamics in this chapter mainly summarizes and follows the notations given in [18] (chapters 4, 6 & 7). The co-moving standard coordinate system of a particle moving periodically on a *closed orbit* in the field lattice of a circular accelerator is shown in fig. 2.1. The transverse coordinates (x, y) describe the particle position in a plane orthogonal to a reference particle's direction. The orbit of the reference

2 Electron cooling in ion storage rings

particle is fixed by the design of the ion optics and often denoted as *ideal orbit*, *reference orbit* or *equilibrium orbit*. The position s gives the arc length to an arbitrarily chosen point along the circumference C_0 and completes the curvilinear (x, y, s) -coordinate system commonly used in accelerator physics (it is left-handed for the sense of rotation adapted here). The position of a particle is now described by the vector

$$\vec{r}(s) = \vec{r}_0(s) + x(s)\vec{u}_x(s) + y(s)\vec{u}_y(s) \quad (2.2)$$

where $\vec{r}_0(s)$ is the ideal orbit and the corresponding line element is

$$d\vec{r} = \vec{u}_x dx + \vec{u}_y dy + \vec{u}_s(1 + hx)ds \quad (2.3)$$

Here $h = 1/\rho_0 = \left| \frac{d\vec{u}_s}{ds} \right|$ is the curvature of the ideal orbit that depends on the deflecting forces. The particle angle in the horizontal and vertical direction is obtained by differentiation along the longitudinal coordinate s

$$x' = \frac{dx}{ds} = \frac{p_x}{p_0} \quad (2.4)$$

$$y' = \frac{dy}{ds} = \frac{p_y}{p_0} \quad (2.5)$$

where $p_{x,y}$ is the particle momentum in the respective transverse coordinate and p_0 is the momentum of the reference particle along its orbit. One can further define the path length difference l and the momentum deviation δ of a particle that passes a certain position s with a time difference $\Delta t = t - t_0$ to the reference particle:

$$l = -v_0 \Delta t \quad (2.6)$$

$$\delta = \frac{p - p_0}{p_0}. \quad (2.7)$$

These longitudinal coordinates are referenced to the lab frame, and not to the co-moving frame (x, y, s) . The complete six-dimensional phase space vector of a particle is finally given by [18]

$$\vec{x}(s) = \begin{pmatrix} x \\ x' \\ y \\ y' \\ l \\ \delta \end{pmatrix}. \quad (2.8)$$

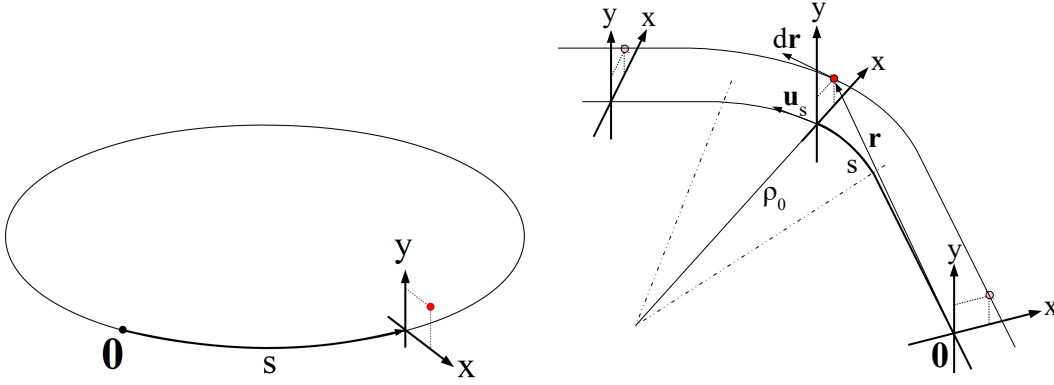


Figure 2.1: Standard coordinates in the co-moving frame of a particle moving on a closed orbit in a circular accelerator; modified from [18] for the sense of rotation of the CSR.

2.1.2 Transverse beam dynamics

In a linear approximation shown in detail for example in [18], the **equation of motion** of a particle in the periodic lattice of a storage ring resembles the motion of objects of mass in periodic external fields found by astronomer G.W. Hill [19]:

$$\frac{d^2x(s)}{ds^2} + k_x(s)x(s) = \frac{\delta}{\rho_0(s)} \quad (2.9)$$

$$\frac{d^2y(s)}{ds^2} + k_y(s)y(s) = 0 \quad (2.10)$$

The periodicity of the coefficients $k_{x,y}(s)$ ¹ along the ring circumference is reflected by

$$k_{x,y}(s) = k_{x,y}(s + C_0) \quad (2.11)$$

Neglecting any off-momentum particles and only considering particles with $\delta = 0$, the equations above turn into the so-called *Hill equation* which is the equation of a pseudo-harmonic oscillator.

¹In accelerator physics literature, the coefficients $k_{x,y}(s)$ are referred to as the quadrupole focusing strength.

Betatron oscillation

The solution of the Hill equation are oscillations around the ideal orbit, denoted as *betatron oscillations*:

$$x(s) = a_x \sqrt{\beta_x(s)} \cos(\Psi_x(s) + \Psi_{0,x}) \quad (2.12)$$

$$y(s) = a_y \sqrt{\beta_y(s)} \cos(\Psi_y(s) + \Psi_{0,y}) \quad (2.13)$$

where Ψ_0 is the starting phase of the particle. The functions $\beta_{x,y}$ are denoted as *betatron functions* and a is the betatron oscillation amplitude of the particle. The amplitude of the pseudo-harmonic oscillations $a \cdot \sqrt{\beta(s)}$ varies with s along the orbit.

Betatron tune and working point

With the knowledge of the betatron functions and their relation to the phase function $\Psi_{x,y}$ of the betatron oscillations given by

$$\Psi_{x,y}(s) = \int_0^s \frac{ds}{\beta_{x,y}(s)} \quad (2.14)$$

one can further define a value called the *betatron tune* or *Q value* that describes the number of betatron oscillations a particle performs in one turn along the ring circumference:

$$Q_{x,y} = \frac{1}{2\pi} \int_s^{s+C_0} \frac{ds}{\beta_{x,y}(s)}. \quad (2.15)$$

The tune values (Q_x, Q_y) of a storage ring define its so-called *working point*. Integer and half-integer values of $Q_{x,y}$ result in resonances where any perturbations of the ideal orbit by dipole or higher order multipole errors become synchronized with the betatron oscillation. Such a perturbation can be caused for example by a field imperfection of the storage ring's magnets or deflectors. When planning or operating a storage ring, one generally uses a resonance diagram (sometimes also called working diagram or tune diagram) to identify possible working points avoiding these tune resonances. Such a resonance or working diagram is shown in fig. 2.2. The resonance lines satisfy the equations

$$\begin{aligned} p &= n \cdot Q_x \\ p &= n \cdot Q_y \\ p &= l \cdot Q_x + m \cdot Q_y, \quad n = |l| + |m| \end{aligned} \quad (2.16)$$

where p, l, m are integer numbers. Resonant lines up to order $n = 4$ are shown

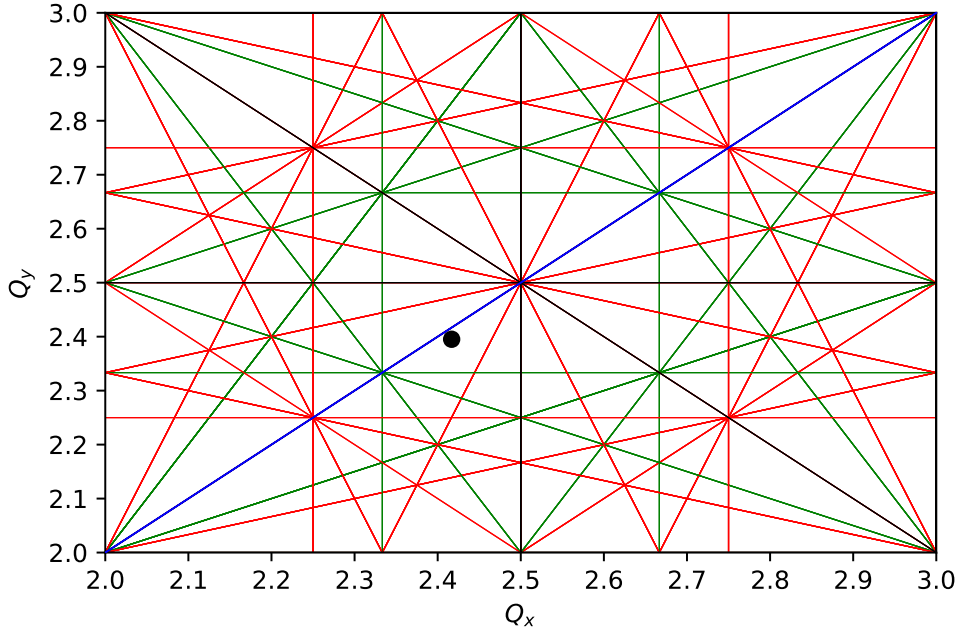


Figure 2.2: Working diagram of the CSR. Black lines: first and second order resonances (including border lines of the plot), green lines: third order resonances, red lines: fourth order resonances. The black dot marks one working point setting where 250 keV HeH⁺ ions have been stored. Blue: line for the the difference resonance $l = -m = \pm 1$.

in the working diagram, together with a measured working point setting of the CSR where 250 keV HeH⁺ have been stored in the beamtime 2018. In the CSR layout [13] operation close to the difference resonance with $l = -m = \pm 1$ is acceptable. A resonance of this type only makes the ion beam sensitive to the coupling of the horizontal and vertical motion.

Transverse emittance and acceptance

The solution of the Hill equation 2.12

$$u(s) = a\sqrt{\beta(s)} \cos(\Psi(s) + \Psi_0) \quad (2.17)$$

and its derivative

$$u'(s) = \frac{a}{\sqrt{\beta(s)}} \left(\frac{1}{2}\beta'(s) \cos(\Psi(s) + \Psi_0) - \sin(\Psi(s) + \Psi_0) \right) \quad (2.18)$$

2 Electron cooling in ion storage rings

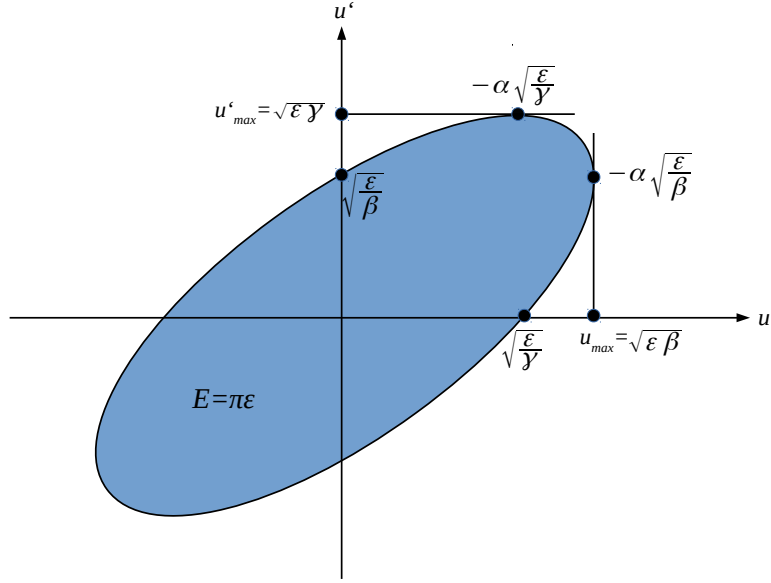


Figure 2.3: Courant-Snyder invariant ϵ displayed as ellipse in the (u, u') phase space (adapted from [18]).

together define the parametrization of an ellipse². The area E of the ellipse

$$E = \pi a^2 = \pi \epsilon = \text{const} \quad (2.19)$$

is defined by the *single-particle emittance* ϵ and can be shown to be a constant of motion (see sect. 2.2). The value ϵ is known as the *Courant-Snyder invariant*. It can be expressed in the (u, u') phase space by the following equation:

$$\gamma(s)u(s)^2 + 2\alpha(s)u(s)u'(s) + \beta(s)u'(s)^2 = a^2 = \epsilon \quad (2.20)$$

where in addition to $\beta(s)$ following from the solution of Hill's equation, $\alpha(s)$ and $\gamma(s)$ are introduced as further *lattice functions*:

$$\alpha(s) = -\frac{1}{2}\beta'(s) \quad (2.21)$$

$$\gamma(s) = \frac{1 + \alpha^2(s)}{\beta(s)}. \quad (2.22)$$

²the variable u here represents both transverse coordinates (x, y)

The lattice functions (in the literature sometimes also called optical functions) define the shape of the phase space ellipse. It is important to note that these functions are defined purely by the ion optics of the storage ring. The phase space ellipse is shown schematically in fig. 2.3. Even though it is derived from the motion of a single particle along the beam line, it will contain all particles with a betatron oscillation amplitude smaller than its own.

However, the density of the particles in the (u, u') coordinates is not homogeneous, but rather described by two-dimensional Gaussian distribution. To make the step from the individual particle description to the definition of a *beam profile*, the two-dimensional intensity distribution is projected onto the u -coordinate. The resulting profile is again a Gaussian distribution and can be measured for example by beam scrapers (see sect. 3.6.1).

The **beam emittance** $\pi\epsilon$ is defined differently throughout the accelerator physics community, depending on the number of standard deviations that are used in the definition of the beam size σ :

$$\sqrt{\epsilon^{1\sigma}\beta(s)} = \sigma_y, \quad \sqrt{\epsilon^{2\sigma}\beta(s)} = 2\sigma_y, \quad \sqrt{\epsilon^{3\sigma}\beta(s)} = 3\sigma_y \quad (2.23)$$

The values

$$u_{max}(s) = \sqrt{\epsilon}\sqrt{\beta(s)} \quad (2.24)$$

$$u'_{max}(s) = \sqrt{\epsilon}\sqrt{\gamma(s)} \quad (2.25)$$

which are also indicated in fig. 2.3 give the beam envelope and its maximum divergence, respectively. The **acceptance** A of a storage ring is defined as the maximum phase space area ϵ_{max} where ions are still stored before being lost by colliding with the vacuum chambers of the beamline or other barriers:

$$A = \pi\epsilon_{max} \quad (2.26)$$

In this thesis, the ion beam is characterized by standard deviations of position and velocity.

2.1.3 Definition of ion beam temperatures

The velocity \vec{v}_i of an ion moving in the beam coordinate system given in sect. 2.1 is given by

$$\vec{v}_i = v_{i,x}\vec{u}_x + v_{i,y}\vec{u}_y + v_{i,s}\vec{u}_s \quad (2.27)$$

The velocity component in direction s is now denoted as the longitudinal velocity component such that $v_{i,s} = v_{i,\parallel} = v_{i,\delta}$, and hence defines the longitudinal beam

2 Electron cooling in ion storage rings

temperature. The transverse temperature T_{\perp} is defined as the average of the horizontal and vertical temperatures $T_x(s)$ and $T_y(s)$, respectively. This leads to

$$k_B T_{\parallel} = M_i \langle v_{i\parallel} \rangle^2 = M_i v_0^2 \sigma_{\delta}^2 \quad (2.28)$$

$$k_B T_{\perp} = \frac{1}{2} M_i [\langle v_{i,x} \rangle^2 + \langle v_{i,y} \rangle^2] = \frac{1}{2} M_i v_0^2 (\sigma_{x'}^2 + \sigma_{y'}^2) \quad (2.29)$$

where v_0 is the longitudinal (laboratory frame) velocity on the closed orbit and where $\sigma_{x'}$, $\sigma_{y'}$ and σ_{δ} are the standard deviations of the respective quantities in eqn. 2.8. Eqns. 2.5, 2.12 & 2.23 are used for the transverse temperature derivation while for the longitudinal momentum deviation the definition of δ from eqn. 2.7 is used.

2.1.4 Phase slip factor and dispersion function

As it can be seen in eqn. 2.9, a momentum spread $\Delta p/p$ of a stored beam affects its horizontal position x . A determination of the momentum spread is possible by measuring the distribution Δf of the revolution frequency f_0 together with the ion optics dependent *phase slip factor* η :

$$\delta = \frac{\Delta p}{p_0} = \frac{1}{\eta} \frac{\Delta f}{f_0} \quad (2.30)$$

where p_0 and f_0 are the momentum and the frequency of the reference ion.

In the derivation of the phase slip factor for an electrostatic storage ring³, as shown in great detail for example in [20], one finds several important relations that will be summarized here.

A deviation $\Delta x(s)$ from the closed orbit $x_0(s)$ is given by the *dispersion function* of the storage ring $D_p(s)$ and by the momentum deviation Δp relative to the reference ion's momentum p_0 or, equivalently, by the energy deviation ΔE relative to the reference ion's energy E_0 :

$$\Delta x(s) = D_p(s) \frac{\Delta p}{p_0} = D_p(s) \frac{1}{2} \frac{\Delta E}{E_0} \quad (2.31)$$

The *momentum compaction factor* α_p relates the circumference C_0 of the closed orbit to the ion momentum and can be expressed via the dispersion function:

$$\alpha_p = \frac{\Delta C/C_0}{\Delta p/p_0} = \frac{1}{C_0} \int_0^{C_0} \frac{D_p(s)}{\rho_0(s)} ds \quad (2.32)$$

³Only ions with non-relativistic velocities are considered here.

where $\rho_0(s)$ is the radius of the central orbit. The phase slip factor is finally calculated from the momentum compaction factor to [20]

$$\eta = 1 - 2\alpha_p \quad (2.33)$$

specifically for an electrostatic storage ring case.

Magnetic fields have a different influence on the ion, since they can only change the direction of the ion velocity but not its absolute value. The phase slip factor η_m of a conventional magnetic storage ring in the non-relativistic approach is therefore instead given by [21]:

$$\eta_m = 1 - \alpha_p \quad (2.34)$$

2.1.5 Longitudinal beam dynamics and Rf-bunching

Applying a time dependent acceleration voltage to a drift tube in a storage ring can imprint a time structure on a circulating ion beam and transforms this *coasting* beam, or dc-beam, into a *bunched* beam that is now composed of discrete ion pulses.

This section gives an insight into the longitudinal dynamics of ion beams during rf-bunching in circular accelerators following [18] (chapters 2 & 8). Theoretical reviews of the topic go back as far as 1966 [22] and detailed formulations of the involved processes can also be found in [21]. The effect of electron cooling on such charged particle bunches will subsequently be discussed in sect. 2.2.

The frequency ω_{rf} of the applied rf-signal is matched to the revolution frequency $\omega_0 = 2\pi f_0$ of the reference ion,

$$\omega_{\text{rf}} = h \cdot \omega_0 \quad (2.35)$$

where h is an integer number. We consider the acceleration in a drift tube of length L with a time of passage $t_f = L/(2v_0)$ and a drift tube voltage of $U_{\text{rf}}(t) = -\hat{U}_{\text{rf}} \cos \omega_{\text{rf}} t$ with $\Phi = \omega_{\text{rf}} t$. Upon passing the drift tube electrode, depending on the rf phase Φ at the time when a particle reached the center of the drift tube it experiences an energy gain ΔE_{rf} per turn given by

$$\Delta E_{\text{rf}} = Ze\hat{U}_{\text{rf}}[\cos(\Phi - \omega_{\text{rf}} t_f) - \cos(\Phi + \omega_{\text{rf}} t_f)] \quad (2.36)$$

where $\omega_{\text{rf}} = h\pi L/C_0$ using $f_0 = 2\pi L/C_0$ and \hat{U}_{rf} is the amplitude of the rf-voltage. For the following considerations it will be more convenient to rewrite eqn. 2.36 in the form

$$\Delta E_{\text{rf}} = Ze\hat{U}_{\text{eff}} \sin \Phi \quad (2.37)$$

2 Electron cooling in ion storage rings

with an effective bunching voltage

$$\hat{U}_{\text{eff}} = 2\hat{U}_{\text{rf}} \sin\left(h\pi \frac{L}{C_0}\right). \quad (2.38)$$

The bunching section of the CSR is composed of two drift tubes of different length (340 mm and 736 mm). For rf-bunching, generally only the shorter drift tube with $L = 340$ mm is used.

Synchrotron oscillation

The longitudinal phase space coordinates (l, δ) defined above in eqns. 2.6 & 2.7 are related to the coordinates $(\Delta E = E - E_0, \Delta\Phi = \Phi - \Phi_0)$, which will be used for the following descriptions, by [18]:

$$l = -\frac{v_0 \Delta\Phi}{h\omega_0} = -\frac{C_0 \Delta\Phi}{2\pi h} \quad (2.39)$$

$$\delta = \frac{\Delta E}{p_0 v_0} \quad (2.40)$$

The time deviation $\Delta t = t - t_0$ is furthermore related to $\Delta\Phi$ by

$$\Delta t = \frac{\Delta\Phi}{\omega_{\text{rf}}}. \quad (2.41)$$

The energy of a particle stays unchanged if it has a phase $\Phi = 0$. A phase $\Phi > 0$ means the particle lags behind the rf-signal and will become accelerated. Reciprocally it will become decelerated if it is ahead of the rf-signal ($\Phi < 0$). A particle with energy $E_0(t)$ that passes the drift tube center always with the same phase Φ_0 and is synchronised to the revolution frequency $\omega_0 = \omega_{\text{rf}}/h$ according to eqn. 2.1.5, is defined as the *synchronous* particle.

Particles that have an energy deviation ΔE and phase deviation $\Delta\Phi$, will start to perform oscillations around the synchronous particle. As also described by [18], this can be seen by imagining a particle with phase deviation $\Phi - \Phi_0$. Assuming $\Delta\Phi > 0$, its energy gain $\Delta E_{\text{rf}}(\Phi)$ will be larger than that of the synchronous particle $\Delta E_{\text{rf}}(\Phi_0)$ (see also fig. 2.4, left). Consequently, it will become faster and pass the rf-bunching tube earlier, making the phase deviation $\Delta\Phi$ smaller and smaller each turn (see fig. 2.4, right). Eventually a maximum of ΔE is reached when $\Delta\Phi = 0$. When the point of negative phase deviations $\Delta\Phi < 0$ is passed, the particle gets decelerated because $\Delta E_{\text{rf}}(\Phi)$ now becomes smaller than $\Delta E_{\text{rf}}(\Phi_0)$. The deceleration in each turn continues until $\Delta E = 0$ at the point of maximum phase deviation $\Phi < 0$ is reached. This phase focusing process that results from the coupling of energy and phase oscillations can be expressed by equations of motion

for a particle in the longitudinal phase space $(\Delta E, \Delta\Phi)$. In order to demonstrate this oscillatory behaviour, one starts by looking at the change of the phase and energy deviations per turn:

$$\Delta(\Delta\Phi) = -\eta \frac{\Delta p}{p_0} 2\pi h \quad (2.42)$$

$$\Delta(\Delta E) = Ze\hat{U}_{\text{eff}} \cdot (\sin \Phi - \sin \Phi_0) \quad (2.43)$$

The time derivatives can be calculated from simply dividing by the revolution period $T_0 = 2\pi/\omega_0$

$$\frac{d}{dt}\Delta\Phi = -\frac{2\pi f_0 h M_i \eta}{p_0^2} \Delta E \quad (2.44)$$

$$\frac{d}{dt}\Delta E = f_0 Ze\hat{U}_{\text{eff}}(\sin \Phi - \sin \Phi_0) \quad (2.45)$$

which can be summarized in a differential equation of second order [18]:

$$\frac{d^2}{dt^2}\Delta\Phi = -\frac{f_0^2 h M_i \eta}{p_0^2} Ze\hat{U}_{\text{eff}}(\sin \Phi - \sin \Phi_0) \quad (2.46)$$

In the case of small deviations $\Delta\Phi$ the approximation $\sin \Phi - \sin \Phi_0 \approx \cos \Phi_0 \Delta\Phi$ becomes applicable in the eqn. of motion 2.46, yielding the equation of a harmonic oscillator:

$$\frac{d^2}{dt^2}\Delta\Phi + \omega_{\text{sync}}^2 \Delta\Phi = 0. \quad (2.47)$$

This can be solved by

$$\Delta\Phi(t) = \Delta\Phi_{\text{max}} \cos(\omega_{\text{sync}} t + \phi_{\text{sync}}) \quad (2.48)$$

where *synchrotron frequency*

$$\omega_{\text{sync}} = \sqrt{\frac{2\pi f_0^2 m_i h \eta}{p_0^2} Ze\hat{U}_{\text{eff}} \cos \Phi_0} \quad (2.49)$$

The solution for ΔE is given by the derivate of $\Delta\Phi$ according to eqn. 2.44:

$$\Delta E = \Delta E_{\text{max}} \sin(\omega_{\text{sync}} t + \phi_{\text{sync}}) \quad (2.50)$$

where

$$\Delta E_{\text{max}} = \frac{\omega_{\text{sync}}}{\omega_0} \frac{p_0^2}{h M_i \eta} \quad (2.51)$$

2 Electron cooling in ion storage rings

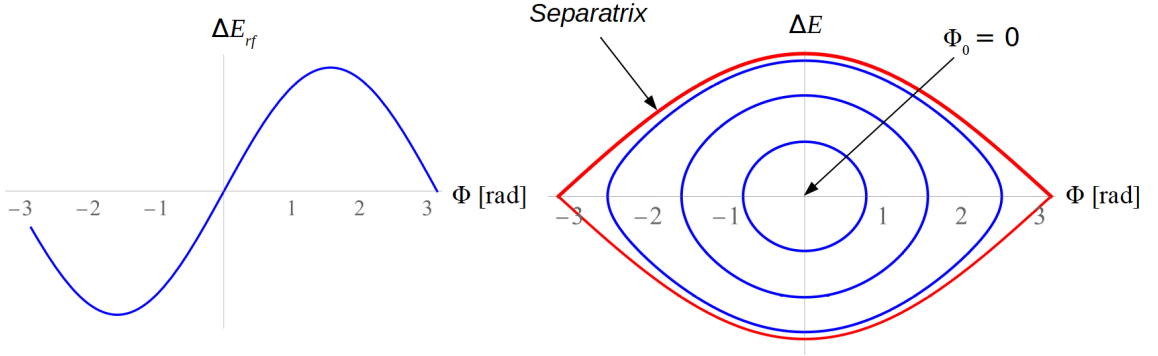


Figure 2.4: The energy gain per turn ΔE_{rf} of a particle passing the bunching drift tube is a periodical function of the rf-phase Φ (left). Right: stationary rf-bucket ($\Phi_0 = 0$). The border of the area of stable trajectories is marked by the separatrix (red line).

eqn. 2.49 further defines a requirement for stable solutions of the oscillatory motion: $Ze\hat{U}_{\text{eff}}\eta \cos \Phi_0 > 0$ (all other factors below the square root in eqn. 2.49 are always positive).

Fig. 2.4 (right) shows example solutions for the synchrotron oscillation in the form of longitudinal phase space diagrams. In the case of a slip factor $\eta > 0$, representing conditions in the CSR, the particles move counter clockwise on their trajectories given by the closed curves. If $\eta < 0$, they would move clockwise in the phase space. The border between stable solutions and unstable solutions of the oscillatory motion is given by the red line, the so-called *separatrix* which defines the maximum energy deviation and phase deviation acceptance (ΔE_{max} , $\Delta \Phi_{max}$) before particles are lost from the bunch. Particles whose trajectory is located inside the stable area can be imagined to be trapped in what is often called the *rf-bucket* or simply *bucket* created by rf-bunching with the sinusoidal signal shown on the left. The number of buckets in which particles can be trapped along the ring's orbit is defined by the number h . For smaller amplitudes the particles move on elliptical orbits (inner blue lines) since they can be described by the harmonic oscillator (eqn. 2.47). The phase space diagram in the right of the figure shows the case of a synchronous phase $\Phi_0 = 0$. The particles always pass the bunching drift tube when the field is at zero, creating a stationary rf-bucket as it is the case in the CSR.

Simulation of the rf-bunching process

With the set of equations above that govern the single-particle motion in the longitudinal phase space, a multi-particle simulation of the rf-bunching process in

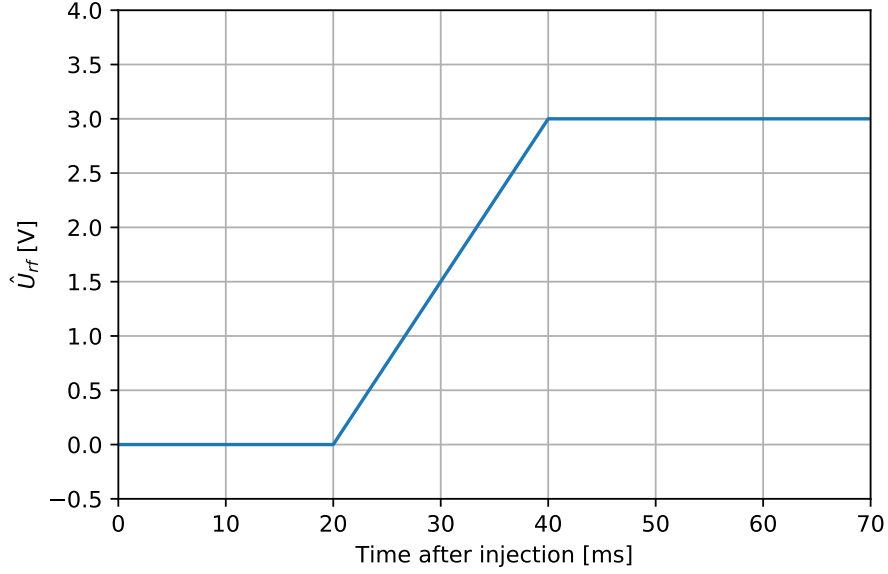


Figure 2.5: Rf-amplitude timing scheme.

the CSR has been performed. The structure is similar to the simulation program that has been used for bunch simulations at the TSR [23]. The time evolution of the longitudinal phase space is calculated under the influence of the CSR rf-voltage ramp shown in fig. 2.5.

A scheme of the simulation program is shown in fig. 2.6. The phase space coordinates ΔE and $\Delta\Phi$ are handled as vectors whose dimension is given by the chosen number of particles. The evolution of the phase space vector is then calculated in steps of revolution turns. The initial energy distribution of the unbunched ion beam is defined by a Gaussian distribution whose width is one of the fixed starting conditions.

The results of such a simulation for a number of $N = 10000$ ions (mass number $A = 5$, charge state $Z = 1$) that are injected at a kinetic energy of $E_{kin} = 250$ keV with initial Gaussian energy spread of $\sigma(E) = 66$ eV is shown in fig. 2.7. For this one-bunch simulation with $h = 1$, the revolution period and bunch period are identical $T_0 = 11.33 \mu s$. In order to demonstrate the motion of the particles according to the synchrotron oscillations shown in fig. 2.4, the number of particles is chosen such that the bunch is not completely filled after the simulated time evolution.

2 Electron cooling in ion storage rings

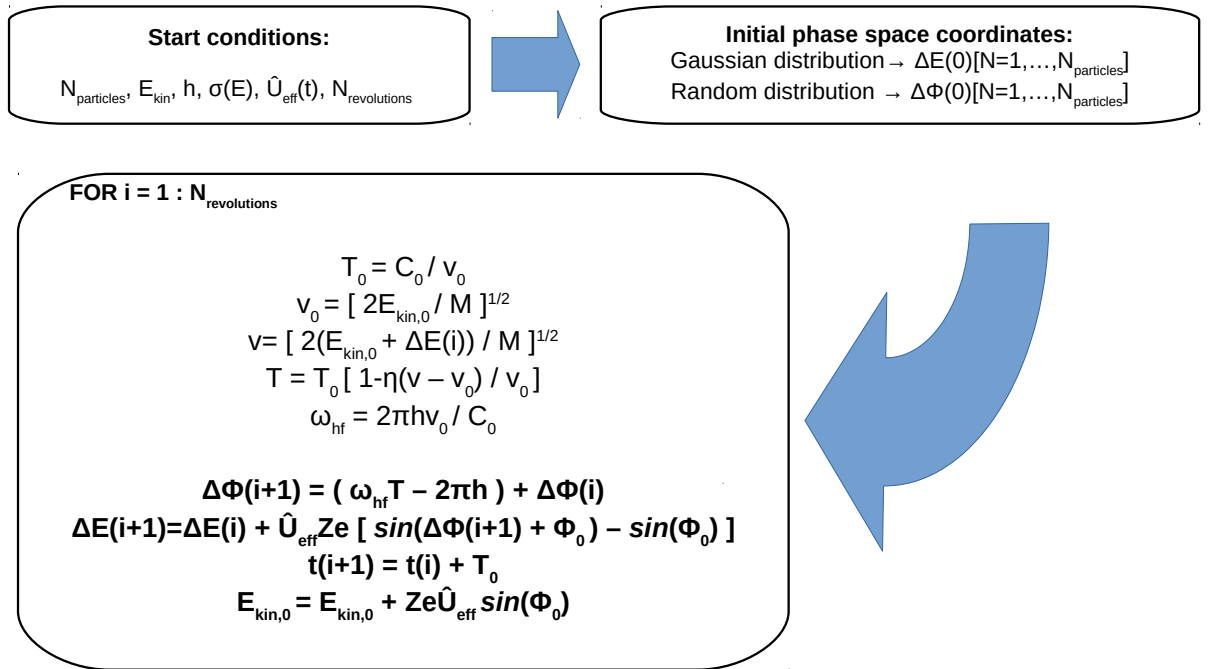


Figure 2.6: Scheme of the simulation program for the longitudinal phase space distribution during rf-bunching. The time t is the time after injection according to fig. 2.5.

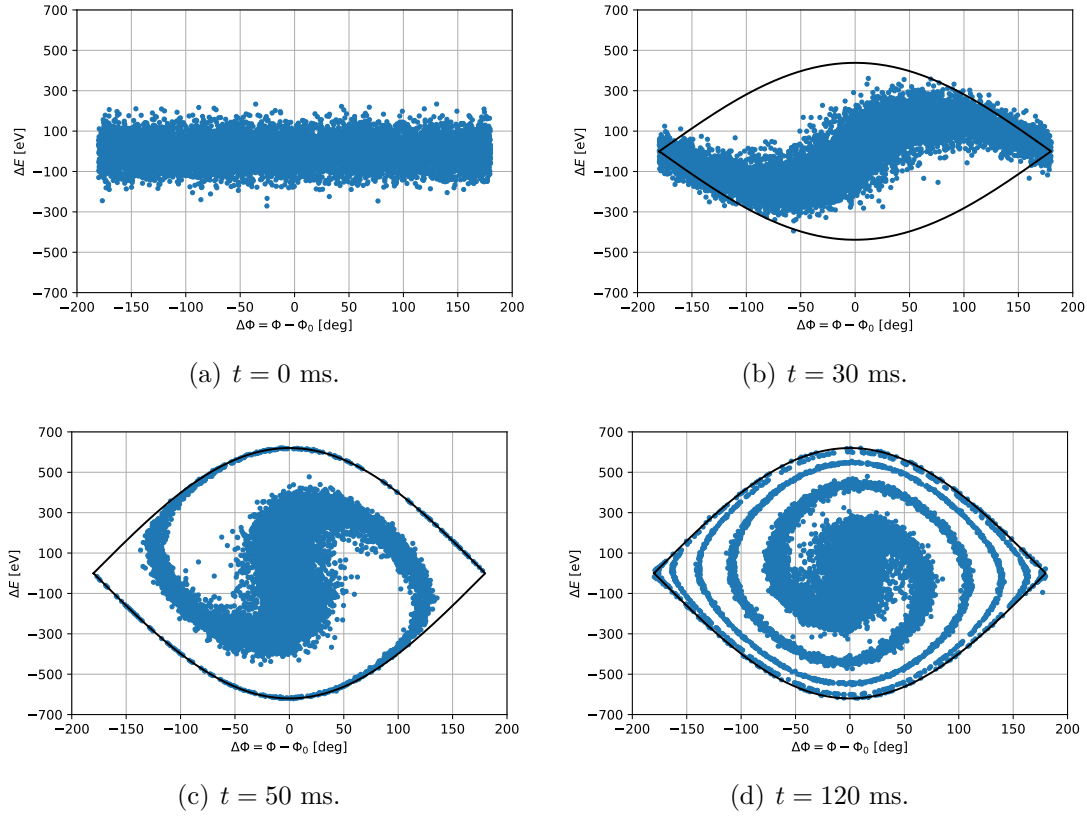


Figure 2.7: Time evolution (in time after injection) of the longitudinal phase space distribution of a number of 10000 particles injected with 250 keV in the CSR under the influence of the rf-bunching ramp shown in fig. 2.5. The black line marks the separatrix. See text for simulation details.

2.2 Electron cooling and diffusion heating

The general concepts that one needs in order to describe and characterize the properties of a stored ion beam were presented in the previous section. Based on this, phase space cooling and its benefits will be first motivated from a general point of view. Electron cooling is then introduced as a powerful tool to improve a stored ion beam's quality and a theoretical model of the cooling force is reviewed. An extensive review on electron cooling related topics that comprises many important aspects from theory to applications was written by H. Poth [24].

2.2.1 Motivation for phase space cooling

The occupied phase space of a stored ion beam given by its emittance can be used in combination with the momentum spread as a measure of the beam quality. By phase space cooling, the beam emittance can be compressed, resulting in a shrinking of the ion beam's radius and divergence. This is especially of advantage when for example electron-ion recombination experiments are performed and one wants to localize the origin of recombination events as precise as possible. A compressed emittance also means that the ions are in average located closer to the central orbit, which can significantly increase the lifetime of a stored beam inside the ring. Another positive effect of phase space cooling is the reduction of momentum spread. A reduced momentum spread can reduce the spread of the relative velocity in ion recombination experiments, which in turn determines the achievable energy resolution when the electron velocity spread becomes smaller than the ion velocity spread.

Without further proof, it is already mentioned in sect. 2.1.2 that the emittance of an ion beam is a constant of motion (eqn. 2.19). This statement is based upon **Liouville's theorem**: *the density of particles in the six-dimensional phase space is conserved under the influence of conservative forces*. Consequently, while any kind of magnetic or electrostatic bending, focusing or shifting operation on a stored ion beam changes the shape and position of the phase space ellipse, the area it encloses is invariant (see also [18], chapter 10).

There are processes that violate Liouville's theorem and hence cause a growth of the emittance, for instance collisions of the stored ion beam with rest gas particles or multiple Coulomb scattering of the charged particles in the beam. Phase space cooling is able to counter such diffusional (heating) processes, accompanied by all the advantages mentioned above. Both aspects, electron cooling and heating by diffusion, will be introduced in this chapter.

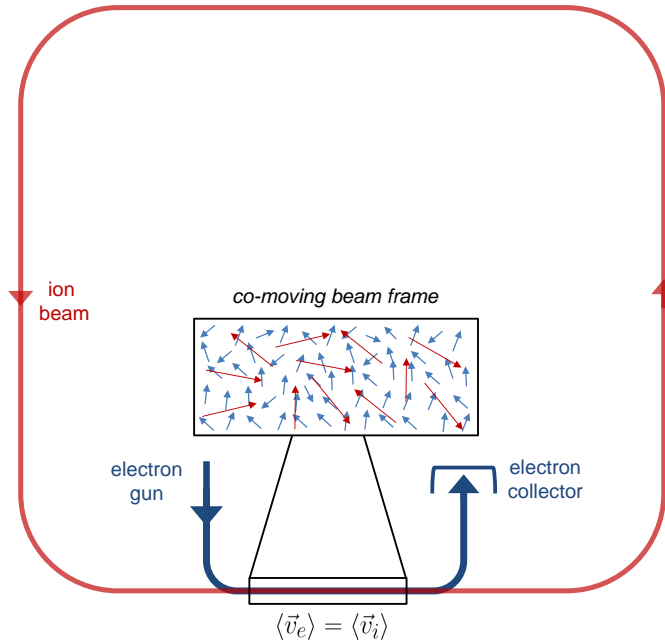


Figure 2.8: Principle of electron cooling in a storage ring. Continuously renewed, cold electrons (blue arrows) are merged with the hot ions (red arrows). The average velocity of the electrons $\langle \vec{v}_e \rangle$ in the laboratory system, determined by the acceleration potential between the electron collector and the electron gun, is matched with the average ion velocity $\langle \vec{v}_i \rangle$. The electron beam is typically guided by a solenoidal magnetic guiding field.

2.2.2 Basic idea of electron cooling

The idea of damping the synchrotron and betatron oscillations of a charged particle beam in storage rings and accelerators by superimposing a co-moving electron beam over a certain length was first proposed by G. I. Budker in the early 1960's [14]. It was first realized in 1974 in the NAP-M storage ring at the BINP in Novosibirsk where the effect was investigated for a beam of 35-80 MeV protons [15].

The principle of electron cooling in a circular accelerator is shown schematically in fig. 2.8. The idea can be visualized in a co-moving beam frame where the particles are moving only due to their thermal energy distribution. The electron beam is accelerated and merged with the ion beam in the way that the average electron velocity matches the average velocity of the ion beam. Ions are typically created at much higher temperatures than electrons. They repeatedly pass the cold and

2 Electron cooling in ion storage rings

dense medium given by the electrons, resulting in a temperature relaxation of the electron-ion plasma. Energy (heat) can be transferred out of the system due to the fact that the heated electrons are collected in a Faraday cup outside of the interaction region and are continuously replaced by new, cold electrons.

The underlying process of the energy transfer from the hotter ions to the colder electrons are Coulomb collisions, taking place every time the ions pass the electron cooling section of the ring. The energy loss ΔE of an ion passing a distance Δx in the electron cooler thus yields an effective *friction force* F :

$$\vec{F} = \frac{\Delta E \vec{v}}{\Delta x v} \quad (2.52)$$

The friction force depends on the velocity of the ions and is opposed to their motion, similar to the drag force an object experiences in a viscous fluid. This friction force does not have to be aligned with \vec{v} , however, $\vec{F}\vec{v} = \Delta E/\Delta t$ is the power of the friction force and $\Delta E/\Delta x$ is the component of \vec{F} in the direction of \vec{v} .

The temperature equilibrium in such an electron-ion plasma picture is governed by the cooling effect on the ions due to the friction force, on the one hand, and the heating effect through diffusion on the other hand. Diffusion arises from multiple scattering processes of the ions, resulting in a blow-up of the ion beam velocity distribution.

2.2.3 Electron cooling rates

Before going into more detail on the derivation of the frictional cooling force and diffusion in the picture of the electron-ion plasma, a definition for an electron cooling rate is derived for a strongly simplified picture, in the case of a “uniform machine”, similar to the considerations by [25].

The equation of motion of a stored ion that experiences a friction force F due to an energy loss in the electron cooling section are expressed by rewriting eqns. 2.9 & 2.10 for a time dependence. The equations of motion for the transverse direction of a coasting beam under the influence of a frictional force can be expressed by:

$$M_i \ddot{u} - F_{cool,\perp} + K_{\perp} u = 0 \quad (2.53)$$

where u again equally stands for both transverse coordinates, x and y , and the restoring term $K_{\perp} u$ reflects the transverse quadrupole focusing of the ion beam

2.2 Electron cooling and diffusion heating

that causes the betatron oscillations. In the longitudinal direction,

$$M_i \ddot{l} - F_{cool,\parallel} = 0 \quad \text{unbunched} \quad (2.54)$$

$$M_i \ddot{l} - F_{cool,\parallel} + K_{\parallel} l = 0 \quad \text{bunched} \quad (2.55)$$

where l is the longitudinal phase space coordinate that is defined by eqn. 2.6 and the longitudinal restoring term K_{\parallel} takes into account synchrotron oscillations from a longitudinal manipulation by rf-bunching.

Cooling rates shall be derived under the assumption that the cooling force depends linearly on the ion velocity. This is valid in the case of small betatron and synchrotron oscillation amplitudes and small relative velocities of ions and electrons [15]. Furthermore, it is assumed for simplicity that the longitudinal force solely depends on the longitudinal velocity, and likewise the transverse component solely depends on the transverse velocity. With these assumptions one can define the friction force coefficients α_{\parallel} and α_{\perp} by:

$$F_{cool,\parallel} = -\alpha_{\parallel} v_{\parallel} \quad (2.56)$$

$$F_{cool,\perp} = -\alpha_{\perp} v_{\perp} \quad (2.57)$$

where \dot{u} is identified by v_{\perp} and \dot{l} by v_{\parallel} .

The second order differential equations 2.53 2.54 & 2.55 can be rewritten in the form

$$M_i \ddot{u} + \alpha_{\perp} \dot{u} + K_{\perp} u = 0 \quad (2.58)$$

$$M_i \ddot{l} + \alpha_{\parallel} \dot{l} = 0 \quad \text{unbunched} \quad (2.59)$$

$$M_i \ddot{l} + \alpha_{\parallel} \dot{l} + K_{\parallel} l = 0 \quad \text{bunched} \quad (2.60)$$

With an exponential Ansatz $e^{\lambda t}$, one obtains the following equations in the longitudinal direction

$$\lambda^2 + \frac{\alpha_{\parallel}}{M_i} \lambda = 0 \quad \text{unbunched} \quad (2.61)$$

$$\lambda^2 + \frac{\alpha_{\parallel}}{M_i} \lambda + K_{\parallel} = 0 \quad \text{bunched} \quad (2.62)$$

which is solved by

$$\lambda = -\frac{\alpha_{\parallel}}{M_i} \quad \text{unbunched} \quad (2.63)$$

$$\lambda_{1,2} = -\frac{\alpha_{\parallel}}{2M_i} \pm \sqrt{\frac{\alpha_{\parallel}^2}{4M_i} - \frac{K_{\parallel}}{M_i}} \approx -\frac{\alpha_{\parallel}}{2M_i} \pm i\sqrt{\frac{K_{\parallel}}{M_i}} \quad \text{bunched} \quad (2.64)$$

where $\sqrt{K_{\parallel}/M_i}$ is identified with the synchrotron oscillation ω_{sync} (eqn. 2.49).

2 Electron cooling in ion storage rings

Analogously, for the transverse direction

$$\lambda_{1,2} = -\frac{\alpha_{\perp}}{2M_i} \pm i\sqrt{\frac{K_{\perp}}{M_i}} \quad (2.65)$$

In the literature, the so-called *damping decrements* are often defined by

$$k_{\perp,\parallel} = \frac{\alpha_{\perp,\parallel}}{M_i} \quad (2.66)$$

With the relations above one is ready to define the *electron cooling rates* $r_{\perp,\parallel}$ (negative real parts of λ) and *electron cooling times* $\tau_{\perp,\parallel}$. One must also consider the finite length of the interaction region of the electrons and ions by introducing the ratio η_c of the electron cooling length to the ring circumference. The cooling rates (times) in the different cases are then given by:

$$\frac{1}{\tau_{\parallel}} = r_{\parallel} = \eta_c \cdot \frac{\alpha_{\parallel}}{M_i} \quad \text{longitudinal cooling rate (coasting beam)} \quad (2.67)$$

$$\frac{1}{\tau_{\parallel}} = r_{\parallel} = \frac{\eta_c}{2} \cdot \frac{\alpha_{\parallel}}{M_i} \quad \text{longitudinal cooling rate (bunched beam)} \quad (2.68)$$

$$\frac{1}{\tau_{\perp}} = r_{\perp} = \frac{\eta_c}{2} \cdot \frac{\alpha_{\perp}}{M_i} \quad \text{transverse cooling rate} \quad (2.69)$$

2.2.4 Fokker-Planck equation

The evolution of a time-dependent distribution function $\rho(\vec{r}, \vec{v}, t)$ for ions in the six-dimensional phase space (\vec{r}, \vec{v}) can be described by the Fokker-Planck equation. The Fokker-Planck equation becomes applicable to systems where fluctuations due to small disturbances are present. It is assumed that these disturbances, e.g. in the form of multiple small-angle scattering in the case of an electron-ion plasma, change the variables of the system in an unpredictable yet very small way [26]. With the Fokker-Planck equation, a time-independent probability function Ψ for finding a scattered particle in a given phase space position can be determined. The process of many small collisions adding up statistically can be seen as a type of diffusion and is therefore sometimes labeled as *diffusion approximation* [24]. The phase space function in this approximation can then be written as:

$$\rho(\vec{r}, \vec{v}, t) = \int \rho(\vec{r}, \vec{v} - \Delta\vec{v}, t - \Delta t) \Psi(\vec{v} - \Delta\vec{v}, \Delta\vec{v}) d\Delta\vec{v} \quad (2.70)$$

A second order Taylor expansion of $\rho\Psi$ yields

$$\begin{aligned}\rho\Psi &= \rho(\vec{r}, \vec{v}, t - \Delta t)\Psi(\vec{v}, \Delta\vec{v}) - \Delta\vec{v}\frac{\partial}{\partial\vec{v}}(\rho\Psi) \\ &+ \frac{1}{2}\Delta\vec{v}_m\Delta\vec{v}_n\frac{\partial^2}{\partial v_m\partial v_n}(\rho\Psi)\end{aligned}\quad (2.71)$$

where $\Delta\vec{v}$ is the velocity change in the time interval Δt . The evolution of the distribution function in time is now given as rate of change resulting from the collisions by

$$\frac{\partial\rho}{\partial t} = \frac{\rho(\vec{r}, \vec{v}, t) - \rho(\vec{r}, \vec{v}, t - \Delta t)}{\Delta t}\quad (2.72)$$

and after integrating over $\Delta\vec{v}$ in eqn. 2.70 finally defines the **Fokker-Planck equation**:

$$\frac{\partial\rho}{\partial t} = \frac{\partial}{\partial v_m} \left[-\rho\frac{\langle\Delta\vec{v}\rangle}{\Delta t} + \frac{\partial}{\partial v_n} \left(\rho\frac{\langle\Delta v_m\Delta v_n\rangle}{\Delta t} \right) \right]\quad (2.73)$$

with

$$\langle\Delta\vec{v}\rangle = \int \Delta\vec{v}\Psi(\vec{v}, \Delta\vec{v})d\Delta\vec{v}\quad (2.74)$$

and

$$\langle\Delta v_m\Delta v_n\rangle = \int \Delta v_m\Delta v_n\Psi(\vec{v}, \Delta\vec{v})d\Delta\vec{v}\quad (2.75)$$

where (m, n) symbolize velocity components in direction x, y, z . With eqns. 2.74 & 2.75 the frictional force \vec{F} and diffusion tensor D_{mn} can be defined [24]:

$$\vec{F} = \frac{M_i\langle\Delta\vec{v}\rangle}{\Delta t}\quad (2.76)$$

$$D_{mn} = \frac{\langle\Delta v_m\Delta v_n\rangle}{\Delta t}\quad (2.77)$$

The relations above also help to clarify the meaning of friction and diffusion. While the frictional force F is obtained as an averaged rate of particle velocity change, the diffusion tensor D_{mn} is related to the increase of the velocity variance.

Taking into account every velocity component in the plasma, the Fokker-Planck equation can be given as a sum of the form [24]

$$\frac{\partial\rho}{\partial t} = \sum_{m,n} \frac{\partial}{\partial v_m} \left[-\rho(F_m/M) + \frac{\partial(\rho D_{mn})}{\partial v_n} \right]\quad (2.78)$$

2 Electron cooling in ion storage rings

In one dimension it is reduced to:

$$\frac{\partial \rho}{\partial t} = \frac{\partial}{\partial v} \left(-\rho \frac{F}{M} + \frac{\partial}{\partial v} (\rho D) \right) \quad (2.79)$$

This equation will be further used in sect. 2.5.

2.2.5 Binary collision model

The electron cooling force can be derived from a simple binary collisional model in the electron beam rest frame, which will be summarized here following the review given in [24]. When ions interact with electrons at relative velocity \vec{v}_r pass the electrons, they undergo multiple Rutherford scattering and momentum is transferred via Coulomb interactions. A schematic picture illustrating the kinematics of the electron-ion collision is shown in fig. 2.9 (a). The momentum that is transferred in such a collision is given by⁴

$$\Delta p = \frac{1}{4\pi\epsilon_0} \int_{-\infty}^{\infty} \frac{Ze^2}{x^2 + b^2} dt = \frac{2Ze^2}{4\pi\epsilon_0 v_r b} \quad (2.80)$$

yielding an energy transfer to the electrons of

$$\Delta E(b) = \frac{(\Delta p)^2}{2m_e} = \frac{2Z^2 e^4}{(4\pi\epsilon_0)^2 m_e v_r^2 b^2} \quad (2.81)$$

As mentioned earlier in sect. 2.2.4, diffusion arises from multiple scattering in the electron-ion plasma. Analogously to eqn. 2.77, this diffusion effect is described by the statistically averaged variance of the momentum components, transferred over the collision planes at a fixed impact parameter b :

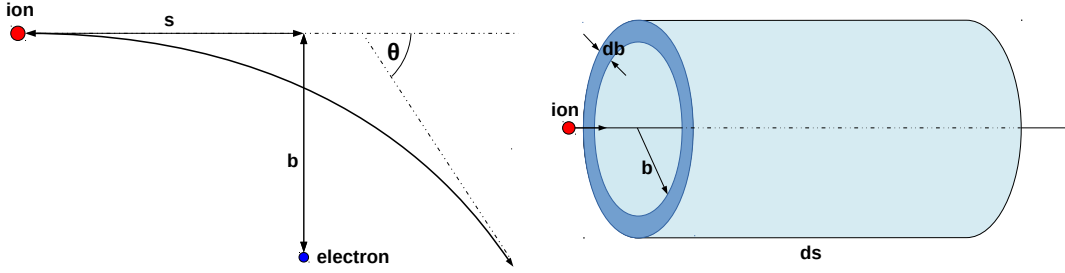
$$\begin{aligned} \langle \Delta p_m \Delta p_n \rangle &= \frac{1}{2} (\delta_{mn} - v_{r_m} v_{r_n} / v_r^2) \Delta p^2 \\ &= (\delta_{mn} - v_{r_m} v_{r_n} / v_r^2) \frac{2Z^2 e^4}{(4\pi\epsilon_0)^2 v_r^2 b^2}. \end{aligned} \quad (2.82)$$

where m and n describe the coordinates of v .

Using the flux $2\pi b n_e v_r$ of colliding electrons, the diffusion tensor (eqn. 2.77) is

⁴Note that only the transverse component of the Coulomb force is considered for the calculation of the momentum transfer. The longitudinal component vanishes when integrating over a symmetric interval.

2.2 Electron cooling and diffusion heating



(a) Scattering of a positive ion from a negative or positive charge with scattering angle Θ_{scatt} and impact parameter b .

(b) Illustration of the integration over possible collision planes and impact parameters b for an ion passing the electrons in their rest frame.

Figure 2.9: Kinematic collision geometry in the electron beam rest frame, modified from [24].

obtained as

$$D_{mn} = \frac{\langle \Delta v_m \Delta v_n \rangle}{\Delta t} \quad (2.83)$$

$$= \frac{1}{M_i^2} \int_0^\infty db \cdot 2\pi b n_e v_r \cdot \langle \Delta p_m \Delta p_n \rangle \quad (2.84)$$

$$= \frac{2\pi n_e}{M_i^2} \frac{2Z^2 e^4}{(4\pi\epsilon_0)^2} \left(\frac{\delta_{mn}}{v_r} - \frac{v_{r,n} v_{r,m}}{v_r^3} \right) \int_0^\infty \frac{db}{b}. \quad (2.85)$$

The non-converging integral is now replaced by

$$\int_0^\infty \frac{db}{b} \rightarrow \int_{b_{min}}^{b_{max}} \frac{db}{b} \quad (2.86)$$

which introduces the so-called *Coulomb logarithm*

$$L_C = \ln \frac{b_{max}}{b_{min}} \quad (2.87)$$

with the maximum and minimum impact parameters b_{max} and b_{min} . The minimum impact parameter can be calculated from the maximum possible momentum transfer (eqn. 2.80) for a head-on collision

$$b_{min} = \frac{Z^2 e^2}{4\pi\epsilon_0 m_e v_r^2} \quad (2.88)$$

2 Electron cooling in ion storage rings

However, for relative velocities that are smaller than the thermal spread of the electrons, the relative velocity v_r in b_{min} is replaced by the transverse thermal electron velocity spread. The transverse spread is used since it is generally much larger than the longitudinal velocity spread. This anisotropic electron beam velocity distribution, with thermal velocity spreads

$$\Delta_{e\parallel} = \sqrt{k_B T_{e\parallel}/m_e} \quad (2.89)$$

$$\Delta_{e\perp} = \sqrt{2k_B T_{e\perp}/m_e} \quad (2.90)$$

is discussed in more detail in sect. 3.3.

A reasonable approach for the maximum impact parameter is the Debye screening length $\lambda_{\perp} = \sqrt{\epsilon_0 k_B T_{e\perp}/(n_e e^2)}$ of an ion inside the electron plasma. Assuming the ion moves through the electron plasma with relative velocity v_r , the screening length can be bigger and is expressed by v_r/ω_{pl} [25] with the plasma frequency

$$\omega_{pl} = \sqrt{\frac{n_e e^2}{\epsilon_0 m_e}} \quad (2.91)$$

This frequency is attributed to oscillations of the initially uniform electron charge density as response to an approaching ion.

From these considerations, the impact parameters b_{max} and b_{min} which, neglecting any magnetic field influence, define the Coulomb logarithm $L_C = \ln(b_{max}/b_{min})$ are given by

$$b_{max} = \max(v_r/\omega_{pl}, \lambda_{\perp}) \quad (2.92)$$

$$b_{min} = \frac{Z^2 e^2}{4\pi\epsilon_0 m_e (\max(v_r, \Delta_{e\perp}))^2} \quad (2.93)$$

A calculation of the impact parameters for typical electron beam properties at the CSR is shown in fig. 2.10.

The frictional force is obtained from the energies transferred into the transversal coordinates of both, electrons and ions,

$$\vec{F} \cdot \vec{v}_r = - \int_0^{\infty} 2\pi b n_e v_r \left(\frac{1}{m_e} + \frac{1}{M_i} \right) \frac{2Z^2 e^4}{(4\pi\epsilon_0)^2 v_r^2 b^2} \quad (2.94)$$

Multiplying with \vec{v}_r , this yields

$$\vec{F} = - \frac{2\pi n_e}{m_r} \frac{2Z^2 e^4}{(4\pi\epsilon_0)^2} \frac{\vec{v}_r}{v_r^3} L_C \quad (2.95)$$

where m_r is the reduced mass of the electron-ion collision system. For cooling of

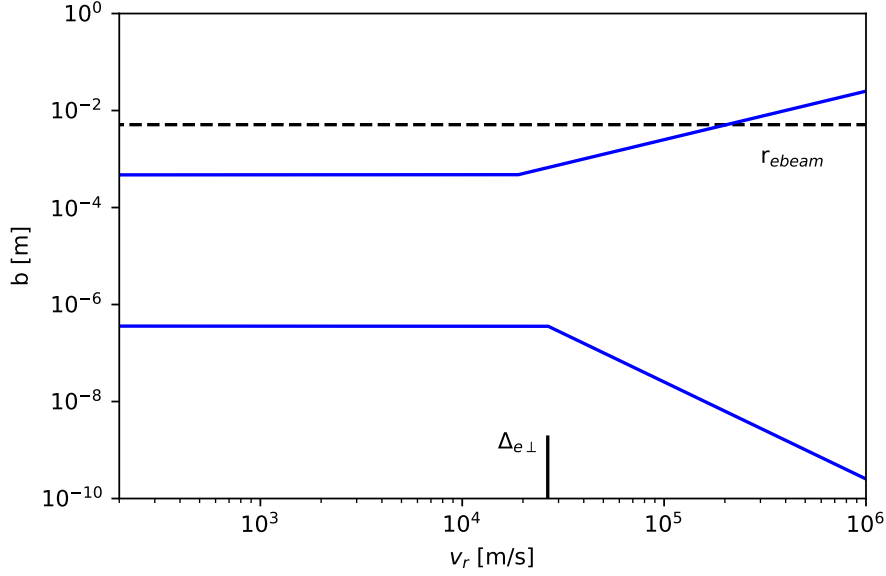


Figure 2.10: Impact parameters (neglecting magnetic field influences) calculated for a singly charged ion and typical electron density $n_e = 5 \cdot 10^5 \text{ cm}^{-3}$, longitudinal temperature $k_B T_{e,\parallel} = 80 \text{ } \mu\text{eV}$ and transverse temperature $k_B T_{e,\perp} = 2 \text{ meV}$. The typical radius of the electron beam (dashed line) is given in sect. 3.7.

atomic ions with $M_i \gg m_r$, m_r can be replaced by m_e with negligible error.

To finally arrive at the realistic expressions for the electron cooling force and diffusion, one has to take into respect the velocity distribution $f(\vec{v}_e)$ of the electrons.

Setting $\vec{v}_r = \vec{v}_i - \vec{v}_e$, the general result for the cooling force is then given by

$$\vec{F}(\vec{v}_i) = -\frac{Z^2 e^4 n_e}{4\pi\epsilon_0 m_e} \int L_C f(\vec{v}_e) \frac{\vec{v}_i - \vec{v}_e}{|\vec{v}_i - \vec{v}_e|^3} d^3 \vec{v}_e \quad (2.96)$$

For an isotropic Maxwellian electron velocity distribution with thermal velocity spread Δ_e , this formula can be approximated by [24]

$$\vec{F}(\vec{v}_i) = -\frac{3}{2} \frac{Z^2 e^4 n_e}{4\pi\epsilon_0^2 m_e} L_C \frac{v_i}{|v_i|^3 + 2\Delta_e^3} \frac{\vec{v}_i}{v_i} \quad (2.97)$$

where $\Delta_e = \sqrt{2k_B T_e / m_e} = \sqrt{2}\sigma_v$. The cooling force as calculated by eqn. 2.97 is shown in fig. 2.11. The maximum of the cooling force appears at $v_i = \Delta_e$. For $v_i \ll \Delta_e$, the cooling force has a linear proportionality to the ion velocity v_i , which

2 Electron cooling in ion storage rings

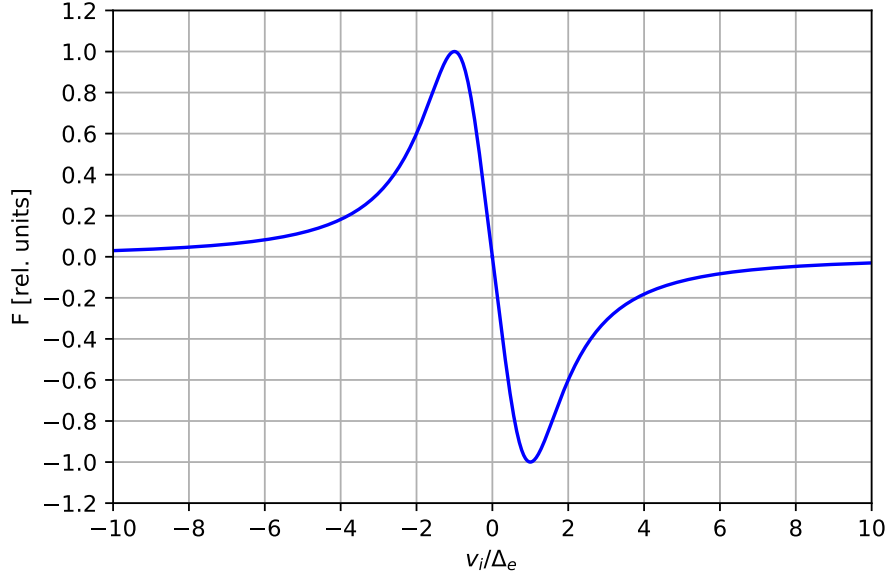


Figure 2.11: Frictional force \vec{F} as a function of the ion velocity for an isotropic electron velocity distribution with velocity spread $\Delta_e = \sqrt{2kT_e/m_e}$ (eqn. 2.97).

is from now on throughout the following chapters often referred to as the *linear regime of the cooling force*.

Influence of a longitudinal magnetic guiding field

Electron cooling devices in storage rings typically realize the merging of the electron and ion beam by guiding the electrons with the help of a longitudinal magnetic field (see chapt. 3 for technical details).

The magnetic field B forces the electrons to rotate around their axis with the cyclotron frequency $\omega_{e,c} = eB/m_e$. The radius of these transverse gyrations is given by the Larmor-radius (or cyclotron radius) $r_L = v_{e\perp}/\omega_{e,c}$.

In the presence of a magnetic field, the impact parameters can be separated into two classes [24]. Binary collisions that have collision times much smaller than the inverse cyclotron frequency (cyclotron period) are labelled as *fast collisions*, or *non-magnetic collisions*, since the confinement by the magnetic field is not visible. If, however, the electrons complete many gyrations within the collision time, one speaks of *adiabatic collisions*. In adiabatic collisions, the transverse velocity of the electrons cancels out (averages to zero) and only the longitudinal

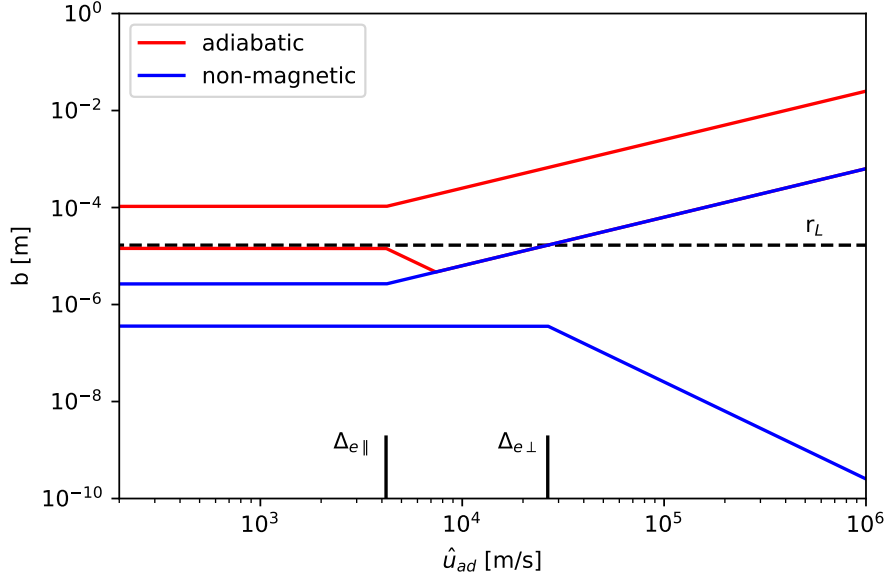


Figure 2.12: Impact parameters of the binary collision model (eqns. 2.98-2.101) as a function of $\hat{u}_{ad} = \max(u_{ad}, \Delta_{e\parallel})$, calculated for a longitudinal magnetic field of $B = 90$ Gauss, $n_e = 5 \cdot 10^5 \text{ cm}^{-3}$, $k_B T_{e,\parallel} = 80 \text{ } \mu\text{eV}$, $k_B T_{e,\perp} = 2 \text{ meV}$ and ion charge $Z = 1$.

velocity component will be considered. The relative velocity v_r is thus replaced by $\vec{u}_{ad} = \vec{v}_i - \vec{v}_{e,\parallel}$. The theory of the binary collision model has been extended to take into account the effect of the longitudinal magnetic field by Derbenev and Skrinsky [27]. Within this treatment the electron cooling force is separated into two contributions originating from the two types of collisions such that $\vec{F} = \vec{F}^{nm} + \vec{F}^{ad}$. The impact parameters b^{nm} for fast collisions and b^{ad} for adiabatic collisions can be summarized to [25]:

$$b_{max}^{nm} = u_{ad}/\omega_{e,c} \quad (2.98)$$

$$b_{min}^{nm} = \frac{Ze^2}{4\pi\epsilon_0 m_e} \frac{1}{(\max(u_{ad}, \Delta_{e\perp}))^2} \quad (2.99)$$

$$b_{max}^{ad} = \max(u_{ad}/\omega_{pl}, \lambda_{\parallel}) \quad (2.100)$$

$$b_{min}^{ad} = \max(u_{ad}/\omega_{e,c}, \frac{Ze^2}{4\pi\epsilon_0 m_e} \frac{1}{(\max(u_{ad}, \Delta_{e\parallel}))^2}) \quad (2.101)$$

yielding the adiabatic and non-magnetic Coulomb-logarithms L_C^{ad} and L_C^{nm} , re-

2 Electron cooling in ion storage rings

spectively, in the presence of a magnetic guiding field, as

$$L_C^{ad} = \ln(b_{max}^{ad}/b_{min}^{ad}) \quad (2.102)$$

$$L_C^{nm} = \ln(b_{max}^{nm}/b_{min}^{nm}) \quad (2.103)$$

where $\lambda_{\parallel} = \sqrt{\frac{\epsilon_0 k T_{e\parallel}}{e^2 n_e}}$ is the longitudinal Debye screening length (compare eqn. 2.92).

The border between adiabatic (fast) and non-magnetic collisions as discussed above is defined by the cyclotron period $\omega_{e,c}$. A calculation of the impact parameters for typical electron beam settings and the typical longitudinal guiding field of $B = 90$ G at the CSR electron-ion merged-beam setup is shown in fig. 2.12. Here, it was considered that the relative velocity $\vec{u}_{ad} = \vec{v}_i - \vec{v}_{e,\parallel}$ has a finite minimum given by $\Delta_{e\parallel}$. For this reason, the impact parameters are calculated and plotted for a relative velocity $\hat{u}_{ad} = \max(u_{ad}, \Delta_{e\parallel})$.

A more detailed discussion of the impact parameters and possible problems in defining adequate impact parameter regions can be found, for example, in [25].

2.2.6 Calculation of electron cooling rates from approximation formulae

In order to compare measured cooling times and cooling rates to theoretical predictions, a calculation of the damping decrement and hence the friction coefficient is needed. In the linear regime of the cooling force, the friction coefficient is directly given by the slope of the cooling force. However, in the general case taking into account an anisotropic velocity distribution for the electrons and ions, each force component depends on both, the longitudinal and the transverse velocity components. That means, in order to calculate a friction coefficient for one component by this approach, the ion velocity in the other component would have to stay fixed, ignoring the fact that the ion velocity is changing in both components in the cooling process. However, readily derived approximation formulae are available and will be tested against the measured results in chapt. 4. The calculation of a cooling rate from these formulae with a simplified approach is shown in the following.

Spitzer plasma relaxation time for an isotropic velocity distribution

An approach originating from plasma physics turned out to be very useful in order to get an easily accessible estimate for the electron cooling time. The relaxation time τ_{plasma} of an electron-ion plasma, describing the exponential time constant that is needed for the ions with temperature T_i to approach a colder, constant temperature T_e of the electrons, has been derived already in the 1940s by L.

2.2 Electron cooling and diffusion heating

Spitzer [28]:

$$\tau_{pl} = - \left(\frac{1}{T_i} \frac{dT_i}{dt} \right)^{-1} = \frac{3(4\pi\epsilon_0)^2 m_e M_i}{8\sqrt{2\pi} n_e Z^2 e^4 L_C^{Spitzer}} \left(\frac{k_B T_i}{M_i} + \frac{k_B T_e}{m_e} \right)^{3/2} \quad (2.104)$$

It is possible to reproduce the structure of this plasma physics formula also from the binary collision approach, when assuming an isotropic electron and ion temperature distribution [29]. In addition, for $k_B T_i/M_i \ll k_B T_e/m_e$, the formula can be simplified and used to explain the basic scaling behaviour of the cooling time:

$$\tau_{pl} = \frac{3(4\pi\epsilon_0)^2}{8\sqrt{2\pi} e^4 L_C m_e^{3/2}} \frac{M_i T_e^{3/2}}{Z^2 n_e} \quad (2.105)$$

The minimum impact parameter for the Coulomb logarithm $L_C^{Spitzer} = \ln b_{max}^{Spitzer}/b_{min}^{Spitzer}$ can be calculated from the momentum transfer Δp under the assumption that the electron-ion collision velocity is governed by the isotropic electron velocity spread:

$$b_{min}^{Spitzer} = \frac{Ze^2}{4\pi\epsilon_0 3k_B T_e m_e} \quad (2.106)$$

The maximum impact parameter is again identified with the Debye screening length:

$$b_{max}^{Spitzer} = \lambda = \sqrt{\epsilon_0 k_B T_e / (n_e e^2)} \quad (2.107)$$

With this definition, the Coulomb logarithm $L_C^{Spitzer}$ is only a function of the electron density n_e and the isotropic electron temperature T_e . The relaxation time τ_{pl} describes the time constant of the temperature relaxation process. In the linear regime of the friction force, it is the relative velocity of the ions and electrons that decreases exponentially. Due to the relation

$$k_{\perp,\parallel} = - \frac{1}{\sqrt{\langle v_{\parallel,\perp}^2 \rangle}} \frac{d\sqrt{\langle v_{\parallel,\perp}^2 \rangle}}{dt} = - \frac{1}{2} \frac{1}{T_i} \frac{dT_i}{dt} = - \frac{1}{2\tau_{pl}} \quad (2.108)$$

where $k_{\perp,\parallel}$ is the damping decrement defined in eqn. 2.66, a factor of 2 has to be considered when comparing τ_{pl} to electron cooling times. Additionally, as discussed in sect. 2.2.3, another factor of two arises when the cooling process is referred to the damping of synchrotron oscillations (shrinking of bunch width) or damping of betatron oscillations (shrinking of beam profile). Furthermore, the ratio of the effective electron cooling length L to the circumference C_0 of the storage ring, defined by $\eta_c = L/C_0$ ($\eta_c \sim 0.75\text{m}/35.12\text{m} \sim 0.021$ for the CSR [30]). An isotropic

2 Electron cooling in ion storage rings

electron cooling rate can be finally calculated from τ_{pl} by

$$\frac{1}{\tau_{Spitzer}} = r_{Spitzer} = \frac{1}{4} \frac{\eta_c}{\tau_{pl}} \quad (2.109)$$

Despite the many assumptions that do not fully reflect realistic electron cooling conditions, cooling time estimates from the Spitzer formula can often be close to measured results or at least reproduce correct orders of magnitude. eqn. 2.105 is therefore used to define a scaling parameter

$$\kappa = \frac{n_e Z^2}{A} \quad (2.110)$$

that will be helpful to compare different electron cooling rates and have a measure of the quality or efficiency of the electron cooling process.

Derbenev and Skrinky approximation for a flattened velocity distribution

In regions of very small and very large ion velocities, it is possible to derive approximations of the electron cooling friction force where also a flattened electron velocity distribution is considered. Asymptotes of the friction force in the linear regime where v_i is small compared to the electron velocity spread, the cooling force from collisions not influenced by a magnetic guiding field is [31] ([24] eqn. (43c)):

$$F_{\parallel}(v_{i\parallel}) \approx -4\sqrt{2\pi} \frac{Z^2 e^4 n_e}{(4\pi\epsilon_0)^2 m_e} L_C(\Delta_{e,\parallel}) \frac{v_{i,\parallel}}{\Delta_{e,\perp}^2 \Delta_{e,\parallel} \sqrt{2}} \quad (2.111)$$

$$F_{\perp}(v_{i\perp}) \approx -\pi\sqrt{2\pi} \frac{Z^2 e^4 n_e}{(4\pi\epsilon_0)^2 m_e} L_C(\Delta_{e,\perp}) \frac{v_{i,\perp}}{\Delta_{e,\perp}^3} \quad (2.112)$$

The Coulomb logarithm L_C is calculated with the impact parameters defined by eqns. 2.92 & 2.93. Different from [24] the full impact parameter range is taken into account in this Coulomb Logarithm as the magnetic field is disregarded. Note further that in reference [24] $\Delta_{e\parallel} = \sqrt{2k_B T_{e\parallel}/m_e}$, eqn. 2.111 therefore here appears with an additional factor $1/\sqrt{2}$.

The friction coefficients in the linear regime are simply given by $\alpha_{\parallel,\perp} = F_{\parallel,\perp}(v_{i\parallel,\perp})/v_{i\parallel,\perp}$ and the electron cooling rates $r_{\parallel,\perp}$ for synchrotron oscillation damping and betatron oscillation damping, respectively, are calculated according to eqns. 2.68 & 2.69:

$$r_{\parallel,\perp, no \ field} = \frac{\eta_c}{2} \frac{\alpha_{\parallel,\perp}}{M_i} = \frac{\eta_c}{2M_i} \left(\frac{dF_{\parallel,\perp}(v_{i\parallel,\perp})}{dv_{i\parallel,\perp}} \right) \quad (2.113)$$

Derbenev and Skrinsky approximation for a strong magnetic guiding field

Approximations have further been calculated by the same authors Derbenev and Skrinsky [27] for the collisions which are strongly influenced by a longitudinal magnetic guiding field, yielding the following formulas for the friction force for $v_i \ll \Delta_{e\parallel}$ ([24], eqn. 54a,b):

$$F_{\parallel}^{ad}(v_{i\perp}, v_{i\parallel}) \approx -\frac{1}{\sqrt{2\pi}} \frac{4\pi Z^2 e^4 n_e}{(4\pi\epsilon_0)^2 m_e} L_C^{ad}(v_{i\perp}) \frac{v_{i\parallel}}{\Delta_{e\parallel}^3 2\sqrt{2}} \quad (2.114)$$

$$F_{\perp}^{ad}(v_{i\perp}) \approx -\frac{1}{\sqrt{2\pi}} \frac{4\pi Z^2 e^4 n_e}{(4\pi\epsilon_0)^2 m_e} \ln(\Delta_{e\parallel}/v_{i\perp}) L_C^{ad}(\Delta_{e\parallel}) \frac{v_{i\perp}}{\Delta_{e\parallel}^3 2\sqrt{2}} \quad (2.115)$$

The adiabatic Coulomb logarithm L_C^{ad} (eqn. 2.102) is calculated with the adiabatic impact parameters b_{ad}^{max} and b_{ad}^{min} (eqns. 2.100 & 2.101). As mentioned above, due to the different definition of $\Delta_{e\parallel}$, these formulas here appear with an additional factor $1/(2\sqrt{2})$.

In the formula for the longitudinal friction force F_{\parallel}^{ad} and F_{\perp}^{ad} the transverse ion velocity $v_{i\perp}$ still appears in the logarithms. Here, the thermal velocity spread of the ions in the transverse direction $\Delta_{i\perp}$ will be used for a reasonable approximation, since it represents the most probable transverse ion velocity. The same is done in the logarithm in the formula for the transverse force.

Within the low-velocity regime $v_{i\perp} < \Delta_{e\parallel}$ the longitudinal cooling rates are therefore approximated by:

$$r_{\parallel,\perp, strong\ field} = \frac{\eta_c \alpha_{\parallel,\perp}}{2 M_i} = \frac{\eta_c}{2 M_i} \frac{dF_{\parallel,\perp}^{ad}}{dv_{i\parallel,\perp}} \quad (2.116)$$

2.3 Ion beam space charge effects

With an increasing number of stored ions, space charge effects in the beam become more important. The Coulomb repulsion between the charged particles in the beam can be seen as a defocusing force, opposed to the focusing force of the ion beam optics. The immediate result of a lower focusing force along the ion beam orbit is a reduced number of betatron oscillations and therefore a lower betatron tune $Q_{x,y}$.

In the case of a bunched beam, space charge effects play an important role for the longitudinal density profile and thus the shape of the ion bunches. An increasing space charge potential during electron cooling creates a lower limit for the bunch length.

Space charge effects belong to the many-particle effects in the ion beam. This

section will treat the betatron tune shift and the lower limit of the bunch length in more detail. Another effect that falls into the category of many-particle effects is intrabeam-scattering which will be treated in section 2.4.

2.3.1 Space charge tune shift

Two kinds of tune shift that are caused by the ion beam itself have to be distinguished. The *incoherent* space charge tune shift ΔQ_{sc} describes the direct effect of the space charge field on the betatron oscillation of a single particle. It is often also simply labeled as *betatron tune shift*. In addition, a *coherent* tune shift ΔQ_c arises from image charges and image currents that the circulating beam induces in the beam pipes. Assuming a perfectly round ion beam profile and a perfectly conducting beam pipe, the coherent tune shift ΔQ_c can be shown to be smaller than the incoherent space charge tune shift by the square of the ratio of the ion beam radius to the beam pipe radius [32]. In the CSR, where the radius of the beam pipe is $R = 5$ cm and the ion beam size is in the millimeter range (see sect. 4.4.2) this means that the magnitude of the coherent tune shift is never higher than a few per cent of the incoherent space charge tune shift. The contribution of ΔQ_c will therefore be neglected.

The derivation of the incoherent space charge tune shift is shown in detail in [33] and therefore not repeated here. For a coasting beam it is given by

$$\Delta Q_{sc} = -\frac{r_p N Z^2}{2\pi A \gamma_0^3 \beta_0^2 \epsilon^{2\sigma}} \quad (2.117)$$

where ϵ is the 2σ -emittance of the ion beam, A its mass number, N the number of ions, Z its charge state, $\beta_0 = v_0/c$ and γ_0 are the relativistic factors of the ion beam and $r_p = e^2/(4\pi\epsilon_0 m_p c^2)$ is the classical proton radius. For a bunched beam with bunch length l_b and harmonic number h , ΔQ_{sc} increases by the factor C_0/hl_b . The relation above can now be used to define a *space charge limit* for the maximal number of ions N_{max} that can be stored in the ring:

$$N_{max} = -B_f \frac{2\pi A}{r_p Z^2} \gamma_0^3 \beta_0^2 \epsilon^{2\sigma} \Delta(Q_{SC})_{max} \quad (2.118)$$

where $B_f = hl_b/C_0$ ($B_f = 1$ for coasting beams and < 1 for bunched beams).⁵

The maximal number of stored ions hence can be increased by increasing the injection energy. Ions are lost when the incoherent tune shift becomes so large that tune resonances are crossed in the working point diagram fig. 2.2. The tune

⁵The bunching factor is often also given as the ratio of the average current I_0 to the bunch peak current I_p : $B_f = \frac{I_0}{I_p}$.

shift given by eqn. 2.117 will drag the working point (Q_x, Q_y) to a lower value $(Q_x + \Delta Q_{SC}, Q_y + \Delta Q_{SC})$ on a diagonal line. A maximum allowed tune shift $(\Delta Q_{SC})_{max} = -0.1$ can be estimated from the CSR working point diagram.

In addition to collective effects, there is also an effect on the ion focusing from the electron beam in the electron-ion interaction section. Ideas exist where a co-propagating low energy electron lens is even used to compensate the ion beam tune shift by its space charge field that is opposed to the one of the ion beam [34, 35]. The tune shift ΔQ_e due to the co-propagating electron beam is given by [34]:

$$\Delta(Q_e)_{x,y} = \frac{Z\beta_{x,y}r_p n_e L}{2A\beta_0^2} \cdot \frac{1 - \beta_0\beta_e}{\gamma_0} \quad (2.119)$$

where L is the electron-ion interaction length, $\beta_e = v_e/c$ is the velocity of the electrons, n_e is the electron density and $\beta_{x,y}$ is the beta function in the interaction section.

Both effects are calculated and investigated in sect. 4.2.5 for a bunched beam 250 keV HeH⁺ electron cooling experiment.

2.3.2 Space charge limit of ion bunch lengths

In this subsection, the expected longitudinal density profile of an electron cooled bunched beam will be discussed with respect to space charge effects. As shown experimentally in sect. 4.2, the linear density profile of an electron cooled ion bunch can be described by a Gaussian distribution

$$\rho_{\parallel}(t) = \frac{ZeN_b}{\sqrt{2\pi}\sigma_b} \exp\left(-\frac{t^2}{2\sigma_b^2}\right) \quad (2.120)$$

where N_b is the number of ions in the bunch, Z its charge state and σ_b the Gaussian bunch width.

It will be shown here that the space charge potential creates a lower limit for the bunch length during electron cooling. A self-consistent model for the phase-space distribution under the influence of the space charge has been published already in 1979 [36]. Experimental studies in storage rings on space charge dominated cooled bunched beams have been carried out for example at the TSR for a 50 MeV ¹²C⁺ beam [37]. At the high energy electron-cooling system at the IUCF the charge line density distribution has been investigated for bunched proton beams in a synchrotron [38].

As discussed in sect. 2.2.6 for a simplified case, applying electron cooling to

2 Electron cooling in ion storage rings

a bunched ion beam introduces a friction force that dampens the synchrotron oscillations of the individual particles in the bunch. As a result, the bunch length is significantly reduced. Finally the bunch shape will be determined by the balance between the longitudinal space charge voltage and the rf-bunching voltage. An important initial assumption for the following calculations is that the longitudinal motion of the particles is completely decoupled from the transverse motion, which is justified when the bunch length is much larger than the beam radius [36]. The longitudinal space charge field is given by [39]:

$$E_{sc}(s) = -\frac{1 + 2 \ln \left(\frac{R_{tube}}{r_{beam}} \right)}{4\pi\epsilon_0\gamma_0^2} \frac{\partial\rho_{\parallel}(s)}{\partial s} \quad (2.121)$$

where $\rho_{\parallel}(s)$ is the charge line density and γ_0 is the relativistic factor of the ion beam. Knowing that the synchrotron oscillation is slow compared to the revolution frequency and thus does not strongly affect the position of a bunch particle during one turn, the longitudinal space charge field can be assumed to dominate the ion motion along s . One further assumes bunches with a short bunch length, where the phase difference of the particles to the synchronous particle $\Delta\Phi = -\omega_{rf}\frac{s}{v_0}$ (eqn. 2.39) is small [37]. From eqn. 2.43 one then obtains the approximate energy gain per turn as $Ze\hat{U}_{eff}\omega_{rf}s/v_0$. On the other hand, the energy gain of a particle with coordinate s in the longitudinal space charge field is given by $ZeE_{sc}(s)C_0$. In equilibrium, this means:

$$-Ze\frac{1 + 2 \ln \left(\frac{R_{tube}}{r_{beam}} \right)}{4\pi\epsilon_0\gamma_0^2} \frac{\partial\rho_{\parallel}(s)}{\partial s} C_0 - Ze\hat{U}_{eff}\omega_{rf}\frac{s}{v_0} = 0 \quad (2.122)$$

By integration it can be now seen that the charge line density which fulfills the condition above has a parabolic shape (see also [36])

$$\rho_{\parallel}(s) = \frac{3N_bZe}{4s_b} \left(1 - \frac{s^2}{s_b^2} \right). \quad (2.123)$$

Integrating the charge line density over the complete bunch length ($2s_b$) yields the number of charged particles N_b in the bunch

$$\int_{-s_b}^{s_b} \rho_{\parallel}(s) ds = N_bZe \quad (2.124)$$

An illustration of this space charge limited parabolic profile is given in fig. 2.13.

The space charge limited bunch length $w = s_b/v_0$ in units of temporal bunch width can finally be calculated from inserting eqn. 2.123 back into eqn. 2.122 (see

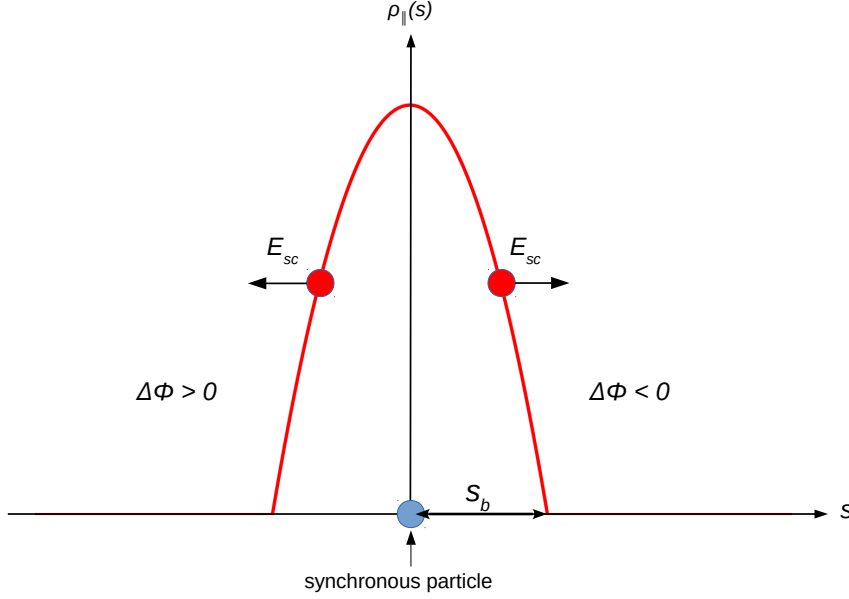


Figure 2.13: Illustration of the parabolic charge line density $\rho_{||}(s)$ of a sparse charge limited bunch with bunch length s_b in the longitudinal space charge field $E_{sc}(s)$.

also [37]) which gives:

$$w = C_0 \sqrt[3]{\frac{3 \cdot (1 + 2 \ln(R_{tube}/r_{beam})) \cdot I}{2^4 \pi^2 c^4 \epsilon_0 \gamma_0^2 h^2 \beta_0^4 U_{eff}}} \quad (2.125)$$

where β_0 is the beam velocity v_0/c and $I = hZeN_b v_0/C_0$ is the ion beam current.

The parabolic profile eqn. 2.123 derived in the space charge limit will be compared in sect. 4.6.1 with the Gaussian profile from eqn. 2.120.

2.4 Intrabeam-scattering

The charged particles within a bunched or coasting ion beam stored in a storage ring will undergo Coulomb collisions between each other due to their betatron oscillations in the transverse directions or synchrotron oscillations in the longitudinal direction. The process of losing ions due to single, large-angle scattering events out of the acceptance limit is called *Touschek effect* [40]. Multiple small-angle Coulomb scattering on the other side leads to an expansion of the ion beam

2 Electron cooling in ion storage rings

emittance in all three spatial dimensions. Without electron cooling to counter the spatial expansion by damping the beam oscillations, the IBS effect leads to a continuous diffusion growth until particles leave the acceptance, which reduces the beam lifetime. The balance of cooling and heating defines the equilibrium size and temperatures of the beam. In the following, a simplified IBS model is presented, based on an analytical model discussed in appendix C. The simplified model will be tested against measurements presented in chapt. 4.5.

2.4.1 Simplified intrabeam-scattering model

Applying the considerations of the analytical IBS model (appendix C) to a stored beam with particles of charge Z and atomic mass A at a non-relativistic velocity ($\gamma_0 \approx 1$), one arrives at a set of three coupled differential equations [41]:

$$\frac{1}{\sigma_i} \frac{d\sigma_i}{dt} = \begin{cases} c_i \frac{Z^4}{A^2} \frac{N}{\beta_0^3 \epsilon_x \epsilon_y \sigma_\delta \sigma_b h} & \text{for bunched beams} \\ c_i \frac{Z^4}{A^2} \frac{N}{\beta_0^3 \epsilon_x \epsilon_y \sigma_\delta C_0} & \text{for unbunched beams} \end{cases} \quad (2.126)$$

where $c_i (i = x, y, \delta)$ are lattice dependent functions that depend on the beam energy only weakly and h is the number of circulating bunches. Further, ϵ_x and ϵ_y are the beam emittances taken to be $\epsilon_x = \sigma_x^2 / \beta_x^2$ and $\epsilon_y = \sigma_y^2 / \beta_y^2$ at any position of the ring with appropriate β functions. In the case of a bunched beam with Gaussian bunch length σ_b , the ring circumference C_0 is replaced with the number of bunches times their length.

The three coupled differential equations 2.126 are simplified by the assumption that the horizontal and vertical emittances, the square of the momentum spread and the square of the bunch length are varying proportional to each other [41]. This yields:

$$\frac{1}{\sigma_i} \frac{d\sigma_i}{dt} = \begin{cases} \frac{c_i \beta_x \beta_y Z^4 N}{A^2 \beta_0^3 h} \frac{1}{\sigma_i^6} & \text{for bunched beams} \\ \frac{c_i \beta_x \beta_y Z^4 N}{A^2 \beta_0^3 C_0} \frac{1}{\sigma_i^5} & \text{for unbunched beams} \end{cases} \quad (2.127)$$

By introducing the *IBS heating term* $\tilde{D}_{i,b}$ for bunched beams and $\tilde{D}_{i,nb}$ for unbunched beams defined by

$$\tilde{D}_{i,b} = \frac{\tilde{c}_i Z^4 N}{A^2 \beta_0^3 h} \quad \text{for bunched beams} \quad (2.128)$$

$$\tilde{D}_{i,nb} = \frac{\tilde{c}_i Z^4 N}{A^2 \beta_0^3 C_0} \quad \text{for unbunched beams} \quad (2.129)$$

2.5 Electron cooling and diffusion in equilibrium

where $\tilde{c}_i = c_i \beta_x \beta_y$, the simplified and decoupled system of differential equations can be expressed as:

$$\frac{1}{\sigma_i} \frac{d\sigma_i}{dt} = \begin{cases} \tilde{D}_{i,b}/\sigma_i^\gamma & \text{for bunched beams} \\ \tilde{D}_{i,nb}/\sigma_i^\gamma & \text{for unbunched beams} \end{cases} \quad (2.130)$$

with $\gamma = 6$ for bunched beams and $\gamma = 5$ for unbunched beams.

eqn. 2.130 can be solved analytically using the substitution $u = \sigma_i^\gamma$, leading to $du/dt = u' = \gamma \tilde{D}_i$. The beam width during the IBS process is given by

$$\sigma_i(t) = (\gamma \tilde{D}_{i,b} t + \sigma_{i,0}^\gamma)^{\frac{1}{\gamma}} \quad \text{for bunched beams } (\gamma = 6) \quad (2.131)$$

$$\sigma_i(t) = (\gamma \tilde{D}_{i,nb} t + \sigma_{i,0}^\gamma)^{\frac{1}{\gamma}} \quad \text{for unbunched beams } (\gamma = 5) \quad (2.132)$$

2.5 Electron cooling and diffusion in equilibrium

The effects of electron cooling and diffusion heating govern the electron cooling process. Eventually, an equilibrium situation develops that defines the properties of a stable, electron-cooled ion beam. In order to obtain the time evolution of the ion distribution function in phase-space, the Fokker-Planck equation, introduced in sect. 2.2.4, has to be solved. The general procedure is to insert the expressions for the friction force F and diffusion D . However, this usually requires a numerical approach. Another complication comes from the fact that the force and the diffusion can depend on the distribution itself [24]. Therefore two simplifications are assumed that are relevant in the thermal equilibrium: the diffusion in the cooling process is constant and the electron cooling friction force is proportional to the ion velocity (linear cooling regime). Moreover, the degrees of freedom are considered separately. In such a case, the velocity distribution function is described by a Gaussian

$$\rho(v_i) = \frac{1}{\sqrt{2\pi}} \exp\left(-\frac{v_i^2}{2\sigma_{v_i}^2}\right) \quad (2.133)$$

When this $\rho(v_i)$ is inserted into the Fokker-Planck eqn. 2.2.4 a differential equation for the time dependence of σ_{v_i} is obtained:

$$\frac{1}{\sigma_{v_i}} \frac{d\sigma_{v_i}}{dt} = -\frac{\alpha_i}{M_i} + \frac{D_i}{\sigma_{v_i}^2} = \left(\frac{1}{\sigma_{v_i}} \frac{d\sigma_{v_i}}{dt}\right)_{cool} + \left(\frac{1}{\sigma_{v_i}} \frac{d\sigma_{v_i}}{dt}\right)_{heat} \quad (2.134)$$

This equation can be used to obtain the cooling to an equilibrium under a constant diffusion D_i , described by the second term on the right hand side ([24],

2 Electron cooling in ion storage rings

chapter 4).

Analogously to the simplified IBS model in sect. 2.4.1, this second term is replaced by the IBS heating rates, yielding (knowing that σ_i is proportional to σ_{v_i} for the stored beam):

$$\frac{1}{\sigma_i} \frac{d\sigma_i}{dt} = -\frac{\alpha}{M_i} + \frac{\tilde{D}_i}{\sigma_i^\gamma} \quad \text{with} \quad \begin{cases} \gamma = 6, \tilde{D}_i = \tilde{D}_{i,b} & \text{for bunched beams} \\ \gamma = 5, \tilde{D}_i = \tilde{D}_{i,nb} & \text{for unbunched beams} \end{cases} \quad (2.135)$$

where $\alpha_i/M_i = k_i$ (eqn. 2.66).

This differential equation can again be solved using the substitution $u = \sigma^\gamma$, leading to

$$\frac{du}{dt} = -\gamma k_i u + \gamma \tilde{D}_i \quad (2.136)$$

and the solution

$$\sigma_i(t) = [a \exp(-\gamma k_i t) + c]^{1/\gamma} \quad (2.137)$$

where

$$a = \sigma_{i,0}^\gamma - \sigma_{i,\infty}^\gamma \quad (2.138)$$

$$c = \sigma_{i,\infty}^\gamma \quad (2.139)$$

with the starting beam width $\sigma_{i,0}$ and the equilibrium beam width

$$\sigma_{i,\infty} = \sqrt[\gamma]{\tilde{D}_i/k_i} \quad (2.140)$$

This describes the equilibrium width with IBS and electron cooling working simultaneously.

With \tilde{D}_i as defined in eqns. 2.128 & 2.129,

$$\sigma_{i,\infty} = \begin{cases} \sqrt[\gamma]{k_i \frac{\tilde{c}_i Z^4 N}{A^2 \beta_0^3 h}} & \text{for bunched beams } (\gamma = 6) \\ \sqrt[\gamma]{k_i \frac{\tilde{c}_i Z^4 N}{A^2 \beta_0^3 C_0}} & \text{for unbunched beams } (\gamma = 5) \end{cases} \quad (2.141)$$

eqn. 2.141 predicts a scaling behaviour of $\sigma_{i,\infty} \propto N^{1/\gamma}$. This will be tested and discussed in sect. 4.6.2 for an electron cooling experiment with bunched beam HeH⁺.

3 The CSR electron-ion merged-beam setup

In this section, the implementation of the electron-ion merged beam setup into the electrostatic cryogenic storage ring CSR is presented. Therefore the section starts with a brief overview of the CSR facility and its most important features. The production of cold electron beams with a GaAs photocathode setup and important electron beam properties are discussed.

The general structure and magnet design as well as the implementation of the setup in the CSR cryostat, realized in the course of this work, are presented. The section concludes with a series of electron beam profile measurements.

3.1 Overview of the CSR facility

The CSR [13] is an electrostatic storage ring where ions can be stored in a closed orbit of 35 m. Ions are injected from a high voltage platform that is equipped with a variety of ion sources that allows for a broad range of storable ions. The kinetic energy range of the ions is 20-300 keV per charge unit, limited by the maximum voltage of the platform and other electrodes in the ring.

A schematic overview of the facility is shown in fig. 3.1. The ring has a four-fold symmetry with equal sets of ion-optical elements in each corner, consisting of two quadrupole electrodes, two 6° minor bending electrodes and two 39° major bending electrodes. Three of the four field-free straight sections are reserved for experiments, one section is dedicated exclusively for ion beam diagnostics.

An rf-bunching system is located in the straight section opposing the diagnostic section. A special feature of the CSR is the possibility to cool the experimental chambers, that are enclosed in a cryostat's isolation vacuum, down to only a few Kelvin by a liquid helium refrigerator system. Due to the extremely low vacuum realized in this cryogenic environment, ion storage times of several 100 s have been observed. The long storage time and the low temperature blackbody radiation field allows infra-red active molecules stored in the CSR to equilibrate to lowest vibrational and rotational quantum states.

Several types of ion reactions are studied in the CSR. In the electron-ion merged

3 The CSR electron-ion merged-beam setup

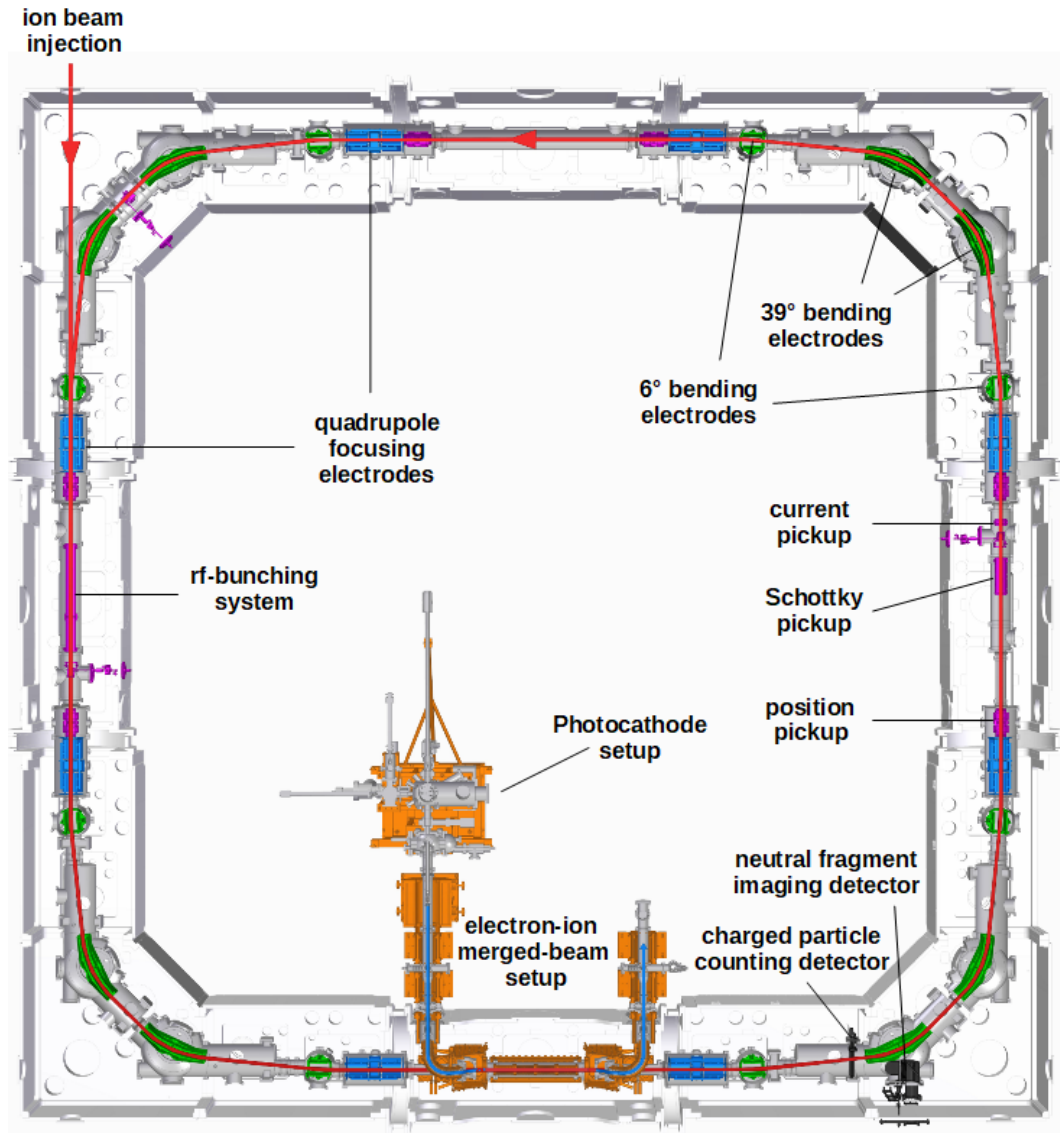


Figure 3.1: Schematic overview of the CSR facility at the MPIK.

beam section not only collisional reactions of electrons and ions, but also photon-ion reactions can be investigated with a merged- or crossed-beam laser setup.

Reaction products can be analyzed by two types of MCP detector systems. Charged fragments that leave the closed orbit of the stored ions can be detected by a *COLD MOvable PArTicle CounTer (COMPACT)*. A second detector (*Neutral Imaging in Cold Environment, NICE*) is equipped to count neutral fragments with high position-sensitivity and high time precision. Imaging experiments with respect to electron cooling measured with this detector are presented in sect. 4.4.

Furthermore, a merged-beam setup that studies collisions of ions with neutral atoms has been added to the CSR facility recently.

3.2 GaAs photocathode cold electron source

In this section the electron beam production for the electron-ion merged beam setup is presented. Photocathode electron sources offer the possibility to produce electron beams that have lower initial energy spreads than those from conventional thermocathodes. A setup for the extraction of dense electron beams from such a source has been designed for operation at the TSR electron target in previous works [16,42,43]. After the shutdown of the TSR in 2012, the setup was transferred to the CSR and taken into operation at the electron-ion merged beam setup as part of this work. Following an overview of the photocathode setup, further means of reducing the electron beam temperature, adiabatic magnetic expansion and kinematic compression, are presented.

3.2.1 NEA GaAs photocathodes

In the photocathode setup, *p*-doped GaAs semiconductor surfaces are coated with monolayers of cesium and oxygen (see fig. 3.2 (a)). As a result a surface state of so-called *Negative Electron Affinity* is reached, where the vacuum level at the surface is reduced below the conduction band minimum [44]. The emission process of electrons that are excited into the conduction band by laser illumination from the back (*transmission mode*) is sketched in fig. 3.2 (b).

In the conduction band, electrons thermalize into a Boltzmann distribution that is defined by the temperature of the crystal and drift towards the crystal surface. The electron can escape into the vacuum by tunneling through the thin potential barrier created by the (Cs,O) layer. This can happen either directly, or after they lost energy in processes like scattering with surface defect states or phonon emission [45]. In the latter case, electrons leave the crystal with a much broader energy distribution. However, when operating the electron beam extraction in the so called *space-charge limited mode* (see further discussion below), high laser intensities and low extraction voltages cause the accumulation of an electron cloud in front of the crystal surface. Very slow electrons are blocked by this potential and the energy distribution of the extracted electrons in this mode is again given by their initial distribution in the bulk GaAs [46,47]. With the NEA GaAs(Cs,O) photocathodes available at the CSR photocathode setup, quantum yields of up to $\sim 20\%$ can be reached.

3.2.2 The electron gun design

The electron gun is designed in a so-called Pierce geometry [48], shown in fig. 3.2 (c), and embedded in a high-field solenoid (compare fig. 3.4). The guiding field of typically 2.0-2.5 kG in the gun region prevents a transverse blow-up of the beam. Electrons are excited with a 808 nm laser (Coherent F6-808-3-2400C) with a typical output power of up to 1 W. The photocathode holder is pressed by a spring onto a copper surface by a spring that is aligned with the gun electrodes. Versus ground, the cathode is held at a potential of $-U_0$. The Pierce shield with an aperture diameter of 3 mm is an important tool for shaping the electron beam (see also sect. 3.7) and typically set to voltages of about +3 V with respect to the cathode potential. The extraction electrode is usually set to +15 V. The use of an intermediate acceleration electrode has turned out to be not necessary and it is therefore connected with the extraction electrode. Following the extraction, the electrons enter a 25 cm long drift tube before magnetic expansion takes place upon leaving the high solenoidal field. This is called the barrier electrode and held to a small positive voltage U_b with respect to ground. It accelerates the electrons to $U_0 + U_b$. Ions produced by electron collisions with residual gas in the grounded regions are rejected by the barrier potential U_b .

Space-charge limited electron gun operation

Two modes of electron extraction are possible for the electron gun. In the current-limited mode, high extraction voltage or low laser intensities result in the extraction of every electron that is emitted from the crystal surface. The emitted current does not depend on the extraction potential, but is defined by the laser intensity and the quantum yield of the photocathode.

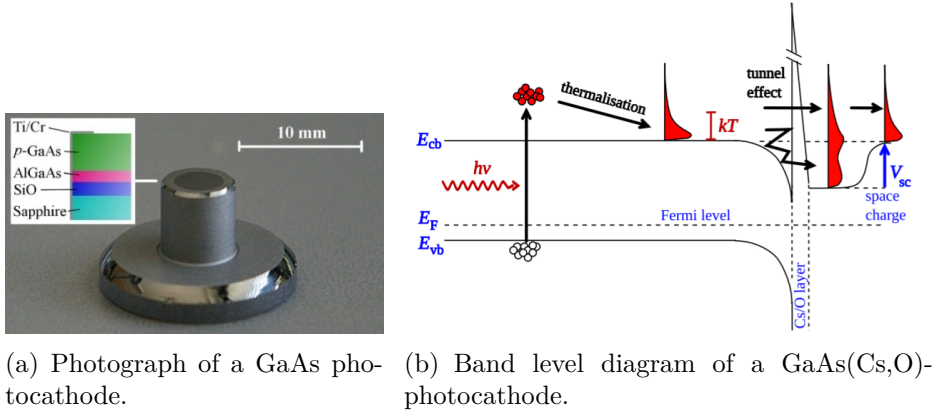
In the *space-charge limited mode*, the electron current I_e that can be extracted from the cathode is related to the extraction voltage U_{ext} by the Child-Langmuir law [24]:

$$I_e = pU_{ext}^{3/2} \quad (3.1)$$

where the perveance p is a gun geometry-dependent parameter with unit 1 perv = $\frac{\text{A}}{\text{V}^{3/2}}$. Operating in this extraction mode has the advantage that one is independent from any fluctuations of the laser intensity as well as degradation of the photocathode surface layers which affects the quantum yield.

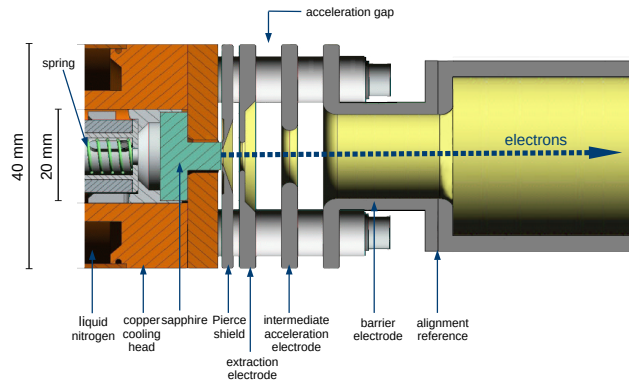
The extracted current from the electron gun that is collected by a Faraday cup (see sect. 3.7) is shown in fig. 3.3 (a) as a function of the laser intensity. For an extraction voltage of $U_{ext} = 15$ V the space-charge limited regime is reached at about 600 mA operating current of the laser diode, corresponding to a laser power

3.2 GaAs photocathode cold electron source



(a) Photograph of a GaAs photocathode.

(b) Band level diagram of a GaAs(Cs,O)-photocathode.



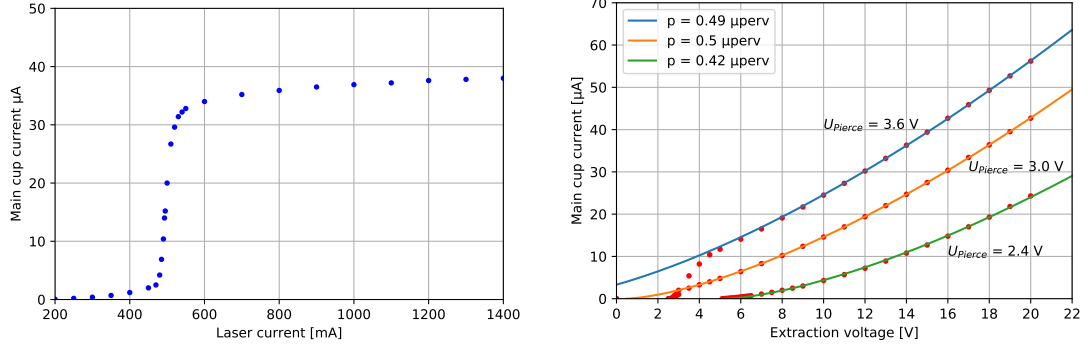
(c) Cut view of the photoelectron gun.

Figure 3.2: GaAs-photocathode cold electron source (figures taken from [46], (c) partly modified).

of ≈ 50 mW.

fig. 3.3 (b) shows the electron current as a function of the extraction voltage (with respect to the cathode potential) for a laser current of 1000 mA (≈ 150 mW) and three different Pierce voltage settings. After a certain threshold extraction voltage is reached, the electron current is clearly described by the space-charge law. The perveance of the electron gun can be extracted from a fit of the function $I_e = a(U_{ext} - U_{off})^{3/2}$ to the space-charge limited regime of the extraction curves. For a pierce voltage of 3.0 V, we find $U_{off} \approx 0$ and $a = p = 0.5 \mu\text{perv}$. This is the usual operation mode of the electron gun at the CSR.

3 The CSR electron-ion merged-beam setup



(a) Electron current as a function of the laser current for fixed extraction voltage $U_{ext} = 15$ V. (b) Perveance curves for different Pierce voltage settings (1000 mA laser current).

Figure 3.3: Photocathode electron gun operation in the space charge limited mode.

3.3 Magnetized electron beam temperatures

The velocity distribution of the electron beam in the electron-ion merged-beam section, given by the electron beam temperatures, determines the electron cooling force (eqn. 2.96). Furthermore, from the point of view where the merged-beam setup is used as an electron target for collision experiments, exact knowledge of this distribution is needed in order to deconvolve measured recombination rates to specify reaction cross sections [49].

Analogously to sect. 2.1.3, the temperatures of the electron beam in the co-moving frame are separated into a longitudinal and transverse component that are defined by:

$$\frac{1}{2}kT_{e\parallel} = \frac{1}{2}m_e\Delta_{e\parallel}^2 \quad (3.2)$$

$$kT_{e\perp} = \frac{1}{2}m_e\Delta_{e\perp}^2 \quad (3.3)$$

$$(3.4)$$

where $\Delta_{e\perp,\parallel}$ are the transverse and longitudinal electron velocity spread, respectively. With this definition

$$\Delta_{e\parallel} = \sigma_{v_{e\parallel}} \quad (3.5)$$

3.3 Magnetized electron beam temperatures

In the general case $\sigma_{v_x} \neq \sigma_{v_y}$,

$$kT_{ex} = m_e \sigma_{v_x}^2 \quad (3.6)$$

$$kT_{ey} = m_e \sigma_{v_y}^2 \quad (3.7)$$

the transverse beam temperature is defined by

$$T_{e\perp} = \frac{1}{2} (T_x + T_y) \quad (3.8)$$

$$kT_{e\perp} = \frac{1}{2} m_e (\sigma_{v_x}^2 + \sigma_{v_y}^2) = \frac{1}{2} m_e \Delta_{e\perp}^2 \quad (3.9)$$

3.3.1 Adiabatic magnetic expansion

The initial transverse temperature of the extracted electron beam can be reduced by an adiabatic expansion of the solenoidal guiding field B . The electrons move on spirals around the magnetic field lines with the cyclotron frequency

$$\omega_c = \frac{eB}{m_e} \quad (3.10)$$

and spiral radius

$$r_c = \frac{m_e v_{e\perp}}{eB} \quad (3.11)$$

The longitudinal distance λ_c that is travelled by an electron during one cyclotron spiral is then given by

$$\lambda_c = 2\pi \frac{v_{\parallel}}{\omega_c} = 2\pi \frac{m_e v_{\parallel}}{eB}. \quad (3.12)$$

When the magnetic field strength B is varied along the beam slowly enough,

$$\left| \frac{dB}{dz} \right| \ll \frac{B}{\lambda_c} \quad (3.13)$$

the ratio $\langle E_{\perp} \rangle / B$ remains constant in the electron beam [50, 51].

An adiabatic magnetic expansion of an initial field B_i to a final field B_f by expansion factor

$$\alpha = \frac{B_i}{B_f} \quad (3.14)$$

thus reduces [51] the mean transverse energy $\langle E_{\perp} \rangle$ and thereby T_{\perp} by

$$T_{\perp,f} = \frac{T_{\perp,i}}{\alpha}. \quad (3.15)$$

3 The CSR electron-ion merged-beam setup

Furthermore, the reduction of the transverse temperature is accompanied by an increase of the electron beam radius R . According to the invariant $R^2 B = \text{const}$ [28], the final expanded beam radius is given by

$$R_f = \sqrt{\alpha} \cdot R_i. \quad (3.16)$$

A reduction of the transverse temperature T_{\perp} by adiabatic magnetic expansion is hence always accompanied by a decrease of the electron beam density n_e .

3.3.2 Longitudinal temperature

The longitudinal temperature component becomes significantly reduced compared to the initial temperature in the laboratory frame due to the electrostatic acceleration of the electrons. After their emission from the cathode with initial temperature T_c and acceleration by the potential U_0 , the final longitudinal temperature is given by [17]:

$$k_B T_{\parallel} = \left(1 + \left(\frac{\alpha - 1}{\alpha}\right)^2\right) \frac{k_B T_c^2}{2E_e} + C \frac{e^2 n_e^{1/3}}{4\pi\epsilon_0} \quad (3.17)$$

The term $k_B T_c^2 / (2E_e)$ describes the kinematic compression due to the acceleration. The final expression in eqn. 3.17 is obtained by taking into account contributions of temperature relaxation effects between the two degrees of freedom. Namely these effects are transverse-longitudinal-relaxation (TLR), caused by energy being shifted from the transverse to the longitudinal degree of freedom during adiabatic magnetic expansion with expansion factor α (see below), and the electron density dependent longitudinal-longitudinal-relaxation (LLR). The LLR effect occurs when the initially disordered electron cloud will restructure during the longitudinal acceleration in order to minimize its potential energy. This is achieved by transferring potential energy into kinetic energy and hence contributes to the longitudinal temperature [52]. The factor C is a measure of the adiabaticity of the acceleration process. For the rather fast acceleration at the photocathode by potentials on the order of tens of eV, $C \approx 1.9$ [52].

3.3.3 Electron velocity distribution

Due to the much stronger compression of the longitudinal temperature as compared to the transverse temperature which is not affected by the electrostatic acceleration, the velocity distribution of the electron beam is highly anisotropic

3.4 Magnetic guiding field for electron beam transport

Table 3.1: Typical electron beam operational settings for electron cooling of the ion species investigated in this work and corresponding electron beam temperatures. The electron density n_e in the electron-ion interaction region is calculated with an estimated effective cathode radius 1.1 mm (sect. 3.7). $T_{e\parallel}$ follows from eqn. 3.17 with $C = 1.9$.

	E_e [eV]	α	I_e [μ A]	n_e [10^5 cm $^{-3}$]	$T_{e\perp}$ [meV]	$T_{e\parallel}$ [μ eV]
250 keV HeH $^+$	27.3	21.59	27.0	6.6	~ 2	90
250 keV HD $^+$	45.7	30	34.7	4.3	~ 2	78
250 keV O $^+$	8.6	30	31.2	11.3	~ 2	163
1.39 MeV F $^{6+}$	46.1	21.59	14.4	2.9	~ 2	66

and thus can be described by a flattened Maxwellian distribution:

$$f(\vec{v}_e) = \left(\frac{m_e}{2k_B T_{\perp}} \sqrt{\frac{m_e}{2k_B T_{\parallel}}} \frac{1}{\pi^{3/2}} \right) e^{-\frac{m_e}{2k_B} \left(\frac{v_{e\perp}^2}{T_{\perp}} + \frac{(v_{e\parallel} - \langle v_{e\parallel} \rangle)^2}{T_{\parallel}} \right)} \quad (3.18)$$

The attainable transverse temperature of electron beams produced with the GaAs-photocathode has been measured in 2007 when the photo-electron gun was still in operation at the TSR. By measuring very narrow (less than 0.1 meV half width) dielectronic recombination resonances of F $^{6+}$ forming F $^{5+}$ in an electron-ion merged beam experiment, the transverse electron temperature could be obtained from a fit of such a resonance where the transverse and longitudinal temperature are the only free fit parameters [46]. For an expansion factor of $\alpha = 20$ and typical electron density $n_e \approx 1 \cdot 10^6$ cm $^{-3}$ a transverse temperature of $T_{\perp} = 2.3(2)$ meV is fitted. An expansion factor of $\alpha = 40$ yields a lower value of $T_{\perp} = 1.6(1)$ meV.

At the CSR electron-ion merged beam setup, where no dedicated measurement of the electron beam temperatures has been performed yet, one thus estimates $T_{e\perp} \approx 2$ meV wherever the transverse electron temperature is needed to calculate cooling rates (see sect. 4.2.4 and 4.4.2). A summary of typical electron beam properties in the electron cooling operation for the different ion species treated in this work can be found in table 3.1.

3.4 Magnetic guiding field for electron beam transport

The structure of the longitudinal magnetic guiding field of the electron-ion merged-beam setup has been created in this work and is shown in fig. 3.4. It differs from

3 The CSR electron-ion merged-beam setup

designs of magnetic guiding fields in conventional high-energy electron coolers [24]. In these S - or U -shaped designs electrons are bent into (and out of) the merging plane horizontally by magnetic toroids that have rather large openings for the ion beam. The inhomogeneity of the magnetic field in these areas of the toroids cause a vertical deflection of the ion beam that is corrected for with dipole compensation coils. However, such a horizontal merging scheme is not suitable for typically slow and light ion beams stored in the CSR where the deflection due to their low rigidity would become so large that it can not be corrected anymore by simple dipole coils.

For this reason, the merging and de-merging of the electron beam into the ion beam plane is performed by a combined dipole and solenoidal field. As proposed by [53] in the early design phase of the setup, the electron trajectory starts above the ring plane. After a 90° bend in a toroid, the beam is merged down into the ion beam orbit by a separate dipole-like field. This net field experienced by the ion beam in this arrangement is much more uniform than a toroidal bending field. The remaining deflection of the ions in this field can (as in the standard setup) be corrected by dipole correction coils before and after the merged-beam section. The realization of the proposed scheme into a magnetic field design that is suitable to be implemented into the CSR has been done by A. Shornikov [54]. The design phase has been completed and the final construction phase of the mechanical components was started by S. Vogel [30], while the final construction of the components and their assembly in the complete system was performed in the present work.

An overview of the magnetic structure and its individual components is shown in fig. 3.4. The setup can be divided into five parts: the electron beam production section, the merging section, the interaction section, the de-merging section and the electron collector section.

The beam axis of the electron beam production section is built 140 mm above the ion beam orbit of the CSR. The photoelectron gun is embedded in a high-field solenoid typically operated at fields of 2000-2500 G. Upon leaving the high-field solenoid, the electrons enter a field of typically 200-250 Gauss, created by three smaller copper solenoids. This is the area of the first magnetic expansion of the electron beam.

The transition from the room temperature beamline into the CSR cryostat takes place when the beam enters the toroidal solenoid. In the toroid, electrons first experience a 90° bend to be parallel to the ion beam orbit. The merging with the ion beam is then realized by another 30° bend downwards in the toroid, using

3.4 Magnetic guiding field for electron beam transport

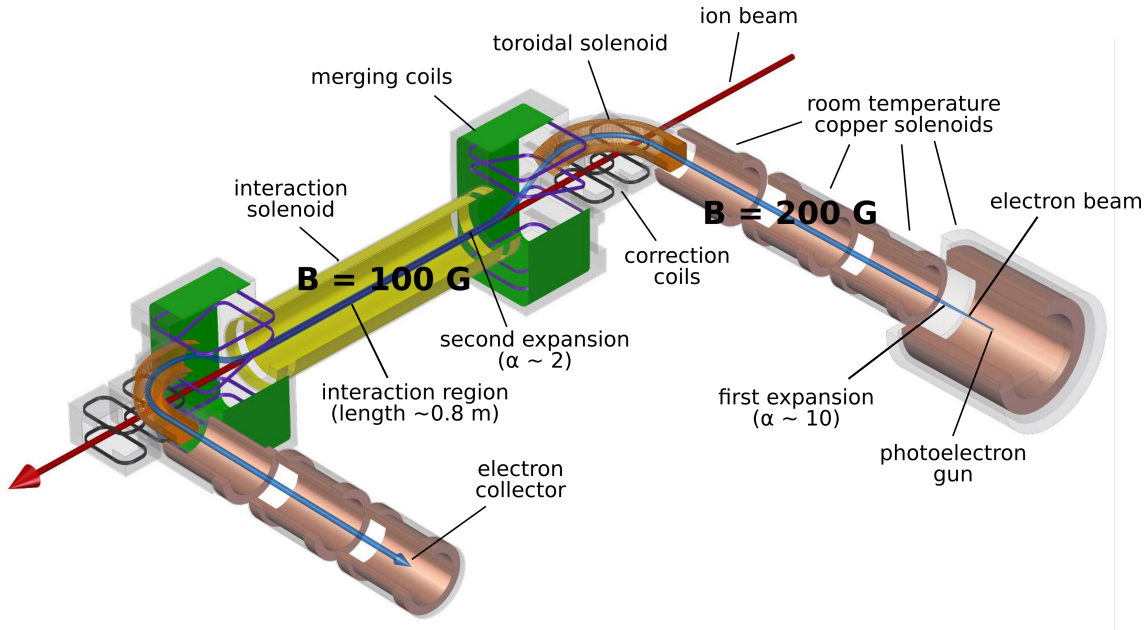


Figure 3.4: Overview of the CSR electron-ion merged-beam setup magnetic structure (modified from [30]).

the above mentioned dipole merging field. The latter is realized by four racetrack coils, two of them positioned above and two of them below the ion beam orbit (“Merging vertical” coils). The racetrack coils are located inside the field of another solenoidal magnet, labeled as merging solenoid. All these components are housed in the CSR cryostat and were home built using high-temperature superconducting material (HTS).

The second magnetic expansion with $\alpha = 2$ takes place in the transition of the merging section into the interaction section. A small 34 mm wide field gap at both ends of the interaction section (compare fig. 3.19 (c)) is necessary to leave space for electrical feedthroughs to the interaction drift tube electrodes, viewports for a crossed beam laser setup, and feedthroughs for the rotary drives of the beam wire scanners (scrapers) (see sect. 3.6.1). The interaction solenoid is therefore split into two smaller solenoids (47 mm) and the main interaction solenoid (944 mm). The length of the drift tube assembly in the main solenoid’s field is 870 mm. The magnetic field dependence along this region will be presented below (fig. 3.19 (c)).

The de-merging of the electrons is performed symmetrically to the merging, with the dipole merging field now obviously being directed upwards. Three copper solenoids operated at the identical field as in the electron production are placed in

3 The CSR electron-ion merged-beam setup

the electron collector section. With the electron collector cup the electron current is monitored continuously and it is routinely used to measure transverse electron beam profiles. The setup is equipped with a blocking electrode that can be used to decelerate the electron beam, and can thus in principal be operated as a retarding field analyzer. The electron collector section and electron beam profile measurements are described in more detail in sect. 3.7.

Two sets of dipole correction coils (“compensator pairs”), also built from HTS material, are placed in front of and behind the interaction region to compensate for the influence of the merging field onto the ion beam. During the storage of a 250 keV HeH⁺ beam it has been observed that the influence of the merging field is so small, that even without operating the correction coils the ion beam is not lost.

The connections of the HTS magnets are realized in a way that in total only 8 connections (4 pairs of current inputs and outputs) and hence only four power supplies are needed to operate the magnetic guiding and merging field as well as the correction coils. All solenoidal magnets are connected in series with the same power supply. The same is true for the two sets of four racetrack coils in the merging (demerging) section that create the dipole merging (demerging) field. Furthermore, the two outer and inner sets of ion beam correction coils are connected to a single power supply, respectively (see also table 3.2). The design currents and corresponding fields of the HTS magnets are summarized in table 3.2. In addition, several steering coils wound from copper wire are placed in the room temperature beamline parts as well as in the cryogenic region for minor corrections of the electron beam position and angle.

3.5 Realization of the setup in the CSR

The implementation of the mechanical structure of the electron-ion merged-beam setup into the very confined space in its dedicated section in the CSR has been a challenging task. This section will give a summary of the final setup and some key features for the operation will be discussed.

Fig. 3.5 shows an overview of the electron-ion merged beam setup inside the CSR. The GaAs-photocathode setup (1) is rather sizable due its set of separate vacuum chambers for photocathode coating and crystal surface cleaning [46]. The transfer of prepared photocathodes between these chambers and the transfer into the electron gun chamber (electron beam production beamline) are performed with vacuum manipulators (2). The vacuum of the room temperature beamlines can be separated from the cryogenic part by two full metal valves (3). The electron

Table 3.2: Design values for the HTS currents for operating at 250 G solenoidal field and 125 G in the interaction solenoid (defined by expansion $\alpha = 2$ in this region) [30]. The HTS currents for operating at an interaction solenoidal field of about 90 G that have been found experimentally in this work to be most suitable regarding heat input. Optimized current settings for electron beam transport and ion beam storage differ slightly (compare sect. 3.7 and sect. 4.1).

HTS magnet	I_{HTS} (design) [A]	I_{HTS} (this work) [A]
Toroids	76	60.8
Merging Solenoids	76	60.8
Interaction Solenoids	76	60.8
Merging Verticals	60	40
Compensator Pair 1	68	54.5
Compensator Pair 2	69	55.2

collector (4) is located above the high-voltage platform (5) where power supplies for drift tubes in the interaction region and the electron gun potentials are installed (for the complete scheme of the electronic circuit see sect. 3.5.1). A cold head and heat exchanger (6) as well as the compressors and flow regulation (7) of a closed-cycle HTS coil-cooling system (sect. 3.5.3) are located on top of the CSR cryostat.

A photograph of the cryogenic part of the merged-beam structure is shown in fig. 3.6 (a). Here, a horizontal cover on the outside of the CSR is lifted from the outer cryostat wall (1). In order to view the inside of the merged-beam structure in the CSR isolation vacuum, the thermal shield (2) and the multilayer-superinsulation foil (3) have to be dismantled.

In the view of the cryogenic part (fig. 3.6 (a)), the iron shields of the HTS magnets in the interaction and merging section are labeled by (4) and (11), respectively. Two high-purity aluminum terminal plates (5) are mounted below the interaction solenoid. The current leads (25 mm² flexible Cu lines) coming from the warm electrical feedthroughs of the cryostat wall are first thermally anchored on these cooled plates. The same is done for any kind of signal leads, for example about 100 temperature sensor cables that are distributed all over the cryogenic part.

Several cooling helium lines at different temperature stages between 2 K and 80 K are available in the CSR isolation vacuum [13]. The terminal plates (5) and the

3 The CSR electron-ion merged-beam setup

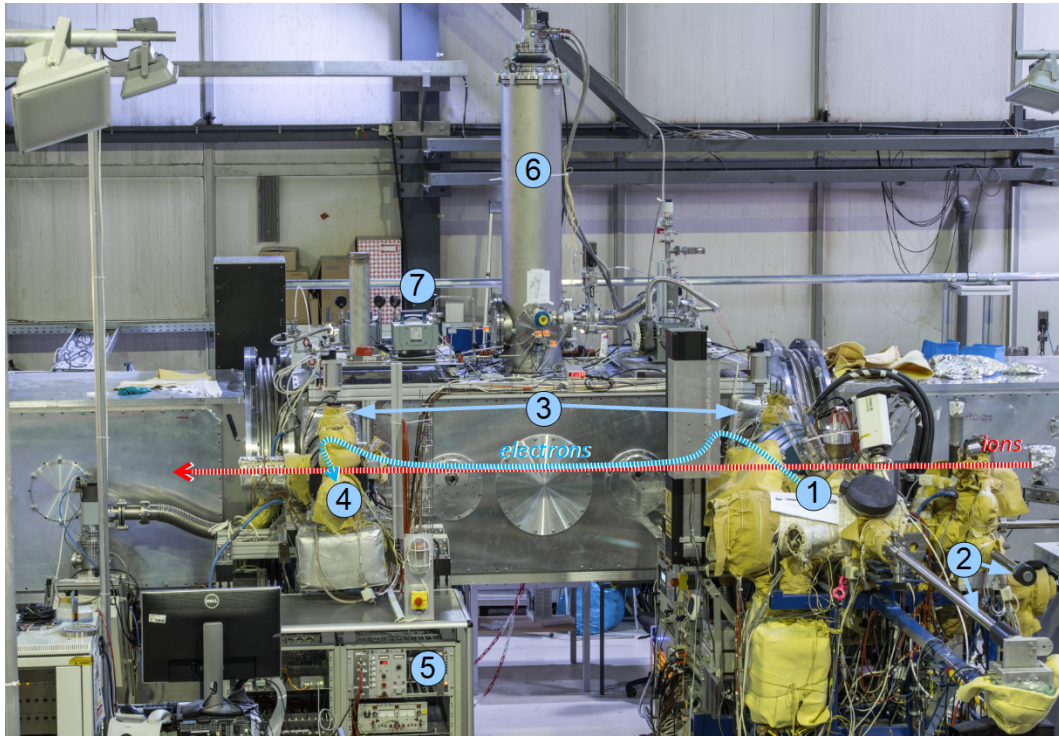


Figure 3.5: Photograph of the electron-ion merged-beam setup: (1) GaAs-Photocathode setup, (2) vacuum manipulators, (3) full metal valves, (4) electron collector, (5) HV platform, (6) cooling tower, (7) cooling system compressors.

thermal shield (2) are in the usual cold operation of the ring connected to the 80 K line. The beamline vacuum chambers are connected to the 2 K liquid helium line. This is demonstrated by label (8) where a copper band that is fixed to one of the 2 K copper cooling blocks is guided through the gap between the small solenoid and the main solenoid and connected to the interaction region vacuum chamber. In order to shield the cold vacuum chamber from heat leaking through this gap section, the area is enclosed as well as possible by several layers of bakeable multilayer insulation (10). The inlet and outlet of the HTS coil-cooling system are marked by labels (14) and (15), respectively.

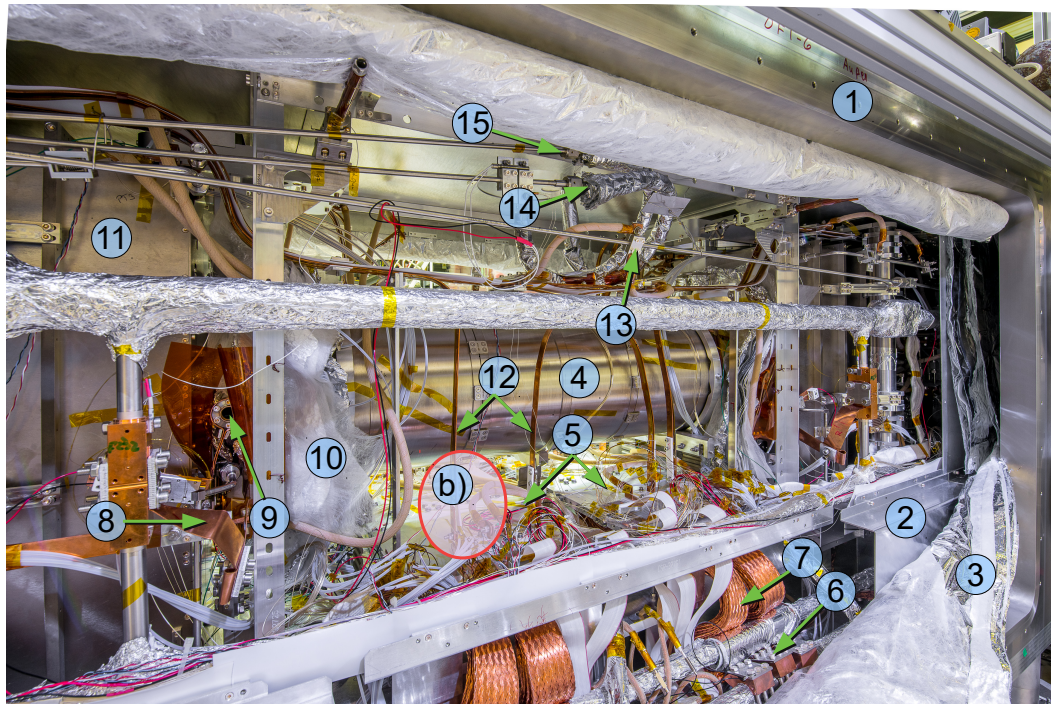
Special care has to be taken for the current distribution to the HTS magnets. At the design current values given in table 3.2 that have been the initial test currents in the commissioning phase, a thermal power input on the terminal plates of ~ 5.5 W per connection pair is estimated solely from the electrical power. Another ~ 3.5 W per pair have to be added for the heat conduction via the 1.6 m long and

3.5 Realization of the setup in the CSR

25 mm² thick copper cables from the room temperature cryostat wall electrical feedthrough to the terminal plate. The operation of the HTS magnets at the design values hence yields a thermal power of about 35 W, which is with roughly 40% of the total estimated thermal power the biggest contribution on the terminal plates and hence on the 80 K cooling line of the CSR [30].

In order to keep this heat input on the 80 K line decoupled from the HTS coil-cooling system (sect. 3.5.3) as efficiently as possible, the anchoring on the terminal plate is constructed as shown in fig. 3.6 (b). The decoupling scheme with details of the construction elements is presented in fig. 3.6 (c). The main element of the design is a flat copper connecting bar that is put on top of a sapphire piece. The sapphire piece and the copper bar are pressed onto the terminal plate by a block of *PEEK* insulator material that is attached to the terminal plate by screws in four positions. The copper bar is thus electrically isolated from the aluminum plate, but has a very good thermal contact. The latter is improved even further by a thin layer of silver foil between the sapphire and the terminal plate. The copper cable is attached to one end of the connecting strip, while the other end is used to realize a thermally decoupled current lead transition to the HTS magnets. This is done by using the same type of HTS band wire that is used in the production of the HTS magnets themselves. The HTS wire is indium-soldered to a copper piece that functions as electrical connection to the copper bar. The HTS band is then mounted onto copper rails (see also (a), label (12)) that are guided close to the current leads of the respective HTS magnets, where the last few cm are again connected by flexible copper cables. To ensure sufficient cooling below the critical temperature of 100 K for the superconducting transport line, the copper rails have several thermal connection points to the HTS coil cooling system gas tubes (see e.g. (a), label (13)). The copper rails are fixed to the copper bar on the terminal with an insulating teflon piece whose only function is to keep the copper rails in place. The electrical connections are hence only realized by the superconducting wire. These superconducting wire lines are used to distribute the current over several meters inside the isolation vacuum. Ohmic heating from the connecting cables could be significantly reduced by this design.

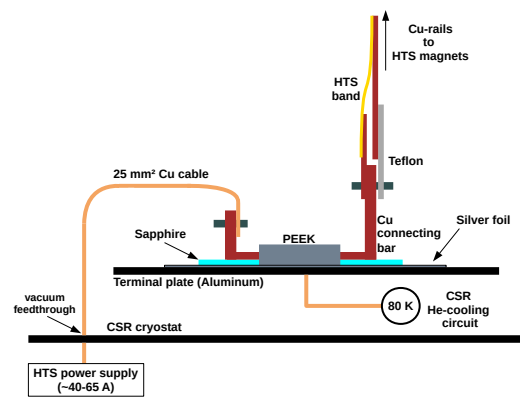
3 The CSR electron-ion merged-beam setup



(a) Realization of the cryogenic part of the electron-ion merged-beam setup inside the CSR cryostat.



(b) High current distribution (up to 76 A) to the HTS magnets.



(c) Scheme of current lead from the room temperature power supply to the cryogenic HTS magnets.

Figure 3.6: Transition of the HTS magnets copper current line to a superconducting wire distribution line on the 80 K terminal plates.

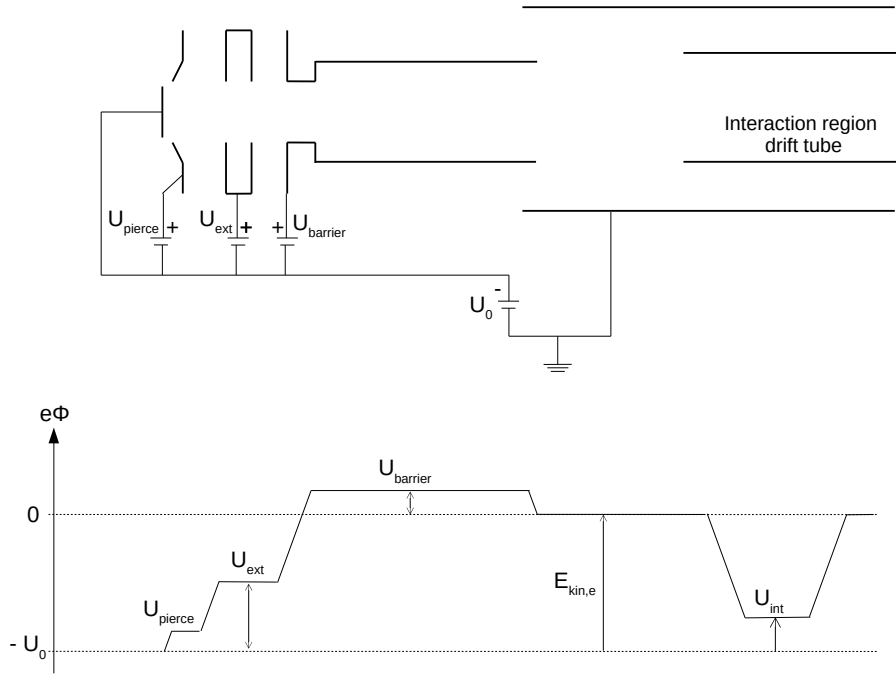


Figure 3.7: Schematic of electron beam formation electrodes and potentials in the electron gun.

3.5.1 High voltage platform and electronic circuit

An overview of the potentials for beam formation in the electron gun is given in fig. 3.7. The various electrode voltages are set with the help of an isolated platform held at the cathode potential U_0 with respect to ground, called the high voltage platform (see also [55]). The kinetic energy of the electrons (see fig. 3.7) in the CSR region is basically set by U_0 .

The electronic circuit of the electron-ion merged-beam setup is shown in fig. 3.8. For the purpose of describing the principle of the circuit, the setup can be divided into three parts, the electron gun part, the interaction region with the drift tube assembly and the electron collector part.

The potentials for the individual gun and collector electrodes are set by power supplies inside a high voltage platform. The platform ground potential, defining the cathode potential in the electron gun, can be set by either solely a slow, but stable power supply of the model Iseg EHQ. On top of that, a fast-switchable bipolar Kepco power supply is used for a detuning of the platform potential and hence a detuning of the electron energy (see sect. 3.5.2 for further details).

3 The CSR electron-ion merged-beam setup

In the interaction region, the electron energy can further be tuned by entering an assembly of drift tubes, held on potential U_{int} such that basically $E_{kin,e} = eU_{int}$ instead of U_0 . An amplifier box on the high voltage platform is used to control the interaction region drift tubes. The drift tubes are assembled symmetrically to the center of the interaction region, with two longer 333 mm electrodes in the middle and three shorter 30 mm long electrodes on each side. The idea of having several stacked electrodes instead of one single, long drift tube is the ability to have very smooth potential transitions along the drift region. The last three drift tube electrodes in beam direction also have a vertical cut (marked by golden and blue electrode pairs in fig. 3.8), which allows to set a potential across the radial direction of the beam axis. This is necessary to extract ions that are produced by electron impact ionization with rest gas ions and can be caught in the radial space charge potential of the electron beam. This set of electrodes are hence called *clearing electrodes*.

In the electron collector part, the electrons hit a main cup at U_{mc} with respect to the cathode. The cup has a pin hole through which some electrons may continue to a retarding field analyzer where the longitudinal electron energy distribution can be obtained from deceleration of the electrons with the retarding potential U_{ret} [48, 56]. The current through the pin hole is also used for electron beam profile measurements (see sect. 3.7). Here, no retarding potential is needed and the collector electrodes are mainly grounded.

Two distinct control systems are placed on the platform for setting and reading parameters. A commercial *Nationals Instruments USB 6343 DAQ card* is used for parameters that need fast switching times, for example the drift tube voltages and the cathode potential detuning with the Kepco power supply. Parameters that will be operated mostly at fixed or slowly changing values are controlled with the in-house developed EUNET control system. A terminal PC communicates with the DAQ card via an USB to fiber converter. The EUNET cards on the platform are connected with an ethernet to fiber converter to their own server network.

3.5 Realization of the setup in the CSR

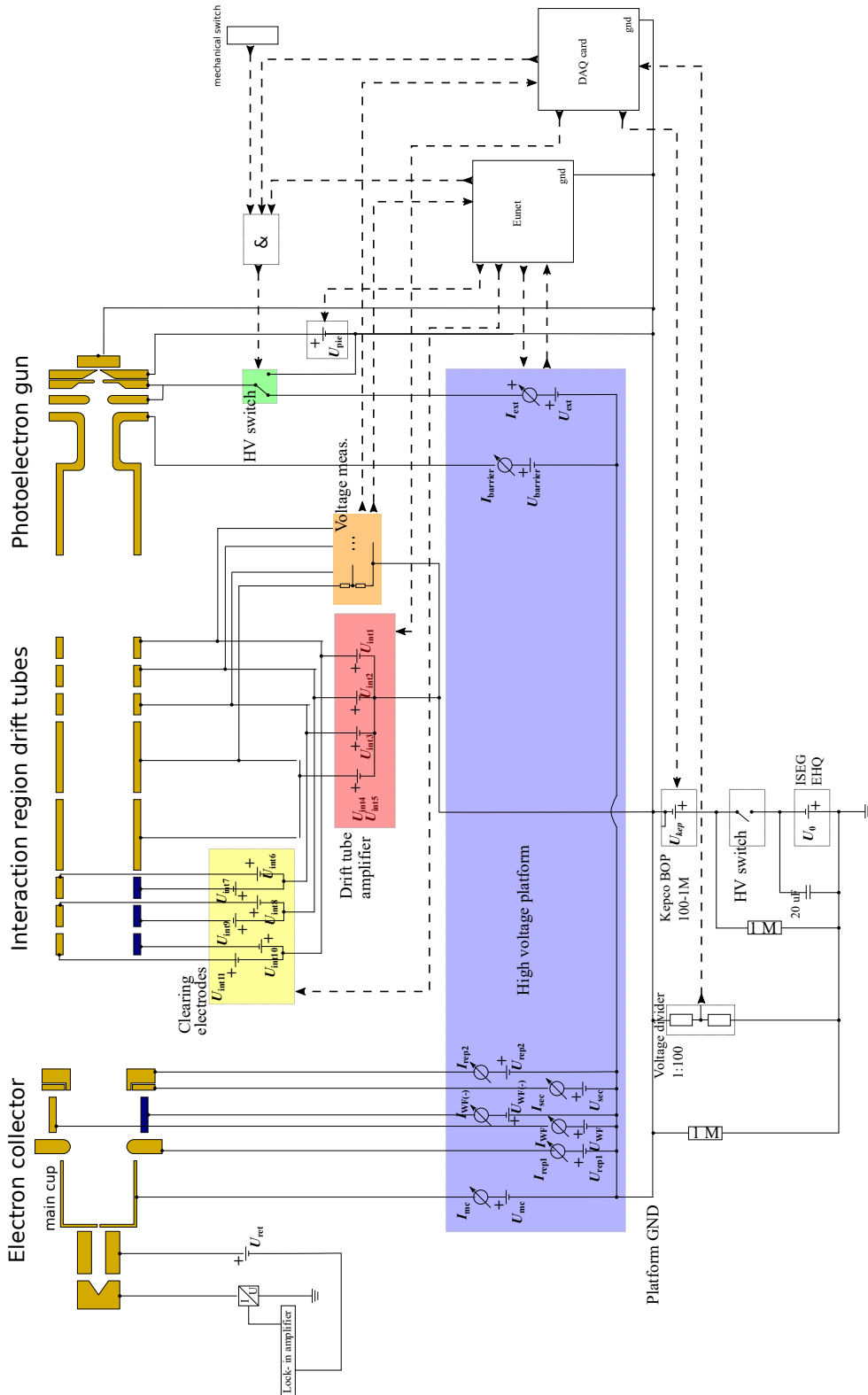


Figure 3.8: Electronic circuit of the CSR electron-ion merged-beam setup.

3.5.2 Electron cooler as a cold-electron target

With the implementation of the electronic circuit as introduced in the previous section 3.5.1, the electron-ion merged beam setup is not limited to the operation as a low-energy electron cooling device, but also represents a versatile tool for studying electron-ion collision experiments in a cryogenic environment as realized in the CSR. The concept of using the merged-beam setup as a cold-electron target shall be briefly introduced here.

Non-zero collision energies in the electron-ion interaction region are realized by detuning the electron energy E_e from the cooling energy E_{cool} at matched velocities

$$E_{cool} = \frac{m_e}{M_i} E_i \quad (3.19)$$

where E_i and M_i are the energy and mass of the stored ion species. The detuned energy E_d , representing the electron-ion collision energy in the center-of-mass frame, is then given by

$$E_d = \frac{1}{2} m u^2 \quad (3.20)$$

$$= \left(\sqrt{E_e} - \sqrt{E_{cool}} \right)^2 \quad (3.21)$$

where

$$\vec{u} = \vec{v}_e - \vec{v}_i \quad (3.22)$$

is the detuned relative electron-ion velocity and an ideal situation is assumed where the electron beam and ion beam are overlapped perfectly parallel to each other. At lowest detuned velocities, the collision energy E_d has a spread that is determined by the velocity distribution of the electron beam (eqn. 3.18). In order to perform high-precision collision studies, the use of a cold electron beam (sect. 3.3) is therefore extremely advantageous.

As mentioned above, a fast detuning of the electron energy is realized with the fast-switchable Kepco power supply located on the high voltage platform of the merged-beam setup. With this technique, where the electron energy is quickly “wobbled” between E_{cool} and $E_e = \left(\sqrt{E_{cool}} + \sqrt{E_d} \right)^2$ in a controlled way, electron-ion collision energies can be scanned with high precision while intermittent electron cooling will guarantee a low-emittance of the stored ion beam.

3.5.3 Performance of the HTS coil-cooling system

The CSR electron-ion merged beam setup is equipped with its own closed-cycle cooling system for the operation of the superconducting magnets (compare fig. 3.5), independent from the He-cooling circuit of the CSR. The system has been designed and developed by A. Shornikov and has later been extended with an automatized flow regulation and stabilization by J. Lion [57]. The construction and commissioning of the cooling system with a HTS prototype magnet is described in [54].

In the original design of the cooling system, neon was foreseen as a suitable cooling medium. Neon has the advantage that it starts to become liquid at temperatures below 30 K. A significant amount of heat can be absorbed due to the high enthalpy that is available in the transition from the gas phase to the liquid phase. However, special care has to be taken regarding the freezing point of neon at 24.5 K. An additional heater is installed that prevents the freezing of neon on the cold head surface and a clogging of the cooling circuit, which would have the dangerous result of a quenching of the HTS magnets. In the commissioning phase of the electron-ion merged-beam setup, it was decided that the first start of the cooling system will be performed with helium gas instead of neon. It turned out that, in spite of its lower heat capacity, the operation of the cooling system with helium gas can still achieve temperatures that are cold enough for the operation of the HTS magnets at the desired currents, this appears as a preferable choice for the cooling medium of the system. Operating with helium does not require a stabilization system for the cold head temperature and avoids possible sources of failure.

fig. 3.9 shows the simplified working principle scheme of the HTS coil-cooling system used in the present work. Helium gas is filled into the closed circle via a pressure regulation valve (PRV). Compressors (Comp) are located on a table on top of the CSR cryostat and circulate the gas through the system. The gas flow is regulated by manual control valve (CV) and an automatic valve (AV). The latter is regulated in response to the mass flow meter measurement with the goal of keeping a stabilized flow at a set value. The warm gas from the compressor table is pre-cooled in a counterflow heat exchanger. In the case of neon operation, the phase transition would take place in the condenser that is cooled by the cold head (Leybold Coolpower, model 140T). The gas flow is then guided by two feedthroughs from the cooling tower cryostat into the isolation vacuum of the CSR cryostat. There, the cooling gas flow through the HTS magnets is realized by stainless steel tubes of 4 mm inner diameter (fig. 3.6 (a), (14) and (15)).

The temperature evolution of several HTS magnets upon turning on the cooling system with helium gas in the start of the 2018 beamtime is monitored with

3 The CSR electron-ion merged-beam setup

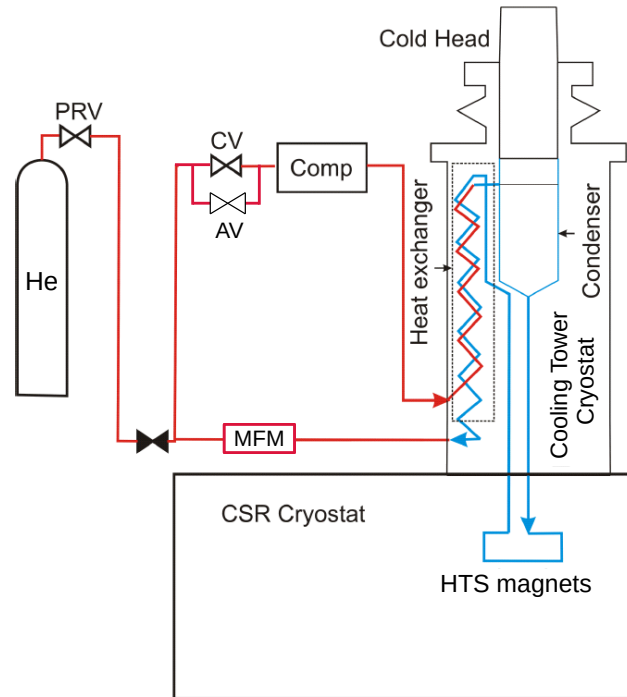


Figure 3.9: Working principle of the HTS coil-cooling system, modified from [54] for the present mode of operation at the CSR.

PT1000 sensors distributed in the isolation vacuum and documented in fig. 3.10. The compressors are turned on at $t = 2$ hrs, when the cold head reached a temperature of about 100 K. The gas flow is initially set to a value of 4 l/s, with a pressure of 1 bar in the gas tubes in the CSR. After 20 minutes, this pressure is increased to 2 bar by refilling warm helium into the cycle. This immediately heats up the temperature sensor located very close to the inlet of the cooling tubes in the CSR cryostat. During the next 35 minutes the flow is increased further in small steps up to 9 l/s.

The flow is directed first to the guns side HTS magnets which explains that an initial heating is visible for the guns side toroid and short solenoid, while e.g. the collectorside toroid is continuously cooled. A final, bigger increase of the flow from 9 l/s to 15 l/s is performed at $t = 3.2$ hrs. The cooling system is kept running in this setting for about 15 hrs, before another smaller flow increase to 17 l/s. It takes about 24 hrs until the temperatures of the HTS magnets approach a stable value between ~ 25 -40 K. This demonstrates that operating the cooling system with helium guarantees magnet temperatures well below the critical temperature of 100 K of the HTS wire.

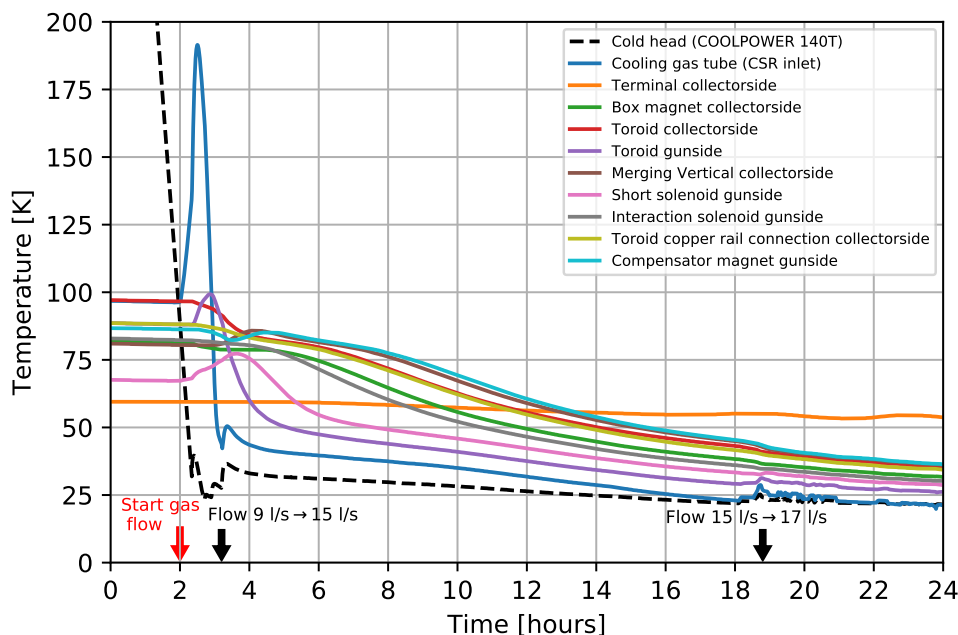


Figure 3.10: Effect of starting the HTS coil-cooling system with helium gas.

Only the terminals of the magnet current leads that are connected to the CSR cooling line (80 K shield layer) are almost unaffected by turning on the HTS coil-cooling system. However, a very slow temperature decrease can be observed after 24 hrs of operation, indicating a weak coupling between the two cooling lines. The temperature of the collectrorside terminal for example stays below 60 K. Since the HTS wires for current distribution (figs. 3.6 (b) and (c)) are directly connected to this temperature stage, this value has to be observed during the HTS magnet operation to avoid excess temperatures.

The effect of starting the HTS magnets with currents of about 40-60 A (see table 3.2) is shown in fig. 3.11. The magnets are started at $t \approx 1.7$ hrs and turned off again at $t \approx 13$ hrs. They heat up only by a few degrees demonstrating a very efficient cooling by the coil-cooling system. As expected, the heating effect is much stronger on the terminal plates due to the resistive heating of the thick copper wires. However, the terminals equilibrate at a temperature of about 70 K and there is still a lot of tolerance to the critical temperature of 100 K. The magnets have finally been operated several days in a row at stable temperature conditions. This is an important achievement considering the aim of long-term, continuous measuring phases during beamtime operation.

3 The CSR electron-ion merged-beam setup

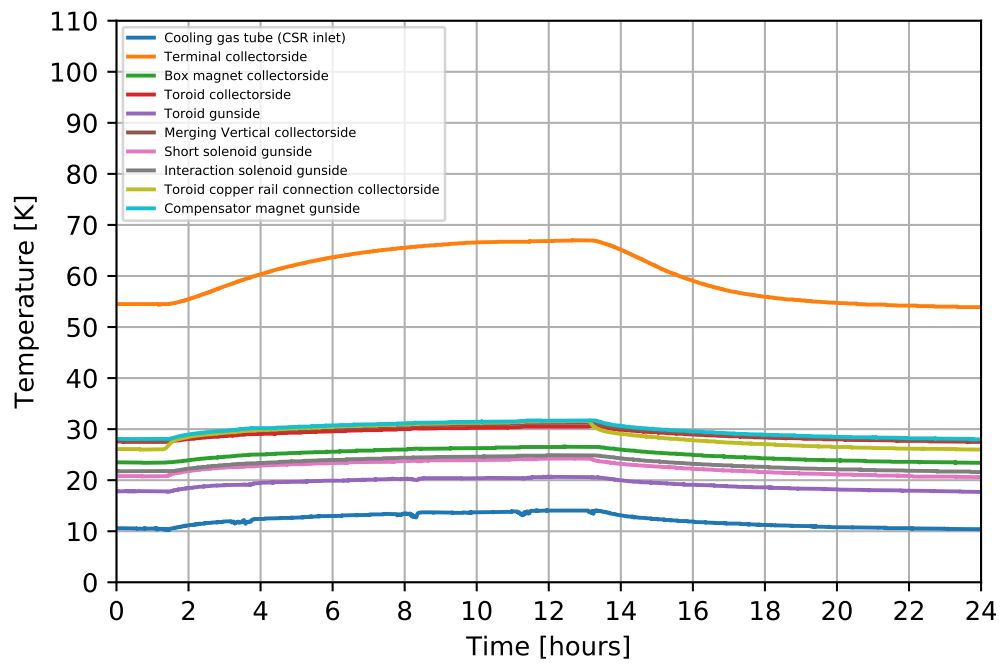


Figure 3.11: Temperature evolution of the HTS magnets and the terminal plates (orange line) during magnet operation.

3.6 CSR ion beam diagnostics for electron cooling studies

The CSR facility offers a rich set of non-destructive ion beam diagnostic tools [30] that can also be employed for the demonstration of electron cooling. In addition, the electron-ion merged beam section is equipped with two rotating wire scanners that can be used to find the beam position of both, electron and ion beam, and confirm their geometrical overlap in the interaction region. A brief overview of these important techniques for the electron cooling operation and the underlying working principles will be presented here.

3.6.1 Wire scanner beam position measurements

Due to the very limited space, two wire scanners (simply called *scrapers*) are used in the electron-ion merged beam section instead of capacitive pick-ups. The design of the scrapers has been developed in the Masters work of S. Lohmann [58], where more detailed description of the mechanics, signal readouts and the mathematical model for the position determination are given. The basic principle of the scraper operation is summarized here and first beam position scraper measurements are presented.

The scrapers are located close before and after the drift tube interaction region (fig. 3.12 (a)). They consist of about 1 mm thick stainless steel wires (1) that can be rotated into the beam axis. A cryogenic worm gear in the rotational stage (2) translates a rotation of the outer axis to a rotation of the inner axis with a transmission ratio of 1 : 360, i.e., rotating the outer axis by a full turn results in an inner rotation angle of 1° . The rotational feedthrough (3) marks the transition between the outside and the isolation vacuum (CSR cryostat). The number of turns are counted by a rotation counter (4) on the outside.

The transverse position of both, electron and ion beam, can be determined from a scraper measurement. In case of the electron beam, the current signal of the continuously produced electron beam caused by electrons hitting the wire can be read out from the scraper's electrical feedthrough pin (5), for example with a pico-amperemeter. A different method is used for the measurement of the much less intense ion beam. Here, the decrease of the remotely measured intensity of the stored ion beam is determined as a function of the rotation angle. For this purpose, the beam is bunched with the rf-system and the intensity of the ion beam signal measured on capacitive current pick-up is observed with a spectrum analyzer. The spectrum analyzer is set to the first harmonic of the bunching frequency in receiver

3 The CSR electron-ion merged-beam setup

mode.

Measurements for the electron beam and the ion beam are demonstrated in fig. 3.12 (a) and (b), respectively. These two measurements represent a case where ion and electron beam were not yet matched. Two peaks (or dips) arise in a rotational scan due to the fact that the wire is shaped in a triangular way [58]. The peak centers α_1 and α_2 hence represent where the beam is hitting the first and second leg, respectively, of the scraper wire. In the first operations of the electron-ion merged-beam setup, the scraper measurements turned out to be a very helpful tool to find the region of good geometrical overlap of the beams. It is usually sufficient to confirm close values of α_1 and α_2 , respectively, being close to each other for both beams. However, from the model described by [58], the transverse beam positions can be calculated from these angles as well. Combining two scraper measurements performed in the collector side as well as in the gun side, one can further obtain information on the angles of the beams along the interaction region.

3.6.2 Capacitive current pick-ups

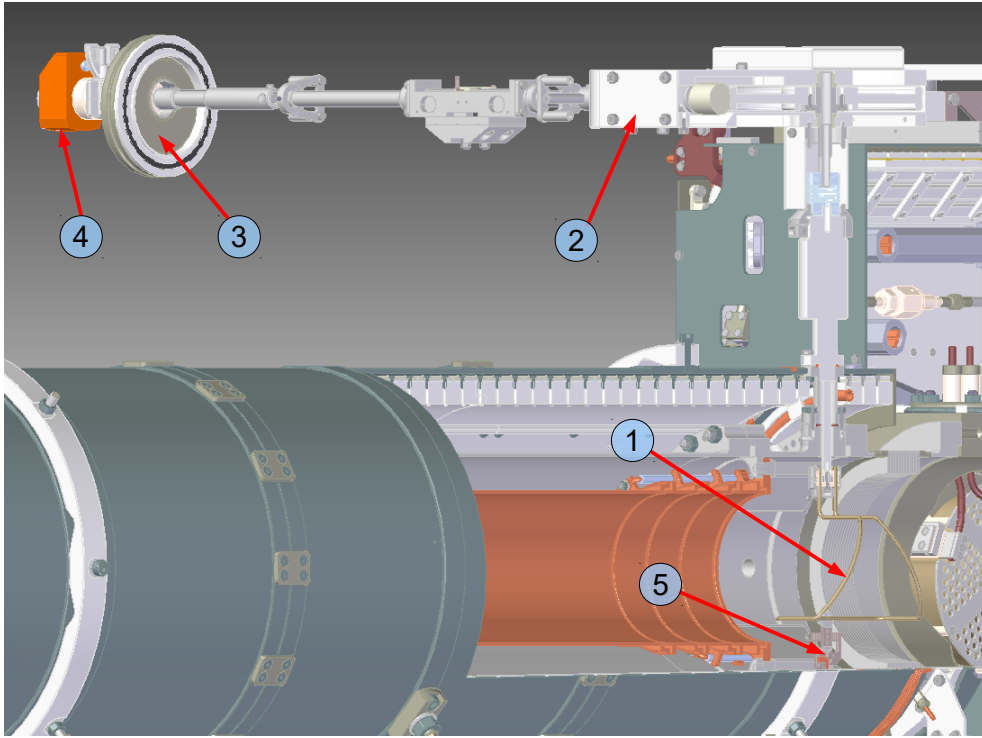
The CSR diagnostic section is equipped with three different capacitive pick-up systems: a beam current pick-up, a Schottky pick-up and six identical ion beam position pick-ups (compare fig. 3.1). The realization of the pick-up systems and their measuring electronics in the cryogenic environment of the CSR has been a technical challenge that is described in great detail by S. Vogel [30]. Specifics of the pick-ups as well as of the rf-bunching system will therefore not be repeated here. The position pick-ups have not been in operation in the 2017 and 2018 electron cooling beam times and will not be discussed here either.

Beam current pick-up for bunched beam detection

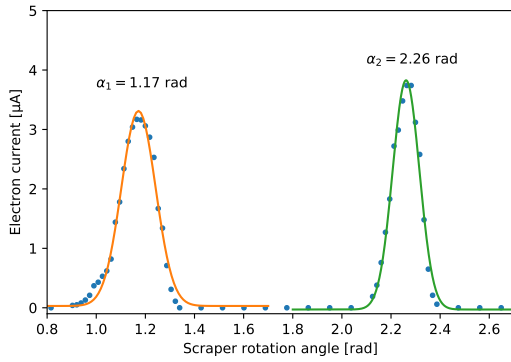
The principle of a current pick-up measurement is shown in fig. 3.13 (a). The pick-up electrode is realized by a hollow tube with an aperture of 100 mm and a length $L_0 = 30$ mm. Stored ions that pass the tube in the time $\Delta t = L_0/v$ induce mirror charges on its wall, that create the outgoing currents $I_R(t)$ and $I_C(t)$ to the grounded experimental vacuum chamber. According to Kirchhoff's junction rule, the in- and outgoing currents satisfy the equation

$$I_{in}(t) - I_o(t) = I(t) - I(t - \Delta t) = I_R(t) + I_C(t) \quad (3.23)$$

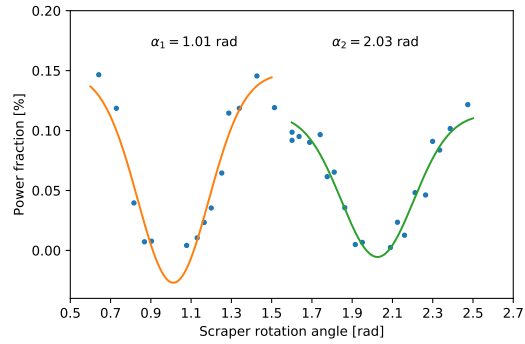
3.6 CSR ion beam diagnostics for electron cooling studies



(a) CAD model of the beam scraper location in the interaction region (collector side).



(b) Electron beam scraper profile.



(c) Ion beam scraper profile (250 keV HeH⁺).

Figure 3.12: Electron beam and ion beam position measurements with the beam wire scanner (scraper) located at the collector side of the interaction region.

which can be Taylor expanded to

$$\frac{dI(t)}{dt} \Delta t + \mathcal{O} \left[\frac{d^2 I}{dt^2} (\Delta t)^2 \right] = I_R(t) + I_C(t) \quad (3.24)$$

3 The CSR electron-ion merged-beam setup

Neglecting the higher order terms on the left-hand side and using the relations $I_R(t) = U(t)/R$ and $I_C(t) = C\dot{U}(t)$, eqn. 3.24 is solved for a sinusoidal time dependence (frequency ω) by

$$i\omega \frac{L_0}{v} I_0 = \left(\frac{1}{R} + i\omega C \right) U_0. \quad (3.25)$$

The amplification system of the CSR has a stable voltage gain of ~ 60 dB in the frequency range of 100-1000 kHz [30] and the capacity C is on the order of a few hundreds of pF. Due to the use of high-resistance amplifiers with $R = 5 \text{ M}\Omega$, one can assume $R \gg 1/(\omega C)$ and eqn. 3.25 simplifies to

$$U(t) = \frac{L_0}{vC} I(t) \quad (3.26)$$

By measuring the signal $U_s t$ of the pick-up voltage in time with an amplifier of gain G , one has a direct way to observe the longitudinal density profile of circulating ion bunches. This is directly obtained as

$$I(t) = \frac{1}{G} \frac{vC}{L_0} U_s(t) \quad (3.27)$$

An important result of eqn. 3.26 is that the sensitivity of the measurement is increased for slower ion beams.

Furthermore, the total number N of ions with charge Ze that are stored in the ring circumference C_0 can be determined by integrating the signal $U_s(t) = GU(t)$

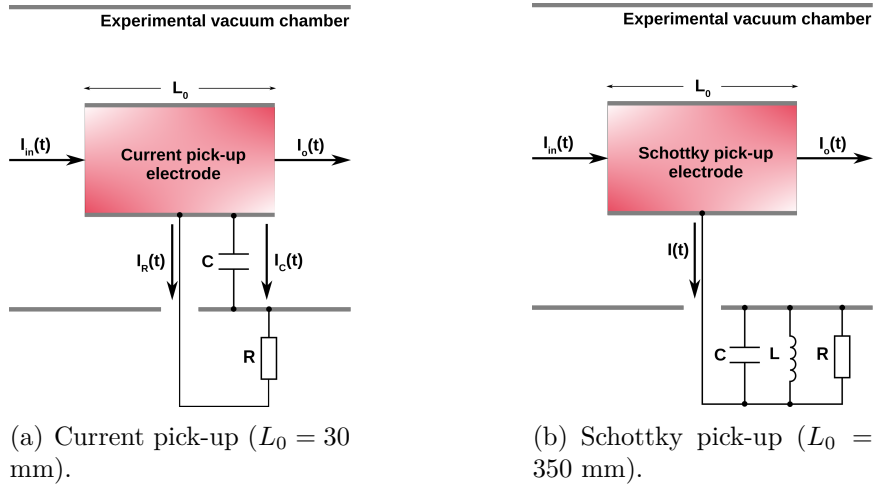


Figure 3.13: Principle of the current pick-up and Schottky pick-up measurement at the CSR (see also [30]).

3.6 CSR ion beam diagnostics for electron cooling studies

over the revolution time T_0 , as $ZeN = \int_0^{T_0} I(t)dt$ and $v = C_0/T_0$,

$$N = \frac{1}{G} \frac{C}{Ze} \frac{C_0}{L_0} \frac{1}{T_0} \int_0^{T_0} U(t)dt \quad (3.28)$$

$$= \frac{F}{ZGT_0} \int_0^{T_0} U(t)dt \quad (3.29)$$

where Z is the charge state of the ion, $G = 2279.5$ is the gain¹ of the amplification system and $F = 701(28) \cdot 10^9 \text{ V}^{-1}$ is denoted as the geometrical coefficient of the pick-up system [30]. The total uncertainty of N was estimated to $\sim 10\%$ in a measurement at a comparable setup at the TSR by comparing the result of eqn. 3.29 to the number of ions determined by other methods [59]. This difference is expected to be dominated by the approximations in the linear pick-up model leading to eqn. 3.29.

Schottky noise pick-up for coasting beam detection

Measuring Schottky noise signals [60] with a current pick-up system as sketched in fig. 3.13 (b) is an often employed tool in storage rings for the monitoring of coasting ion beams. These signals arise from the fact that a coasting ion beam can not purely be seen as a dc-current, but is instead comprised of individual charges that are statistically fluctuating in time. The fluctuations induce a measurable signal on the Schottky pick-up electrode that can be observed at harmonic numbers h of the revolution frequency ω_0 . Schottky signals are usually detected with a spectrum analyzer, where the Schottky signal power is measured with respect to the analyzer's impedance. The Schottky power spectrum $P_0(h\omega_0)$ is given by (see [59] for detailed derivation):

$$P_0(h\omega_0) = \left(\sum_{i=1}^N \hat{U}_h(h\omega_0) \cos \phi_i \right)^2 \quad (3.30)$$

where \hat{U} is the amplitude of a single ion in the Schottky spectrum and ϕ_i its statistically distributed phase. Assuming a large number of ions N , the squared sum over the phases reduces to

$$\left(\sum_{i=1}^N \cos \phi_i \right)^2 = \frac{N}{2} \quad (3.31)$$

¹See [30] for the error determination of the coefficient F for the current pick-up. The gain of the amplification chain has been measured before the 2018 beamtime by Dr. M. Grieser.

3 The CSR electron-ion merged-beam setup

which yields

$$P_0(h\omega_0) = \frac{N}{2} \hat{U}_h^2(h\omega_0) \quad (3.32)$$

eqn. 3.32 describes discrete lines in the power spectrum, occurring at $h\omega_0$ with integer h . Taking into account a realistic energy distribution or frequency distribution $h\Delta\omega_0$ broadens these lines and one speaks of so-called *Schottky bands*. The total power in each of these Schottky bands is constant [61]. As a result, with increasing harmonic number h , the maximum amplitude of these bands decreases proportionally to $1/\omega_0$.

With respect to electron cooling experiments one can particularly benefit from measuring the time evolution of the frequency spread $\Delta\omega/\omega_0$. The frequency spread is related to the momentum spread $\Delta p/p_0$ via the slip factor of the storage ring (eqn. 2.30). The time evolution of $\Delta p/p_0$ during electron cooling yields the longitudinal cooling rate for a coasting ion beam.

3.6.3 Bunched-beam detection of electron cooling and cooling energy

As described above, observing the signal induced by a rf-bunched beam on a capacitive current pick-up yields a direct measurement of the longitudinal density profile of the circulating bunches (eqn. 3.26). This signal can simply be observed on an oscilloscope triggered synchronously to the bunching rf-frequency.

Bunch profiles $I(t) = Zev_0\rho_{\parallel}(t)$ can be predicted using the longitudinal phase space simulation program that is presented in sect. 2.1.5. For the test run presented, the program is started with $N = 10000$ particles with $E_{kin} = 250$ keV, mass number $A = 5$ and charge state $Z = 1$, hence, the revolution time is given by $T_0 = 11.33 \mu\text{s}$. Rf-bunching is simulated with a bunching frequency $f_{rf}(h = 4) = 4f_0$, representing typical conditions for the later presented HeH⁺ bunched beam experiments. The simulated longitudinal phase space distribution, 60 ms after the rf-amplitude ramp is completed, is shown in fig. 3.14. From this distribution and with the conversion

$$t = \frac{\pi}{2} + \frac{\Delta\Phi}{2\pi f_{rf}} \quad (3.33)$$

the bunch spectrum as a function of time t can be extracted from a histogram of the phases $\Delta\Phi$. The bunch profiles are well described by the function (compare [23])

$$\rho_{\parallel}(t) = A \cos^2(\pi t f_{rf}) \quad (3.34)$$

3.6 CSR ion beam diagnostics for electron cooling studies

(see fig. 3.14 (b)). The fourier transformation of $\rho_{\parallel}(t)$ (see fig. 3.14 (c)) yields a frequency spectrum which for $f > 0$ is mainly composed of a single component at the first harmonic of the bunching frequency f_{rf} .

Applying electron cooling dampens the synchrotron oscillations and therefore compresses the longitudinal phase space distribution. The bunch profiles (longitudinal density profiles) are transformed to more narrow, peak-like shapes (see experimental results sect. 4.2.3). The effect of a linear electron cooling friction force F on the phase space distribution $(\Delta E, \Delta\Phi)$ is realized in the simulation program by the following considerations:

$$F = -\alpha\Delta v = -\alpha v_0\delta = -\frac{\alpha v_0}{2E_0}\Delta E \quad (3.35)$$

where

$$\delta = \frac{\Delta v}{v_0} = \frac{1}{2} \frac{\Delta E}{E_0}. \quad (3.36)$$

The energy δE that an ion loses in each turn when passing the electron cooling length L is hence given by

$$\delta E = FL = -k\Delta E \quad (3.37)$$

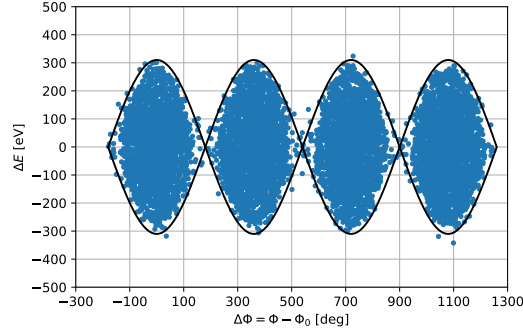
where

$$k = L \frac{\alpha v_0}{2E_0}. \quad (3.38)$$

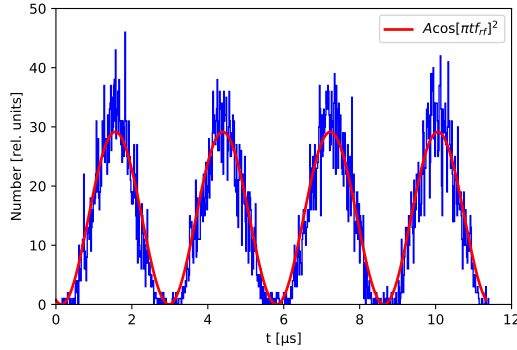
The effect of electron cooling is thus simulated by extending the equation for the calculation of the phase space coordinate ΔE in each turn (see eqn. 2.43 & fig. 2.6) with an additional term $-k\Delta E$. fig. 3.15 shows the result of choosing an arbitrary value $k = 0.1$ in the friction term. The immediate result is the emergence of higher harmonic components in the frequency spectrum.

An obvious way to demonstrate the effect of electron cooling in an experiment is thus given by the monitoring of the time evolution of the signal of the second harmonic of the bunching frequency $2f_{rf}$ in the frequency spectrum. The steepness of the rise of this signal when turning on electron cooling serves as a measure of the electron cooling efficiency. This can be performed with a spectrum analyzer in receiver mode. As it will be shown in sect. 4.1, the monitoring of the second harmonic signal is a very sensitive method to find the precise point of velocity-matched electron cooling when scanning through a range of electron energies in the electron-ion merged beam setup. Electron cooling is optimal for a voltage U_0 where the electron velocity matches the ion velocity $v_0 = C_0 f_0 = C_0 f_{rf}/h$. The electrons then have the cooling energy $E_{cool} = (m_e/M_i)E_i$ where, non-relativistically, $E_i = (M_i/2)v_0^2$.

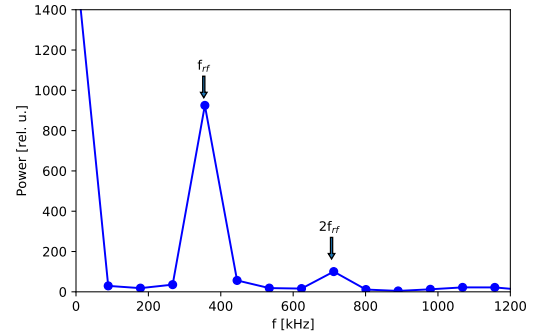
3 The CSR electron-ion merged-beam setup



(a) Longitudinal phase space distribution with rf-bunching, in the absence of electron cooling (black line: separatrix).



(b) Bunch distribution time spectrum in one revolution period.



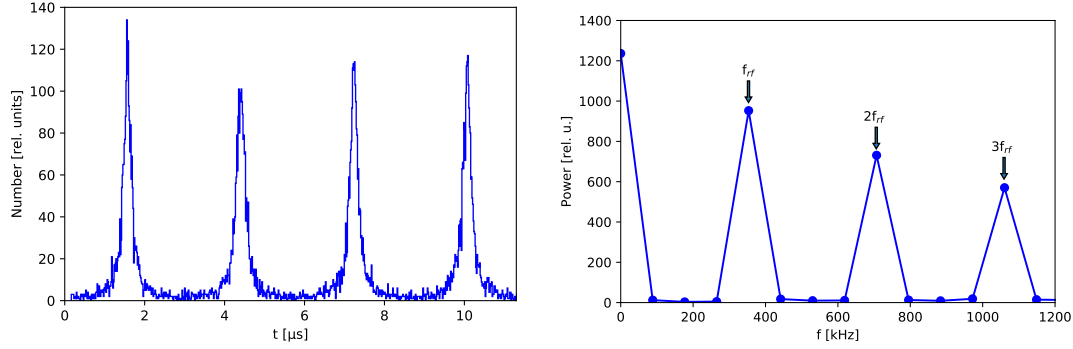
(c) FFT of the bunch distribution.

Figure 3.14: Simulated longitudinal phase space distribution and bunch profiles in one revolution period for 250 keV HeH⁺ ions (see text for details) in the absence of electron cooling. The bunch spectrum can be described by $\rho_{\parallel}(t) = A \cos^2(\pi t f_{rf})$ (red line in (b)). The fast Fourier transform of the simulated bunch distribution yields a frequency spectrum which is mainly composed of a component at $f = 0$ and one component at the first harmonic of the bunching frequency f_{rf} .

The energy of the electrons is mainly defined by the optimized cathode potential U_0 , but work functions of the cathode (W_c) and the anode (W_a) as well as the electron beam space charge potential U_{sc} typically have contributions of $\sim eV$. The electron energy E_e in the center of the electron beam is expressed by

$$E_e = e|U_0| - e|U_{sc}(r = 0)| - (W_c - W_a) \quad (3.39)$$

3.6 CSR ion beam diagnostics for electron cooling studies



(a) Bunch distribution time spectrum in one revolution period.

(b) FFT of the bunch distribution.

Figure 3.15: Simulated longitudinal density distribution under the influence of a friction force (a) and corresponding fast Fourier transform (b), composed of components at higher harmonics of the bunching frequency f_{rf} .

where the space charge potential U_{sc} is given by

$$U_{sc}(r) = \frac{n_e e R_{beam}^2}{4\epsilon_0} \begin{cases} 1 + 2 \ln \frac{R_0}{R_{beam}} - \left(\frac{r}{R_{beam}}\right)^2 & r < R_{beam} \\ 2 \ln \frac{R_0}{r} & r > R_{beam} \end{cases} \quad (3.40)$$

with the electron beam radius R_{beam} and the beam pipe radius R_0 . Practically, the optimized electron energy E_{cool} can be determined from a pick-up measurement of the revolution frequency of the ion beam, $f_0 = f_{rf}/h$. Reciprocally, by finding the cathode potential U_0 for velocity-matched electron cooling and further calculating the space charge contribution, one has an experimental method at hand to find the difference of contact potentials ($W_c - W_a$). This yields the predicted

$$E_{cool} = \frac{m_e}{2} v_0^2 = \frac{m_e}{2} C_0^2 (f_{rf}/h)^2 \quad (3.41)$$

and the optimized electron acceleration voltage is

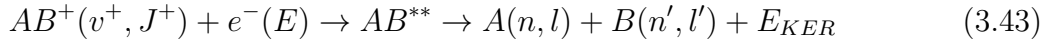
$$U_0 = E_{cool} + e(U_{sc}(r=0)) + (W_c - W_a) \quad (3.42)$$

3.6.4 Transverse ion beam profile measurements by neutral fragment imaging

Transverse ion beam profiles are measured with the help of a position sensitive, multi-coincidence imaging detector. The development and implementation of this neutral-fragment imaging detector in the cryogenic environment of the CSR was realized in the Ph.D. work of A. Becker [62].

Binary collisions of stored molecular or atomic ions and electrons take place in the interaction region of the electron-ion merged beam setup. Depending on the collision energy, several reaction outcomes are possible that can lead to the formation of neutral products. Here, the merged-beam setup has to be viewed as a free electron target (sect. 3.5.2) rather than an electron cooling device. Singly-charged atomic cations can be neutralized in processes such as radiative recombination or resonant dielectronic recombination. A comprehensive overview of electron-ion recombination processes is given in [63].

The main focus of the work in hand are low-energy electron cooling studies with molecular cations of the form AB^+ . In the meV collision energy range, the most important fragmentation process for diatomic molecular cations that leads to the formation of two neutral atomic fragments A and B is dissociative recombination (DR). At these low collision energies that are present during the velocity-matched electron cooling operation, a molecular ion can capture a free electron into a repulsive doubly-excited neutral Rydberg state AB^{**} via the following reaction pathway [64]



where (v^+, J^+) is the rovibrational quantum state of the molecular system and $n(n'), l(l')$ denote the principal and angular momentum quantum numbers of the final atomic states. The energy which is released in this exothermic reaction is called the kinetic energy release E_{KER} . Fragmentation by DR can also be triggered by electron capture into an often even lower-lying, singly-excited molecular Rydberg state AB^* from where it couples to the repulsive state AB^{**} . This process is thus labeled *indirect* DR ².

The neutral fragments that are produced by DR in the collinear electron-ion

²A discussion of these processes in greater detail and its relevance in astrophysical plasmas such as molecular clouds goes beyond the scope of this work, but is the subject of a large number of earlier merged-beam storage ring experiments. Even more importantly, ongoing DR studies at the CSR electron-ion merged beam setup can yield new insights into molecular ion recombination rates in a realistic cryogenic environment resembling conditions in the interstellar medium.

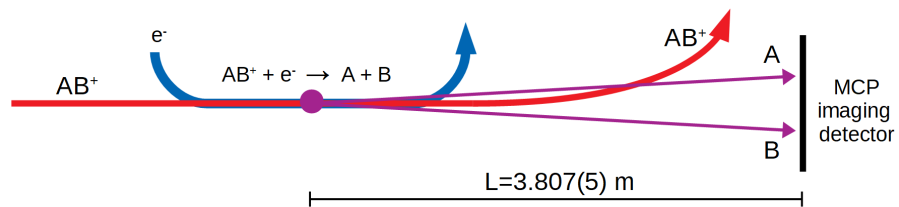
3.6 CSR ion beam diagnostics for electron cooling studies

interaction region are not affected by the electrostatic deflectors of the CSR and proceed to the imaging detector on a straight path, schematically shown in fig. 3.16 (a). The detector surface is composed of a multi-channel plate (MCP) with a large sensitive area of 120 mm that is oriented perpendicular to the merged beams axis. The distance between the two fragment impact positions on the MCP is determined by the kinetic energy release in the DR reaction (see [62], [64] for details). Each hit on the MCP surface releases an avalanche of electrons that produces a luminous spot on a phosphor screen located behind the MCP (fig. 3.16 (b)). An aluminium mirror deflects the light at an angle of 90° and couples it outside the CSR via a view-port where it is detected by a high-speed CCD camera.

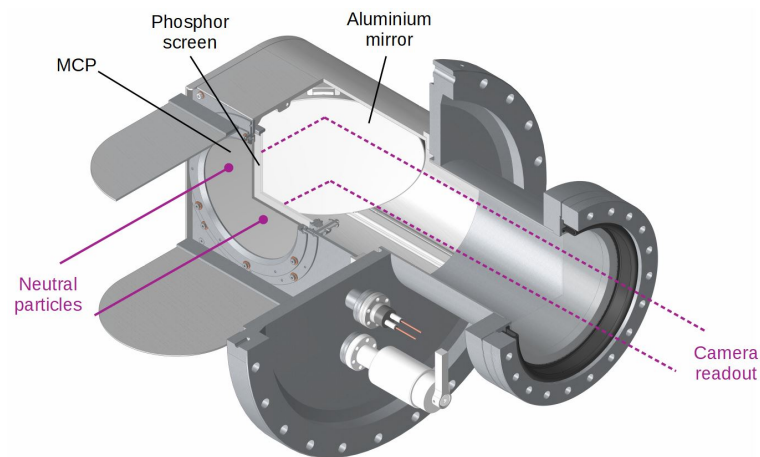
The imaging detector does not only measure the neutral fragments from DR. In addition, one has to consider neutral products from dissociative excitation (DE), where only one of the atomic constituents of AB^+ becomes neutral by electron excitation while the other keeps the positive charge, and collisions of the stored ions with residual gas molecules that can also yield one or two fast neutrals. The background contribution from the latter can be subtracted by implementing an *electrons off* period in a measurement cycle. The neutral fragment imaging algorithm can filter for events that are caused by two co-incident impacts on the detector only, and disregards all other events. For deriving the ion beam profile, center of mass (CM) for such double events are determined in the detector plane. Producing two-dimensional CM position plots yield a profile of the ion beam projected onto the detector. Measured CM distributions are presented in sect. 4.4. It is important to consider that these distributions are only projections of the beam-profile in the interaction region onto the imaging detector. The beam-profile Gaussian widths in the interaction region can be obtained with the betatron functions of the CSR $\beta_x = 13.009$ m and $\beta_y = 1.4095$ m in the center of the interaction region [13] and the distance $L = 3.807$ m (see fig. 3.16 (a)) to the surface of the MCP detector:

$$\sigma_{x,y} = \sigma_{x,y(detector)} \left[1 + \left(\frac{L}{\beta_{x,y}} \right)^2 \right]^{-\frac{1}{2}}. \quad (3.44)$$

3 The CSR electron-ion merged-beam setup



(a) Scheme of DR fragment imaging.



(b) CAD model of the MCP imaging detector (see also [62]).

Figure 3.16: Transverse profile measurement of a stored di-atomic molecular ion by position-sensitive, multi-coincidence imaging of neutral fragments from dissociative recombination.

3.7 Electron beam profile measurements

3.7.1 Setup

A precise knowledge of the electron beam profile properties and in particular the electron beam density n_e in the electron-ion interaction region is important not only for electron cooling applications. A non-homogenous beam profile that does not fully enclose the ion beam complicates the interpretation of the electron cooling force and electron cooling rate calculations. The electron beam density is further a crucial parameter when measuring rate coefficients of electron-ion recombinations [49] where the electron cooler is used as an electron target.

The electron-ion merged beam setup is therefore equipped with electron beam collectors that can probe the current at a single position within the electron beam through a pin hole (see sect. 3.5.1). Moreover, two of such collectors were created.

The electron collector in the dedicated collector section for the electron beam leaving the CSR cryostat (see sect. 3.5.1) has been designed and constructed in the course of two masters projects ([58], [55]). Its successful commissioning and first measurements were performed in the course of the present work. It took place during the first electron beam operations of the completed electron-ion merged beam setup and marks an important step towards the first low-energy electron cooling experiments presented in chapter 4.

Additionally, between beamtimes 2017 and 2018, an electron collector with the same working principle was installed at ~ 0.8 m behind the electron gun, before the electron beam enters the CSR cryostat. It was set up in a vacuum cross between the first and second low-field room temperature copper solenoid that follow the high-field solenoid enclosing the photocathode (see fig. 3.19 (a)). The mechanical structure of the collector cup was modified to adjust it for the dimensions in the new location in the gun section. The diameter of the main cup is reduced from 40 mm to 35 mm, while the pinhole in the main cup keeps its 0.8 mm diameter. With the help of a linear vacuum manipulator the cup can be moved into the electron beam trajectory. It is a major improvement and a flexible diagnostic tool for photocathode tests whenever it is not possible to operate the superconducting magnets in a cooled CSR cryostat.

Furthermore, the gun section collector structure has an additional right-angle prism mirror attached to it (fig. 3.17). With the prism mirror it is now possible to shine a laser through a view-port from the other side of the vacuum cross and operate the photocathode in the so-called *reflection mode*. Compared to the usual *transmission mode* operation, the cathode is irradiated from the (Cs,O) side of the GaAs crystal which allows non-thermalised electrons to be extracted, which also

3 The CSR electron-ion merged-beam setup

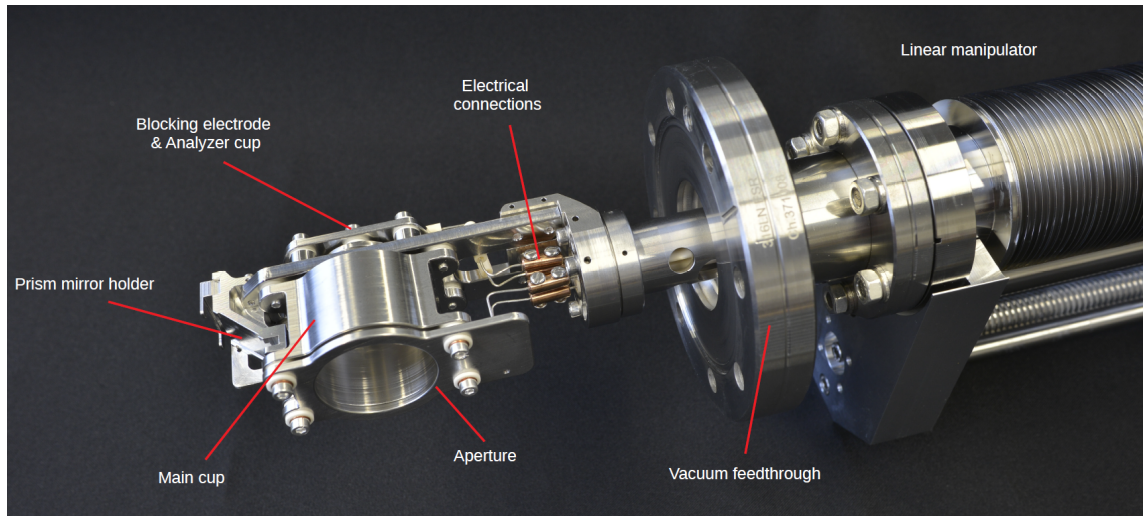


Figure 3.17: Movable analyzer cup in the gun section. The blocking electrode and analyzer cup behind the main cup are not visible in their full size in this view. The right angle prism mirror allows for front illumination of photocathodes.

is beneficial for spectral response diagnostics [46].

Beam profiles are measured by using the horizontal and vertical steerers in the room temperature beamlines to sweep the electron beam over the pinhole, while monitoring the current in the analyzer cup with an I/U-converter. The collector main cup and all of its electrodes are grounded in order to leave the electron beam undisturbed. The experimental setup for a beam profile measurement with the collector section cup is sketched in fig. 3.18³. The calibration factors that convert the steering coil currents into the transverse dimension are obtained by steering a centered, non-expanded electron beam over the total height and length of the apertures of the collector cups in the two sections (see appendix A). With the image of the main cup apertures that is now visible in the current signal of the main cup and the known aperture sizes, the calibration factors in [mm/A] (measured for operating the low-field solenoids with 10.8 A) can be determined (table 3.3).

In this section, the measured beam profiles are analyzed in order to derive an

³It should be noted here that the setup described in fig. 3.18 can also be used to measure the longitudinal energy distribution of the electron beam by ramping up the retarding potential on the blocking electrode (*electron deceleration curve* measurements, see [48] for details on this technique). Experiments in this direction are ongoing but will not be discussed in this work.

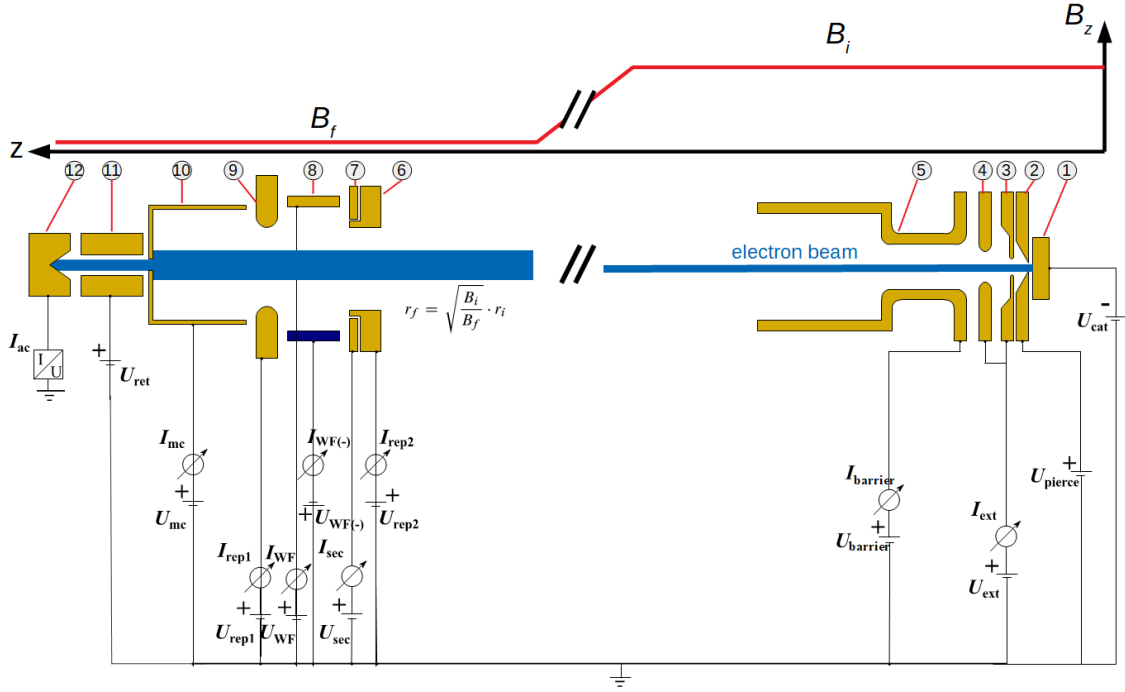


Figure 3.18: Experimental setup for electron beam profile measurements with the collector section cup. The several elements are (1) GaAs photocathode, (2) Pierce shield, (3+4) extraction electrodes, (5) drift tube, (6) repeller, (7) secondary electron collector, (8) Wien filter electrodes, (9) aperture, (10) main cup, (11) blocking electrode and (12) analyzer cup. For electron beam profile measurements, all electrodes in the collector section (left side) are grounded. The expansion of the magnetic field along the electron beam trajectory is symbolized by the red curve.

Table 3.3: Steering coil current calibration factors $k_{x,y}$ for electron beam profile scans.

	\varnothing aperture [mm]	k_x [$\frac{mm}{A}$]	k_y [$\frac{mm}{A}$]
Gun section	40	4.180	4.098
Collector section	35	6.148	6.664

effective cathode radius r_{eff} , corresponding to the initial electron beam radius before the magnetic field expansion. The magnetic field values at locations of the pin holes in the main cup has to be known precisely. With the effective cathode radius, the electron beam radius and thus the electron beam density at any position along the electron trajectory can be determined. Calculated and

3 The CSR electron-ion merged-beam setup

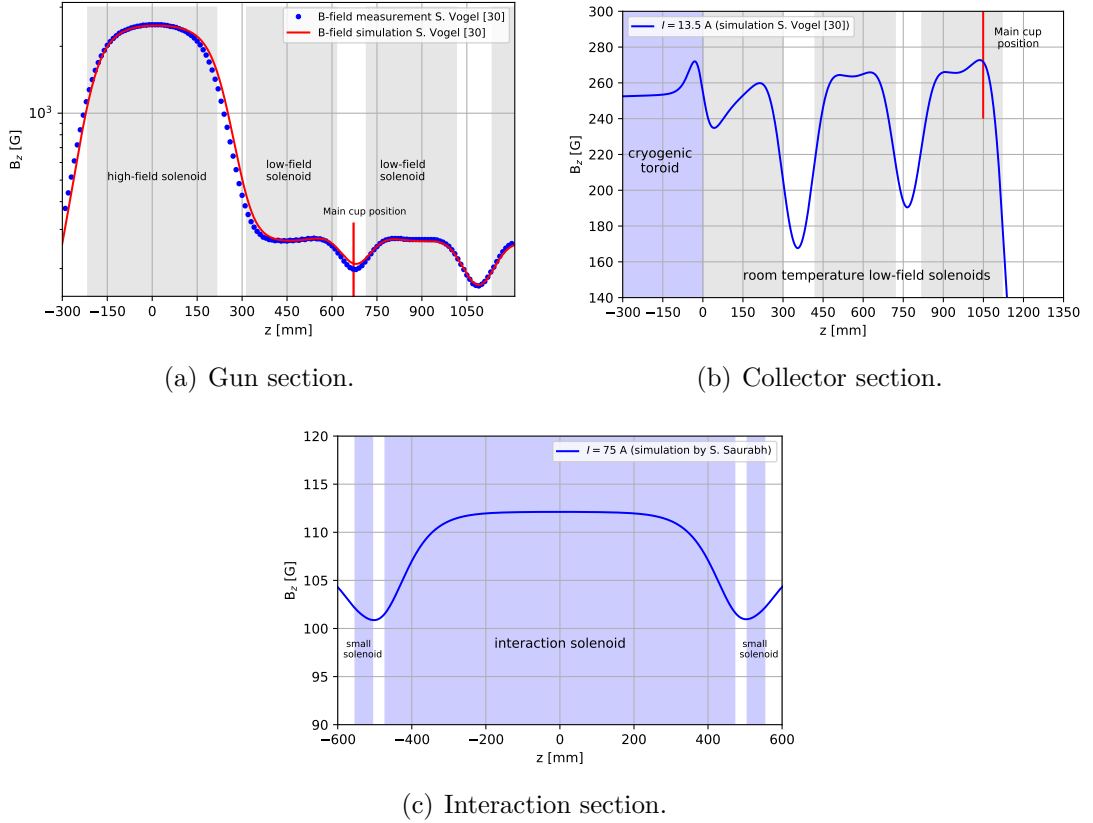


Figure 3.19: Magnetic field along the electron beam trajectory in the gun section [30], collector section [30], and interaction section (made available by group member S. Saurabh). The position $z = 0$ mm marks the position of the photocathode in the gun section, the transition between the cryogenic and room temperature part in the collector section, and the center of the interaction section, respectively. For this measurement and in the simulations, the current in the high-field and low-field solenoids is 775 A and 13.5 A, respectively. Low-field solenoids in the gun and collector section are always operated at the same current. The cryogenic superconducting solenoids in the interaction section are powered with a current of 75 A.

measured magnetic field strengths as function of the longitudinal position z in the gun, collector and interaction section are shown in fig. 3.19. The values of the field strength for a certain operating current at the longitudinal positions z of the collector main cups and in the interaction region are summarized in table 3.4. For a set of magnet currents as they are used in the 2018 HeH⁺ beamtime,

Table 3.4: Measured and calculated magnetic field strengths at the collector positions and in the interaction region (compare fig. 3.19).

	z [mm]	I [A]	B-field [G]
Gun section main cup (measurement)	670.5	13.5	199.0
Gun section main cup (simulation)	670.5	13.5	210.86
Interaction region center (simulation)	0	75	112.12
Collector section main cup (simulation)	1049.2	13.5	272.51

Table 3.5: Summary of the magnetic fields and expansion values at the beam profile measuring positions and in the interaction region for operational currents of 600 A (1.936 kG) in the high-field solenoid (calibration curve given in [30], p. 84), 10.8 A in the room temperature low-field solenoids and 60.8 A in the cryogenic HTS solenoids, obtained by a linear scaling from the measured and calculated values given in table 3.4.

	B-field [G]	expansion α (1.936 kG high-field)	field ratio to interaction region
Gun section main cup (measurement)	159.20	12.16	1.78
Gun section main cup (simulation)	168.08	11.47	1.88
Interaction region center	89.70	21.58	1
Collector section main cup	218.01	8.88	2.43

the magnetic expansion values are calculated by a linear scaling of the solenoidal fields ($B \propto I$) and summarized in table 3.5.

3.7.2 Measurements

Fig. 3.20 shows two beam profile scans measured with the gun section cup and the collector section cup. The beam profiles represent the field conditions summarized in table 3.19. These settings are also used for the longitudinal electron cooling of bunched HeH^+ (sect. 4.2). The scans are measured with the same photocathode and quickly after each other to ensure comparable conditions.

Moreover, a beam profile at an increased current in the high-field magnet of 929.656 A, corresponding to $B = 3$ kG, is measured with the collector section cup. The low-field solenoids stay at a current of 10.8 A (table 3.5), hence $B = 218$ G at

3 The CSR electron-ion merged-beam setup

the collector section main cup position. This field ratio yields an expansion factor of $\alpha = 13.76$. The measured profile is presented in fig. 3.21 and corresponds to the settings for the transverse electron cooling studies with a coasting HD⁺ beam (sect. 4.4.3).

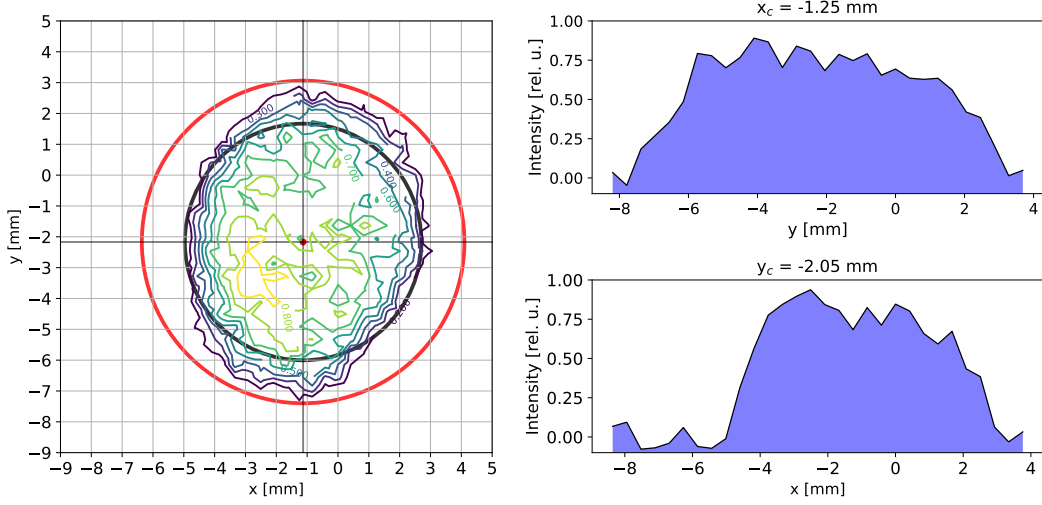
It can be seen that the shape of the measured profiles is rather oval than circular, similarly in the gun and collection section. However, the vertical and horizontal cuts through the center of the beam profiles presented next to each measured profile in figs. 3.20 & 3.21, show a flat top of the electron beam that is sufficient enough for measurements in the electron-ion interaction region.

Furthermore, the offsets of the measured beam profile centers in the collector section cup (figs. 3.20 (b) & 3.21), at two different expansions, are about the same. In case of a misaligned cathode, higher expansion factors would move the electron beam profile centers to higher transverse coordinates as well. An almost identical offset for these two different expansion measurements therefore means the cathode is well-aligned in the center.

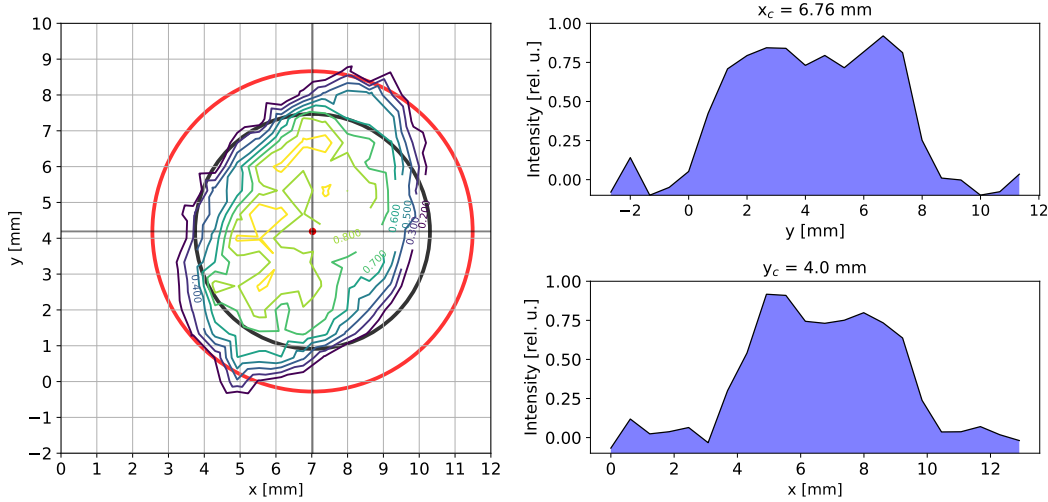
It is further obvious that the beam profiles are neither circular, nor do they fill the theoretically expected area defined by the Pierce shield radius of 1.5 mm and the corresponding expansion factors. The profiles are rather described by an ellipse shape, very similar to those presented in [30] measured with an electron collector test setup but at the electron beam production section already in its present state. In earlier measurements, the elliptical shape was assigned to the misalignment of the collector center and low-field axis as discussed above. Recently, the cause of this deformed profiles is traced back to originate from the oval shape of the shields around the vacuum tube inlet and outlet of the high-field solenoid.

The effect of replacing these oval closing shields with perfectly round shields is presented in fig. 3.22. At a relatively high fixed extraction voltage of $U_{ext} = 30$ V, beam profiles are measured in a range of $U_{pierce} = 3.2 - 4.0$ V. Compared to the earlier situation with the oval closing shields, in general higher pierce voltages above 3 V are now necessary to obtain a uniform, flattop-like profile.

3.7 Electron beam profile measurements



(a) Gun section scan ($\alpha = 8.88$, $I_e = 27.0 \mu\text{A}$).



(b) Collector section scan ($\alpha = 12.16$, $I_e = 27.8 \mu\text{A}$).

Figure 3.20: Electron beam profile scans in the gun and collector section with the high-field solenoid at $B = 1.936 \text{ kG}$. The cathode voltage is $U_0 = 30.65 \text{ V}$, $U_{ext} = 15 \text{ V}$ ($I_e \approx 27 \mu\text{A}$) and $U_{Pierce} = 2.5 \text{ V}$. The red spot is the measured profile center. The red circle marks the ideal flattop area for a cathode radius $r_{cath} = 1.5 \text{ mm}$ that is expected from the Pierce shield radius. The black circle marks the expanded measured effective cathode radius r_{eff} (see text for details). Shown on the right of each profile is a vertical (top) and horizontal (bottom) cut through the center of the beam profile.

3 The CSR electron-ion merged-beam setup

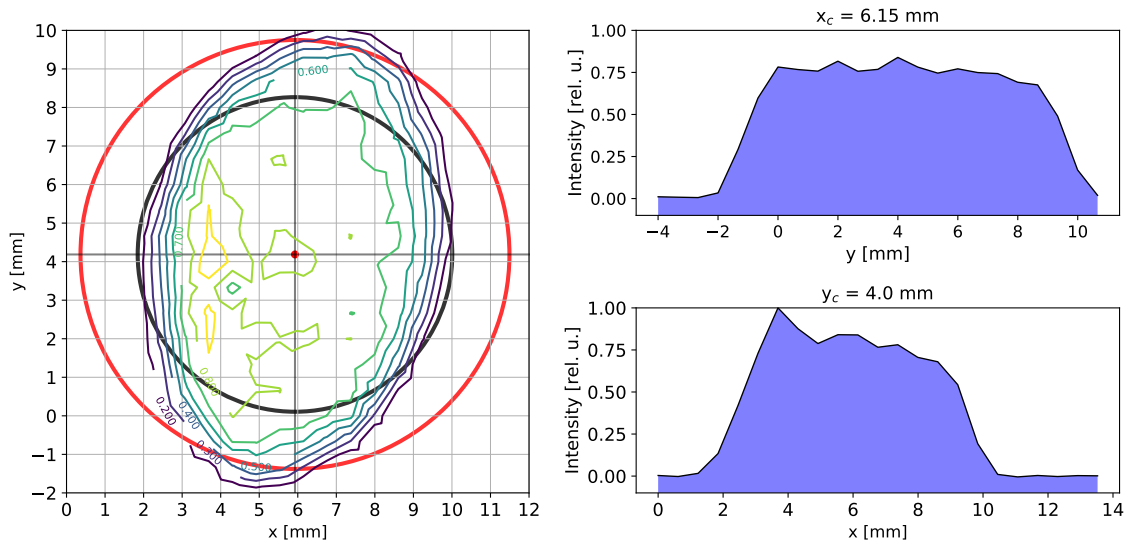
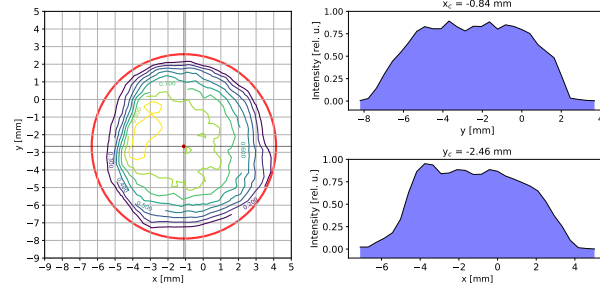
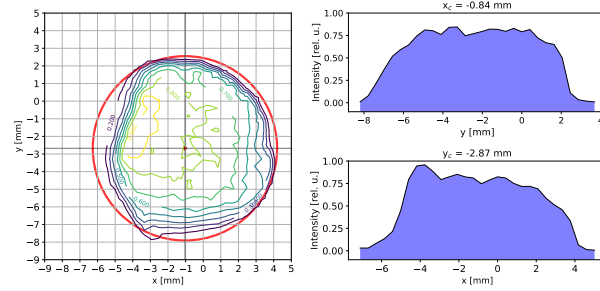


Figure 3.21: Electron beam profile scan in the collector section with the high-field solenoid at $B = 3$ kG. The cathode voltage is $U_0 = 48.27$ V, $U_{ext} = 16.15$ V and $U_{Pierce} = 2.5$ V. At the measuring position, $\alpha = 13.76$ and $I_e = 34.0$ μ A. Shown on the right of each profile is a vertical (top) and horizontal (bottom) cut through the center of the beam profile.

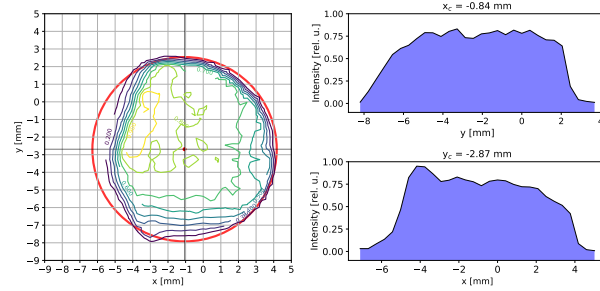
3.7 Electron beam profile measurements



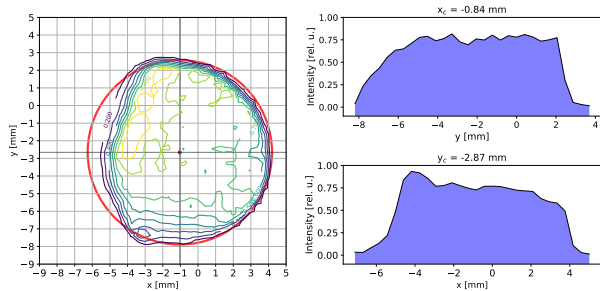
(a) $U_{pierce} = 3.2$ V.



(b) $U_{pierce} = 3.6$ V.



(c) $U_{pierce} = 3.8$ V.



(d) $U_{pierce} = 4.0$ V.

Figure 3.22: Beam profile scans in the gun section for a variation of pierce voltages after replacing the shields of the high-field solenoid (see text for details). The cathode voltage is $U_0 = 33$ V, the extraction voltage is $U_{ext} = 30$ V. The electron currents (from the lowest to the highest pierce voltage setting) are $I_e = 81.1, 98.7, 108.4$ and $118.6 \mu\text{A}$.

Effective cathode radius for electron density determination

The method to obtain an effective cathode radius from a flat-top shaped profile, that allows for the determination of the electron beam density at any position along the electron beam trajectory, is performed as follows:

- the center of the beam (x_c, y_c) is calculated from the mean of the intensities $I_i(x, y)$ at every scanned point i
- the background level b_{avg} of the profile is obtained by averaging over the points that clearly lie outside the beam boundary visible in the horizontal and vertical line intensities through (x_c, y_c)
- the height of the flat top h_{avg} is calculated from averaging in the horizontal and vertical line intensities over the area that is defined as the flat top area of the profile
- after subtracting the background level b_{avg} , the intensity data $I_i(x, y)$ is summed over all the measured points i . The radius r_{cyl} of a cylinder with a "volume" that corresponds to the integrated points $\sum_i (I_i(x, y) - b_{avg})$ is defined by:

$$\pi r_{cyl}^2 h_{avg} = \sum_i (I_i(x, y) - b_{avg}) \Delta x \Delta y \quad (3.45)$$

where Δx and Δy are the step sizes of the profile scan

- the non-expanded effective cathode radius r_{eff} is finally given by:

$$r_{eff} = \frac{r_{cyl}}{\sqrt{\alpha}} \quad (3.46)$$

where α is the expansion factor at the position where the profile is measured

The electron density of a uniform, flat-top beam at any position z along the solenoidal field axis for a known expansion factor $\alpha(z)$ is then simply calculated by

$$n_e(z) = \frac{I_e}{ev_e \pi r_{eff}^2 \alpha(z)} \quad (3.47)$$

where I_e is the electron beam current and v_e the electron velocity.

3.7 *Electron beam profile measurements*

In addition to the beam profiles shown in fig. 3.20, three more profile scans (one gun section and two collector section scans) are performed. The averaged result of the evaluation of these scans by the method described above yields an effective cathode radius of

$$\overline{r_{eff}} = 1.112(15) \text{ mm} \tag{3.48}$$

4 Low-energy electron cooling studies of keV ion beams in the CSR

After the implementation of the electron-ion merged beam setup into the CSR cryostat and successful tests of the electron beam transport through the electron cooler section, low-energy electron cooling experiments at the CSR were performed for the first time in the course of the June 2017 beam time campaign.

This chapter will start with the first demonstration of electron cooling in the CSR, realized for a bunched F^{6+} beam. The subsequent sections are dedicated to an investigation of the strength of the cooling force by measuring longitudinal and transverse electron cooling rates for a number of atomic and molecular ion beams. First Schottky spectra showing longitudinal cooling of a coasting ion beam are presented and analyzed with respect to the influence of the electron beam space charge in the interaction region on the ion beam position.

Moreover, in the absence of electron cooling, the growth of emittance (*blow up*) of an ion beam due to intrabeam-scattering (IBS) is investigated for coasting and bunched beams and compared to a simplified theoretical model.

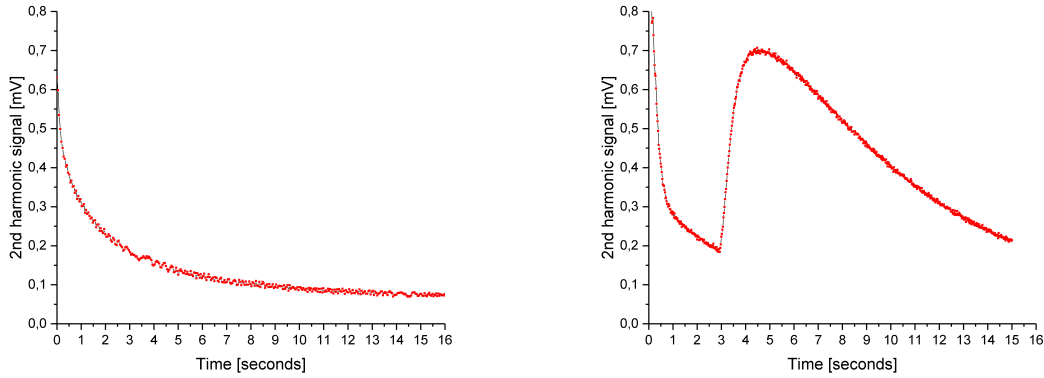
Finally, the electron cooled equilibrium bunch widths of bunched beams are investigated for space charge effects and also IBS.

4.1 First demonstration and tuning of electron cooling

During the commissioning phase of the electron-ion merged beam setup in June 2017, the available ion beam diagnostic tools at the CSR (introduced in sect. 3.6) were limited. The MCP imaging detector was not functioning yet, thus making it impossible to observe the effect of electron cooling on the transverse emittance of the ion beam by measuring the evolution of transverse ion beam profiles. In addition, Schottky noise signals of a coasting beam could not be detected due to technical problems of the preamplifiers in the Schottky signal readout system. However, with the remaining capacitive current pick-ups, it was possible to measure the signal induced by a rf-bunched beam.

In the first electron cooling run, a 1.397 MeV F^{6+} ion beam was injected into the CSR and rf-bunching at the second harmonic of the revolution frequency ($2f_0$) was applied (experimental settings summarized in table 4.1).

Fig. 4.1 (a) shows the signal amplitude at $4f_0$ without an ion beam as a function of time following the ion injection. The initial time structure of the injected ion beam consists of a rectangular pulse. The length of the ion pulse is defined to



(a) Electrons off.

(b) Electrons turned on at $t = 3s$ (cathode potential $U_0 = -43.58. eV$).

Figure 4.1: Signal of the second harmonic of the bunching frequency $f_{rf} = 214.52$ kHz, measured with a spectrum analyzer in receiver mode. The experimental method is explained in sect. 3.6.3, experimental settings are summarized in table 4.1.

Table 4.1: Experimental settings for longitudinal electron cooling of F^{6+} .

E_{ion} [MeV]	f_0 [kHz]	h	E_e [eV]	U_0 [V]	I_e [μA]	α	n_e [10^5 cm^{-3}]	r_{cath} [mm]
1.397	107.26	2	40.35	-43.58	14.4	21.59	2.91	1.10

be comparable to the circumference of the ring [30], using a fast-switching electrostatic deflector (chopper) located in the transfer beamline between the high voltage platform and the CSR. The second harmonic signal then rapidly becomes small as these rectangular pulses are transformed into the \cos^2 -structure during the rf-bunching process (see sect. 3.6.3, eqn. 3.34).

Fig. 4.1 (b) shows the effect of turning on the electron beam at 3 seconds after injection at the end of the electron cooling optimization. For optimization, first the geometrical overlap of the electron and ion beam is confirmed with the help of the wire scrapers (sect. 3.6.1). Then, the cathode potential U_0 is scanned in steps of 0.01 eV while observing the second harmonic signal on a spectrum analyzer at the time of switching on the electron beam. The electron beam is turned on at $t = 3s$. A steep rise of the signal is finally found for $U_0 = -43.58(1)$ V, marking the first proof of (longitudinal) electron cooling in a cryogenic electrostatic storage ring machine.

In this experiment, the cooling energy predicted from the bunching frequency and the storage ring circumference $C_0 = 35.12(5)$ m was $E_{cool} = 40.35$ eV (eqn. 3.41). Based on the electron beam profile measurements (sect. 3.7), an electron density of $n_e = 2.845(77) 10^5 \text{ cm}^{-3}$ is predicted. This leads to an electron beam space charge potential in the center of the beam according to eqn. 3.40

$$U_{sc}(r = 0) = \frac{n_e e R_{beam}^2}{4\epsilon_0} \left(1 + 2 \ln \frac{R_0}{R_{beam}} \right) = 0.190(1) \text{ V} \quad (4.1)$$

where $R_0 = 0.05$ m is the beam pipe radius of the CSR and $R_{beam} = \sqrt{\alpha} r_{cath}$ where $r_{cath} = 1.112(15)$ mm (see sect. 3.7) is the magnetically expanded radius of the electron beam. With eqn. 3.39 one can obtain a value for the contact potential offset

$$(W_c - W_a) = 3.04(1) \text{ V}. \quad (4.2)$$

This calculation of the difference of contact potential is carried out with the exact cathode radius value as it is measured in sect. 3.7, $r_{cath} = 1.112(15)$ mm. In the following sections, always a value of $r_{cath} = 1.10$ mm is used.

4.2 Longitudinal cooling of bunched beams

The first systematic studies performed in the 2017 and 2018 CSR beamtimes concerned bunched beam electron cooling. The main parameters of the HeH⁺ beam time are summarized in table 4.2.

Table 4.2: Experimental settings for longitudinal electron cooling of HeH⁺.

E_{ion} [keV]	f_0 [kHz]	h	E_e [eV]	U_0 [V]	I_e [μ A]	α	n_e [10^5 cm ⁻³]	r_{cath} [mm]
250	88.261	4	27.32	-30.32	26.7	21.59	6.55	1.10

4.2.1 Measurement procedure

The method was first elaborated during the 2017 beam time and then further developed for the beam time campaign of summer 2018. In particular, bunch shapes were studied by a numerical oscilloscope (*Picoscope 5000*) systemically regarding electron cooling and possible effects of space charge and intrabeam-scattering (IBS).

A sketch of the measurement scheme and devices is shown in fig. 4.2. The Picoscope's input channels are used for simultaneously recording the signals of the Schottky pick-up, the current pick-up and the CSR rf generator. The latter is also connected to the rf-bunching system. A measurement cycle is started by the ion beam injection trigger of the CSR. After a chosen delay time, a pulse generator starts a set of pulse bursts which are evenly spaced in time and fed to the Picoscope external trigger. Each of the pulses then starts a 40 ms waveform measurement of the three input signals with 14 bit resolution. The number of recorded samples

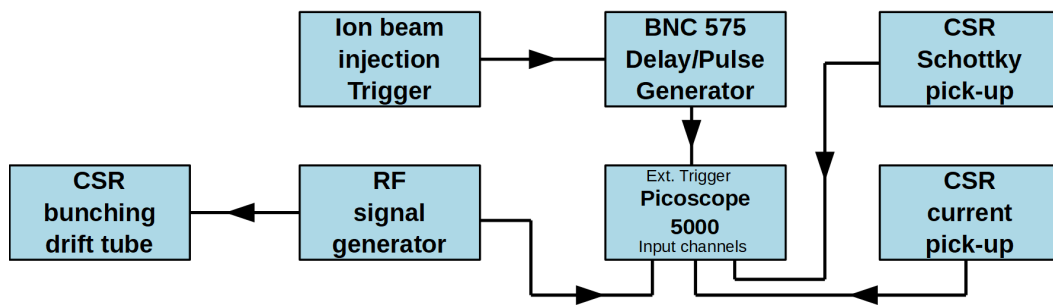


Figure 4.2: Simplified measurement scheme of the longitudinal electron cooling measurements of rf-bunched beams in the CSR. Details on the signal amplification and readouts etc. are described in [30].

4 Low-energy electron cooling studies of keV ion beams in the CSR

with this resolution is precisely $5 \cdot 10^6$, yielding a sample period of 8 ns. The bunches in the waveforms measured with the Schottky and current pick-ups are triggered at a fixed phase on the rising flank of the rf-signal and averaged over an arbitrary number of revolution periods for further analysis.

The averaging process is demonstrated in fig. 4.3 by the example of a bunched, electron cooled 250 keV HeH⁺ beam with the experimental settings described in table 4.2. If not mentioned otherwise, the waveforms are in general averaged over the total number of revolution periods contained in the measurement period of 40 ms.

As mentioned earlier, the initial injection pulse length is defined by an electrostatic deflector (chopper) in the injection beam line. The length of this rectangular pulse is about 8 μ s ($\sim 75\%$ of the revolution period). The phase overlap with the rf-buckets upon injection defines the number of ions that are captured into the individual bunches, as seen by the different pulse amplitudes particularly in fig. 4.3 (d).

Determination of bunch ion number

The number of ions contained in a bunch of a waveform as shown in fig. 4.3 can be determined by integrating the area of the bunch profile in the measured current pick-up voltage signal $U(t)$ given by $\int U(t)dt$. This area can be obtained by a simple summation (numerical integration) of the signal in the time interval defined by the bunch length. Since the baseline of a waveform, measured with an AC-coupled oscilloscope, can experience a shift due to a charging effect of the pick-up electrode capacity (discussed also in [30], p. 123), a baseline-subtraction is done first using the signals between the bunches. With the calculated bunch area, eqn. 3.29 can be used to determine the number of ions in the bunch from the known calibration factors of the current pick-up.

The bunch area can also be obtained directly from a fit of the longitudinal density distribution ρ_{\parallel} represented by the Gaussian profile eqn. 2.120. Both methods show to agree within about 10 %.

4.2 Longitudinal cooling of bunched beams

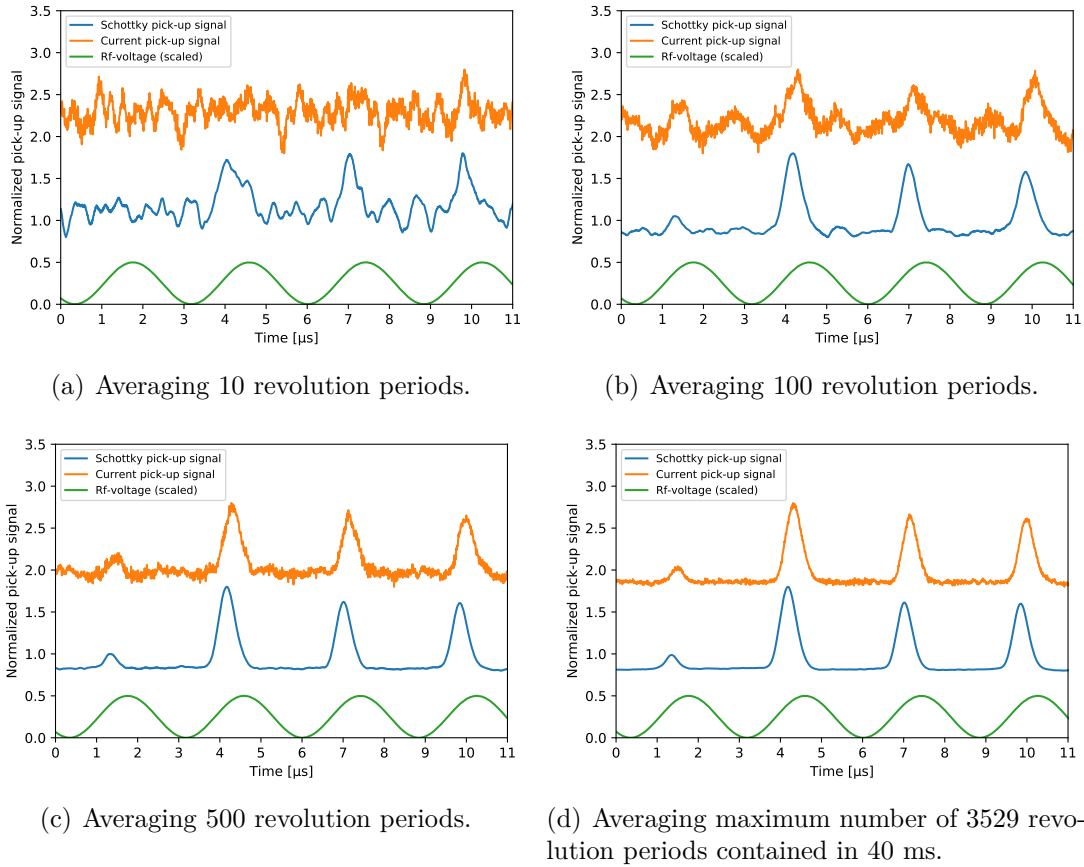


Figure 4.3: Waveform averaging process shown for a measurement of electron cooled, bunched HeH^+ with the Schottky pick-up electrode and the current pick-up electrode over different numbers of revolution periods $t_0(250 \text{ keV HeH}^+) = 11.33 \mu\text{s}$. The waveforms are triggered on the rising flank of the rf-signal.

4.2.2 F^{6+} bunched-beam cooling

Fig. 4.4 shows the time evolution of the longitudinal density profiles measured over one revolution period after injection for F^{6+} in the preliminary setup of the 2017 beamtime. It should be noted that here, each of the displayed waveforms represents a new injection of F^{6+} ions into the storage ring. The measurement procedure described above, capable of tracing a single injection, was only used later in 2018. Conditions between injections, e.g., the ion number, may vary in this initial scheme. Another uncertainty is introduced by the fact that the waveform measurements were triggered manually at a specified delay after injection.

In order to obtain a cooling time from the observed compression of the bunch profiles, the waveforms of the first bunch (between 0–5 μs in fig. 4.4) are fitted with a Gaussian distribution according to eqn. 2.120. fig. 4.5 shows the fitted bunch profiles at 0.5, 5.5 and 10.5 s after injection. The evolution of the bunch width σ_b as a function of the time after injection is shown in fig. 4.6. It should be governed by electron cooling and diffusion, and be described by the exponential decay function given in eqn. 2.137. The appropriateness of this function for the

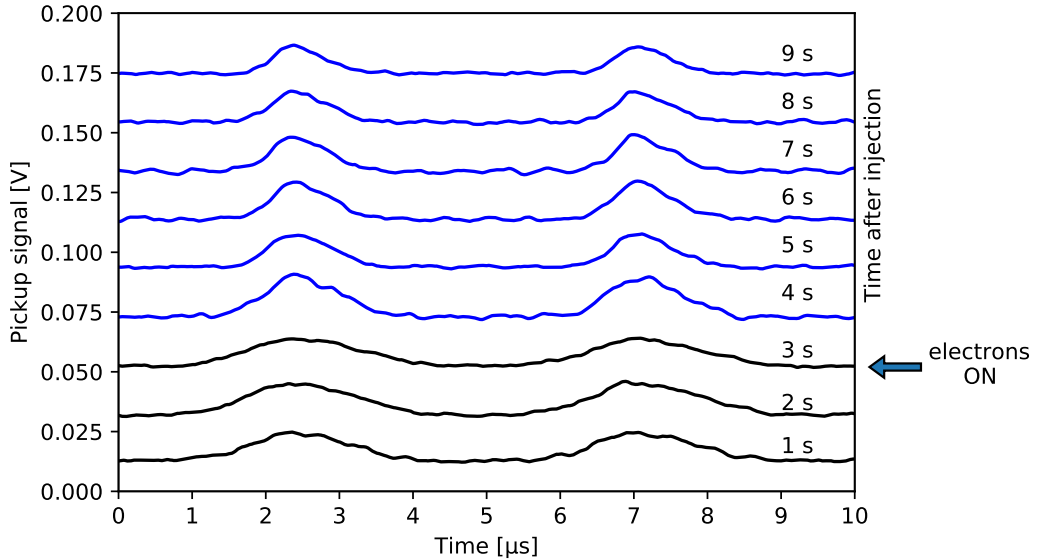


Figure 4.4: Two 1.397 MeV F^{6+} bunches are stored in the CSR with $f_{rf} = 214.52$ kHz. Each waveform, displayed in one second steps after injection, is the result of a new injection. Electron cooling is turned on 3 seconds after injection with $n_e = 2.91 \cdot 10^5 \text{ cm}^{-3}$ (electron current $I_e = 14.4 \mu\text{A}$, expansion $\alpha = 21.59$). The number of injected ions is $\sim 1 \cdot 10^6$.

4.2 Longitudinal cooling of bunched beams

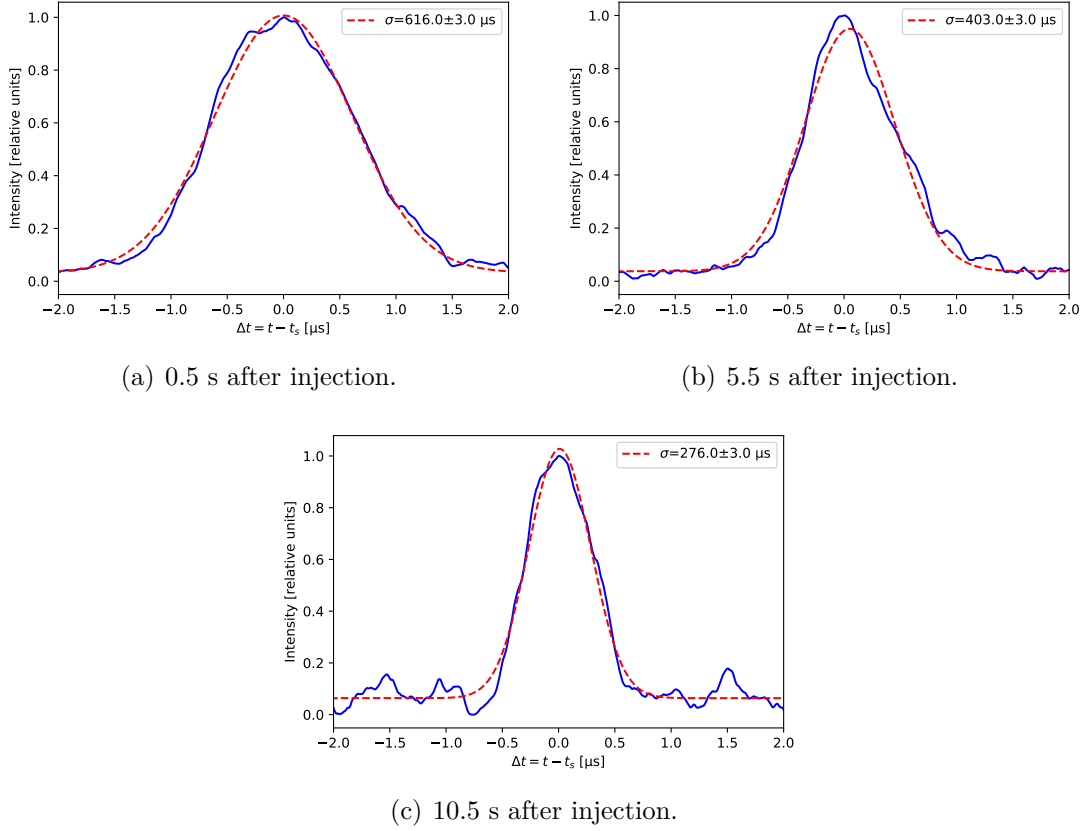


Figure 4.5: Evolution of longitudinal density profile of bunched 1.397 MeV F^{6+} (compare fig. 4.4). The time on the x-axis is given with respect to the reference time $t_0 = 0$ defined by the synchronous particle in the center of the bunch. Electrons are turned in 3 s after injection.

extraction of the cooling time will be discussed again in more detail below at the example of HeH^+ . A fit of this function to the evolution of the bunch widths σ_b is shown in fig. 4.6, yielding a cooling time of $\tau_{\parallel} = 3.55(6)$ s.

Another way to obtain an estimate of the cooling time is to look at the time it takes for the second harmonic signal (fig. 4.1 b)) to reach its maximum value, which is about 1.5 s.

Furthermore, neglecting any influence of the magnetic field, the measured cooling time is compared to the Spitzer plasma relaxation rate (eqn. 2.109), which is calculated for an assumed isotropic electron temperature of $T_e = 2$ meV. This estimate yields a value of $\tau_{\parallel, Spitzer} = 1.57$ s.

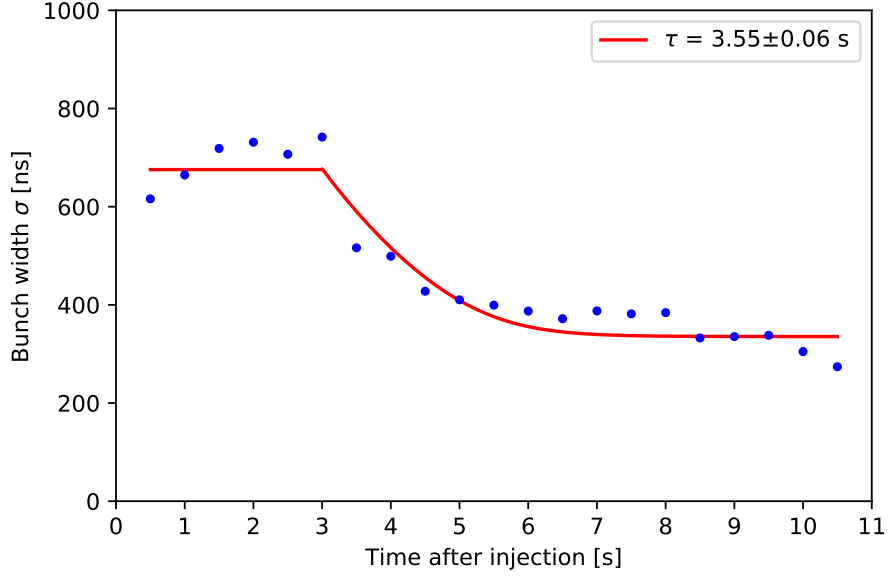


Figure 4.6: Bunch width σ_b obtained from Gaussian bunch profile fits of the first bunch in the time spectra (0-5 μ s) shown in fig. 4.4, as a function of time after injection (storage time). Electron cooling is turned on 3 seconds after injection.

4.2.3 HeH⁺ bunched-beam cooling

With the experimental setup described in sect. 4.2.1, one is ready to measure the temporal evolution of the longitudinal density profile of a bunched ion beam at a number of equally spaced points during the storage time. Electron cooling can be turned on and off at any desired times. Before starting cooling time measurements, the geometrical overlap of the electron and ion beam centers is again confirmed to be within ~ 1 mm with the help of the wire scrapers (sect. 3.6.1). Furthermore, the efficiency of the cooling process is always checked beforehand with the second harmonic method (sect. 3.6.3) and additionally serves as a fine-tuning tool for the correct cathode voltage U_0 or the settings for the electron beam steering magnets.

A longitudinal density profile (bunch shape) measurement with the experimental settings of table 4.2 is presented in fig. 4.7 (a), where electron cooling is started three seconds after injection. The bunch waveforms are measured, after a delay of two seconds after injection, in 300 ms steps. As described above, a Gaussian profile (eqn. 2.120) is fitted to the bunches and the widths σ_b are plotted as a function of the storage time (time after injection) in order to analyze the bunch length compression due to phase space cooling. The procedure is shown at the

Table 4.3: Longitudinal cooling times for three 250 keV HeH⁺ ion bunches shown in fig. 4.7 from fits of the function eqn. 4.4. The experimental settings are summarized in table 4.2.

Bunch	τ_{\parallel} [ms]
2	1419±16
3	1403±16
4	1447±14
average	1422±18

example of Bunch 2 in fig. 4.7 (b). This representative measurement is further used here to discuss the possible influence of IBS on these cooling measurements. Further studies on IBS will be presented in sect. 4.5. As discussed in sect. 2.5, cooling can lead to enhanced diffusion during the cool down. The cooling curve should then change from simple exponential decay

$$\sigma(t) = (\sigma_0 - \sigma_{\infty}) \exp[-(t - t_0)/\tau] + \sigma_{\infty} \quad (4.3)$$

to the function (eqn. 2.137)

$$\sigma_i(t) = [(\sigma_0^{\gamma} - \sigma_{\infty}^{\gamma}) \exp(-\gamma(t - t_0)/\tau) + \sigma_{\infty}^{\gamma}]^{1/\gamma} \quad (4.4)$$

with $\gamma = 6$ for bunched beams and in both equations σ_0 is the width at the time t_0 when the electrons are turned off and σ_{∞} is the equilibrium cooled width.

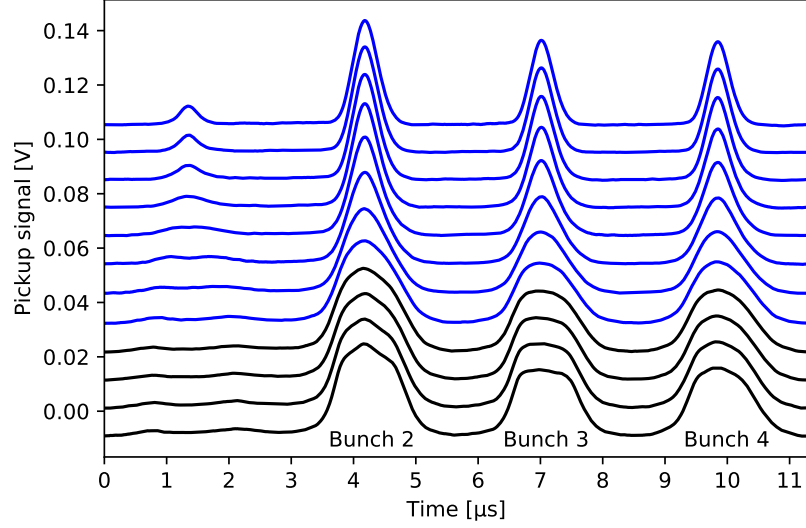
Fig. 4.7 (b) shows fits using both types of function. The plot of residuals in fig. 4.7 (c) shows that the IBS formula (with $\gamma = 6$) yields a fit with much better quality and represents better the longitudinal bunched cooling. The longitudinal cooling times for bunched 250 keV HeH⁺ extracted from the cooling curves in fig. 4.7 (b)-(c) by a fit of eqn. 2.137 and their weighted average are summarized in table 4.3. A comparison to theoretical cooling rates will be given in the following chapter.

As already shown for F⁶⁺ in sect. 4.1, with the optimized electron cooling settings given in table 4.2 and a calculation of the space charge potential contribution in the center of the electron beam given by eqn. 2.121 with $U_{sc}(r = 0) = 0.43$ V, the difference of work functions ($W_c - W_a$) can be calculated by eqn. 3.39

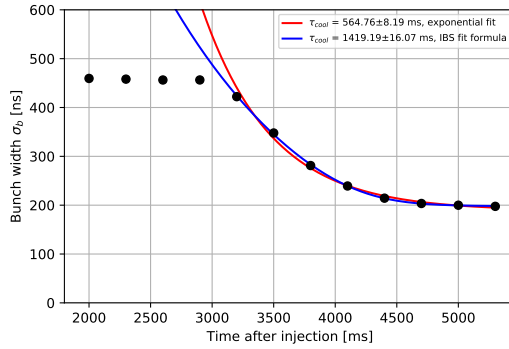
$$\begin{aligned} (W_c - W_a) &= -e|E_e| + e|U_0| - e|U_{sc}| \\ &= 2.57(1) \text{ V} \end{aligned} \quad (4.5)$$

where the error is given by the uncertainty in the experimental determination of the optimized cathode potential U_0 .

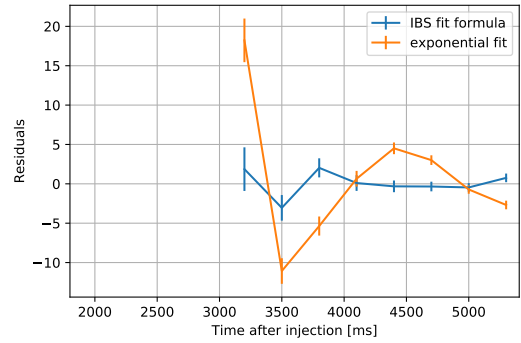
4 Low-energy electron cooling studies of keV ion beams in the CSR



(a) Waveforms showing one revolution period, averaged over 40 ms, recorded in steps of 300 ms (shown from bottom upwards), starting 2 s after injection. Electron cooling is turned on 3 s after injection (blue waveforms).



(b) Cooling curve for Bunch 2.



(c) Plot of residuals demonstrating the better fit quality when using the IBS function eqn. 2.137.

Figure 4.7: Evaluation of a longitudinal cooling time measurement of bunched 250 keV HeH⁺ measured with the Schottky pick-up electrode. Electron cooling is turned on at $t_0 = 3$ s (see table 4.2 for experimental settings).

4.2.4 Dependencies of the longitudinal cooling rate

Cooling time measurements with bunched 250 keV HeH⁺ were repeated for several injections at four different electron densities in the electron-ion interaction region (see table 4.4). The measured cooling rates are the result of evaluating the time evolution of the bunch width σ_b of individual bunches during electron cooling, analogously to the procedure demonstrated above in fig. 4.7. The IBS fit formula with $\gamma = 6$ was used in all cases. The cooling rates for each bunch are presented in fig. 4.8 as a function of the bunch ion number N_b . As seen in fig. 4.8, the cooling rates are independent of the ion number as expected. The ion numbers are determined from a numerical integration of the voltage signal in the bunch area, as described above in sect. 4.2.1.

The results for the longitudinal cooling rate r_{\parallel} are given in table 4.4 as an error-weighted average of the individual bunch cooling times separately for different electron densities. The density-dependent longitudinal electron beam temperatures $T_{e\parallel}$ are calculated by eqn. 3.17 with an accelerating potential of $U_0 = -30.3$ V for a room-temperature cathode. The transverse temperature is estimated to be $T_{e\perp} \sim 2$ meV as discussed in sect. 3.3.3).

Table 4.4: Experimental parameters and measured longitudinal cooling rate r_{\parallel} for 250 keV HeH⁺ (electron density n_e calculated with $r_{cath} = 1.10$ mm).

I_e [μA]	n_e [10^5 cm^{-3}]	B_{int} [G]	α	$T_{e\parallel}$ [μeV]	$T_{e\perp}$ [meV]	r_{\parallel} [s^{-1}]
26.7	6.55	90	21.59	89	~ 2	0.678(113)
25.6	6.28	90	21.59	88	~ 2	0.575(55)
10.2	2.49	90	21.59	71	~ 2	0.217(31)
4.6	1.12	90	21.59	60	~ 2	0.134(34)

Comparison to theory

Fig. 4.9 shows a comparison of the measured longitudinal cooling rates to several theory lines that are based on the electron cooling rate approximation formulae presented in sect. 2.2.6 and will be discussed here. Table 4.9 summarizes the results and comparisons to theoretical cooling rates.

For a first estimate, the Spitzer cooling rate (cyan line) is calculated as described by eqn. 2.109 for the case of an assumed isotropic electron temperature distribution that is defined by $T_e = T_{e\perp} = 2$ meV. The influence of the magnetic field is completely ignored with this approach. The calculated Spitzer rate is about a

4 Low-energy electron cooling studies of keV ion beams in the CSR

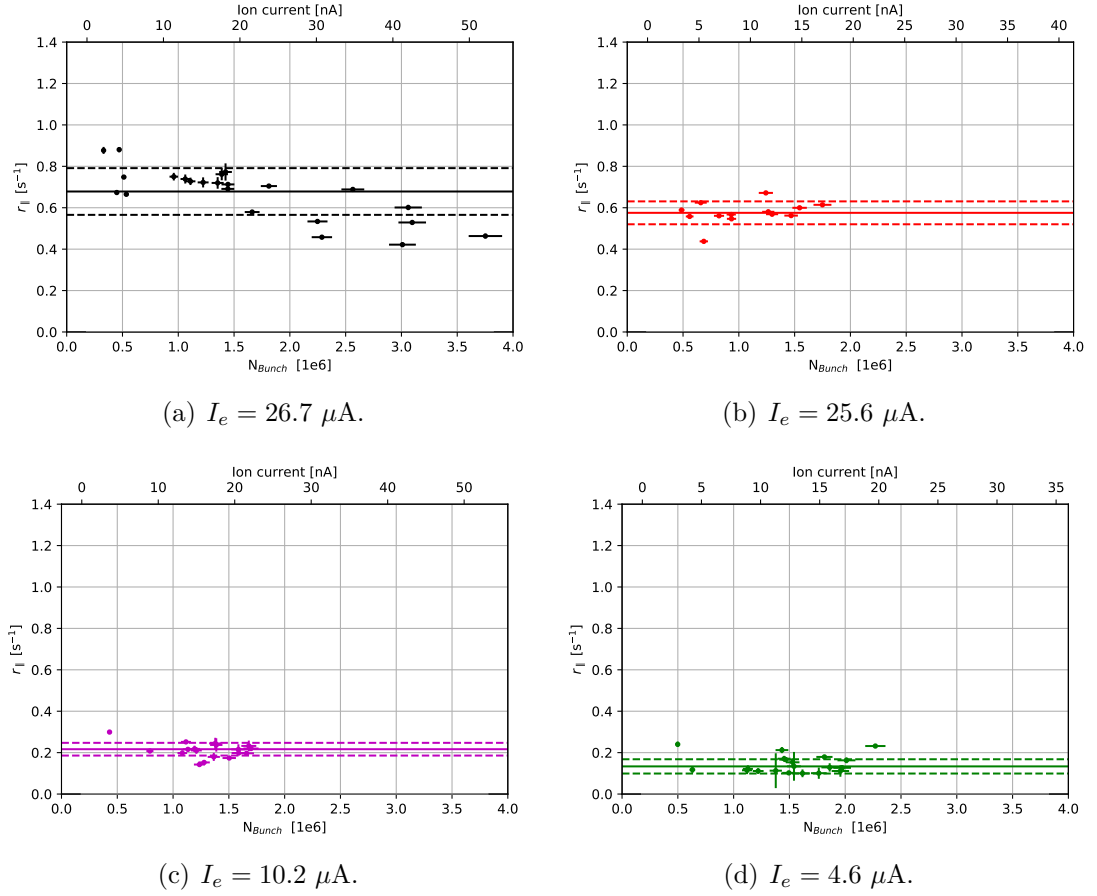


Figure 4.8: Longitudinal cooling rates measured for bunched 250 keV HeH^+ at four different electron densities as a function of the ion current. The horizontal lines and dashed lines in each graph represent the weighted average and the standard deviation, respectively, of the longitudinal cooling rates.

factor of ~ 3 smaller than the measured rate.

The actual flattened electron velocity distribution (sect. 3.3.3, electron beam temperatures in table 4.4) is taken into account by the asymptotic approximation of the longitudinal cooling force derived by Derbenev and Skrinsky [31]. However, this prediction includes only collisions not influenced by the magnetic field, corresponding to a reduced Coulomb logarithm L_C calculated with impact parameters eqns. 2.92 & 2.93. The approximation as given by eqn. 2.111 is derived for the linear regime of the electron cooling friction force, where the ion velocity is

Table 4.5: Experimental parameters and measured longitudinal cooling rate r_{\parallel} for 250 keV HeH⁺.

n_e [10^5 cm^{-3}]	$L_C^{Spitzer}$	L_C	L_C^{ad}	r_{\parallel} [s^{-1}]	$r_{Spitzer}$ [s^{-1}]	$r_{\parallel, no \text{ field}}$ [s^{-1}]	$r_{\parallel, strong \text{ field}}$ [s^{-1}]
6.55	7.44	7.04	3.54	0.678(113)	0.186	0.889	4.94
6.28	7.46	7.06	3.56	0.575(55)	0.178	0.850	4.840
2.49	7.92	7.52	4.02	0.217(31)	0.075	0.401	3.005
1.12	8.32	7.92	4.42	0.134(34)	0.035	0.207	1.920

assumed to be much smaller than both, the transverse and longitudinal velocity spread of the electrons. The calculated longitudinal cooling line as a function of the electron density (red line) overestimates the measured values by a factor of ~ 2 .

The electron cooling experiments presented throughout this work are always performed with a magnetic guiding field of $B_{int} = 90 \text{ G}$ in the electron-ion interaction region. As discussed in sect. 2.2.5, the transverse motion of the electrons averages to zero in the gyration trajectories that arise in such a longitudinal magnetic guiding field. Hence the cooling force in the linear regime is mainly defined by the longitudinal velocity spread of the electrons. This is represented in the approximation formulae that have been extended for the influence of a strong magnetic field, given by eqn. 2.114, also derived by Derbenev and Skrinsky [27]. The calculated rate with this approach¹, as explained in sect. 2.2.6, is given by the purple dashed line in fig. 4.9, being far away from the measured points and overestimating the data by up to a factor of ~ 16 for the lowest measured density. However, the electron cooling force in this adiabatic approximation depends strongly on the longitudinal electron beam temperature and assumes that the electron-ion relative velocities become as small as corresponds to the longitudinal temperature only. Higher relative velocities can, for example, be caused by a not perfectly aligned magnetic guiding field, inducing an additional electron velocity spread [46].

In dependency of the ion charge and mass and of the electron density, the cooling performance is calculated by the reduced rate $r_{\parallel}^* = r_{\parallel}/\kappa$ with $\kappa = n_e[\text{cm}^{-3}]Z^2/A$ (eqn. 2.110). A line fit to $r_{\parallel}(n_e)$ yields r_{\parallel}^* as given in table 4.6.

¹As shown in sect. 2.2.6, the adiabatic Coulomb logarithm L_C^{ad} is calculated with the transverse ion velocity spread. For HeH⁺, an initial transverse ion temperature of $T_{\perp} = 1.4 \text{ eV}$ is estimated (see appendix B.3) yielding the transverse thermal ion velocity spread $\Delta_{i\perp} = \sqrt{2k_B T_{\perp}/M_i}$.

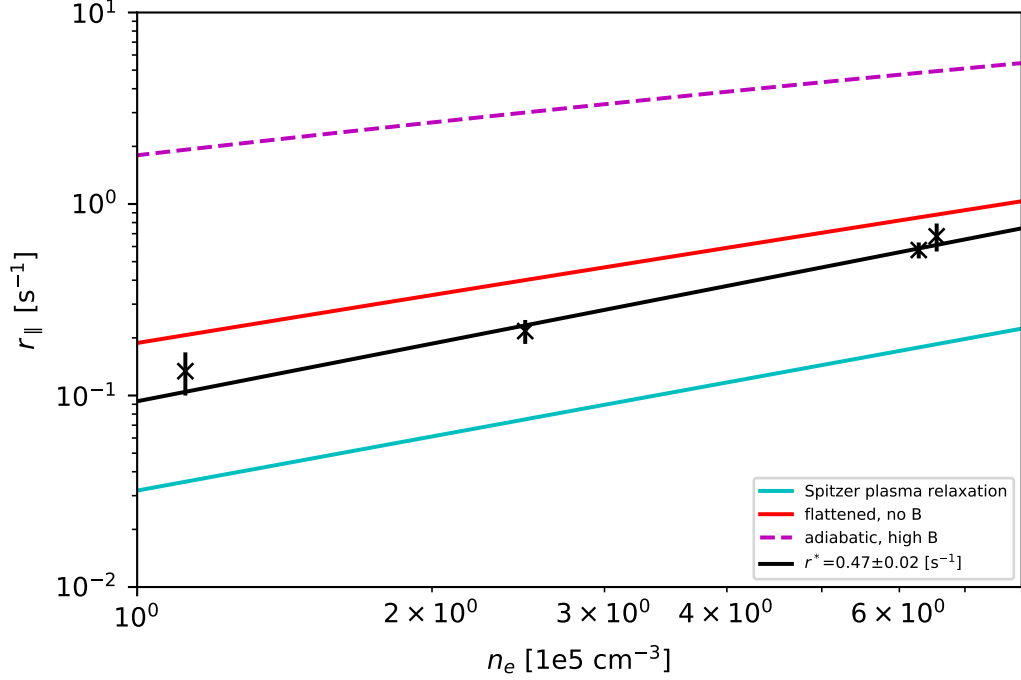


Figure 4.9: Longitudinal bunch length electron cooling rate of 250 keV HeH⁺ as a function of the electron beam density in the interaction region.

Table 4.6: Fit of the scaled longitudinal cooling rate $r_{\parallel}^* = r_{\parallel}/\kappa$ to the measured points and theoretical curves calculated from the Spitzer plasma relaxation (eqn. 2.104), no B-field approximation (eqn. 2.111) and strong B-field approximation (eqn. 2.114), shown in fig. 4.9.

$r_{\parallel,measured}^*$	$r_{\parallel,Spitzer}^*$	$r_{\parallel,no\ field}^*$	$r_{\parallel,strong\ field}^*$
0.467(22)	0.147	0.690	4.073

4.2.5 Ion beam intensity evolution during electron cooling

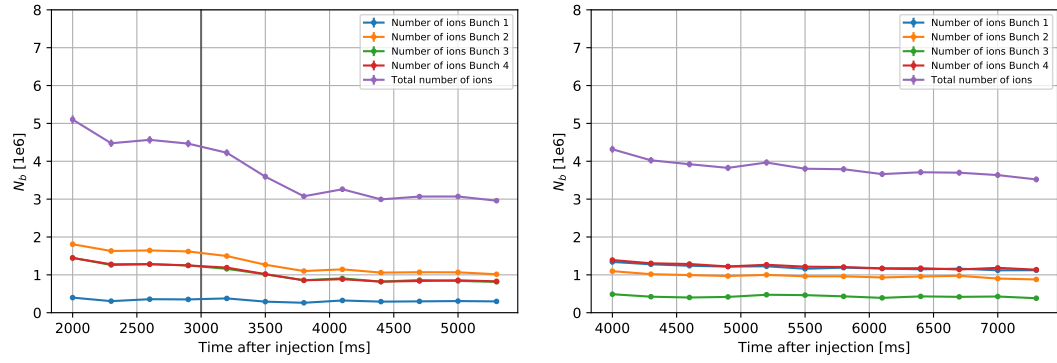
The evolution of the ion number contained in each bunch is shown in fig. 4.10 for three different electron current settings. The ion number evolutions given there are examples of cooling curve measurements that are part of the series shown above in sect. 4.2.4. Therefore, the same experimental settings as given in table 4.4 are still valid here.

As explained in sect. 4.2.1, the bunch ion number N_b can be determined either from a simple numerical summation (integration) of the current pick-up voltage signal in the bunch profile area or is directly obtained from the Gaussian peak area of the fitted longitudinal density profile. Since the ring is only filled to about 75% of its circumference, one of the four rf-buckets in the bunched beam HeH⁺ storage captures only a very low amount of ions. This smaller ion bunch only develops a Gaussian profile when the longitudinal phase space is compressed due to electron cooling (demonstrated in fig. 4.7 (a)). Thus a bunch ion number for the small bunch can be obtained by the Gaussian peak fit method only when the cooling process has almost finished.

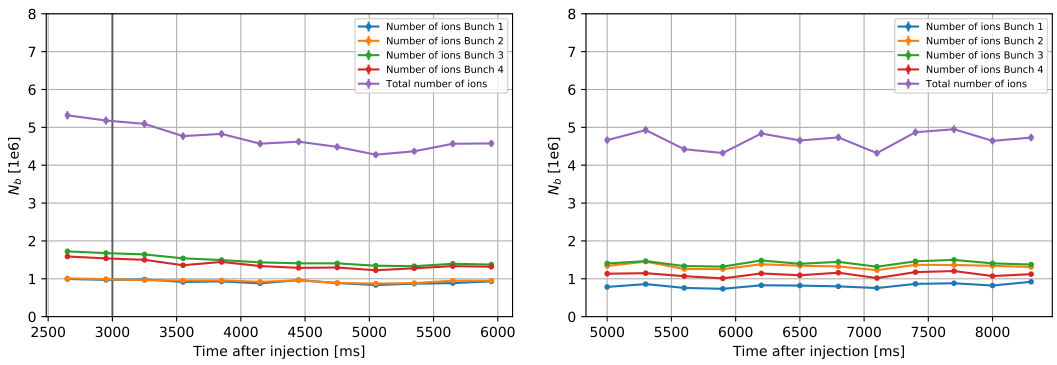
The evolution of the bunch ion number when turning on the electron beam at 3 seconds after injection is investigated in fig. 4.10 for three different electron current (electron density) settings. The bunch ion number N_b is determined with the numerical method in order to also demonstrate the evolution of the small bunch. For each current setting, two injections are investigated. One injection shows the time regime when electron cooling is turned on around 2-6 seconds (left side) and another injection is measured in the time regime starting 1-2 seconds after electrons are turned on to up to about 8.5 seconds after injection (right side).

An effect of turning on the electron beam is most visible in the higher electron current measurement with $I_e = 26.7 \mu$ ($n_e = 6.55 \cdot 10^5 \text{ cm}^{-3}$) (fig. 4.10 (a)). In the decay of the total number of ions given by the sum of the individual bunch ion numbers N_b (purple dashed curve) a kink is clearly visible as soon as electron cooling is turned on, before the ion number seems to stabilize after about 1-2 seconds. About 40% of the ions are lost with this high electron current setting during the cooling process, but resulting in a stabilized ion number in the supposed equilibrium. With decreasing electron current, the effect of losing ions during the cooling process becomes smaller, even reaching almost unaffected bunch ion numbers at the lowest electron current setting of $I_e = 4.6 \mu\text{A}$.

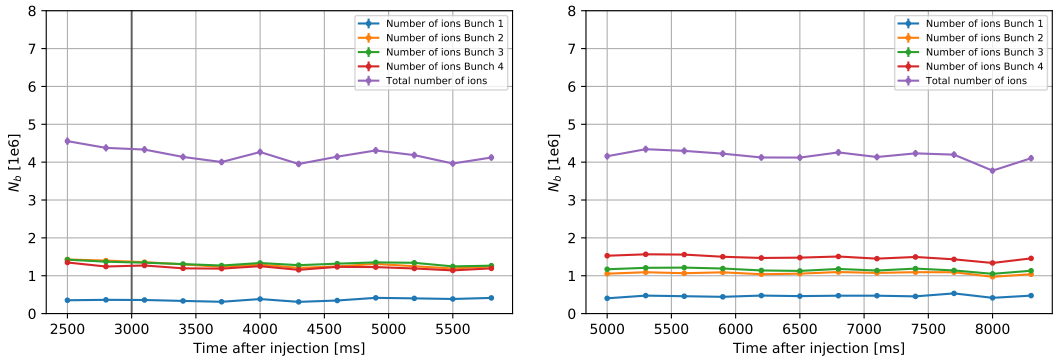
4 Low-energy electron cooling studies of keV ion beams in the CSR



(a) $I_e = 26.7 \mu\text{A}$.



(b) $I_e = 10.2 \mu\text{A}$.



(c) $I_e = 4.6 \mu\text{A}$.

Figure 4.10: Evolution of the bunched ion beam intensity during electron cooling for different electron densities. Every plot represents a separate ion beam injection. Electron cooling is always turned on at $t = 3000$ ms after injection.

Investigation of tune shifts

In order to find an explanation for the strong loss of ions during electron cooling with currents higher than about $\sim 20 \mu\text{A}$, the strength of the incoherent space charge tune shift and the tune shift due to the lensing effect of the electron beam (sect. 2.3.1) in the electron-ion interaction region are calculated by eqns. 2.119 & 2.117.

The quantities that are needed for the calculation are summarized in table 4.7. The betatron functions $\beta_{x,y}$ in the electron-ion interaction region are given in [13]. The transverse beam widths $\sigma_{x,y}$ is estimated from a transverse ion beam profile measurement of a coasting 250 keV HeH⁺ beam (see fig. 4.16 below). The uncooled beam widths $\sigma_{x,0}$ and $\sigma_{y,0}$, analyzed as described in sect. B.3, are used. The bunching factor $B_f = hl_{bunch}/C_0$ is estimated from the uncooled bunch width $\sigma_{b,0} \sim 480$ ns as measured in fig. 4.7. With these parameters and the estimated maximum tolerable shift for the CSR working point of $\Delta Q_{max} = -0.1$, a maximum number of storable ions $N_{max} \sim 3.6 \cdot 10^8$ can be estimated for a bunched beam. This number is much higher than typical ion numbers of $< 5 \cdot 10^6$ during bunched beam electron cooling experiments (fig. 4.10).

The calculated tune shifts are given in table 4.8. The bunched beam ion number $N_{b,0}$ before electrons are turned on is obtained from the ion beam intensity evolution shown in fig. 4.10. The incoherent space charge tune shifts and the tune shifts due to the lensing effect of the electron beam are < 0.002 by amount and largest in the horizontal direction. As they have opposite signs they can partially cancel each other. For the higher electron current $I_e = 26.7 \mu\text{A}$ the magnitude of the lensing effect is higher than the incoherent tune shift.

Due to the very small magnitude of the calculated tune shifts, the reason for losing ions in the electron cooling process with higher currents may require different explanations. Thus, it is not clear whether the ion beam and electron beam are perfectly overlapped in the interaction region in the beginning of the cooling process. The ideal situation for electron cooling is a small ion beam that is completely immersed in the electron beam. The consequences of a wider ion beam that might only partly overlap with the electron beam are difficult to estimate and complicate the so far assumed picture of the linear regime of the cooling force. Nevertheless, it can already be said here that more systematic studies are needed in the future in order to have a better understanding of this process and to guarantee high, constant numbers of stored ions.

Table 4.7: Summary of quantities needed for the calculation of the space charge tune shifts by eqns. 2.119 & 2.117 (see text for details and appendix B.3 for uncooled transverse beam widths $\sigma_{x,0}$ and $\sigma_{y,0}$ for HeH⁺).

β_x [m]	β_y [m]	$\sigma_{x,0}$ [mm]	$\sigma_{y,0}$ [mm]	B_f	β_0 [10 ⁻³]	$N_{max}(\Delta Q = -0.1)$ [10 ⁸]
13.009	1.4095	5.60(3)	3.28(2)	~ 0.17	10.3	~ 3.6

Table 4.8: Calculation of tune shifts caused by the incoherent space charge tune shift ΔQ_{sc} and the tune shift due to the lensing effect of the electron beam ΔQ_e (eqns. 2.119 & 2.117).

$N_{b,0}$ [10 ⁶]	I_e [μA]	$\Delta Q_{sc,x}$ [10 ⁻³]	$\Delta Q_{e,x}$ [10 ⁻³]	$\Delta Q_{sc,y}$ [10 ⁻³]	$\Delta Q_{e,y}$ [10 ⁻³]
5.10(11)	26.7	-1.42(3)	1.91(2)	-0.44(1)	0.60(1)
5.32(11)	10.2	-1.48(3)	0.73(1)	-0.47(1)	0.230(3)
4.55(10)	4.6	-1.27(3)	0.328(4)	-0.40(1)	0.104(1)

4.3 Longitudinal cooling of Schottky spectra

First Schottky spectra of coasting, non electron-cooled $^{40}\text{Ar}^+$ and Co_2^- ion beams with 60 keV energy have been measured in course of the 2015 CSR commissioning phase [13]. In this section, the first experimental studies of longitudinal electron cooling in the Schottky noise spectra of coasting ion beams (sect. 3.6.2) in the CSR are presented. Signals were affected by external pickup, but initial studies showing the equilibrium of ion and electron velocities in the cooling of coasting ion beams could be demonstrated.

4.3.1 Space charge cooling point

For the interpretation of the Schottky spectra shown below, it is important to understand in particular the effect of the electron beam space charge in the electron-ion interaction region. The ion beam is ideally fully immersed in the electron beam if both beams are overlapped correctly in the interaction region of the electron cooler. However, due to its space charge the electron beam has a mean velocity profile of parabolic shape in its radial direction r [65]:

$$\langle v_e(r) \rangle = v_{e,0} \cdot \left(1 + \frac{r^2}{r_e^2} \right) \quad (4.6)$$

where

$$r_e^2 = \frac{4\epsilon_0 m_e v_{e,0}^2}{e^2 n_e} \quad (4.7)$$

and $v_{e,0}$ is the electron beam lab frame velocity in its center (on-axis). This is equivalent to eqn. 3.40 for $r < R_{beam}$.

As a result the longitudinal energy \hat{E} of an electron beam with on-axis energy E_e as given by eqn. 3.39 can be expressed as a function of the horizontal position x by

$$\hat{E}(x) = E_e + k \cdot (x - x_0)^2 \quad (4.8)$$

where $k = n_e e / (4\epsilon_0)$ and x_0 is the horizontal center of the electron beam.

As it will be shown below, the important result from eqn. 4.6 & 4.8 is that changing the accelerating cathode potential and hence the electron beam energy E_e results in a shift of the horizontal position x of the ion beam to a new *cooling point* or equilibration point of the beam velocities $v_{0,ion} = \langle v_e(r_0) \rangle$. The cooling force will drag the ion beam to this new point of velocity-matching in the electron beam velocity profile. A displacement of the horizontal position $\Delta x = x - x_0$ of the ion beam's closed orbit is connected to a momentum change $\Delta p = p - p_0$ via

4 Low-energy electron cooling studies of keV ion beams in the CSR

the dispersion D_x (sect. 2.1.4). Deviations of the electron and ion beam velocities from the closed orbit (reference) velocity v_0 , given by δ_e and δ_{ion} , respectively, are related to a shift of the horizontal beam position Δx of each beam by

$$\delta_e = \left(\frac{v - v_0}{v_0} \right)_e = \frac{1}{2} \frac{E_e + k(\Delta x)^2 - E_0}{E_0} \quad (4.9)$$

$$\delta_{ion} = \left(\frac{v - v_0}{v_0} \right)_{ion} = \frac{\Delta x}{D_x} \quad (4.10)$$

where eqn. 4.9 follows from eqn. 4.8 and $D_x = 2.10$ m is the dispersion in the electron-ion interaction region [13] and E_0 is the reference electron cooling energy defined by v_0 . The space charge cooling point can finally be obtained from

$$\delta_e = \delta_{ion} \quad (4.11)$$

which yields

$$\frac{\Delta x}{D_x} = \frac{1}{2E_0} (E_e + k(\Delta x)^2 - E_0) \quad (4.12)$$

and has the solutions

$$(\Delta x)_{1,2} = \frac{E_0}{kD_x} \pm \sqrt{\frac{E_0^2}{k^2 D_x^2} - \frac{(E_e - E_0)}{k}} \quad (4.13)$$

Only $(\Delta x)_2$ fulfills $\Delta x = 0$ for $E_e = E_0$ and will be taken as the relevant solution for the space charge cooling point. From eqn. 4.13 & 2.30 one finds for the relative frequency shift as a function of the relative energy shift $\Delta E/E_0$:

$$\frac{\Delta f}{f_0}(\Delta E/E_0) = \eta \frac{\Delta x}{D_x} = \frac{\eta E_0}{kD_x^2} \left(1 - \sqrt{1 - \frac{kD_x^2}{E_0} \left(\frac{\Delta E}{E_0} \right)} \right) \quad (4.14)$$

Table 4.9: Experimental settings for Schottky noise spectra measurements of 250 keV HD⁺ (r_e and n_e calculated with $r_{cath} = 1.10$ mm).

I_e [μA]	α	r_e [mm]	n_e [10^5 cm^{-3}]	$U_{sc}(r=0)$ [eV]	$(W_c - W_a)$ [V]	f_0 [Hz]	E_0 [eV]
35.1	30	6.03	4.8	0.76	2.3(1)	113666(3)	45.16

4.3.2 Electron cooled Schottky spectra for HD⁺

Longitudinal electron cooling is investigated by measuring Schottky noise spectra (sect. 3.6.2) of a 250 keV HD⁺ coasting beam. Electron cooling with the electron beam settings listed in table 4.9 is optimized with the usual rf-bunching second harmonic method (sect. 3.6.3) and found to be most efficient for a cathode voltage setting of $U_0 = -48.28$ V. Rf-bunching is then turned off again and Schottky spectra of the coasting beam are measured with a spectrum analyzer at the first harmonic of the revolution frequency f_0 for a set of different cathode potentials U_0 in the range of 48.10-48.55 V.

Unfortunately, a high background noise contribution was always present in these measurements with various peaks from unclear sources, some of them even changing their position in time. The suppression of these effects has been possible only in a recent revision (2019) of the measurement electronics. The spectra are therefore obtained by averaging 20 traces of 1.5 s sweeps in a frequency span of 500 Hz around the first harmonic of the revolution frequency. A pulse generator is triggered 500 ms after the ion beam injection into the CSR, and then every following 1.55 s another trace is recorded with the spectrum analyzer. Since the background noise peaks in the measured frequency band are not stable and do not appear at fixed positions, no background subtraction is performed in this case. In order to observe the effect of electron cooling, electron cooled and uncooled spectra are always compared in one plot. Uncooled Schottky spectra are measured for separate ion beam injections, when no electron beam is present. However, this was not repeated before every measurement of an electron cooled spectra, i.e., many cooled spectra are compared with the same uncooled spectra. The electron cooled ion beam Schottky peak is fitted with a Gaussian distribution to obtain the revolution frequency given by the center of the Gauss peak. The various measured spectra that have been analyzed with this procedure are given in appendix A.1 (fig. A.1).

Fig. 4.11 demonstrates the effect of longitudinal electron cooling in the Schottky spectra for an electron energy of $E_e = 45.11$ eV. A frequency deviation Δf of about 29 kHz between the Gaussian peak position in the case when electrons are turned

4 Low-energy electron cooling studies of keV ion beams in the CSR

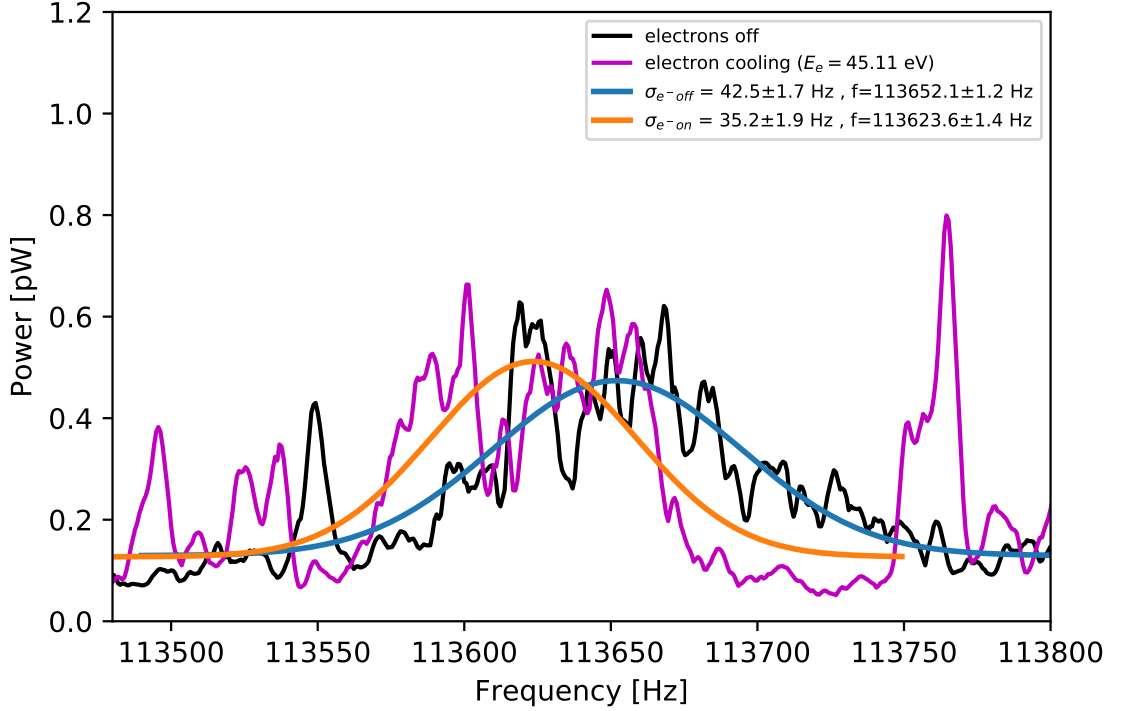


Figure 4.11: Schottky spectrum of a coasting 250 keV HD^+ beam (black line). Merging the ions with an electron beam with energy $E_e = 45.11$ eV shifts the ion beam to a lower revolution frequency (purple line). The fitted Gaussian width of the uncooled ion beam Schottky peak (blue line) decreases by about 20% due to electron cooling (orange line).

off to the peak position of the electron cooled longitudinal ion beam profile is observable. The frequency deviation is related to a shift of the ion beam horizontal position due to electron cooling via eqn. 4.14. As shown above, this ion beam *dragging* can be interpreted such that the cooling point, given by the intersection of the parabolic velocity profile of the electron beam with the ion beam dispersion line in the CSR, lies off the center of the injected beam.

In fig. 4.12, the relative deviations $\Delta f/f_0$ of the measured revolution frequencies of the electron cooled ion beams to a reference frequency f_0 are plotted as a function of the corresponding relative electron energy deviation $\Delta E/E_0$ to the reference electron energy E_0 . Here, $\Delta E = (E_e - E_0)$ is obtained from the change of the electron acceleration voltage. The reference frequency $f_0 = 113666(3)$ Hz and

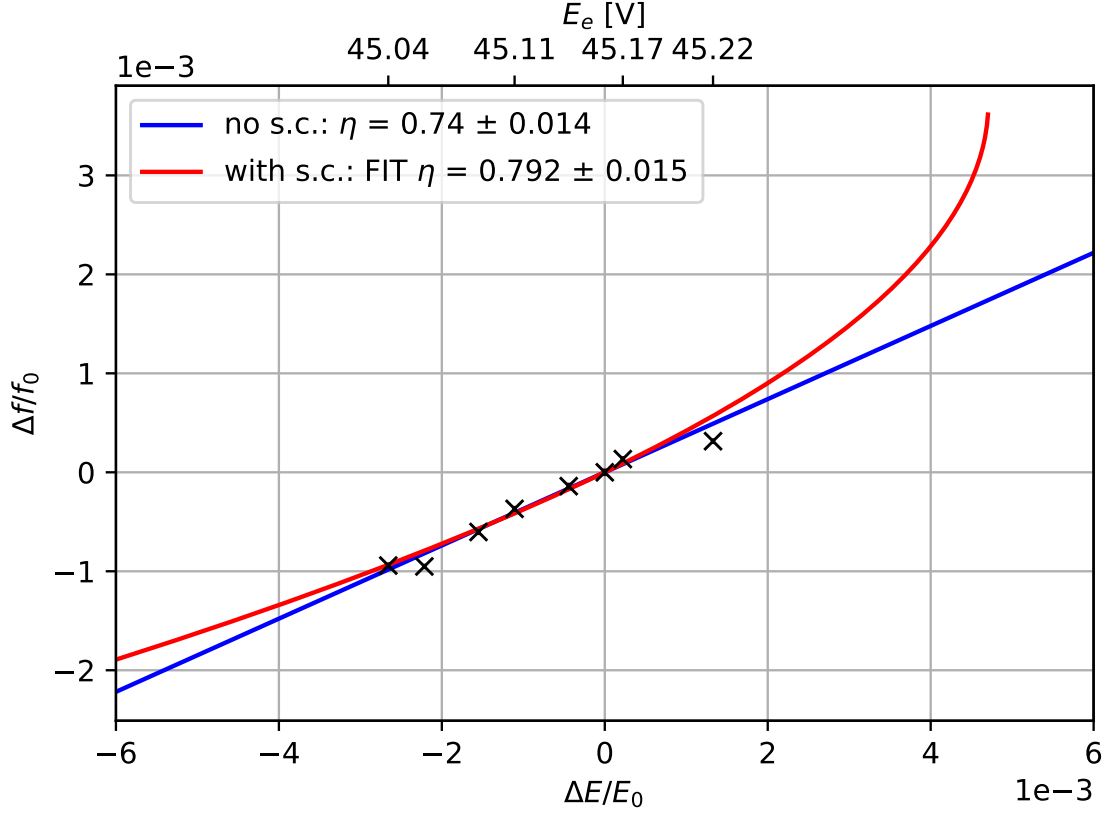


Figure 4.12: Measured relative frequency shifts of the closed orbit from the reference frequency $f_0 = 113666(3)$ Hz for different electron energies E_e in the range of 45.04 eV to 45.22 eV. The reference point is given by $E_0 = 45.16$ eV (see text for details). The ion beam’s horizontal position is thus assumed to be centered for E_0 . The red solid line shows a fit of the space charge model described by eqn. 4.14 to the measured points, with the slip factor η as the only fit parameter. Ignoring space charge effects gives the blue solid line.

reference energy $E_0 = 45.16$ eV (cathode potential $U_0 = -48.22$ V) are obtained from the Schottky spectra where electron cooling does not seem to drag the ion beam and hence the cooling point is assumed to be centered in the horizontal position. The difference of work functions $W_c - W_a = 2.3(1)$ V can be calculated by eqn. 3.39 with $U_{sc}(r = 0) = 0.76$ V (these values are used here to convert accelerating cathode potentials U_0 to their respective electron energy E_e in the interaction region).

4 Low-energy electron cooling studies of keV ion beams in the CSR

The observed dependence of $\Delta f/f$ on $\Delta E/E$ is found to be linear (fig. 4.12). The last shown point in the higher (right side) end of the $\Delta E/E_0$ -axis is given by $E_e = 45.22$, even though one might still suspect a Schottky peak in the spectra for $E_e = 45.39$ eV (see fig. A.1). However, the square root in eqn. 4.14 defines an upper limit $E_{e,max}$ for the equilibrium cooling point in the space charge model for a given reference energy E_0 . For $E_0 = 45.16$ eV this point is given by $E_{e,max} = 45.38$ eV. Furthermore it has to be noted that Schottky peaks have been observed on the spectrum analyzer also for lower energies than $E_e = 45.04$ eV, but the data of these spectra is lost due to a failure in the data saving process.

A fit of eqn. 4.14 with η as a free parameter (fixing the space charge parameters) yields a measurement of the slip factor η of the CSR. Within this space charge model, a value of $\eta = 0.792(15)$ is obtained (red line). A linear fit, neglecting the space charge term, yields $\eta = 0.740(14)$. Both values deviate somewhat from the slip factor $\eta = 0.680(1)$ measured in the 2015 CSR commissioning phase [13].

The space charge cooling point model is visualized in fig. 4.13. The velocity deviations Δv are calculated from the measured frequency shifts Δf via eqn. 2.30 with the measured slip factor $\eta = 0.792(15)$. Those are related to horizontal closed-orbit shifts Δx by the dispersion relation given by eqn. 4.10 with the theoretical dispersion of the CSR and define the position of the measured red points. The black line through the red data points hence represents the CSR dispersion line. It has to be noted that due to the almost identical measured value $\Delta f/f_0$ for both, $E_e = 45.04$ eV and $E_e = 45.06$ eV, their respective points on the dispersion line in fig. 4.13 are not distinguishable by eye. The parabolic velocity profiles of the electron beam for the various electron energies E_e can be calculated from eqn. 4.6 or eqn. 4.8 (colored curves). The electron beam dimension (vertical green dashed lines) is given by its magnetically expanded radius r_e (table 4.9).

With the visualization of the space charge cooling model, it can be (tried to) explain why the ion beam profile in the Schottky spectra is vanishing outside a certain frequency range. Not all of the measured points are located at the calculated intersection of the space charge parabola and the CSR dispersion line (the theoretical cooling point). However, a different, higher or smaller slip factor value would move the points along the dispersion line closer or further away, respectively, from the fixed reference point. Moreover, as already mentioned above and now demonstrated in fig. 4.13, for electron energies higher than $E_{e,max} = 45.38$ eV, the dispersion line has no intersection with the parabolic velocity profile, i.e. there is no defined equilibrium cooling point which explains well the vanishing of ion beam profiles in the higher end of the electron energy and corresponding revolution frequency range. The limit in the lower range has not been determined experimentally, but a prediction for a maximum frequency and momentum devi-

4.3 Longitudinal cooling of Schottky spectra

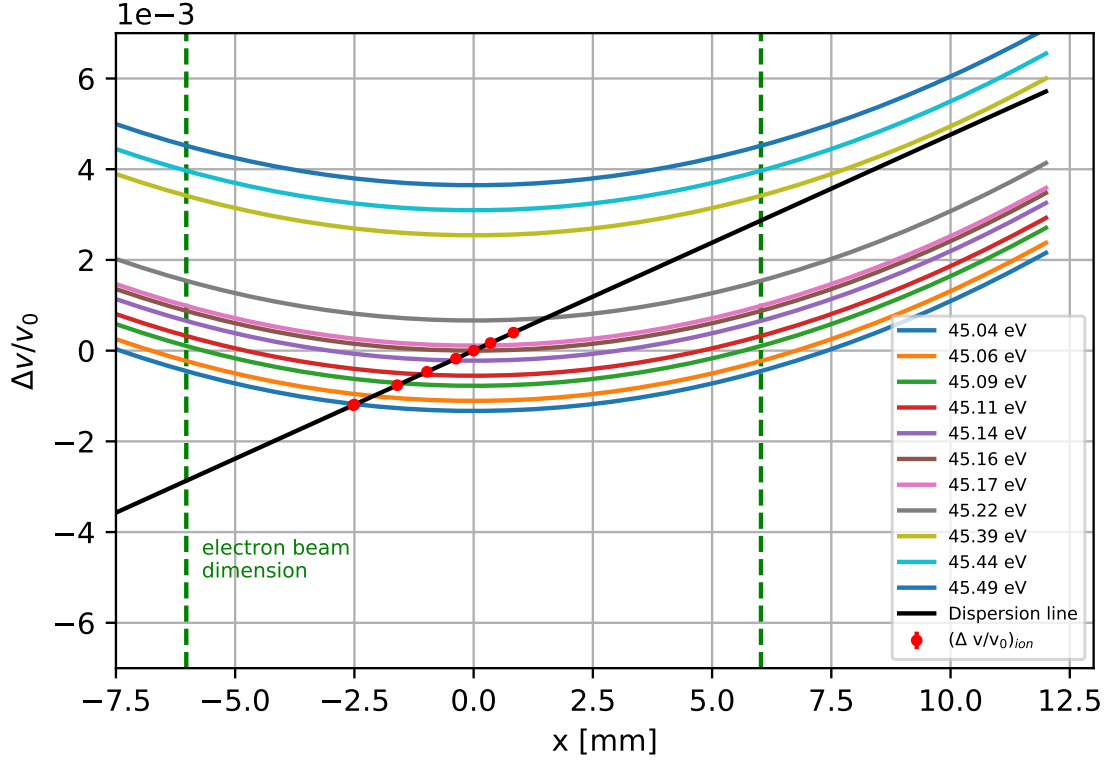


Figure 4.13: The relative velocity shifts of the closed orbit (red points) of 250 keV HD^+ are calculated from the measured relative frequency shifts and the measured slip factor (see fig. 4.12). The points at the lowest and highest x-position correspond to Schottky measurements at $E_e = 45.04$ eV and 45.22 eV, respectively.

ation can be made if it is assumed that a stable point of electron cooling is lost as soon as the ion beam is dragged to the edge of the electron beam dimension. For $\Delta x = r_e = 6.025$ mm, the dispersion relation yields $|\Delta v/v_0| = 2.87 \cdot 10^{-3}$ and with the measured slip factor this translates into $|\Delta f/f_0| = 5.05 \cdot 10^{-3}$. The corresponding electron energy which would drag the ion beam to the edge of the electron beam in the negative x-direction is calculated with eqn. 4.9 to $E_{e,min} = 44.63$ eV, indicating that even well below the last measured value of $E_e = 45.04$ eV, electron cooled ion beam profiles should be observable in the Schottky spectra.

4.4 Transverse electron cooling measurements of coasting ion beams

One of the main goals of the 2018 CSR beamtime campaign was to deliver a proof of low-energy transverse electron cooling of coasting keV ion beams, in addition to the longitudinal electron cooling of bunched ion beams that has already been realized in the commissioning phase of 2017. Therefore, transverse electron cooling experiments are carried out with the molecular ion beams 250 keV HeH⁺, 250 keV HD⁺ and atomic ion beam 250 keV O⁺.

After a brief introduction of the measurement procedure the shrinking of the ion beam emittance as an effect of electron cooling is demonstrated for each of the mentioned ions. The section further includes an analysis of the dependence of the transverse electron cooling rate on the electron beam density.

4.4.1 Measurement procedure

The experimental setup for measuring transverse ion beam profiles at the CSR by neutral fragment imaging is already discussed in sect. 3.6.4. The measured transverse beam profiles with this technique are given by 2D center of mass distributions and plotted in the form of colormaps (figs. 4.15, 4.17 & 4.19). The structure of the measurement cycles that are used in the electron cooling imaging experiments presented in this section are in general equal to those that are used for DR rate measurements. During DR rate measurements, the electron-ion collision energy is scanned by a detuning of the electron energy E_e as explained in sect. 3.5.2. During electron cooling, however, the velocities of the electron and ion beam are matched and the electron-ion collision energy at the corresponding cooling energy $E_e = E_{cool}$ of the electrons is zero ($E_d = 0$ eV). The measurement cycle structure is sketched in fig. 4.14. Each cycle starts with a certain time t_{cool} at which the energy E_e of the electrons is set to E_{cool} . A waiting time t_{wait} is implemented to take into account the time it takes to adjust the potential that defines the electron energy. The electron cooling and waiting time interval is then followed by a generally shorter measurement step at a detuned collision energy E_d realized by setting an electron energy $E_e = E_{ref}$. This measuring time at a detuned reference collision energy is used to obtain a background rate when performing DR resonance energy scans. The reference point is chosen at a collision energy where the expected DR rate coefficient is at its lowest value. The data measured at the reference point can then later be subtracted. In the DR resonance spectrum of HD⁺ for example, this is the case at $E_d \approx 1$ eV [66]. For the purpose of evaluating the measurement cycles with respect to electron cooling only, no such background subtraction is needed since one is only interested in the center of mass distribution

4.4 Transverse electron cooling measurements of coasting ion beams

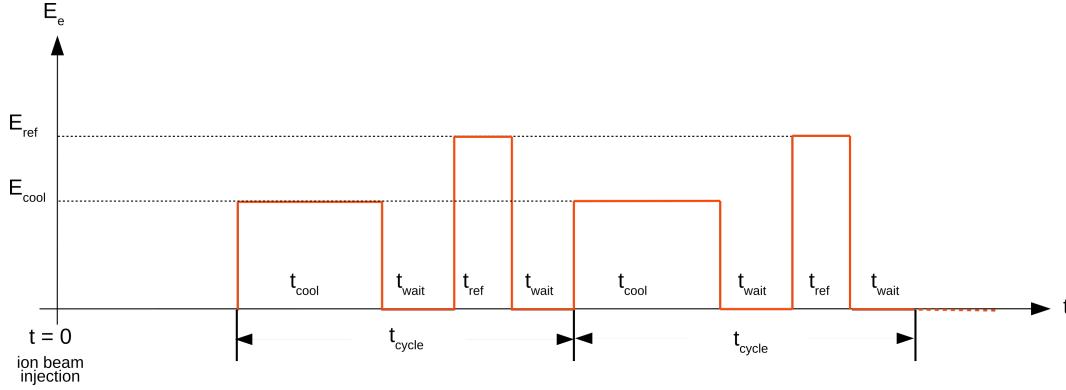


Figure 4.14: Scheme of a typical measurement cycle used during ion beam imaging experiments. Times are $t_{cool} = 0.1$ s, and further times according to the text.

of the neutral fragments at collision energy $E_d = 0$ eV. The presented profiles are thus exclusively obtained from events which are detected in the electron cooling steps t_{cool} of the cycle.

As it will be shown in the following presentation of the experimental results, the measured CM distributions mostly have an elliptical shape that in some cases also rotates around its center during electron cooling, which can likely be assigned to a perturbation of the stored ion beam by a coupling to the solenoid guiding field in the merged-beam section [67], but is still under investigation and not fully understood yet. In order to analyze the evolution of the beamprofile during electron cooling, the detected events during the measurement are binned into time sequences that are chosen to contain integer numbers of the measurement cycle time t_{cycle} . The beam-projections in these time sequences are fitted with 2D Gaussian profiles that take into account the rotating ellipse effect by adding an additional angle to the x- and y-axis as a further fit parameter:

$$f(x, y) = f_0 + A \exp\left(-\frac{\hat{x}^2}{2\sigma_a^2} - \frac{\hat{y}^2}{2\sigma_b^2}\right) \quad (4.15)$$

with

$$\hat{x} = (x - x_0) \cos \Phi + (y - y_0) \sin \Phi \quad (4.16)$$

$$\hat{y} = -(x - x_0) \sin \Phi + (y - y_0) \cos \Phi \quad (4.17)$$

where σ_a (σ_b) are the widths along the major (minor) axis of the ellipse. The angle ϕ describes the clockwise rotation of the major axis with respect to the x-axis.

In order to obtain electron cooling curves from the evolution of the beam profiles,

the fitted Gaussian widths of each projection are plotted against the mean time value of the time sequence in which the projection was measured.

4.4.2 Transverse electron cooling times

HeH⁺

The time evolution of the transverse projected beamprofile of a coasting beam of 250 keV HeH⁺ is displayed in fig. 4.15. Each colormap represents a recording time sequence of 420 ms, chosen to contain four times the measurement cycle defined for this run. The measurement cycle is started 3.15 seconds after injection and structured as follows:

- 100 ms electron cooling
- 5 ms waiting time

which is repeated 70 times per injection.

The experimental settings for electron cooling are summarized in table 4.10. The number of injected ions is about $2.2 \cdot 10^7$. The projected shape resembles the above mentioned rotated ellipse, with a relatively constant angle Φ during the electron cooling process (fig. 4.16 (c)). The widths $\sigma_{a,b}$ obtained from the 2D Gaussian fits of the ellipse profiles are shown in fig. 4.16 (a) and (b). Analogously to the bunched longitudinal case, the cooling curves are fitted with both, the IBS formula given by eqn. 2.137 and a simple exponential decay function (eqn. 4.3). The appropriateness of the fits to describe the measured data is again judged with the help of the residual plots shown in fig. 4.16 (c) and (d). In this case, the simple exponential function, neglecting any influence of the IBS process yields the more suitable result for the measured curve. Tentatively, this result can be explained by the limited validity of the simplified IBS model. In particular, $T_{\perp} > T_{\parallel}$ for the ions, hence, less effect from IBS on the transverse degrees of freedom is expected. Therefore, the transverse cooling curves in this section will be consistently evaluated by eqn. 4.3.

Table 4.10: Experimental settings for transverse electron cooling of HeH⁺.

E_{ion} [keV]	f_0 [kHz]	E_e [eV]	U_0 [V]	I_e [μ A]	α	n_e [10^5 cm^{-3}]	r_{cath} [mm]
250	88.261	27.32	-30.32	26.0	21.59	6.4	1.10

4.4 Transverse electron cooling measurements of coasting ion beams

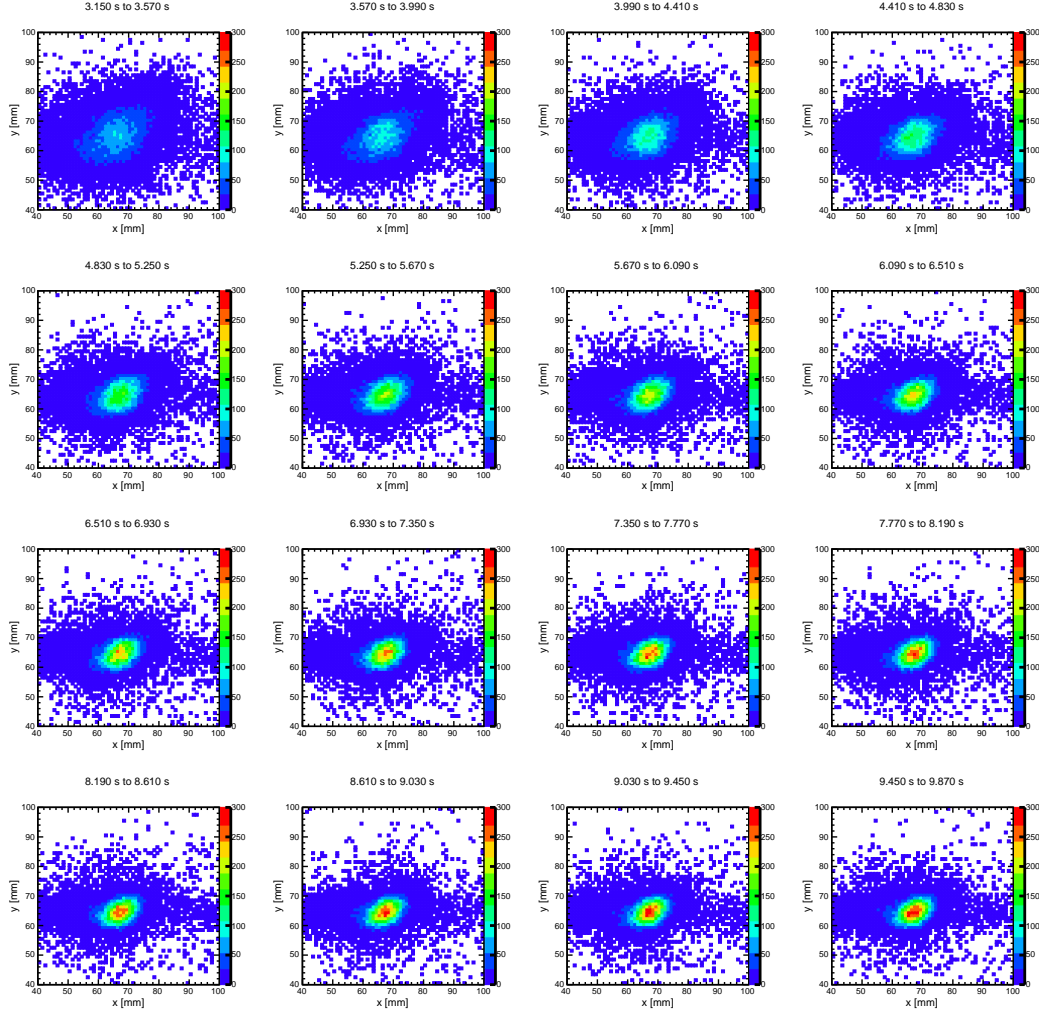
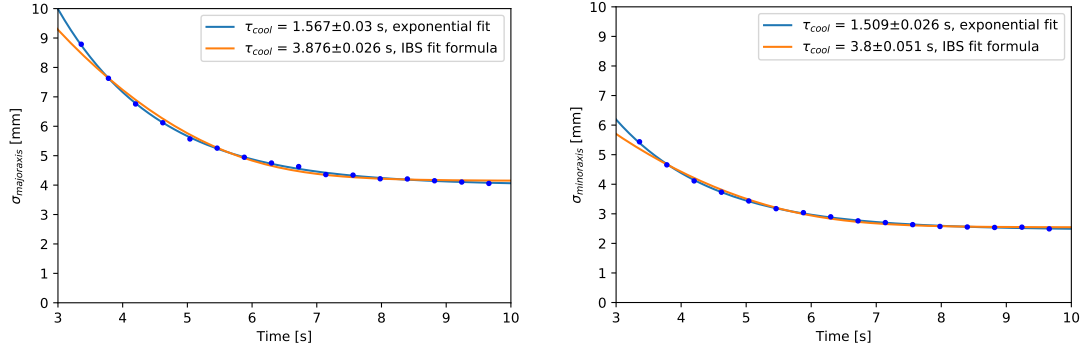


Figure 4.15: Time evolution of the center of mass distribution of co-incident double impact events on the imaging detector measured during electron cooling of 250 keV HeH^+ .

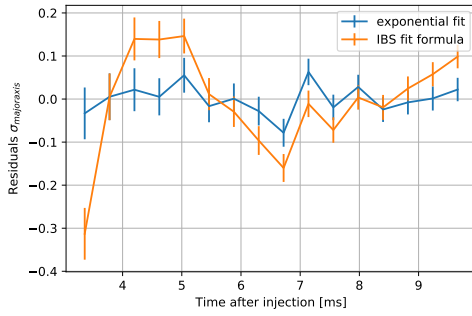
Electron cooling times of $\tau_{cool,a} = 1.567(30)$ s and $\tau_{cool,b} = 1.509(26)$ s can be assigned to the compression of the major and minor axis of the ellipse, respectively.

4 Low-energy electron cooling studies of keV ion beams in the CSR

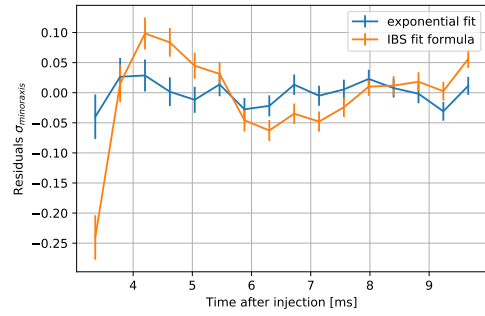


(a) Major axis of beam-projection ellipse.

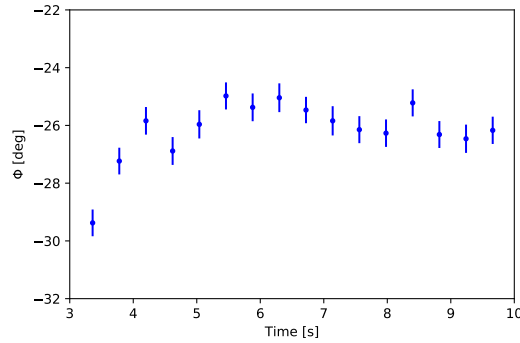
(b) Minor axis of beam-projection ellipse.



(c) Major axis fit residual plot.



(d) Minor axis fit residual plot.



(e) Ellipse rotation angle Φ .

Figure 4.16: Cooling curve evaluation of coasting 250 keV HeH⁺ and comparison of fit procedures (see text for details).

4.4 Transverse electron cooling measurements of coasting ion beams

HD⁺

The time evolution of the transverse projected beamprofile of a coasting 250 keV HD⁺ beam is shown in fig. 4.17. Each colormap represents a recording time sequence of 464 ms, which is again chosen to contain an integer number of the measurement cycle defined for this run. The measurement cycle is started 1.3 seconds after injection and structured as follows:

- 100 ms electron cooling
- 3 ms waiting time
- 10 ms measuring at detuned (collision) energy $E_d = 1$ eV
- 3 ms waiting time

which is repeated 100 times per injection.

The experimental electron cooling settings are summarized in table 4.11. The number of injected ions for this run is about $1 \cdot 10^7$. In the projected profiles, a strong electron cooling effect is already visible in the first ~ 2 seconds as the intensity distribution seems to peak towards the center of the beam. The projected shape is again clearly more a rotated ellipse rather than a circular profile. The electron cooling curve obtained by fitting the Gaussian widths of the ellipse axis with eqn. 4.15 is shown in fig. 4.18. Electron cooling times of $\tau_{cool,a} = 1.052(045)$ s and $\tau_{cool,b} = 0.97(02)$ s can be assigned to the compression of the major and minor axis of the ellipse, respectively.

Table 4.11: Experimental settings for transverse electron cooling of HD⁺.

E_{ion} [keV]	f_0 [kHz]	E_e [eV]	U_0 [V]	I_e [μ A]	α	n_e [10^5 cm ⁻³]	r_{cath} [mm]
250	113.583	45.71	-48.27	34.7	30	4.28	1.10

4 Low-energy electron cooling studies of keV ion beams in the CSR

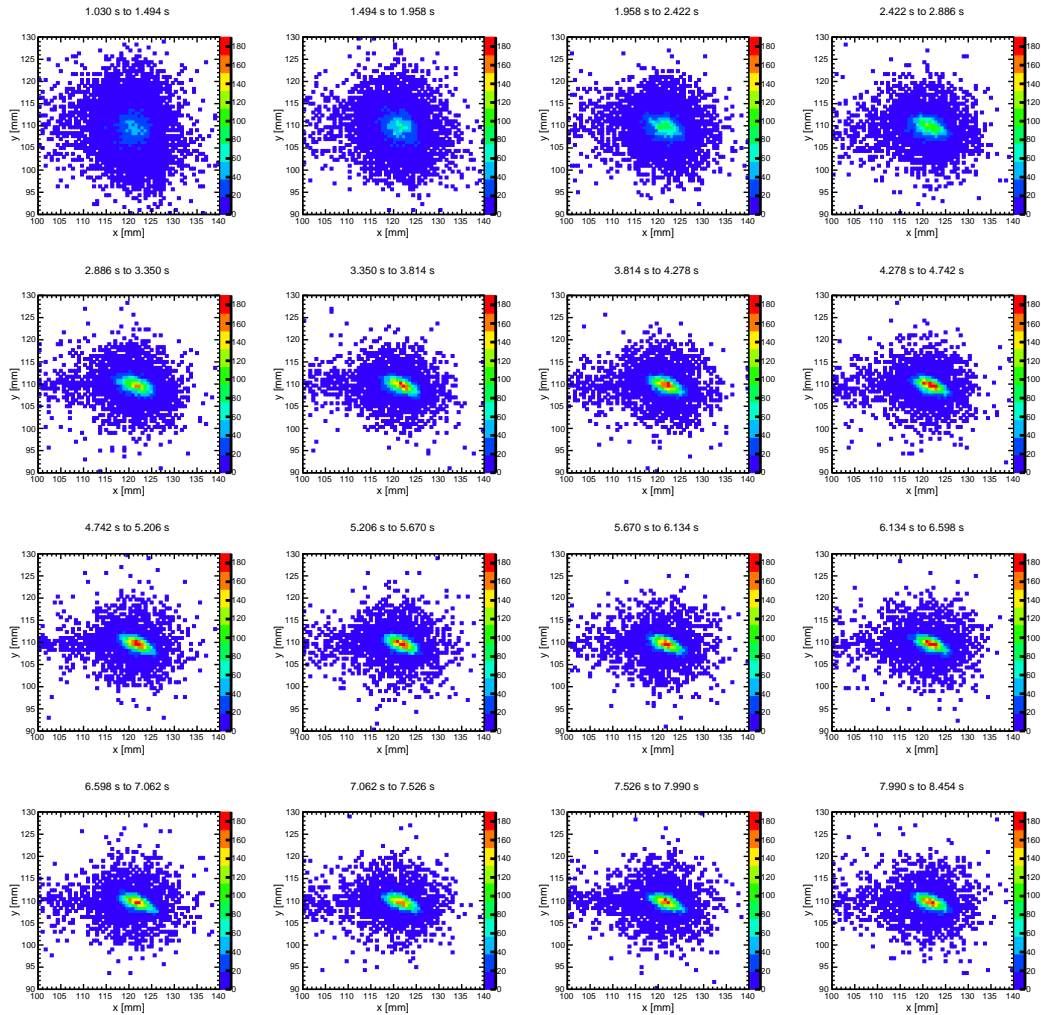
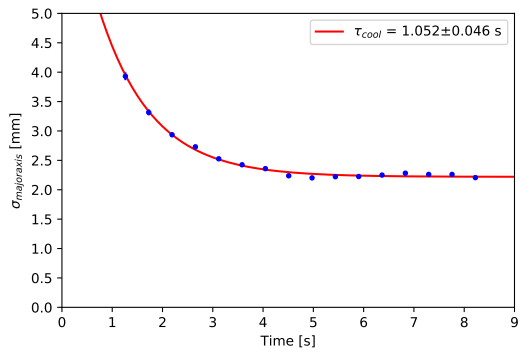
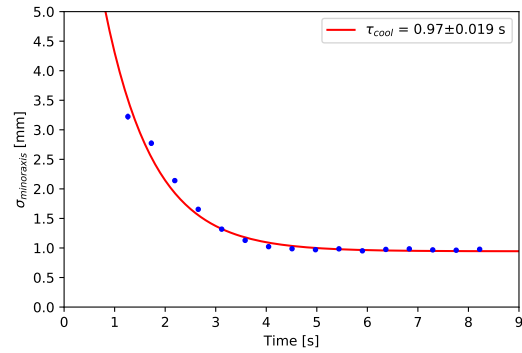


Figure 4.17: Time evolution of the center of mass distribution of co-incident double impact events on the imaging detector measured during electron cooling of 250 keV HD^+ .

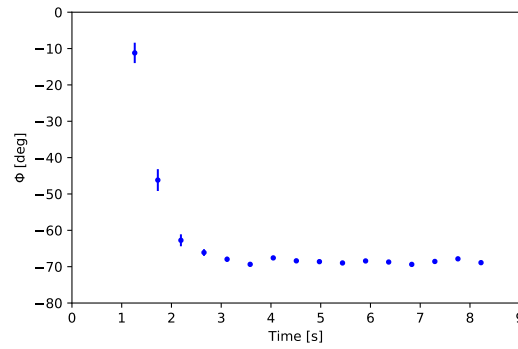
4.4 Transverse electron cooling measurements of coasting ion beams



(a) Major ellipse axis cooling curve.



(b) Minor ellipse axis cooling curve.



(c) Ellipse rotation angle Φ .

Figure 4.18: Electron cooling curve evaluation of coasting 250 keV HD⁺.

O⁺

In comparison to the above presented results for molecular ions HD⁺ and HeH⁺, the electron cooling investigation for the atomic ion O⁺ in the beam time campaign 2018 stands out regarding several points. It should be also noted here that these measurements are the result of what was rather planned to be a mere try if electron cooling can be observed at all within the very short experimental time that was left at the very end of the 2018 beamtime.

Since there is no DR process taking place as for the molecular ions, all single impacts of neutral fragments on the imaging detector from the recombination of O⁺ to O are directly assigned as a center of mass position. In addition, with $M_i = 16$ amu, O⁺ is much heavier than the molecular ions with masses ≤ 5 amu. As a consequence, a much lower electron energy of $E_e = 8.57$ eV is necessary to match the velocity of the 250 keV O⁺ ions. Therefore, for this measurement the *ultra-low energy electron deceleration scheme* as proposed and tested for the GaAs photocathode setup in the Ph.D. work of A. Shornikov [54] is used instead of the so far grounded drift tube operation. The electron deceleration scheme is implemented by setting a higher cathode potential of $U_0 = -33$ V. The electron energy needed for velocity matching is then realized by operating the drift tubes in the interaction region at the lower „cooling“ potential $U_{cool} = -12.18$ V with the Kepco power supply on top of the HV platform (compare fig. 3.8). In space charge limited electron gun operation (sect. 3.2.2), extracting electrons with a higher accelerating potential allows to extract electron beams with a higher density.

The time evolution of the transverse projected beamprofile of a coasting beam of 250 keV O⁺ is displayed in fig. 4.19. Each colormap represents a recording time sequence of 3.275 s. The measurement cycle is directly triggered upon ion beam injection and structured as follows:

- 100 ms electron cooling
- 3 ms waiting time
- 25 ms measuring at detuned (collision) energy $E_d = 1eV$
- 3 ms waiting time

Table 4.12: Experimental settings for transverse electron cooling of ¹⁶O⁺.

E_{ion} [keV]	f_0 [kHz]	E_e [eV]	U_0 [V]	U_{cool} [V]	I_e [μ A]	α	n_e [10^5 cm ⁻³]	r_{cath} [mm]
250	49.448	8.57	-33.0	-12.18	31.2	30	11.3	1.10

4.4 Transverse electron cooling measurements of coasting ion beams

which is repeated 1000 times per injection.

The experimental settings for electron cooling are summarized in table 4.12. The number of injected ions for this run is about $7.8 \cdot 10^7$. The widths $\sigma_{a,b}$ obtained from the 2D Gaussian fits of the ellipse profiles are shown in fig. 4.20. Electron cooling times of $\tau_{cool,a} = 10.96(26)$ s and $\tau_{cool,b} = 9.649(127)$ s can be assigned to the compression of the major and minor axis of the ellipse, respectively. The first two points in the cooling curve of the major axis are not taken into account for the cooling time determination. These points are not assigned to the exponential cooling process. It is possible that the beam overlap in these first few seconds of the measured curve is not perfect yet, but improves at later times due to the compression of the beam width.

4 Low-energy electron cooling studies of keV ion beams in the CSR

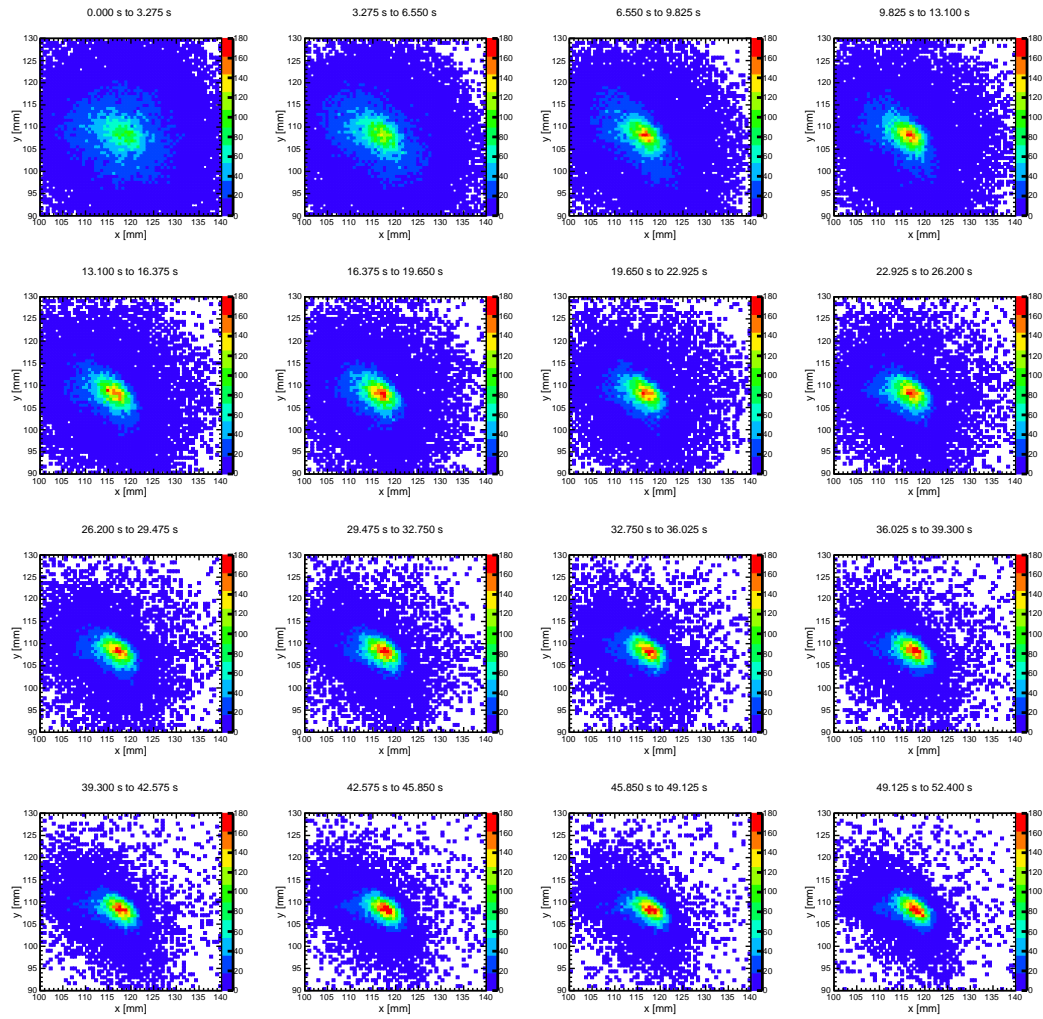
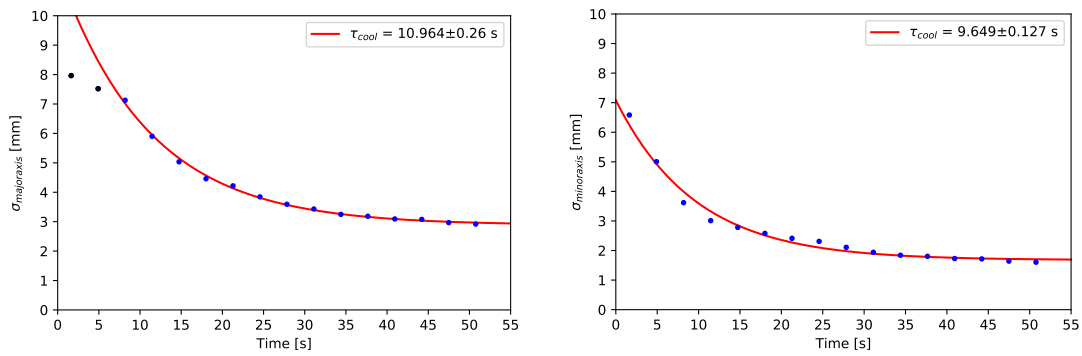


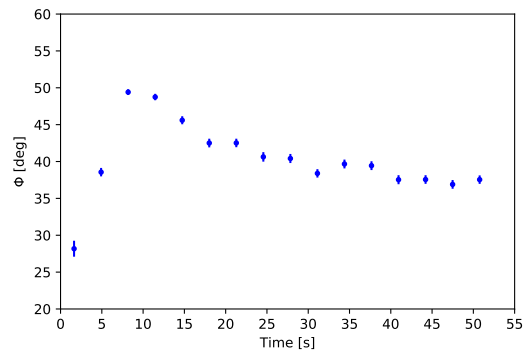
Figure 4.19: Time evolution of particle impacts on the imaging detector measured during electron cooling of 250 keV O^+ .

4.4 Transverse electron cooling measurements of coasting ion beams



(a) Major axis of beam-projection ellipse.

(b) Minor axis of beam-projection ellipse.



(c) Ellipse rotation angle Φ .

Figure 4.20: Electron cooling curve evaluation of coasting 250 keV O^+ .

4.4.3 Dependency of the transverse cooling rate on the electron beam density

In order to analyze the transverse electron cooling rate as a function of the electron beam density, the measurement cycle shown above for 250 keV HD⁺ is repeated for five different electron beam density settings. The experimental settings for this measurement series are summarized in table 4.13. In contrast to the measurements of the longitudinal cooling rate dependence (sect. 4.2.4), the magnetic expansion is set to $\alpha = 30$. The value of the longitudinal guiding field in the interaction region is kept at $B = 90$ Gauss. The measured transverse electron cooling rates $r_{\perp,a}$ and $r_{\perp,b}$ for the major and minor ellipse axis, respectively, obtained by a fit of eqn. 4.3 to the time evolution of the Gaussian beam widths, are given in table 4.13.

Table 4.13: Experimental parameters for electron cooling and measured transverse cooling rates $r_{\perp,a}$ and $r_{\perp,b}$ for 250 keV HD⁺ (n_e calculated with $r_{cath} = 1.10$ mm).

U_0 [V]	I_e [μ A]	n_e [10^5 cm ⁻³]	$T_{e\parallel}$ [μ eV]	$r_{\perp,a}$ [s ⁻¹]	$r_{\perp,b}$ [s ⁻¹]
48.27	34.7	4.74	80	0.858(46)	1.056(20)
48.20	25.0	3.41	73	1.000(29)	0.811(21)
48.03	15.0	2.05	64	0.885(133)	0.648(29)
47.97	10.0	1.36	57	0.488(29)	0.346(7)
47.93	5.0	0.68	48	0.232(23)	0.156(6)

4.4 Transverse electron cooling measurements of coasting ion beams

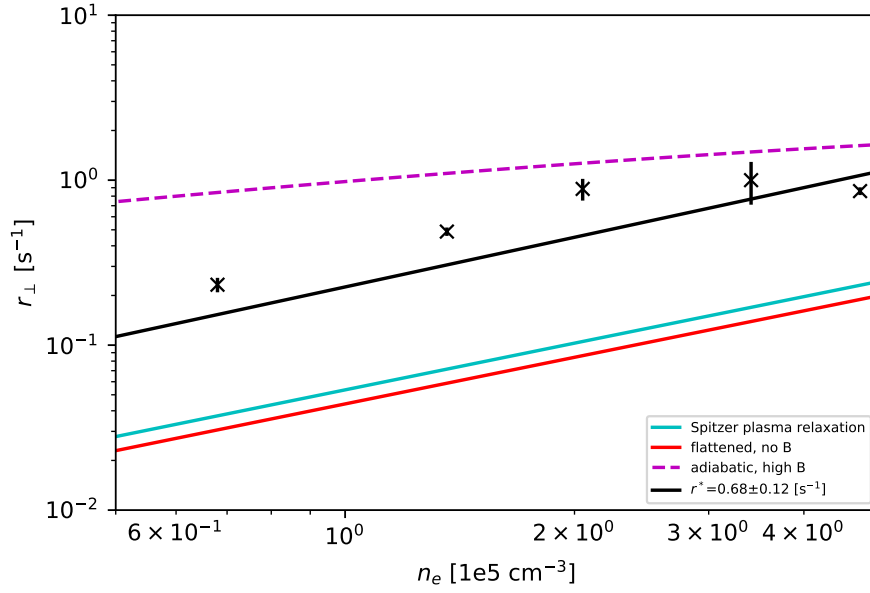


Figure 4.21: Transverse electron cooling rate $r_{\perp,a}$ of coasting 250 keV HD⁺, obtained from the exponential shrinking of the major axis of the beam-profile ellipse, as a function of the electron density n_e .

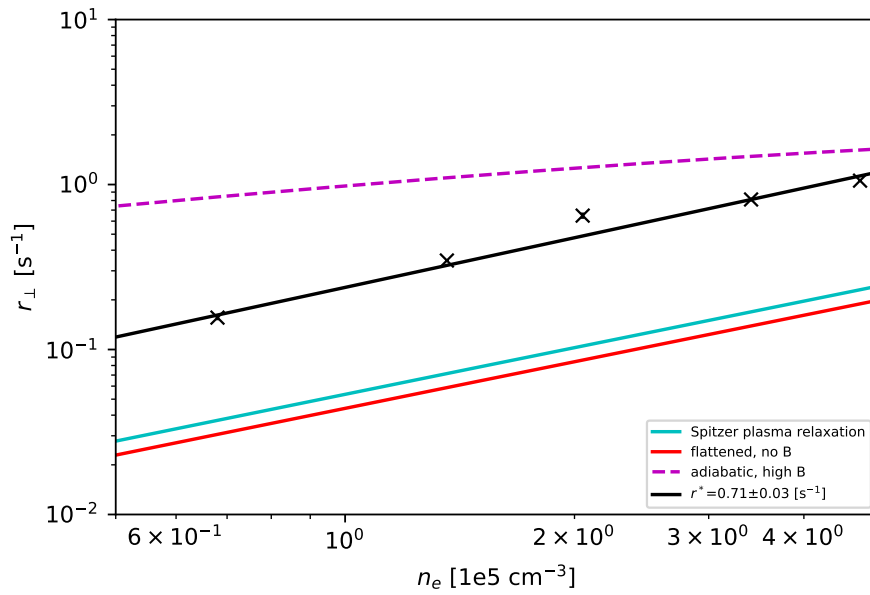


Figure 4.22: Transverse electron cooling rate $r_{\perp,b}$ of coasting 250 keV HD⁺, obtained from the exponential shrinking of the minor axis of the beam-profile ellipse, as a function of the electron density n_e .

Comparison to theory

Analogously to the investigation of the electron density dependence of the longitudinal electron cooling rate presented in sect.4.2.4, in figs. 4.21 & 4.22 the measured transverse cooling rates are compared to the calculated rates from the Spitzer plasma relaxation and the approximation formulae by Derbenev and Skrinsky (sect. 2.2.6).

For the transverse temperature $T_e = T_{\perp} = 2$ meV is assumed. As expected, the Spitzer formula (cyan line) underestimates the cooling rates r_{\perp} since neither magnetized collisions nor a longitudinal compression of the electron velocity distribution (the lower value of $T_{e\parallel}$) are considered. Multiplying the calculated Spitzer rates $r_{Spitzer}$ with a factor of $\sim 3-4$ brings them very close to the measured values.

Furthermore, the asymptotic approximation $r_{\perp, no\ field}$ of the transverse electron cooling friction force is calculated also in the case where magnetized collisions are neglected (red line, calculated by eqn. 2.112). While these values overestimated the measured rates in the longitudinal case by a factor of about 2, in the transverse case they are very close to the Spitzer rate. This is not surprising considering the fact that both the Spitzer approximation and the Derbenev and Skrinsky approximation formula eqn. 2.112 have the same scaling behaviour with the transverse electron velocity spread $\Delta_{e\perp}$.

In the case of the strong-field approximation² (purple dashed line in figs. 4.21 & 4.22) the measured rates are overestimated by roughly a factor $\sim 2-3$. However, as mentioned above in sect. 4.2.4, misalignment effects in the interaction region would increase the longitudinal electron beam temperature and thereby decrease the adiabatic electron cooling force and cooling rate values.

The calculated Coulomb logarithms and longitudinal cooling rates with experimental settings given in table 4.13 are summarized in table 4.14. A scaling of the measured data and the calculated theory line with the scaling parameter $\kappa = n_e[\text{cm}^{-3}]Z^2/A$, performed in the same way as for the longitudinal case in sect. 4.2.4, is carried out here as well. The results of fitting the individual lines and the measured points (black line) with the function $r_{\perp} = r_{\perp}^* \kappa$ yield r_{\perp}^* as given in table 4.15.

²Analogously to the longitudinal case for bunched HeH⁺ (sect. 4.2.4), the transverse temperature estimate $T_{\perp} = 0.31$ eV for HD⁺ as shown in appendix B.3 is used for the transverse ion velocity spread $\Delta_{i\perp} = \sqrt{2k_B T_{\perp}/M_i}$ in order to replace the dependence of the transverse ion velocity in eqn. 2.115 (see sect. 2.2.6).

4.4 Transverse electron cooling measurements of coasting ion beams

Table 4.14: Experimental parameters and measured transverse cooling rates $r_{\perp,a}$ and $r_{\perp,b}$ for 250 keV HD⁺. The Spitzer Coulomb logarithm L_C and cooling rate are calculated with an assumed isotropic temperature of $T_e = 2$ meV (see text for details).

n_e [10^5 cm^{-3}]	$L_C^{Spitzer}$	L_C	L_C^{ad}	$r_{\perp,a}$ [s^{-1}]	$r_{\perp,b}$ [s^{-1}]	$r_{Spitzer}$ [s^{-1}]	$r_{no \text{ field}}$ [s^{-1}]	$r_{strong \text{ field}}$ [s^{-1}]
4.74	7.66	7.55	1.69	0.858(46)	1.056(20)	0.230	0.189	1.620
3.41	7.82	7.71	1.72	1.000(29)	0.811(21)	0.169	0.139	1.482
2.05	8.08	7.97	1.77	0.885(133)	0.648(29)	0.105	0.063	1.267
1.36	8.28	8.17	1.81	0.488(29)	0.346(7)	0.072	0.059	1.100
0.68	8.62	8.51	1.91	0.232(23)	0.156(6)	0.037	0.031	0.842

Table 4.15: Fit of the scaled longitudinal cooling rate $r_{\perp,major}^* = r_{\perp,major}/\kappa$ to the measured points and theoretical curves calculated from the Spitzer plasma relaxation (eqn. 2.104), no B-field approximation (eqn. 2.111) and strong B-field approximation (eqn. 2.114), shown in fig. 4.21.

$r_{\perp,major}^*$	$r_{\perp,minor}^*$	$r_{Spitzer}^*$	$r_{\perp,no \text{ field}}^*$	$r_{\perp,strong \text{ field}}^*$
0.676(116)	0.714(30)	0.149	0.122	1.286

4.5 Investigation of Intrabeam-scattering at the CSR

To investigate the dynamics and effect of IBS on stored ions in the longitudinal dimension, a rf-bunched beam of HeH⁺ is stored at 250 keV and electron-cooled to an equilibrium bunch width of a few hundred nanoseconds. The time evolution of individual bunches is observed using the measurement technique as described in chapter 4.2.1 and the blow-up of the bunch width is followed for several seconds after turning off electron cooling. Furthermore, the blow-up of the transverse dimensions of an electron cooled beam when turning off electron cooling is investigated for a coasting 250 keV HD⁺ beam, using the neutral fragment imaging technique to observe the time evolution of the transverse beam profiles (sect. 3.6.4). The results of the IBS investigations of bunched HeH⁺ and coasting HD⁺ in the CSR are presented in this chapter.

4.5.1 IBS of bunched beams

The experimental settings used for cooling a bunched HeH⁺ beam down to an equilibrium bunch width are summarized in table 4.16 and are equal to those presented in longitudinal cooling time measurements discussed above in sect. 4.2.3.

Fig. 4.23 shows a representative ion beam injection, demonstrating the effect of IBS in the longitudinal density profile of the bunches which have been electron cooled to an equilibrium bunch length for a period of 7 seconds before turning off the electrons at 10 seconds after injection. The IBS blow-up of the bunch is followed in steps of 0.6 s until 15.6 s after injection. In fig. 4.24 an example evaluation of the time evolution of the bunch width is shown for the third bunch in fig. 4.23 for a storage time period from 9.0-15.6 seconds after injection. The blow-up is fitted with the function derived from the simple IBS model (eqn. 2.130).

The fit is performed in the way that the averaged beam width $\sigma_{0,b}$ before the blow-up and $\gamma = 6$ are fixed parameters while the other parameters are fitted within reasonable boundary conditions. The IBS heating term, defined by eqn. 2.130, that is obtained by this procedure for this bunch is

Table 4.16: Experimental settings for longitudinal IBS experiments with an equilibrium cooled bunched HeH⁺ beam.

E_{ion} [keV]	f_0 [kHz]	h	E_e [eV]	U_0 [V]	I_e [μ A]	α	n_e	r_{cath}
[keV]	[kHz]		[eV]	[V]	[μ A]		[10^5 cm^{-3}]	[mm]
250	88.261	4	27.32	-30.32	26.7	21.59	6.55	1.10

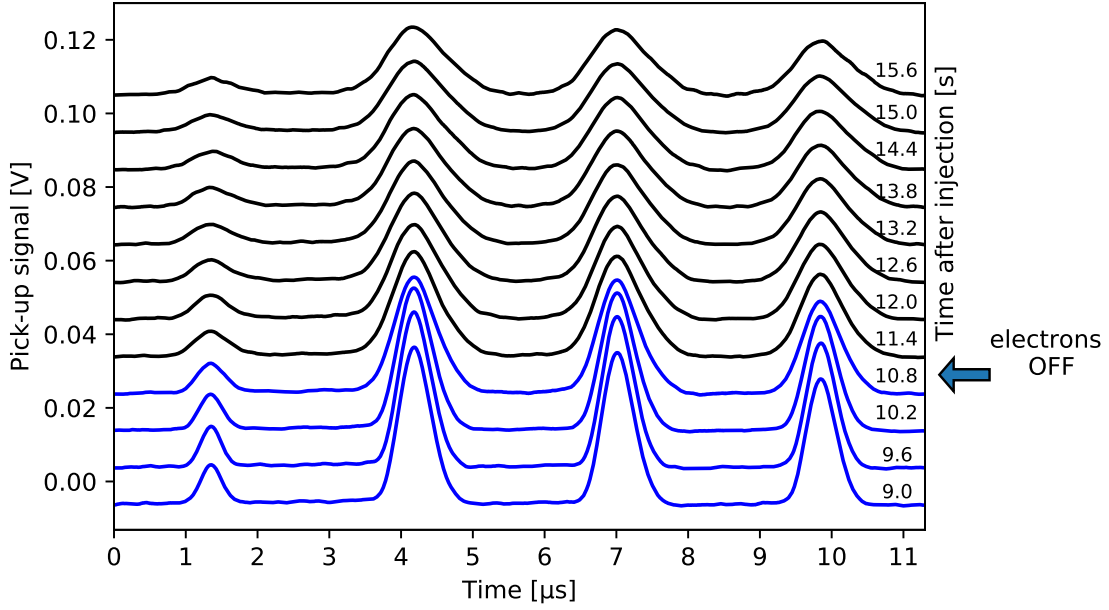


Figure 4.23: Bunch profile time evolution during IBS blow-up measured with the Schottky pick-up electrode.

$$\tilde{D}_b = 13.08(16) \cdot 10^{13} \text{ ns}^\gamma/\text{s}.$$

The blow-up is evaluated for 9 injections of bunched HeH^+ , yielding a total number of 36 bunches with different ion numbers N_b . Storage times up to 22 seconds after injection are analyzed. The results of evaluating the bunches with ion numbers in the range of $N_b \sim 0.1\text{-}1.2 \cdot 10^6$ for the IBS heating term is shown in fig. 4.25. As expected from eqn. 2.130, the heating term is a linear function of the bunch ion number N_b . A linear fit through the origin yields

$$\tilde{D}_b(N_b) = 10.9(2) \cdot 10^7 \cdot N_b \text{ [ns}^\gamma/\text{s]} \quad (4.18)$$

where $\gamma = 6$.

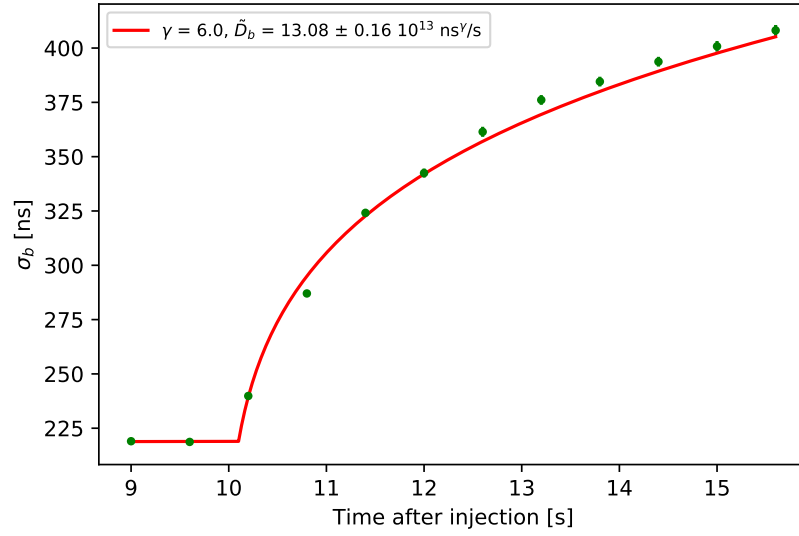


Figure 4.24: Time evolution of bunch width σ_b of the third bunch (from left) shown in fig. 4.23 (current pick-up measurement). The number of ions in this bunch is $N_b = 1.03(4) \cdot 10^6$. The red line is a fit of the simplified IBS model described by eqn. 2.130.

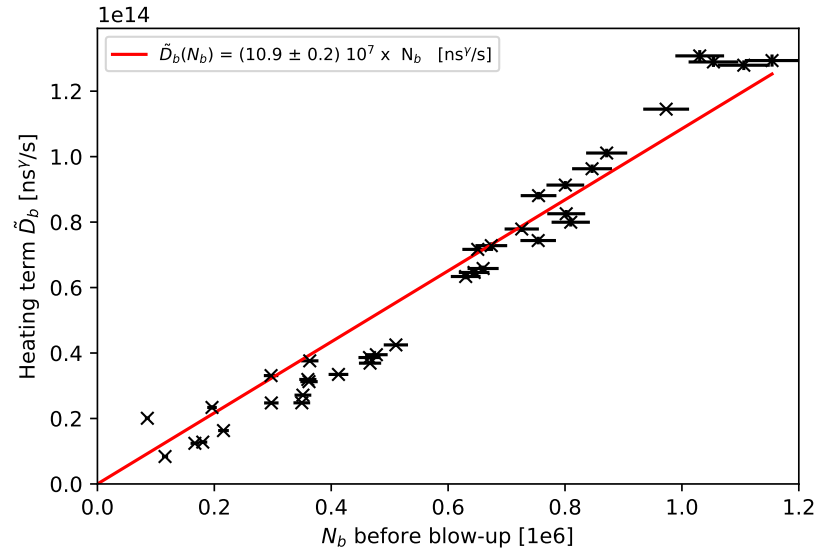


Figure 4.25: The IBS heating term \tilde{D}_b is measured for $\gamma = 6$ in a series of bunch blow-up measurements for 250 keV HeH⁺. The red line is a linear fit through the origin, according to the predicted linear proportionality of the heating term with the bunch ion number (see eqn. 2.130).

4.5.2 IBS of coasting beams

The investigation of IBS effects in the transverse beam dimensions was not a dedicated goal of the 2018 HD⁺ beamtime at the CSR. However, there is a dataset of in total three beam injections available where it is possible to observe the beam profile evolution of a beforehand equilibrium cooled coasting HD⁺ beam when the electrons are turned off. Out of these three injections, only two show a very similar countrate on the detector with a relative ion number difference below 10%. Thus only these two injections with comparable conditions are merged and analyzed for the evolution of the transverse beam profiles. Even though statistics are rather low for this measurement, it is possible to follow the blow-up of the two axis of the ellipse-shaped projected beam-profile (fig. 4.26).

For this measurement, electron cooling is applied for a period of 10.3 s with the settings summarized in table 4.17. The injected ion current is $I_{ion} \approx 149$ nA. Upon turning off the electrons, the IBS induced blow-up of the transverse Gaussian profile widths is observed for about 50 seconds. The measurement is compared with the simple IBS model (sect. 2.4.1), as shown above for the bunched beam case.

However, here it has to be considered for these longer storage time runs that the assumption of the simplified approach of a constant number of ions during the IBS blow-up does not hold anymore. Therefore, the ion number N_b in eqn. 2.126 will be replaced by:

$$N(t) = N_0 \exp\left(-\frac{t-t_0}{\tau}\right) \quad (4.19)$$

where t_0 is the time when the electrons are turned off. The solution of eqn. 2.130 is then given by:

$$\sigma_{a,b}(t) = \left[N_0 \hat{D}_{a,b} \tau \gamma \left(1 - \exp\left(-\frac{t-t_0}{\tau}\right) \right) + \sigma_{a0,b0}^\gamma \right]^{\frac{1}{\gamma}} \quad (4.20)$$

with

$$\tilde{D}_{a,b} = N_0 \hat{D}_{a,b} \quad (4.21)$$

Table 4.17: Experimental settings for transverse IBS experiments with an equilibrium cooled coasting HD⁺ beam.

E_{ion} [keV]	f_0 [kHz]	E_e [eV]	U_0 [V]	I_e [μ A]	α	n_e [10^5 cm ⁻³]	r_{cath} [mm]
250	113.583	45.71	-48.27	33.4	30	4.56	1.10

4 Low-energy electron cooling studies of keV ion beams in the CSR

which introduces the ion beam lifetime τ as a further parameter in the model and a (b) denote the index for the major (minor) beam profile ellipse axis.

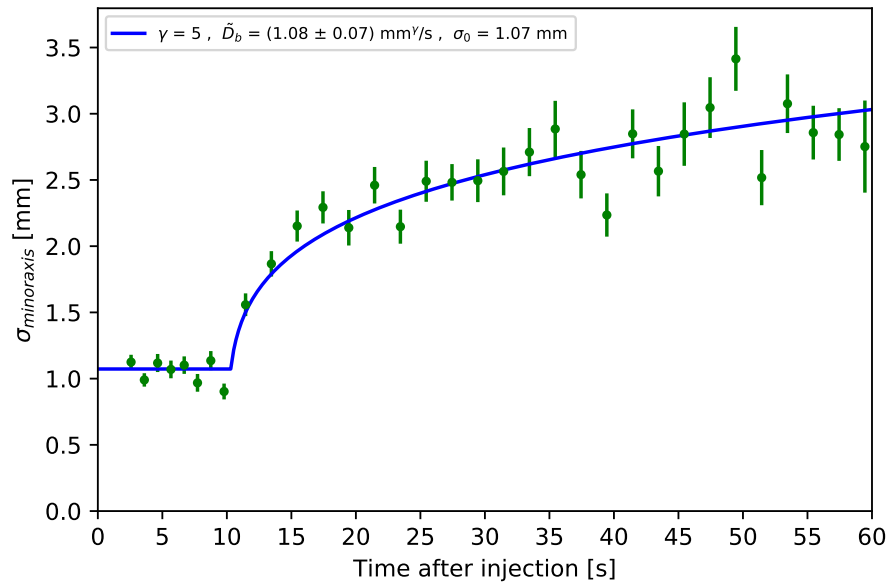
From the countrate on the imaging detector as a function of storage time shown in fig. 4.27, one can clearly observe a rather strong decay of the signal. At $t \approx 60$ s, the decay of the countrate seems to become even stronger. One thus regards both time regions, smaller and greater than 60 seconds, seperately and assigns two different decay time constants from exponential fits. The origin of the faster decay starting at $t \approx 60$ s might be explained by the fact that the ion beam has blown up to the point where the acceptance limit is reached and ions are lost by wall collisions. Since the blow-up here is only observed for times ≤ 60 s, the decay constant $\tau = 465$ s is used for the analysis of the data by fitting of eqn. 4.20. With $\tau = 465$ s, $t_0 = 10.3$ s and the theoretically expected value $\gamma = 5$, one obtains the blue fit curves shown in fig. 4.26 (a) for the minor ellipse axis and fig. 4.26 (b) for the major ellipse axis, respectively. The result for the minor axis $\hat{D}_b N_0 = 1.08(7)$ mm⁵/s is significantly smaller than the major axis value $\hat{D}_a N_0 = 57(4)$ mm⁵/s. The injected current of ≈ 149 nA gives an ion number of $N_0 \approx 8.2 \cdot 10^6$. This yields the measured IBS heating rates

$$\frac{1}{\sigma_{a,b}} \left. \frac{d\sigma_{a,b}}{dt} \right|_{IBS} = \frac{N_0 \hat{D}_{a,b}}{\sigma_{a,b}^5} \quad (4.22)$$

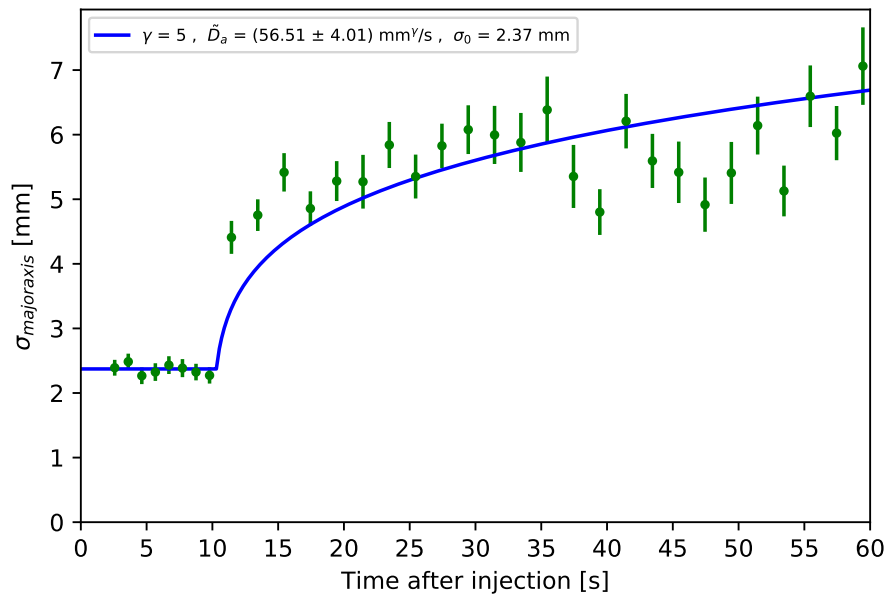
with $\hat{D}_a = 6.70(5) \cdot 10^{-6}$ mm⁵/s for the major axis and $\hat{D}_b = 1.32(9) \cdot 10^{-7}$ mm⁵/s for the minor axis.

Analyzing the ratio of the widths of the major and minor axis of the projected beamprofile during the blow-up yields another test of the simple IBS model. It assumes a constant ratio of these two values during the IBS induced blow-up, which is roughly confirmed by the measurement in fig. 4.28. However, in the end, this low-statistics measurement of the transverse IBS effect, obtained by averaging only two injections, can only serve as a rough check of the simplified IBS model.

4.5 Investigation of Intrabeam-scattering at the CSR



(a) IBS blow-up of the minor ellipse axis.



(b) IBS blow-up of the major ellipse axis.

Figure 4.26: IBS blow-up of an ellipse shaped projected beamprofile of a coasting 250 keV HD^+ beam measured with the imaging detector. Electron cooling is turned off at $t_0 = 10.3$ s.

4 Low-energy electron cooling studies of keV ion beams in the CSR

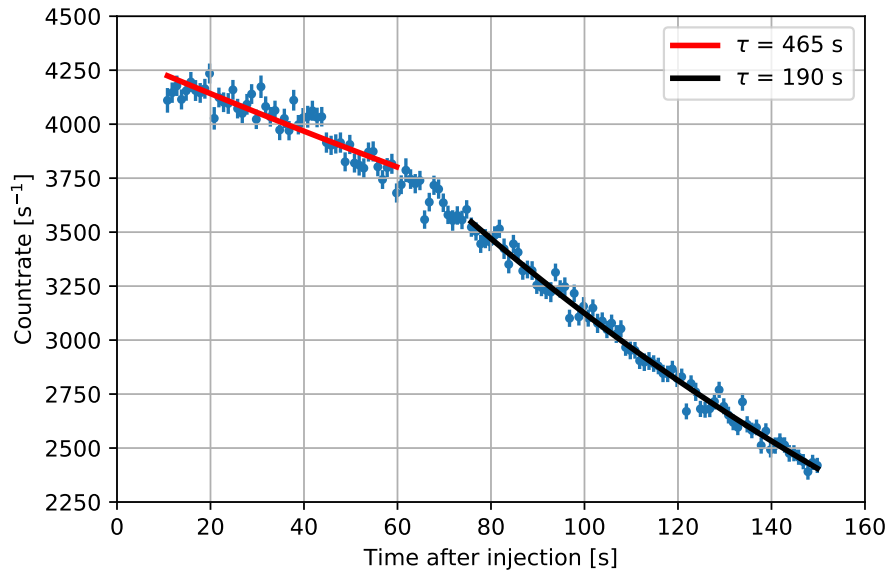


Figure 4.27: Countrate measured on the imaging detector induced by the stored 250 keV HD⁺ beam.

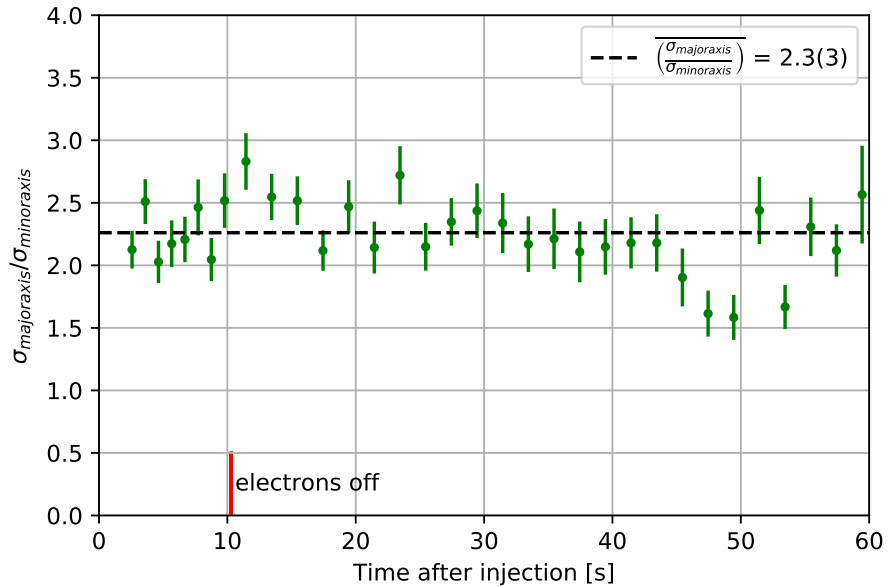


Figure 4.28: Ratio of the Gaussian width σ of the major axis of the ellipse shaped projected beamprofile to the minor axis during the IBS induced blow-up. The simple IBS model assumes a constant ratio.

4.6 Equilibrium cooled beam

In chapt. 2 two effects are introduced that become important for ion beams that are electron cooled to an equilibrium situation. Diffusional heating, for example from multiple scattering processes like IBS (sect. 2.4), is a process that is always present in stored ion beams and is countered by electron cooling.

Furthermore, in rf-bunched ion beams the space charge effects of the particles in the bunch can create a lower, stable limit of the bunch length during electron cooling. Both aspects shall be investigated at the example of experimental results in this section.

4.6.1 Space charge limit of electron cooled ion bunches

In sect. 2.3.2 it is shown that the electron cooling friction force can not compress the length (bunch width) of an ion bunch below a certain limit that is defined by the space charge potential in the bunch and the rf-bunching potential. In this space charge limit, the longitudinal density profile is described by a parabolic function (eqn. 2.123). In the following, the measured longitudinal bunch profiles of F^{6+} and HeH^+ are investigated for this limit in the electron cooled equilibrium.

F^{6+}

The effect of electron cooling on the bunch shape is already shown above in fig. 4.6 where the compression of the bunch width is analyzed and the bunches are fitted with Gaussian profile fits (fig. 4.5). About 7 s after electron cooling is turned on, an equilibrium situation is assumed for the measured bunch lengths. Fig. 4.29 shows a comparison of the equilibrium bunch for F^{6+} , fitted with a Gaussian profile and the parabolic profile.

It is possible to compare the measured bunch length in the assumed equilibrium at $t = 10.5$ s to a calculation of the space charge limited bunch length defined by eqn. 2.125. The number of ions in the bunch can be obtained from the fitted bunch area as shown in sect. 4.2.5. For the calculation of the space charge limit, the bunch ion number N_b obtained from a Gaussian profile fit is used. With the CSR circumference $C_0 = 35.12$ m, $h = 2$, rf-amplitude $\hat{U}_{rf} = 3.25$ V ($U_{eff} = 0.395$ V) and the CSR beamline radius $R = 0.05$ m, one obtains $w = 235(2)$ ns, corresponding to a full width half maximum of $FWHM = w/\sqrt{2} = 167(3)$ ns. The width σ_b^* for Gaussian profile with equal half width is given by

$$\sigma_b^* = \frac{w_{theo}}{2\sqrt{\ln 2}} \quad (4.23)$$

and yields a calculated value of $\sigma_b^* = 142(2)$ ns. The experimental values are

Table 4.18: Comparison of measured F^{6+} electron cooled bunch widths w and σ_b obtained by parabolic and Gaussian profile fits, respectively, to the calculated bunch widths w and σ^* in the space charge limit.

N_b (Gauss peak)	N_b (parabola)	w	w_{theo}	σ_b	σ_b^*
[1e6]	[1e6]	[ns]	[ns]	[ns]	[ns]
0.038(2)	0.034(1)	539(3)	235(2)	276(3)	142(2)

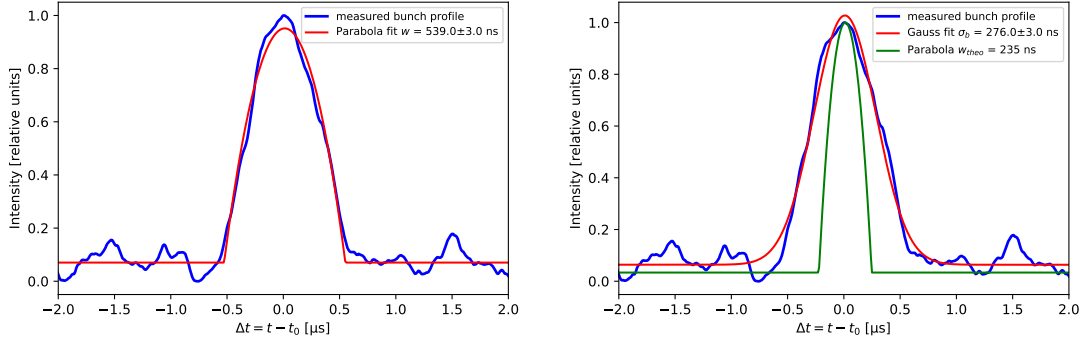
compared with these theoretical space charge limits in table 4.18. The calculated bunch width w_{theo} and the measured parabolic bunch width w differ by almost a factor of two. This relative difference between measurement and theoretical limit is only slightly smaller in the case a Gaussian profile is assumed, suggesting the assumption that electron cooling in this setting does not bring the bunch shape close to its space charge limit yet.

It also has to be mentioned that for the calculation of the space charge limit with eqn. 2.125 the ion beam radius r , averaged by two times the standard deviation $r = 2\sigma_r = 2 \cdot 2.36$ mm of the beam profile, is assumed to be within ~ 6 mm as a result of the ion beam imaging experiments presented in sect. 4.4.2 (see table 4.20). Since the imaging detector was not available yet during the 2017 F^{6+} measurements and no ion beam profile measurements are available for F^{6+} , this value is used as a reasonable approximation.

HeH⁺

The electron cooled equilibrium bunch length is further analyzed for 250 keV HeH⁺ at the example of the bunch cooling measurement shown above in fig. 4.7. The expected Gaussian bunch widths σ_b^* in the space charge limit are calculated with the same ion beam size as shown above for F^{6+} , but a slightly different rf-voltage amplitude of $\hat{U}_{rf} = 3.05$ V ($U_{eff} = 0.74$ V).

The measured bunch profiles in the electron cooled equilibrium are shown in fig. 4.30. The baseline is subtracted as described in sect. 4.2.1. In this case, a Gaussian profile always is more suitable for the description of the bunches than a parabola profile. The fitted Gaussian bunch widths σ_b are compared to the theoretical space charge limited Gaussian bunch widths σ_b^* (eqn. 4.23) in table 4.19. The theoretical bunch width space charge limit is in the bunches with higher ion numbers closely approached. If the calculated values are trusted, the reason why no indications of a parabola profile are observed yet must lie somewhere else. The greatest uncertainty should be in the determination of the correct transverse



(a) F^{6+} ion bunch in the electron cooled equilibrium (compare fig. 4.6). (b) F^{6+} ion bunch in the electron cooled equilibrium (compare fig. 4.6).

Figure 4.29: Evolution of longitudinal density profiles of a bunched F^{6+} ion beam and comparison of fits with a parabola profile (a) and a Gaussian profile (b). Electron cooling is applied 3 s after injection with settings given in table 4.1. The time on the x-axis is given with respect to the reference time t_0 defined by the synchronous particle in the center of the bunches.

ion beam size. Here, one relies on a single measurement of a coasting HeH^+ beam (see table 4.20). Small changes of less than 1 mm already have a strong effect in the calculation of the theoretical space charge limit. A discussion for both cases, F^{6+} and HeH^+ follows below.

Discussion

Even though it seems like the electron cooled bunch profile for F^{6+} in the equilibrium adopts the predicted parabolic shape in the space charge limit, the calculation shows that the limit is not even reached closely. This raises the question if the

Table 4.19: Comparison of measured HeH^+ electron cooled bunch widths σ_b obtained by Gaussian profile fits, to the calculated bunch widths σ_b^* in the space charge limit.

Bunch	N_b [1e6]	σ_b [ns]	σ_b^* [ns]	$\frac{\sigma_b}{\sigma_b^*}$
1	0.12(1)	143(3)	89(2)	1.61
2	0.85(3)	194(1)	172(2)	1.13
3	0.65(3)	174(1)	159(2)	1.10
4	0.64(3)	179(1)	156(2)	1.15

4 Low-energy electron cooling studies of keV ion beams in the CSR

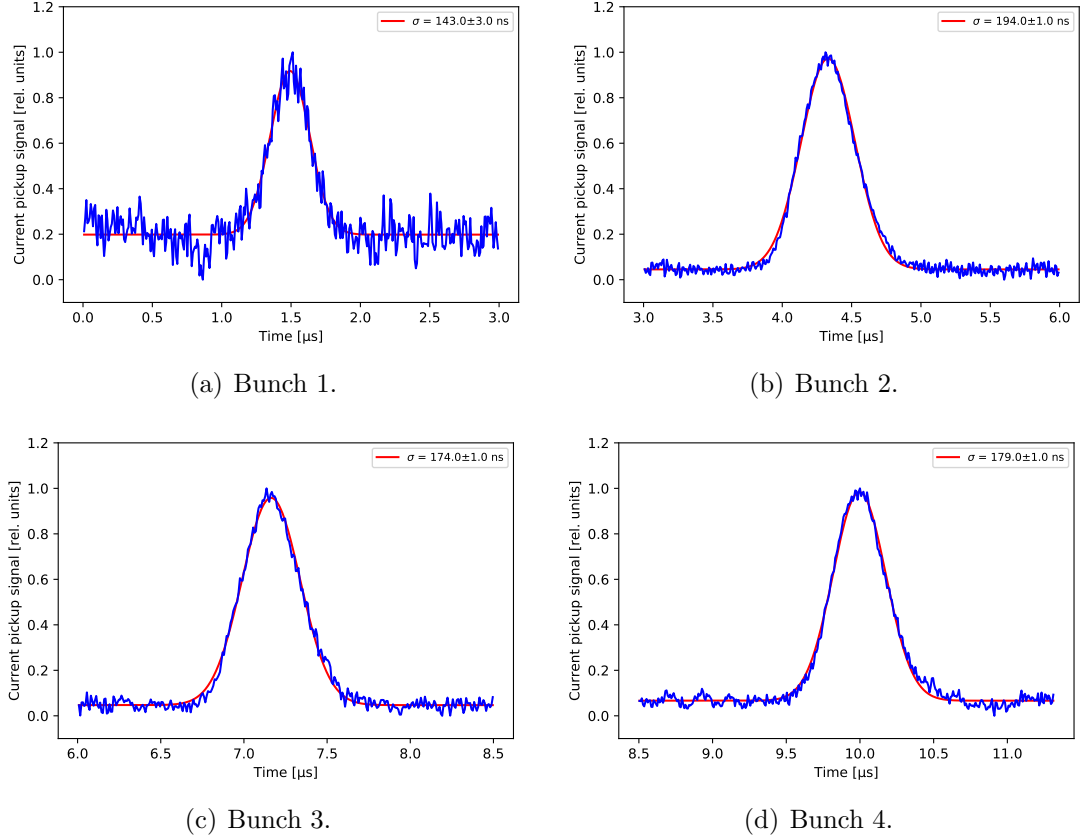


Figure 4.30: Longitudinal bunch profiles of 250 keV HeH^+ measured with the current pick-up (baseline subtracted). The shown ion bunch profiles correspond to fig. 4.7, measured at $t = 5300$ ms after injection, when the bunch length approaches an equilibrium due to electron cooling.

minimum bunch length is in fact determined by other processes, e.g. intrabeam-scattering, rather than the space charge effect. For a further investigation in this direction, the electron cooled equilibrium bunch width will be analyzed for its scaling behaviour with the ion number in sect. 4.6.2.

Surprisingly, in the case of HeH^+ the calculated space charge limited bunch widths are very close to the measured widths. However, the bunches do not seem to have parabolic profiles. On the other hand, the description of the bunch shape in the space charge limit as a parabolic profile completely neglects any internal motion of the ions.

At this point it is also worth mentioning that a diffusive broadening of the ion beam momentum distribution in the CSR has been observed in Schottky-power measurements [13]. There, this diffusion is brought into connection with a ripple on

the electrostatic deflector and quadrupole elements of the CSR. It is not excluded that this kind of diffusion is present in all of the presented experiments.

4.6.2 Equilibrium of electron cooling and IBS

For the investigation of the ion beam blow-up of a bunched beam due to IBS in the absence of electron cooling as shown above in sect. 4.5, the bunches have always been cooled down to their equilibrium bunch length first. The electron cooled equilibrium beam widths $\sigma_{\infty,b}$ of these bunches are now used to analyze the scaling behaviour with the ion number N_b in the bunch, extracted from the usual Gaussian profile fits. The results are plotted in fig. 4.31. A power law fit yields

$$\sigma_{b,\infty} \propto N_b^{1/4.117(11)} \quad (4.24)$$

The exponent can be compared to the predictions of the space charge limit model (sect. 2.3.2) and the IBS model (sect. 2.5). In case of a space charge dominated minimum bunch width, the bunch width can be described by the parabolic profile eqn. 2.125 and one expects a scaling of $\sigma_{b,\infty} \propto N_b^{1/3}$.

Eqn. 2.141 describes the scaling behaviour of $\sigma_{b,\infty}$ with the ion number in the case of an equilibrium between electron cooling and IBS. In this case, the expected proportionality is $\sigma_b \propto N_b^{1/\gamma}$ where $\gamma = 6$ for bunched beams. The difference to the space charge limit, which is simply derived from a balance of the rf-potential and the space charge potential of the ion beam, is that the electron beam properties (cooling rate) in the IBS dominated limit enter in the equilibrium bunch width. The equilibrium bunch widths with respect to IBS should therefore only be investigated when they are cooled by the same electron cooling settings.

The measured result does not allow a clear answer on whether it is the space charge effect or the IBS that dominates the equilibrium bunch length. The fact that the measured HeH⁺ bunches in the equilibrium theoretically should be very close to the space charge limit as shown above, but no parabola profile is observed, contributes to the uncertainty in this question. However, the fact that the exponent in the result from fig. 4.31 is significantly smaller than expected in case of the space charge effect suggests that intrabeam-scattering at least to some degree influences the result.

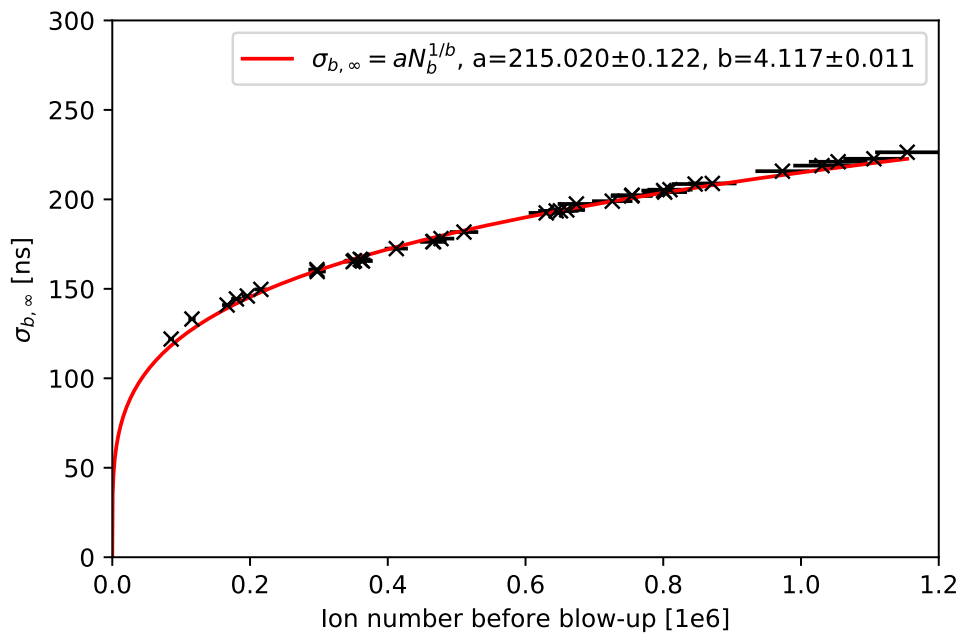


Figure 4.31: The electron cooled equilibrium bunch width $\sigma_{b, \infty}$ is fitted with a power law $\sigma_{b, \infty} = a N_b^{1/b}$. See table 4.16 for experimental parameters.

4.7 Summary of electron cooling performance

A summary of the evaluated transverse electron cooling measurements is shown in table 4.20. The measured rates are compared to cooling times $\tau_{Spitzer}$ calculated by the Spitzer plasma relaxation (eqn. 2.109). In most cases, the measured cooling times are faster by a factor of about 5 compared to the Spitzer estimates.

The fact that the measured ion beam profiles in the imaging detector plane (x, y) are represented by rotated ellipses rather than circular profiles makes it difficult to identify correct values for the real profile widths $\sigma_{x,y}$ in the interaction region, calculated by eqn. 3.44. The betatron functions in the center of the CSR electron-ion interaction region are $\beta_x = 13.009$ m and $\beta_y = 1.4095$ m [13]. From these values, one expects a much stronger divergence in the vertical than in the horizontal direction. Thus the broader, major axis of the beam-projection ellipse is assumed to originate from the width of the vertical coordinate y in the interaction region whereas the minor axis is assigned to x . The equilibrium beam widths $\sigma_{x,\infty}$ and $\sigma_{y,\infty}$ and the electron cooling time constants in the horizontal and vertical direction lie mostly close to each other, which can be interpreted as a sign of good alignment of the electron and ion beam in the electron-ion interaction region. The strongest difference can be seen for HeH⁺ where the equilibrium beam widths for the two directions are about 1 mm apart. Furthermore, electron cooled beam widths lower than ~ 0.9 mm and cooling times faster than ~ 1 s could be reached for HD⁺, marking the best values reached at the CSR so far.

The measured transverse and longitudinal rates, together with results obtained in earlier electron cooling studies with the TSR electron cooler as well as the TSR electron target, are shown in table 4.21. To compare the results from the different electron cooling devices, all rates are normalized to $r^* = r/\kappa$ with the scaling parameter $\kappa = \frac{n_e[\text{cm}^{-3}]Z^2}{A}$ (eqn. 2.110).

The uncertainties given in table 4.21, typically amounting to only a few per cent of the measured rate values, are given only by the errors of the electron cooling time fit in the respective cooling curves. An additional relevant systematic uncertainty propagates from an estimated uncertainty $\Delta r_{cath} = \pm 0.03$ mm on the cathode radius r_{cath} and amounts to about 5.5 % at all values of r^* .

The fraction of the effective electron cooling length to the storage ring circumference is about equal for both the TSR and CSR ($\eta_c(CSR) \sim \eta_c(TSR) \sim 0.021$) and hence not further regarded when comparing cooling rates between these machines.

The normalized transverse cooling rates for the CSR electron cooler and the

4 Low-energy electron cooling studies of keV ion beams in the CSR

TSR electron target agree within the scatter of the values. The TSR electron target has been operated with the same photocathode electron gun setup.

More surprisingly, at the CSR the measured normalized longitudinal rates in the case of HeH^+ are of the same size as the measured transverse rates. This result goes against the expectation for a flattened electron velocity distribution. The longitudinal cooling force component should be enhanced as compared to the transverse. For example, at the TSR electron cooler, the measured transverse rate is a factor of 4-8 smaller than the longitudinal one [25]. To draw further conclusions, it might be helpful to consider the electron beam temperatures for all three devices. The major difference between the TSR electron cooler and electron target regarding the transverse electron beam temperature is that the TSR electron cooler uses a thermocathode for the electron beam production, whereas the TSR electron target is equipped with the photocathode electron gun (sect. 3.2) that has later been transferred to the CSR electron cooler. Hence, the transverse electron temperatures of $T_{e\perp} \approx 2$ meV at the CSR and TSR electron target are much lower than the temperature of $T_{e\perp} \approx 10$ meV at the TSR electron cooler.

In the longitudinal guiding field for the electrons the influence of the transverse thermal electron velocity spread on the cooling force should be negligible compared to the influence of the longitudinal thermal electron velocity spread (eqns. 2.114, 2.115). On the other side, the longitudinal electron beam temperatures ranging from a few tens of μeV up to about 100 μeV are very comparable for all three setups. At the TSR electron cooler the accelerating potential U_0 for the

Table 4.20: Summary of the evaluated transverse electron cooling measurements for 250 keV HD^+ , HeH^+ and O^+ in the CSR evaluated by 2D Gaussian profile fits of ellipse shaped beam-projections on the imaging detector. The major (minor) ellipse axis is assigned to the vertical (horizontal) dimension in the interaction region, respectively (see text for details).

	E_e [eV]	n_e [10^5 cm^{-3}]	$\tau_{cool,x}$ [s]	$\tau_{cool,y}$ [s]	$\sigma_{x,\infty}$ [mm]	$\sigma_{y,\infty}$ [mm]	$\tau_{Spitzer}$ [s]
HD^+	45.71	4.28	0.97(2)	1.05(5)	0.906(5)	0.770(4)	4.81
		4.74	0.95(2)	1.17(6)	0.87(1)	0.742(2)	4.37
		3.41	1.23(3)	1.0(3)	0.900(4)	0.813(3)	5.92
		2.05	1.54(7)	1.13(17)	0.83(1)	0.86(1)	9.52
		1.36	2.89(6)	2.05(12)	0.88(1)	0.98(1)	13.90
		0.68	6.41(23)	4.30(43)	0.90(3)	1.09(1)	27.03
HeH^+	27.32	6.40	1.51(3)	1.57(3)	2.36(1)	1.39(1)	5.50
O^+	8.57	11.3	9.65(13)	10.96(26)	1.00(1)	1.61(1)	10.3

4.7 Summary of electron cooling performance

electron beam has to be set to much higher values in the keV range to match the velocities of the presented ion beams with energy of 6.1 MeV/u. Therefore, the kinematic compression term in eqn. 3.17 is negligible and the longitudinal electron beam temperature is determined by the $n_e^{1/3}$ -term. A typical electron density of $n_e = 1 \cdot 10^8 \text{ cm}^{-3}$ for this machine and velocity $\beta_0 = 0.1$ yields about 64 μeV , with only 2 μeV coming from the kinematic term [25]. The electron energy needed to match the CF^+ ions investigated in the transverse cooling experiment at the TSR etarget is $E_e = 54 \text{ eV}$ [46], which yields a longitudinal temperature of $T_{e\parallel} \approx 25 \mu\text{eV}$ at $n_e = 3.5 \cdot 10^6 \text{ cm}^{-3}$ for a photocathode that is cooled to liquid nitrogen temperature of 77 K³. If it is the longitudinal velocity spread $\Delta_{e\parallel}$ that should mainly determine the strength of the electron cooling force it is not surprising that the longitudinal cooling rates are still comparable. From there one might jump to the assumption that transverse cooling proceeds either exceptionally fast at the CSR electron cooler (and TSR electron target) or exceptionally slow at the TSR electron cooler.

Not considered yet is any influence of the fitting function that is chosen to extract the electron cooling time constants, as shown for two examples in figs. 4.7 and 4.16. Both, the transverse cooling rates for the TSR etarget and the CSR are obtained by the simple exponential decay function eqn. 4.3 whereas the longitudinal cooling rates for the CSR, and for the TSR ecool in general, are obtained with function 2.137 taking into account the diffusion heating due to IBS.

Furthermore, the effect of the magnetic field strength of the solenoidal guiding field in the interaction region has not been investigated at the CSR at all, but a strong dependence of the transverse cooling rate is found for the $^{12}\text{C}^{6+}$ measurements at the TSR electron cooler. For increasing magnetic field strength in the interaction region, the transverse cooling rates show a rather continuous increase while the longitudinal rate stays unaffected above a threshold field of 350 G [68]. An investigation of this effect at the CSR might be a first step to a deeper understanding of the very similar cooling rates in all three dimensions as measured for HeH^+ . Furthermore, it might be helpful to measure longitudinal cooling rates with another experimental technique on a coasting ion beam.

³No electron cooling studies with an electron beam extracted from a photocathode that is cooled down to liquid nitrogen temperature have been performed at the CSR yet. However, the LN₂-cooling system is now operational and studies in that direction can be planned for future beam times.

Table 4.21: Electron cooling rates scaled by $\kappa = n_e[\text{cm}^{-3}]Z^2/A$ for the different ion species measured at CSR within this work in comparison to electron cooling studies with the TSR thermocathode electron cooler and the TSR photocathode electron target. Any rates that are stated without an error were read out of plots given in the corresponding references.

	n_e [$\frac{10^5}{\text{cm}^3}$]	$r_{cool,x}^*$ [$\frac{1}{\text{s}}$]	$r_{cool,y}^*$ [$\frac{1}{\text{s}}$]	$r_{cool,\parallel}^*$ [$\frac{1}{\text{s}}$]
CSR ecool				
HD ⁺	4.74	0.67(1)	0.54(3)	
	3.41	0.71(2)	0.88(3)	
	2.05	0.95(4)	1.30(19)	
	1.36	0.76(2)	1.00(6)	
	0.68	0.69(3)	1.02(10)	
HeH ⁺	6.40	0.52(1)	0.50(1)	
	6.55			0.52(5)
	6.28			0.46(4)
	2.49			0.44(6)
	1.12			0.60(15)
O ⁺	9.70	0.171(2)	0.151(4)	
TSR ecool				
¹² C ⁶⁺ [68]	80	0.0817(72)	0.0833(42)	0.27
D ⁺ [25]	40	0.12	0.12	0.87
⁶ Li ³⁺ [25]	26.7	0.1	0.1	0.45
O ⁸⁺ [25]	26	0.06	0.06	0.22
TSR etarget				
CF ⁺ [46]	35	0.61(2)	0.76(3)	

5 Conclusion and outlook

In this work, essential parts of the electron-ion merged beam setup have been assembled and implemented in the electrostatic cryogenic storage ring CSR. The realized setup was subsequently commissioned in the course of two beamtime campaigns. First systematic low-energy electron cooling studies have been performed, demonstrating efficient phase space electron cooling for atomic and molecular ions even at very low electron densities.

The electron beam production section was realized by transferring an existing semiconductor photocathode setup previously operating at the electron target of the Test Storage Ring (TSR). For low-energy electron cooling operation, electron currents on the order of up to a few tens of μA were extracted.

The electron beam is guided towards the electron-ion interaction region in the CSR cryostat by a solenoidal magnetic field. In the cryogenic region, guiding and merging the electrons with the ion beam is realized by a set of high-temperature superconducting magnets. A special design for the distribution of currents up to about 75 Amperes to the superconductors was developed and taken into operation, significantly reducing Ohmic heating from connecting cables and enabling long-term operation of the merged-beam setup. Moreover, within this work these superconductors have been assembled and together with other electron cooler elements they have been implemented in the CSR cryostat.

For electron beam diagnostic measurements, two electron collector systems outside the cryogenic electron-ion interaction region have been taken into operation. Profile measurements of adiabatically magnetically expanded electron beams were carried out, showing flat top profiles that are essential for uniform electron densities needed in electron-ion reaction studies.

First low energy electron cooling in a cryogenic electrostatic storage ring was realized in a 2017 beam time campaign. Longitudinal electron cooling was realized for a bunched 1.397 MeV F^{6+} ion beam that was overlapped with an electron beam of about 40 eV at matched velocities.

In a following beam time in 2018, systematic electron cooling studies of coasting and bunched keV ion beams were performed, including 250 keV HeH^+ , HD^+ and O^+ . These measurements represent the first investigation of electron cooling in the CSR and in particular in the new regime of very low electron energies down to ~ 9 eV at electron densities typically below $10 \cdot 10^5 \text{ cm}^{-3}$. Longitudinal and

5 Conclusion and outlook

transverse electron cooling times on the order of 1 s were measured for molecular ions HeH^+ and HD^+ with 250 keV energy. Transverse ion beam sizes less than 1 mm were realized for the electron cooled ion beams.

In dependence of the electron beam density, measured longitudinal and transverse cooling rates of bunched HeH^+ and coasting HD^+ , respectively, were compared to existing theoretical cooling rate approximations. A simple model from plasma physics, calculating the temperature relaxation time of an electron-ion plasma often yields reasonable estimates despite its many assumptions that do not fully reflect realistic electron cooling conditions. Furthermore, an approximation taking into account the anisotropic electron velocity distribution and an estimate from a cooling force formula that considers collisions influenced by a longitudinal guiding field were used. Overestimates for the magnetic cooling force approximation are assumed to be due to misalignment effects which increase the longitudinal velocity spread of the electrons and thereby decrease the cooling force in a more realistic situation. In addition, the theory of magnetic collisions in electron cooling available for comparison is based on a number of approximations that may not be fulfilled in the realistic case.

Moreover, first Schottky spectra showing longitudinal electron cooling for a coasting 250 keV HD^+ beam were measured. The movement of the stored ion beam in the horizontal direction for detuned electron energies was investigated with respect to space charge effects of the electron beam.

The electron cooling studies were extended by an investigation of diffusional heating of the stored ion beams due to intrabeam-scattering (IBS). IBS effects were analyzed for coasting and bunched beams in the frame of a simplified model. IBS heating rates were measured and the simplified model was tested for its validity. The IBS formalism has further been used to describe the time evolution of ion beam bunch widths and transverse beam widths during electron cooling. The formalism turned out to be more applicable for the description of longitudinal cooling curves of bunched beam widths, than for the compression of the transverse beam widths of coasting beams. This is assumed to be due to the higher temperature in transverse direction resulting in lower sensitivity of the transverse degrees of freedom to the diffusion heating by IBS.

A theoretical lower limit for the compression of the bunch length of a bunched ion beam during electron cooling, introduced by the balance between the longitudinal space charge voltage and the rf-bunching voltage, has been investigated. This theoretical bunch length scales with the number of ions in the bunch to the power of 1/3. However, if the bunch length is dominated by the equilibrium between electron cooling and diffusion heating by IBS, a different scaling behaviour

to the power of $1/6$ is expected. Investigating the electron cooled bunch length as a function of the number of ions experimentally yielded a scaling to about the power of $1/4$, suggesting that both the space charge and the IBS contribute in this case.

It can be summarized that the CSR electron-ion merged-beam setup has not only been successfully completed based on previous works and commissioned in the present work, but a broad range of measurements investigating electron cooling of bunched and coasting keV ion beams, as well as the related diffusional heating process by IBS, was carried out. These measurements will serve as the basis for future studies exploring more systematics of electron cooling and diffusion heating in the low electron energy and low electron density regime.

The device is designed to achieve efficient ion beam phase space cooling at electron energies down to 1 eV, a limit that still remains to be tested in coming beam times. Furthermore, electron energy spreads on the order of 1 meV are expected to be attainable with the cold electron photocathode setup. The electron beam energy spread will be determined experimentally in the future, for example by measuring a very narrow resonance in an electron-ion recombination experiment. Such sharp resonances with widths even below 0.1 meV, are present in di-electronic recombinations of atomic systems like F^{6+} .

The functioning electron-ion merged-beam setup represents a significant hardware upgrade to the CSR experimental facility that opens up new experimental possibilities. Phase space compression of ion beams by electron cooling can improve the energy resolution in collision experiments performed at any of the various targets in the CSR. In recent beamtimes, the electron-ion merged beam setup was successfully employed as an electron target for state-of-the-art dissociative recombination experiments of astrophysically relevant molecular ions like HeH^+ and HD^+ . The device represents an ideal tool to benchmark the quantum-dynamics theories for molecules in well-defined individual states. Moreover, measured recombination cross sections can help to understand complex reaction networks in astrophysical plasmas like cold molecular clouds.

Appendices

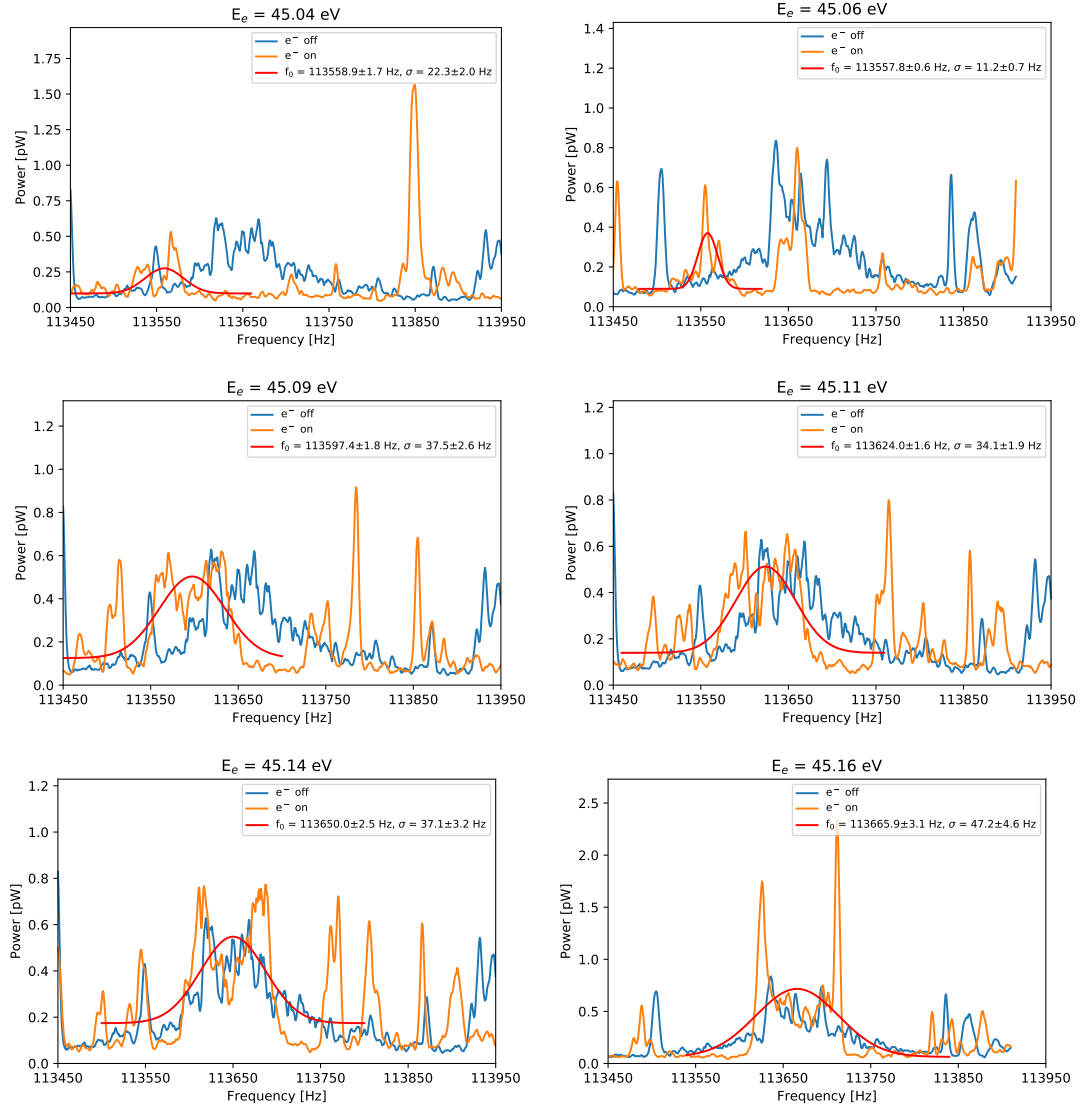
A Schottky noise spectra measurements

A.1 HD⁺

Below, the measured Schottky spectra for longitudinal electron cooling of a coasting 250 keV HD⁺ beam, as discussed in sect. 4.3.2, are presented. The title of each spectra shows the electron energy E_e in the center of the electron-ion interaction region. When tuning the cathode potential and thereby the electron energy, the ion beam experiences a frequency shift that is related to a shift of its horizontal position x (closed orbit shift).

In sect. 4.3.2, this movement of the electron cooled ion beam is analyzed with respect to the influence of the space charge velocity profile of the electron beam in the interaction region. In fig. A.1, the electron cooled spectra (orange) are compared to uncooled ion beam Schottky spectra (electrons off, blue).

A Schottky noise spectra measurements



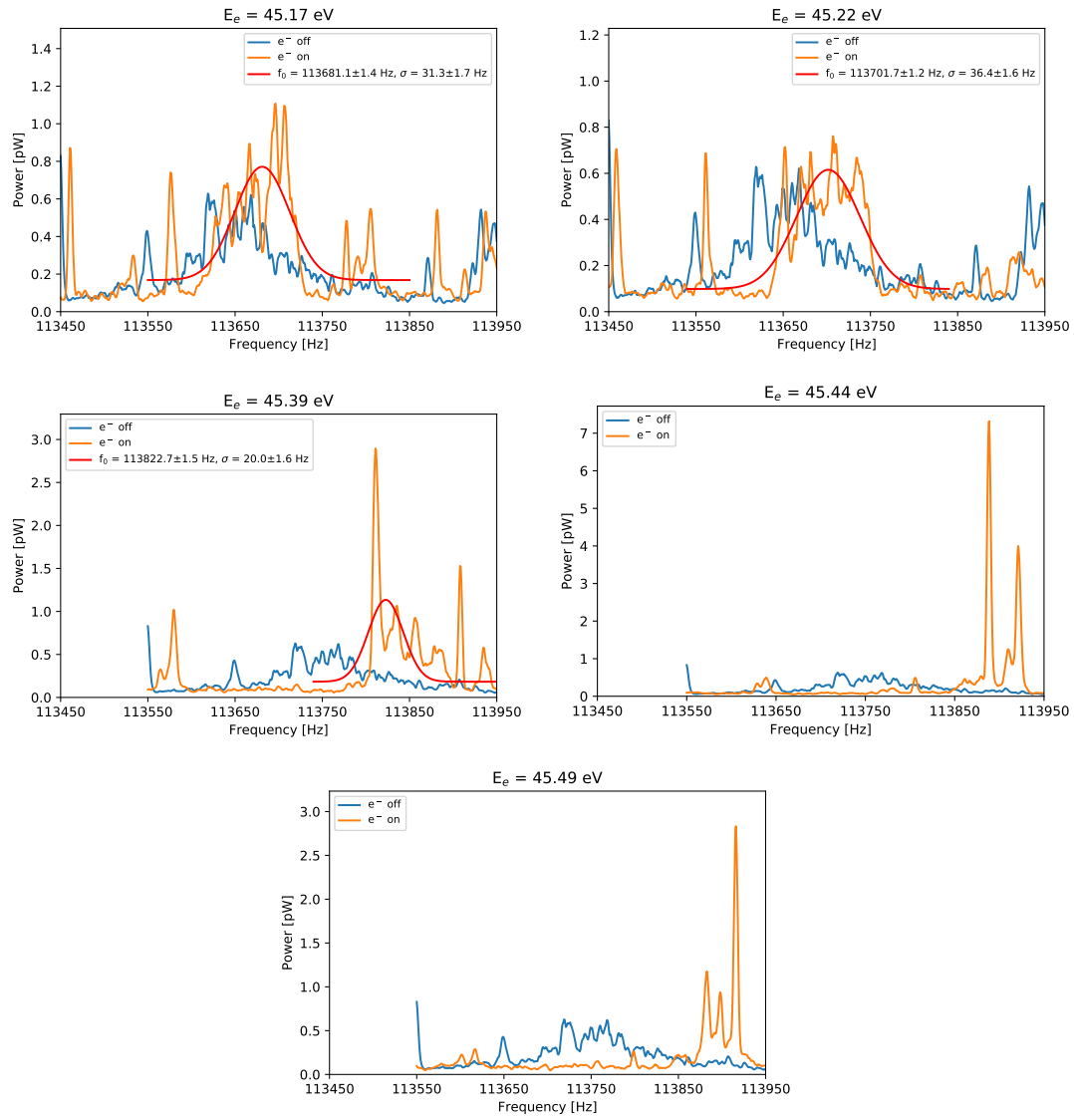


Figure A.1: Schottky spectra of a coasting 250 keV HD^+ beam.

B Estimate of initial ion beam temperatures

B.1 Longitudinal ion beam temperature from rf-bunching simulation

In order to estimate the longitudinal temperature of 250 keV HeH⁺ upon beam injection, before electron cooling is applied, a simulation of the bunching process as described in section 2.1.5 with the rf-ramp shown in fig. 2.5 for a beam with an initial Gaussian energy distribution with $\sigma = 66$ eV is performed. To reproduce conditions during the bunched beam HeH⁺ measurements, the injected pulse length is chosen to be 75% of the revolution period (sect. 4.2.1). A certain time after the rf-voltage has finished its ramp, the calculated bunch profiles are then compared to the measured bunch spectrum in order to verify the estimated longitudinal beam temperature of the initial distribution. The longitudinal phase space distribution in the coordinates $(\Delta E, \Delta\Phi)$ is calculated for 10000 ions.

The simulation results after 100 ms (about 8826 revolution periods), where $t = 0$ s is defined by the start of the rf-voltage ramp, are shown in fig. B.1 and compared to a measured waveform that was triggered 300 ms after beam injection. The measured waveform is the result of averaging about 3530 revolution periods, thus showing the bunch situation long after the 20 ms of the rf-voltage ramp-up have passed.

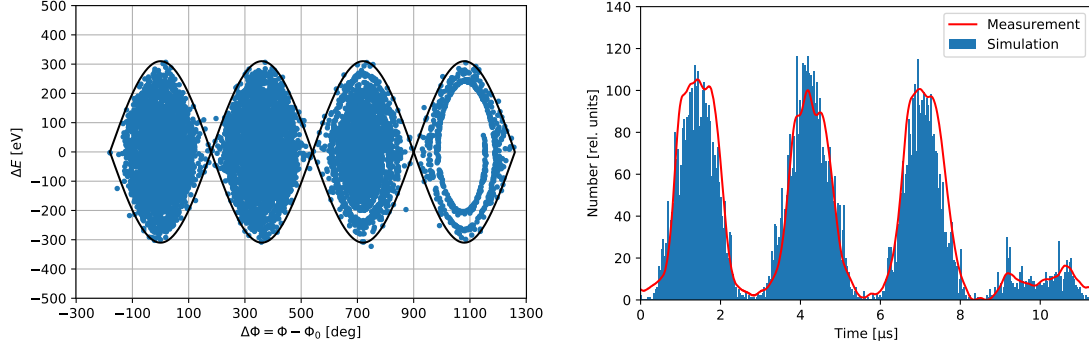
The longitudinal intensity distribution of the ions as a function of the energy spread is analyzed in fig. B.2. The injected, non-bunched ion beam is well described by a Gaussian profile with width $\sigma = 67$ eV. With this value, the longitudinal beam temperature T_{\parallel} is estimated by:

$$k_B T_{\parallel} = \Delta v_{\parallel}^2 M_i = \left(\frac{67 \text{ eV}}{2 \cdot 250 \text{ keV}} \right)^2 v_0^2 M_i \approx 17 \text{ meV} \quad (\text{B.1})$$

where $v_0 = \sqrt{2 \cdot 250 \text{ keV} / M_i}$.

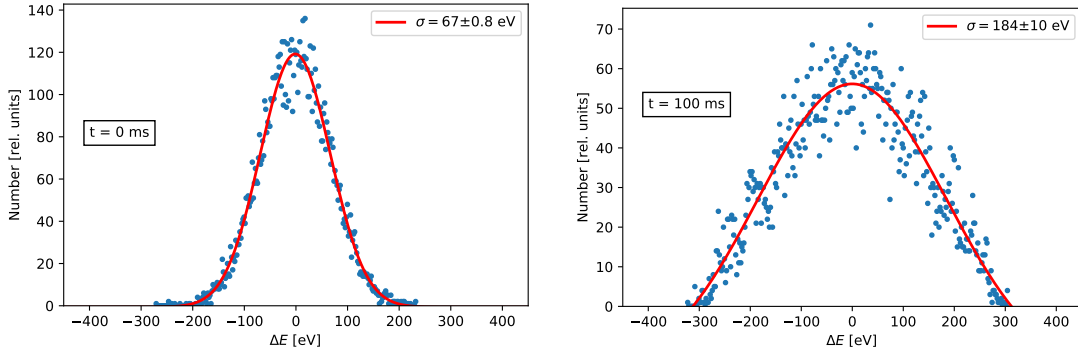
For the rf-bunched beam, 60 ms after ramping up the rf-voltage, the profile fit

B.1 Longitudinal ion beam temperature from rf-bunching simulation



(a) Simulated longitudinal phase space distribution. The blue spots mark single particles, the black curve represents the separatrix. (b) Simulated time spectra of one revolution period of the ion bunches (in form of a histogram) compared to a measured bunch waveform.

Figure B.1: Simulation results of the rf-bunching process of 250 keV HeH⁺ with a bunching frequency of $f_{\text{rf}} = 4f_0 = 353.044$ kHz.



(a) Longitudinal energy distribution right after injection, before rf-bunching. (b) Longitudinal energy distribution 100 ms after injection (80 ms after the rf-bunching ramp has finished).

Figure B.2: Simulated longitudinal energy spread before bunching (right after injection) and 100 ms later (80 ms after the rf-bunching ramp has finished).

yields:

$$k_B T_{\parallel} = \Delta v_{\parallel}^2 M_i = \left(\frac{184 \text{ eV}}{2 \cdot 250 \text{ keV}} \right)^2 v_0^2 M_i \approx 68 \text{ meV} \quad (\text{B.2})$$

B.2 Longitudinal ion beam temperature from Schottky noise spectra measurement

From the measured frequency spread $\frac{\Delta f}{f} = 0.370(17) \cdot 10^{-3}$ of the uncooled HD⁺ beam shown in fig. 4.11, the longitudinal ion beam temperature can be determined. By converting the frequency spread to the velocity spread

$$\frac{\Delta v_{\parallel}}{v_0} = \frac{\Delta f}{f} \frac{1}{\eta} = 0.544(25) \cdot 10^{-3} \quad (\text{B.3})$$

with the CSR slip factor $\eta = 0.674$ [30] and with the longitudinal velocity v_0 the absolute longitudinal velocity spread Δv_{\parallel} is calculated by

$$\Delta v_{\parallel} = \left(\frac{\Delta v_{\parallel}}{v_0} \right) \sqrt{\frac{2 \cdot 250 \text{keV}}{M_i}} = 2182(100) \frac{\text{m}}{\text{s}} \quad (\text{B.4})$$

The longitudinal ion temperature T_{\parallel} is then determined to (eqn. 2.28):

$$T_{\parallel}(250 \text{ keV HD}^+) = \frac{\Delta v_{\parallel}^2 M_i}{k_B} = 1717(157) \text{K} = 148(14) \text{meV} \quad (\text{B.5})$$

B.3 Transverse ion beam temperatures

An estimate of the transverse ion beam temperature can be obtained from the exponential fits of the electron cooling curves.

With the definition of the betatron functions $\beta(s)_{x,y}$ and emittance $\epsilon(s)_{x,y}$ as discussed in sect. 2.1.2

$$(\sigma_x, \sigma_y) = (\sqrt{\epsilon_x \beta_x}, \sqrt{\epsilon_y \beta_y}) \quad (\text{B.6})$$

$$(\epsilon_x, \epsilon_y) = (xx', yy') \quad (\text{B.7})$$

the transverse position (x, y) and divergence (x', y') of any particle in the beam can be determined along the longitudinal coordinate s . For the transverse velocity spread $\Delta v_{x,y}$ one can now define

$$\Delta v_x = v_0 \cdot \sigma_{x'} \quad (\text{B.8})$$

$$\Delta v_y = v_0 \cdot \sigma_{y'} \quad (\text{B.9})$$

where $v_0 = \sqrt{\frac{2 \cdot 250 \text{keV}}{M_i}}$.

An estimate of the horizontal and vertical temperatures T_x and T_y , respectively, can then be calculated as follows:

$$T_x = M_i \Delta v_x^2 = M_i v_0^2 \left(\frac{\epsilon_x}{\beta_x} \right) = M_i v_0^2 \left(\frac{\sigma_x^2}{\beta_x^2} \right) \quad (\text{B.10})$$

$$T_y = M_i \Delta v_y^2 = M_i v_0^2 \left(\frac{\epsilon_y}{\beta_y} \right) = M_i v_0^2 \left(\frac{\sigma_y^2}{\beta_y^2} \right) \quad (\text{B.11})$$

and with the relation

$$T_{\perp} = \frac{1}{2}(T_x + T_y) \quad (\text{B.12})$$

one obtains

$$T_{\perp} = \frac{1}{2} \left(\left(M_i v_0^2 \left(\frac{\sigma_x^2}{\beta_x^2} \right) \right) + \left(M_i v_0^2 \left(\frac{\sigma_y^2}{\beta_y^2} \right) \right) \right) \quad (\text{B.13})$$

The uncooled beam widths $\sigma_{0x,0y}$ of the profile in the interaction region that can be extracted from the fit of the cooling curve of HD^+ (fig. 4.18). Using eqn. 3.44 where the minor axis of ellipse beam profile is assigned to the horizontal and the major axis to the vertical direction, respectively (see discussion in sect. 4.7), these beam widths are

$$\sigma_{0,x} = 4.03(6) \text{ mm} \quad (\text{B.14})$$

$$\sigma_{0,y} = 1.52(3) \text{ mm} \quad (\text{B.15})$$

B Estimate of initial ion beam temperatures

yielding a transverse ion beam temperature estimate of

$$T_{\perp} = 0.31(3) \text{ eV} \tag{B.16}$$

Analogously to the procedure shown above for HD^+ , the equilibrium beam widths of the 250 keV HeH^+ beam profile can be obtained from the exponential fit of the cooling curve shown in fig. 4.16:

$$\sigma_{0,x} = 5.60(3) \text{ mm} \tag{B.17}$$

$$\sigma_{0,y} = 3.28(2) \text{ mm} \tag{B.18}$$

yielding a transverse ion beam temperature estimate of

$$T_{\perp} = 1.4(2) \text{ eV} \tag{B.19}$$

C Analytical IBS model

The first theoretical framework of the IBS phenomenon in a storage ring has been formulated already in 1974 by A. Piwinski [69] for bunched as well as unbunched beams. With increasing interest of the effect due to further development and construction of storage ring machines in the eighties especially at CERN, Piwinski's model has been extended by several authors [70]. The Piwinski model neglects variations of the betatron and dispersion functions along the ring orbit, which is acceptable for storage ring machines with weak focusing. An extended Piwinski model for strong focusing machines was derived for example by M. Martini [71] and J. D. Bjorken and S. K. Mtingwa [72]. In the analytical model based on [69, 71] summarized here, the ion beam is assumed to have a Gaussian distribution in phase space.

For the distribution of scattering angles $\bar{\Psi}$ of charged particles in a repulsive Coulomb field, it is assumed that the particle velocities in the center of mass system (c.m.s.) are non-relativistic [71]. Thus the differential cross-section $d\bar{\sigma}/d\bar{\Omega}$ for scattering into the solid angle $d\bar{\Omega}$ at fixed angles $\bar{\Psi}$ and $\bar{\Phi}$ in the c.m.s. is given by the well known Rutherford formula:

$$\frac{d\bar{\sigma}(\bar{\Psi})}{d\bar{\Omega}} = \frac{1}{4} \left(\frac{e^2}{8\pi\epsilon_0\bar{E}_0} \right)^2 \frac{1}{\sin^4(\bar{\Psi}/2)} \quad (\text{C.1})$$

$$d\bar{\Omega} = \sin(\bar{\Psi}) d\bar{\Psi}d\bar{\Phi} \quad (\text{C.2})$$

where \bar{E}_0 is the c.m.s. kinetic energy of the colliding particles.

The derivatives of the mean value of the horizontal and vertical emittances as well as the mean momentum spread, respectively, can then be expressed by three integrals as given in [71], eqn. (28). Further evaluating these integrals, the growth rates $1/\tau_{x'}$, $1/\tau_{y'}$, $1/\tau_{\delta}$ for the three dimensions can be expressed by the set of equations [71]

C Analytical IBS model

$$\frac{1}{\tau_\delta} = \left\langle \frac{nA}{2} \left(1 - \frac{\sigma_\delta^2 D^2}{\sigma_x^2} \right) f_1 \right\rangle \quad (\text{C.3})$$

$$\frac{1}{\tau_{x'}} = \left\langle \frac{A}{2} \left[f_2 + \left(\frac{\sigma_\delta^2 D^2}{\sigma_x^2} + \frac{\sigma_\delta^2 \tilde{D}^2}{\sigma_x^2} \right) f_1 \right] \right\rangle \quad (\text{C.4})$$

$$\frac{1}{\tau_{y'}} = \left\langle \frac{A}{2} f_3 \right\rangle \quad (\text{C.5})$$

where the brackets $\langle \dots \rangle$ mean averaging of the functions around the accelerator lattice and $n = 1$ for a bunched beam and $n = 2$ in the case of an unbunched beam. A scattering function f_i has been introduced that depends on lattice parameters of the ring and the ion beam distribution (see [71] for details). As mentioned above, in contrast to the standard Piwinski model [69], this extended model by Martini also takes into account derivatives of the beta functions and dispersion. In eqns. C.3 & C.4, D is the dispersion and $\tilde{D} = \alpha_x D + \beta_x D'$ where α_x and β_x are the lattice functions as defined in eqn. 2.21.

The factor A in eqns. C.3-C.5 depends on the number of circulating ions. In the Martini model, it is expressed by

$$A = \frac{\sqrt{1 + \alpha_x^2} \sqrt{1 + \alpha_y^2} c r_0^2 \lambda}{16\pi \sqrt{\pi} \epsilon_x \epsilon_y \sigma_\delta} \quad (\text{C.6})$$

where

$$\lambda = \begin{cases} N_b / (2\sqrt{2\pi}\sigma_b) & \text{for bunched beams} \\ N/C_0 & \text{for unbunched beams} \end{cases} \quad (\text{C.7})$$

c is the speed of light, N is the number of particles in the beam and N_b is the number of particles in the bunch, respectively. Moreover, r_0 is the classical proton radius and σ_b , σ_δ are the standard deviations of the bunch length and the momentum spread, respectively.

Bibliography

- [1] R. A. Phaneuf, C. C. Havener, G. H. Dunn, and A. Müller. Merged-beams experiments in atomic and molecular physics. *Reports on Progress in Physics*, 62:1143, 1999.
- [2] Holger S.P. Müller, Frank Schlöder, Jürgen Stutzki, and Gisbert Winnewisser. The Cologne Database for Molecular Spectroscopy, CDMS: a useful tool for astronomers and spectroscopists. *Journal of Molecular Structure*, 742:215–227, 2005.
- [3] A.I. Florescu-Mitchell and J.B.A. Mitchell. Dissociative recombination. *Physics Reports*, 430(5-6):277–374, 2006.
- [4] V. Zhaunerchyk, F. Hellberg, A. Ehlerding, W. D. Geppert, M. Larsson, C. R. Vane, M. E. Bannister, E. M. Bahati, F. Österdahl, M. af Ugglas, and R. D. Thomas. Dissociative recombination study of PD_2^+ at CRYRING: absolute cross-section, chemical branching ratios and three-body fragmentation dynamics. *Molecular Physics*, 103(20):2735–2745, 2007.
- [5] T. Tanabe, I. Katayama, S. Ono, K. Chida, T. Watanabe, Y. Arakaki, Y. Haruyama, M. Saito, T. Odagiri, K. Hosono, K. Noda, T. Honma, and H. Takagi. Dissociative recombination of HeH^+ isotopes with an ultra-cold electron beam from a superconducting electron cooler in a storage ring. *J. Phys. B: At. Mol. Opt. Phys.*, 31:L297–L303, 1998.
- [6] K. Seiersen, O. Heber, M. J. Jensen, C. P. Safvan, and L. H. Andersen. Dissociative recombination of dications. *The Journal of Chemical Physics*, 119(2):839, 2003.
- [7] H. B. Pedersen, H. Buhr, S. Altevogt, V. Andrianarijaona, H. Kreckel, L. Lam-mich, N. de Ruelle, E. M. Staicu-Casagrande, D. Schwalm, D. Strasser, X. Urbain, D. Zajfman, and A. Wolf. Dissociative recombination and low-energy inelastic electron collisions of the helium dimer ion. *Physical Review A*, 72:012712, 2005.
- [8] S. Pape Møller. ELISA, an electrostatic storage ring for atomic physics. *Nuclear Instruments and Methods in Physics Research A*, 394:281–286, 1997.

Bibliography

- [9] S. Jinno, T. Takao, Y. Omata, A. Satou, H. Tanuma, T. Azuma, H. Shiromaru, K. Okuno, N. Kobayashi, and I. Watanabe. TMU electrostatic storage ring designed for operation at liquid nitrogen temperatures. *Nuclear Instruments and Methods in Physics Research A*, 532(1):477–482, 2004.
- [10] T. Tanabe, K. Noda, and E. Syresin. An electrostatic storage ring with a merging electron beam device at KEK. *Nuclear Instruments and Methods in Physics Research A*, 482(3):595–605, 2003.
- [11] R. D. Thomas et al. The double electrostatic ion ring experiment: A unique cryogenic electrostatic storage ring for merged ion-beams studies. *Review of Scientific Instruments*, 82:065112, 2011.
- [12] Y. Nakano, W. Morimoto, T. Majima, J. Matsumoto, H. Tanuma, H. Shiromaru, and T. Azuma. A cryogenic electrostatic storage ring project at RIKEN. *Journal of Physics: Conference Series*, 388:142027, 2012.
- [13] R. von Hahn et al. The cryogenic storage ring CSR. *Review of Scientific Instruments*, 87(063115), 2016.
- [14] G. I. Budker. An effective method of damping particle oscillations in proton and antiproton storage rings. *Atomic Energy*, 22(5):438–440, 1967.
- [15] G.I. Budker, N.S. Dikansky, V.I. Kudelainen, I.N. Meshkov, V.V. Parchomchuk, D.V. Pestrikov, A.N. Skrinsky, and B.N. Sukhina. Experimental Studies of Electron Cooling. *Particle Accelerators*, 7(197):197–211, 1976.
- [16] S. Pastuszka, M. Hoppe, D. Kratzmann, D. Schwalm, and A. Wolf. Preparation and performance of transmission-mode GaAs photocathodes as sources for cold dc electron beams. *Journal of Applied Physics*, 88:6788, 2000.
- [17] D. Orlov, H. Fadil, M. Grieser, C. Krantz, J. Hoffmann, O. Novotny, S. Novotny, and A. Wolf. Electron cooling with photocathode electron beams applied to slow ions at TSR and CSR. *Proceedings of COOL 2007*, 2007.
- [18] Frank Hinterberger. *Physik der Teilchenbeschleuniger und Ionenoptik*. Springer Verlag, 1997.
- [19] G.W. Hill. On the part of the motion of the lunar oerigee which is a function of the mean motions of the sun and moon. *Acta Mathematica*, 8(1):7, 1886.
- [20] M. Grieser, R. von Hahn, S. Vogel, and A. Wolf. The phase slip factor of the electrostatic cryogenic storage ring CSR. *Journal of Physics: Conf. Series*, 874(012049), 2017.

- [21] J. Le Duff. Longitudinal beam dynamics in circular accelerators. *CERN Accelerator School: General Accelerator Physics*, pages 125–143, 1984.
- [22] H. Bruck. *Accélérateurs Circulaires de Particules*. Presses Universitaires de France, 1966.
- [23] Robin Bastert. Erzeugung kurzer Ionenpulse in einem Speicherring. Master's thesis, Universität Heidelberg, 2009.
- [24] H. Poth. Electron cooling: Theory, Experiment, Application. *Physics Reports (Review Section of Physics Letters)*, 196(3 &4):135–297, 1990.
- [25] Michael Beutelspacher. *Systematische Untersuchungen zur Elektronenkühlung am Heidelberger Schwerionenspeicherring TSR*. PhD thesis, Universität Heidelberg, 2000.
- [26] H. Risken. *The Fokker-Planck Equation*. Springer Verlag, second edition edition, 1996.
- [27] YA. S. Derbenev and A. N. Skrinsky. The effect of an accompanying magnetic field on electron cooling. *Particle Accelerators*, 8:235, 1978.
- [28] L. Spitzer. *Physics of fully ionized gases*. Wiley & Sons, 2nd edition edition, 1962.
- [29] Andreas Wolf. *Elektronenkühlung für niederenergetische Antiprotonen*. PhD thesis, Universität Karlsruhe, 1985.
- [30] Stephen Vogel. *Developments at an Electrostatic Cryogenic Storage Ring for Electron-Cooled keV Energy Ion Beams*. PhD thesis, Universität Heidelberg, 2016.
- [31] YA. S. Derbenev and A. N. Skrinsky. Kinetics of electron cooling of beams in heavy particle storage rings. *Particle Accelerators*, 8:1, 1977.
- [32] R. Singh, O. Boine-Frankenheim, O. Chorniy, P. Forck, R. Haseitl, W. Kaufmann, P. Kowina, K. Lang, and T. Weiland. Interpretation of transverse tune spectra in a heavy-ion synchrotron at high intensities. *Physical Review Special Topics - accelerators and beams*, 16, 2013.
- [33] Karlheinz Schindl. Space charge. *Cern Accelerator School: Intermediate Course on Accelerator Physics*, 2003.
- [34] W. D. Stern and O. Boine-Frankenheim. Using an electron cooler for space charge compensation on the GSI synchrotron SIS18*. In *Proceedings of HB2016*, 2016.

Bibliography

- [35] William D Stem and Oliver Boine-Frankenheim. Pushing the space charge limit: electron lenses in high-intensity synchrotrons? *Journal of Physics: Conf. Series*, 874, 2017.
- [36] David Neuffer. Longitudinal motion in high current ion beams - a self-consistent phase space distribution with an envelope equation. *IEEE Transactions on Nuclear Science*, NS-36(3):3031–3033, 1979.
- [37] M. Grieser, S. Artikova, R. Bastert, K. Blaum, and A. Wolf. Cooling Activities at the TSR Storage Ring. In *Proceedings of COOL2013*, pages 89–93, 2013.
- [38] Sergei S. Nagaitsev, Timothy J.P. Ellison, Michael J. Ellison, and Daniel Anderson. The investigation of space charge dominated cooled bunched beams in a synchrotron. *CERN-1994-003*, 94:405, 1993.
- [39] A. Hofmann. Single-beam collective phenomena - longitudinal. *CERN yellow report 77-13*, page 143, 1977.
- [40] C. Bernardini, G. F. Corazza, G. Di Giugno, G. Ghigo, J. Haissinski, P. Marin, R. Querzoli, and B. Touschek. Lifetime and Beam Size in a Storage Ring. *Physical Review Letters*, 10(9):407, 1963.
- [41] S. Artikova, M. Grieser, and J. Ullrich. Investigation of Intreabeam Scattering in the Heavy Ion Storage Ring TSR. *Proceedings of IPAC2011*, 2011.
- [42] Stefan Pastuszka. *Erzeugung kalter Elektronenstrahlen durch Photoemission aus GaAs*. PhD thesis, Universität Heidelberg, 1997.
- [43] Udo Weigel. *Cold Intense Electron Beams from Gallium Arsenide Photocathodes*. PhD thesis, Universität Heidelberg, 2004.
- [44] J. J. Scheer and J. van Laar. A New Type of Photoemitter. *Solid State Commun.*, 3(189), 1965.
- [45] D. A. Orlov, V. É. Andreev, and A. S. Terekhov. Elastic and Inelastic Tunneling of Photoelectrons from the Dimensional Quantization Band at a p⁺-GaAs-(Cs,O) Interface into Vacuum. *Journal of Experimental and Theoretical Physics Letters*, 71:151–154, 2000.
- [46] Claude Krantz. *Intense Electron Beams from GaAs Photocathodes as a Tool for Molecular and Atomic Physics*. PhD thesis, Universität Heidelberg, 2009.
- [47] D. A. Orlov, U. Weigel, D. Schwalm, A. S. Terekhov, and A. Wolf. Ultra-Cold Electron Source with a gaas-photocathode. *Nuclear Instruments and Methods in Physics Research A*, 532:418–421, 2004.

- [48] Udo Weigel. *Cold Intense Electron Beams from Gallium Arsenide Photocathodes*. PhD thesis, Universität Heidelberg, 2003.
- [49] O. Novotný, A. Becker, H. Buhr, C. Domesle, W. Geppert, M. Grieser, C. Krantz, H. Kreckel, R. Repnow, D. Schwalm, K. Spruck, J. Stützel, B. Yang, A. Wolf, and D.W. Savin. Dissociative recombination measurements of HCl^+ using an ion storage ring. *Astrophysics Journal*, 54, 2013.
- [50] T. M. O’Neil and P.G. Hjorth. Collisional dynamics of a strongly magnetized pure electron plasma. *Phys. Fluids*, 28(11):3241–3252, 1985.
- [51] S. Pastuszka, U. Schramm, M. Grieser, C. Broude, R. Grimm, D. Habs, J. Kenntner, H.-J. Miesner, T. Schübler, D. Schwalm, and A. Wolf. Electron cooling and recombination experiments with an adiabatically expanded electron beam. *Nuclear Instruments and Methods in Physics Research A*, 369(1):11–22, 1996.
- [52] N.S. Dikansky, V.I. Kudaleinen, V.A. Lebedev, I.N. Meshkov, V.V. Parkhomchuk, A.A. Sery, A.N. Skrinsky, and B.N. Sukhina. Ultimate possibilities of electron cooling. *preprint*, 1988.
- [53] H. Fadil, D. Orlov, M. Grieser, and A. Wolf. Design of a low energy electron cooler for the Heidelberg CSR. *Proceedings of EPAC 2006*, page 1, 2006.
- [54] A. Shornikov. *An electron cooler for ultra-low energy cryogenic operation*. PhD thesis, Universität Heidelberg, 2012.
- [55] Marius Rimmler. Operating a low-energy Electron Cooler at the Cryogenic Storage Ring CSR. Master’s thesis, Universität Heidelberg, 2017.
- [56] Frank Sprenger. *Production of cold electron beams for collision experiments with stored ions*. PhD thesis, Universität Heidelberg, 2003.
- [57] Jorrit Lion. Das mit flüssigneon gekühlte supraleitende magnetsystem des elektronenkühlers am kryogenen ionen-speicherring csr. Bachelor’s thesis, 2015.
- [58] Svenja Lohmann. Beam diagnostics and collector for the electron cooler of the cryogenic storage ring CSR. Master’s thesis, Universität Heidelberg, 2015.
- [59] F. Laux. *Entwicklung von kapazitiven Positions-, Strom- und Schottkysignal-Messsystemen für den kryogenen Speicherring CSR*. PhD thesis, Universität Heidelberg, 2011.

Bibliography

- [60] W. Schottky. Über spontane Stromschwankungen in verschiedenen Elektrizitätsleitern. *Annalen der Physik*, 382(23):541–567, 1918.
- [61] F. Caspers. Schottky signals for longitudinal and transverse bunched beam diagnostics. *CERN Accelerator School: Course on Beam Diagnostics, CERN-2009-005*, page 407, 2008.
- [62] Arno Becker. *Imaging of Neutral Fragmentation Products from Fast Molecular Ion Beams: Paving the Way for Reaction Studies in Cryogenic Environment*. PhD thesis, Universität Heidelberg, 2016.
- [63] Yukap Hahn. Electron-ion recombination processes - an overview. *Reports on Progress in Physics*, 60:691–759, 1997.
- [64] Steffen Novotny. *Fragmentation of molecular ions in slow electron collisions*. PhD thesis, Universität Heidelberg, 2008.
- [65] M. Beutelspacher, M. Grieser, K. Noda, D. Schwalm, and A. Wolf. Dispersive electron cooling experiments at the heavy ion storage ring TSR. *Nuclear Instruments and Methods in Physics Research A*, 512:459–469, 2003.
- [66] F. O. Waffeu Tamo, H. Buhr, O. Motapon, S. Altevogt, V. M. Andrianarijaona, M. Grieser, L. Lammich, M. Lestinsky, M. Motsch, I. Nevo, S. Novotny, D. A. Orlov, H. B. Pedersen, D. Schwalm, F. Sprenger, X. Urbain, U. Weigel, A. Wolf, and I. F. Schneider. Assignment of resonances in dissociative recombination of HD⁺ ions: High-resolution measurements compared with accurate computations. *Physical Review A*, 84(2):022710, 2011.
- [67] S. Peggs. Coupling and decoupling in storage rings. *IEEE Trans. Nucl. Sci.*, 30(4):2460–2462, 1983.
- [68] M. Beutelspacher, M. Grieser, D. Schwalm, and A. Wolf. Longitudinal and transverse electron cooling experiments at the Heidelberg heavy ion storage ring TSR. *Nuclear Instruments and Methods in Physics Research A*, 441:110–11, 2000.
- [69] A. Piwinski. Intra-Beam-Scattering. *Proc. 9th Int. Conf. on High Energy Acc.*, page 405, 1974.
- [70] J. Le Duff. Single and Multiple Touschek Effects. *Proceedings of the CERN Accelerator School*, 1989.
- [71] M. Martini. Intrabeam scattering in the ACOL-AA machines. *CERN-PS-84-9-AA*, 1984.

- [72] J. D. Bjorken and S. K. Mtingwa. Intrabeam Scattering. *Particle Accelerators*, 1983.

Danksagung

An dieser Stelle möchte ich allen Personen danken, die zum Erfolg der Arbeit beigetragen haben.

Bei Prof. Andreas Wolf bedanke ich mich herzlich für die tolle Betreuung während meiner Doktorandenzeit, sowie viele hilfreiche Diskussionen und Kommentare beim Anfertigen dieser Dissertation und für die Möglichkeit, ein so spannendes Projekt von der Konstruktionsphase bis zur Inbetriebnahme begleiten zu dürfen. In freudiger Erinnerung werden mir auch gemeinsame Auslandsreisen zu Workshops nach Israel und in die USA bleiben.

Bei Prof. André Schöning möchte ich mich für die freundliche Übernahme des Zweitgutachtens bedanken.

Dr. Oldřich Novotný gebührt großer Dank für die tolle und herausragende Betreuung und Unterstützung in der Arbeit im CSR Ecool-Team. In diesem Zusammenhang möchte ich auch Dr. Claude Krantz danken, der immer für entscheidende Arbeiten und Fragen bezüglich der Photokathode zur Verfügung stand und steht.

Dr. Stephen Vogel möchte ich für die Einführung in das Projekt zu Beginn meiner Tätigkeit am MPIK und die weitere Begleitung bei jeglichen Fragen zum Elektronenkühler auch nach seiner Postdoc-Tätigkeit danken.

Dr. Manfred Grieser danke ich für zahlreiche Diskussionen zur Elektronenkühlung und der herausragenden Unterstützung während allen Strahlzeiten im Allgemeinen.

Marius Rimmler möchte ich für die tolle gemeinsame Arbeit in der Aufbauphase des Elektronenkühlers sowie eine gute Zeit in Heidelberg auch abseits des Instituts danken.

Daniel Paul und Ábel Kálosi danke ich herzlich für die Zusammenarbeit bei Strahlzeitvorbereitung und -betrieb im Labor und im Kontrollraum, sowie jegliche Hilfe bezüglich Datenaufnahme und -auswertung und zahlreiche fruchtbare Diskussionen im Büro.

Ein großes Dankeschön für die unkomplizierte und hilfreiche Zusammenarbeit gilt natürlich auch den Einrichtungen im Hause des MPIK, der mechanischen Werkstatt um Thorsten Spranz und dem Konstruktionsbüro um Frank Müller. Auch Thomas Weber stand bei Konstruktionsfragen zum Aufbau des Elektronenkühlers immer mit schnellen Antworten zur Verfügung.

Ebenso bedanke ich mich bei der Beschleunigerwerkstatt um Christian Kaiser;

für die Unterstützung im Cryo-Labor und am CSR durch Dirk Kaiser; und den Truppen um Manfred König. Bei Oliver Koschorreck bedanke ich mich besonders für die tatkräftige Unterstützung bei jeglichen Arbeiten am und im Kühler. Rolf Epking danke ich für tatkräftige Unterstützung am Kontrollsystem und IT-Fragen im Allgemeinen.

Der Arbeitsgruppe Blaum im Ganzen, dem CSR Team und dem Ecoool-Team danke ich für die herausragende Arbeitsatmosphäre an einem spannenden Projekt und eine schöne gemeinsame Zeit.

Zuletzt möchte ich meiner Familie, für ihre bedingungslose Unterstützung über all die Jahre, sowie meiner Freundin Shaohan, dafür an meiner Seite zu stehen, danken. Auch danke ich meinen Freunden Dennis und Sunny, für eine tolle gemeinsame Doktorandenzeit in Heidelberg und unterwegs in Deutschland.